POLITECNICO DI TORINO

SCUOLA DI DOTTORATO

Dottorato in Matematica per le Scienze dell'Ingegneria

Ph.D. Thesis

Cell and cell-aggregate mechanics: remodelling, growth and interaction with the extracellular environment.

Chiara GIVERSO

Supervisor
Prof. Luigi Preziosi

March 2013

Dedicated to
Pietro

Acknowledgments

Alla conclusione di questi tre anni di dottorato, mi sembra doveroso ringraziare le persone che mi sono state vicino ed hanno contribuito al mio percorso.

Anzitutto, un grazie al Prof. Luigi Preziosi per avermi seguito con pazienza durante il lavoro di questi anni, trasmettendomi l'entusiasmo per la ricerca.
Un grazie ad Dr. Alfio Grillo, conosciuto durante l'ultimo anno di questo mio percorso, ma che fin da subito ha saputo coinvolgermi nei suoi studi ed allo stesso tempo immergersi nei miei.

Un ringraziamento speciale va alla mia famiglia, che ha sempre supportato le mie scelte. In particolare un grazie a mia mamma, la quale mi ha trasmesso fin dalle elementari la passione per lo studio e per la matematica.
Un grazie di cuore va a Pietro, che con pazienza ha sopportato i miei sbalzi di umore e le mie paranoie da stress, incoraggiandomi ogni volta a dare il meglio di me.

Inoltre, questi anni di dottorato non sarebbero stati altrettanto divertenti, senza i miei colleghi-amici. Un grazie in particolare a Paolo, per le lunghe chiacchierate e le risate, che risolvevano ogni problema (matematico e non) ed a Stefano, per i pomeriggi e le sere passate a preparare le esercitazioni di Analisi I.
Con loro, voglio anche ringraziare Silvia, Francesco, Carlo, Matteo, Anna e Moreno.

Dai corsi seguiti durante il dottorato e dai miei studi ho imparato molto, ma ancora di piú ho imparato dalle persone che ho incontrato.

Grazie!

Contents

Introduction

The scope of this dissertation is to give a contribution to the understanding of the mathematical description of cell and cellular aggregate mechanics, focusing on remodelling and growth processes which occur inside living structures and on the interactions among cells and the extracellular environment, during the process of cell migration.

Studying the mechanical behaviour of living systems, either as isolated cells or as multicellular aggregates is of great interest both from the biological and the mathematical point of view. Indeed, cellular aggregates have been shown to play an important role in many biological phenomena and it has been recently found that many pathologies are accompanied by an alteration of cell mechanical behaviors and hence the response of soft biological tissues may serve as an important diagnostic parameter in the early detection of the disease [100, 138]. Moreover, cell mechanics plays an important role in the capability of tumor cell to proliferate inside the host tissue and then to migrate and invade the surrounding tissue, influencing tumor metastatic potential [159]. Therefore a more detailed description of aggregates mechanical properties is needed.

From the mathematical point of view, describing the mechanics of living materials is a really challenging task. Indeed, cells and biological tissues are complex materials, made of multiple subelements, characterized by a non-homogenous localization of mechanical properties inside them and a high hetereogeneity among them [153, 155]. Furthermore, cells are able to actively respond when subjected to stresses (mechanotransduction) [34, 111, 155] and to interact with each other to form tissues and multicellular aggregates in some stages of their life.
This ability of cells to deform and generate forces in an active manner and their capability to interact with each other and with the extracellular environment, coupled with their extreme complexity and the high heterogeneity in their composition and in subcellular properties outlines the need of a specific mathematical model to describe cellular dynamics.

Our goal is to make a step towards a more detailed understanding of cell and cellular aggregate mechanics, developing a comprehensive continuum model in which, from the macroscopic point of view, remodelling due to cell-cell bonds rupture, growth in response to nutrients and the influence of the surrounding healthy tissue are considered. We therefore start considering quiescent aggregates, in which cells do not proliferate and we then move towards proliferative aggregates. Finally we look at the last step of the biological process: at some stage of tumor progression, cells can eventually detach from the primary cancer mass and migrate in the extracellular environments, in order to invade the whole tissue and the whole organism. In this last step, mechanical properties of single cells may play an important role, even though they have always been neglected in mathematical models aiming at describing this phenomenon. Therefore we look at the influence on cell migration of the interplay between nucleus deformability and cell capability to actively respond as a consequence of a cell-ECM bond formation, with the aim to incorporate this information in the macroscopic model.
Our level of spatial detail is coarse enough, that we can formulate our problem in the framework of continuum mechanics, with the aid of mixture theory, when cells and extracellular fluid are separately considered. Indeed the most essential model of soft biological tissues, whose main constituents are cells and extracellular fibers composing a "solid" porous structure and an interstitial fluid, is a biphasic mixture.

This project was set in the Ph.D. in Mathematics for Engineering Sciences at the Politecnico di Torino, and, thus, both mathematical modelling and applications of analytical/numerical methods are presented. In every chapter the motivations that guided the work are highlighted, then the mathematical model is presented and an application of the model is exploited. Results are discussed at the end of each chapter. When possible, the behaviour of the solution are analytically proved and the biomechanical meaning is pointed out.
In Chapter 1, we review the basis of the classical *Theory of Mixtures*, introducing the kinematics and dynamics of multiphase mixtures, that are useful for the comprehension of this work. We also explain how these concepts can be adapted to the description of living tissues, considering structural changes inside cellular aggregates. Possible biological applications of the classical Theory of Mixture and of Continuum Mechanics in general are then exploited in the following chapters.
In particular, in Chapter 2, we apply the concepts presented in Chapter 1 to the description of a cylinder of soft biological tissue undergoing a confined compression. The influence of anelastic phenomena on the distribution of cell volumetric fraction and pressure inside the specimen is

highlighted. In this preliminary study anelastic process are assumed to be constant in time and homogeneously distributed.
In Chapter 3 the evolution of anelastic deformation is introduced. In particular anelastic phenomena are empirically related to the rupture of bonds between cells and to the reorganization of cytoskeletal structures. The model is applied to the description of cell aggregate compression, under different conditions (constant stress, constant force or constant deformation) and subsequent release. Results are compared with biological assays, when possible.
Anelastic phenomena related to growth of cells inside spheroids are then considered in Chapter 4. Here, the interplay between growth and remodelling inside tumor spheroids surrounded by healthy tissues is studied for different morphologies (e.g. necrotic liquid core or necrotic calcified core) and situations (e.g. nutrients availability, stress application, presence of surrounding healthy tissue).
We then move to the microscopic scale, with the aim of introducing information deriving from the smaller scale into continuum models. In Chapter 5 the influence of nucleus mechanical deformability and cell contractility in response to adhesive bond formation is exploited. In particular we focus on cell adhesion and deformation while entering inside cylindrical structures, composing the extracellular matrix networks.
Finally, in the Conclusions, we summarize the main achievements of this work, highlighting the improvements that have been done.

Chapter 1

Elements of classical Continuum Mechanics

In this Chapter we will give an overview of the fundamental concepts of Continuum Mechanics, without claiming to be exhaustive, but with the sole purpose of helping the comprehension of this work. In particular we will focus on mixture theory, that it is employed throughout this Thesis.
The first subsections are devoted to the introduction of some fundamental notation in the mechanics of porous media and to recall the basic concepts of the kinematics of continua, presenting both the Lagrangian and Eulerian descriptions. We then move to the classical formulation of dynamics, presenting balance laws. Finally, in the last section we will discuss the application of classical mechanics to the description of living tissues and we will described the framework of "materials with evolving natural configurations", introduced in [86, 87, 126, 143].

1.1 Theory of Mixtures

1.1.1 Preliminary Definitions

Continuum Mechanics is the mathematical description of the behaviour of deformable media under the action of external forces (possibly in a generalized sense). In this work, we shall be concerned with the study of "simple" continua, i.e., those media which can be studied in the Euclidean space or on manifolds [105] and we will not treat generalized continua, i.e., those media which may require higher order dimensional spaces (e.g., liquid crystals).
A body is said to be a continuum if the smallest characteristic length established by a certain interaction is much greater than the molecular, or atomic, characteristic distances [21, 44].

In particular this chapter is concerned with some fundamental aspects of the *theory of mixtures*, which is used this work. Mixture theory is used to model multiphase systems, i.e., bodies composed of different substances, using the principles of continuum mechanics. The basic assumption is that, at any instant of time, all phases are present at every material point. The equations governing the coarse-scale evolution of biphasic systems can be found by averaging the relations that describe the systems at a smaller scale. The averaging procedures are often based on volume- and mass-average methods [19, 80]. These assume the existence of a *Representative Elementary Volume (REV),* $\Omega(\mathbf{x}) \in \mathbb{R}^3$, which supplies information about the composition and structure of the mixture at the point $\mathbf{x} \in \mathbb{R}^3$, where $\mathbb{R}^3$ is the ambient space. The characteristic size of the REV depends on the system under investigation. The subvolume $\Omega_\alpha(t,\mathbf{x})$, where the subscript α indicates the α-constituent, represents the subset of $\Omega(\mathbf{x})$ occupied by the α-th phase at time t. The *volumetric fraction* (or *volume ratio*) of the α-constituent is

$$\phi_\alpha(t,\mathbf{x}) := \frac{|\Omega_\alpha(t,\mathbf{x})|}{|\Omega(\mathbf{x})|} \equiv \frac{1}{|\Omega(\mathbf{x})|}\int_{\Omega(\mathbf{x})} \xi_\alpha(t,\mathbf{x}+\mathbf{s})dV_\mathbf{s}$$

where $|(\cdot)|$ denotes the measure of $(\cdot)$ and $\xi_\alpha(t,\mathbf{x}+\mathbf{s})$ is the characteristic function of the α-constituent, i.e.

$$\xi_\alpha(t,\mathbf{x}+\mathbf{s}) = \begin{cases} 1 & \text{if}(t,\mathbf{x}+\mathbf{s}) \in \Omega_\alpha \\ 0 & \text{otherwise}. \end{cases}$$

In the following, the abbreviations $\mathscr{P}_\alpha$ is used to denote the α-phase in the mixture.
The distribution of mass of $\mathscr{P}_\alpha$ in Ω_α is called the *"true" mass density* of $\mathscr{P}_\alpha$, and is denoted here by $\hat{\rho}_\alpha$. The product $\rho_\alpha = \rho_\alpha(t,\mathbf{x}) = \phi_\alpha(t,\mathbf{x})\hat{\rho}_\alpha$ measures the distribution of mass of $\mathscr{P}_\alpha$ in Ω, and is called *"apparent" mass density* (or simply mass density) of $\mathscr{P}_\alpha$. The density of the mixture in $\mathbf{x}$ at time t is

$$\rho = \rho(t,\mathbf{x}) = \sum_{\alpha=1}^{N} \rho_\alpha(t,\mathbf{x})\,. \tag{1.1}$$

1.1.2 Elements of Continuum Kinematics

We formulate the kinematic description of the mixture introducing standard definitions, that can be found in several treatises about the classical Theory of Mixtures (cf., for example, [14, 21, 119, 147]).
We consider N continuous bodies $\mathscr{B}_1,\ldots,\mathscr{B}_N$. Each of them is visualized by the region it occupies in $\mathbb{R}^3$. For a mixture, these N bodies, are allowed to occupy common portions of physical space

and are called phases. Then every portion $\mathbf{x}$ in the mixture is occupied by N particles.
As in continuum theory of single materials, each phase is assigned a motion, defined by χ_α, which is called the *deformation function* for the α-constituent (or α-motion, [118]), $\chi_\alpha(t,\cdot): \mathscr{B}_\alpha \mapsto \mathbb{R}^3$, such that

$$\mathbf{x} = \chi_\alpha(t,\mathbf{X}_\alpha), \tag{1.2}$$

where $\mathbf{X}_\alpha$ is the position of a particle of the α-body, or constituent, in its initial configuration and $\mathbf{x} \in \mathbb{R}^3$ is the spatial position occupied at time t by the same particle. We remark that with lower cases we refer to *spatial coordinates*, while upper cases indicates *material coordinates*.
The function χ_α is assumed invertible for each time t and every $\alpha = 1,\ldots,N$

$$\mathbf{X}_\alpha = \chi_\alpha^{-1}(t,\mathbf{x}). \tag{1.3}$$

The invertibility of the map χ_α ensures that a particle of $\mathscr{B}_\alpha$ at $\mathbf{X}_\alpha$ cannot occupy two spatial positions (i.e., no ruptures) and that two particles with positions $\mathbf{X}_{\alpha,1}$ and $\mathbf{X}_{\alpha,2} \neq \mathbf{X}_{\alpha,1}$ cannot occupy the same spatial position (i.e., no overlapping). Moreover, all functions are assumed to be sufficiently smooth, in order to make any needed mathematical operations meaningful.
The gradient of deformation for $\mathbf{X}_\alpha$ at time time t is defined by the linear transformation

$$\mathbb{F}_\alpha = \mathrm{Grad}\chi_\alpha(t,\mathbf{X}_\alpha), \tag{1.4}$$

where the symbol Grad denotes the gradient computed with respect to material coordinates (material gradient), i.e.

$$F_{\alpha,jK} = \frac{\partial x_j}{\partial X_{\alpha,K}}, \tag{1.5}$$

with $\mathbb{F}_\alpha = F_{\alpha,jK}\,\mathbf{i}_j \otimes \mathbf{i}_K$, $\mathbf{x} = x_j\,\mathbf{i}_j$ and $\mathbf{X}_\alpha = X_{\alpha,K}\,\mathbf{i}_K$.
The *determinant* of $\mathbb{F}_\alpha$, $\det(\mathbb{F}_\alpha) = J_\alpha$ accounts for the change of volume of the α-constituent and it is always positive, being χ_α invertible.
The linear transformation inverse to $\mathbb{F}_\alpha$ is

$$\mathbb{F}_\alpha^{-1} = \mathrm{grad}\chi_\alpha^{-1}(t,\mathbf{x}), \tag{1.6}$$

where the symbol grad denotes the gradient with respect to spatial coordinates.
We remark that

$$\mathbb{F}_\alpha\mathbb{F}_\alpha^{-1} = \mathbb{F}_\alpha^{-1}\mathbb{F}_\alpha = \mathbb{I}, \tag{1.7}$$

where $\mathbb{I}$ is the *identity* linear transformation.
The *velocity* of $\mathbf{X}_\alpha$ at time t is defined as the time derivative of χ_α

$$\boldsymbol{v}_\alpha(t,\mathbf{x}) = \boldsymbol{v}_\alpha(t,\chi_\alpha(t,\mathbf{X}_\alpha)) = \frac{\partial \chi_\alpha(t,\mathbf{X}_\alpha)}{\partial t} \tag{1.8}$$

where the subscript α means that the material derivative follows the motion of the α-constituent and velocities can be regarded as functions of $(t,\mathbf{x})$, due to (1.3). It is possible to define the *velocity gradient* at $(t,\mathbf{x})$ as

$$\mathbb{L}_\alpha = \operatorname{grad} \boldsymbol{v}_\alpha(t,\mathbf{x})\,. \tag{1.9}$$

Applying the chain rule, it is possible to show that

$$\mathbb{L}_\alpha = \dot{\mathbb{F}}_\alpha \mathbb{F}_\alpha^{-1}\,. \tag{1.10}$$

The *mean velocity*, also called the *velocity of the mixture* at $(t,\mathbf{x})$ is

$$\boldsymbol{v} = \frac{1}{\rho}\sum_{\alpha=1}^{N} \rho_\alpha \boldsymbol{v}_\alpha(t,\mathbf{x})\,. \tag{1.11}$$

In particular, considering a two-phase mixture, composed of a solid, $\mathscr{P}_s$, and a liquid phase, $\mathscr{P}_\ell$, the velocities $\boldsymbol{v}_s$ and $\boldsymbol{v}_\ell$, characterise the standard motion of $\mathscr{P}_s$ and $\mathscr{P}_\ell$.
The velocity of the centre of mass of the mixture, which is defined as in (1.11), becomes

$$\boldsymbol{v} := \frac{\rho_s \boldsymbol{v}_s + \rho_\ell \boldsymbol{v}_\ell}{\rho}\,, \tag{1.12}$$

where, $\rho := \rho_\ell + \rho_s$, from 1.1, denotes the mass density of the mixture as a whole.
One of the most used kinematic quantities in mixture theory is the relative velocity of $\mathscr{P}_\ell$ with respect to $\mathscr{P}_s$, $\boldsymbol{w}_{\ell s} := \boldsymbol{v}_\ell - \boldsymbol{v}_s$. Other important quantities are the fluctuation velocities $\tilde{\boldsymbol{v}}_\ell := \boldsymbol{v}_\ell - \boldsymbol{v}$ and $\tilde{\boldsymbol{v}}_s := \boldsymbol{v}_s - \boldsymbol{v}$, which describe the relative motion of each phase with respect to the motion of the mixture as a whole.
The velocity gradient of the mixture at $(t,\mathbf{x})$ is

$$\mathbb{L} = \operatorname{grad} \boldsymbol{v}(t,\mathbf{x})\,. \tag{1.13}$$

We recall that, the *material derivative*, following the motion of the α-constituent, of a differentiable function of $(t,\mathbf{x})$, that we will generically call $g(t,\mathbf{x})$, is defined by

$$\dot{g}_\alpha = D_\alpha g = \frac{\partial g}{\partial t}(t,\mathbf{x}) + \text{grad}\,(g(t,\mathbf{x}))\boldsymbol{v}_\alpha(t,\mathbf{x})\,, \tag{1.14}$$

whereas the derivative following the motion of the mixture is

$$\dot{g} = Dg = \frac{\partial g}{\partial t}(t,\mathbf{x}) + \text{grad}\,(g(t,\mathbf{x}))\boldsymbol{v}(t,\mathbf{x})\,. \tag{1.15}$$

Therefore, for each phase, we denote by $\boldsymbol{a}_\alpha$ (with $\alpha = \ell,s$ in the case of a biphasic mixture) the acceleration of that phase, which is defined by the convective derivative of $\boldsymbol{v}_\alpha$ with respect to the motion of the phase $\mathscr{P}_\alpha$, i.e.

$$\boldsymbol{a}_\alpha := \partial_t \boldsymbol{v}_\alpha + \text{grad}(\boldsymbol{v}_\alpha)\boldsymbol{v}_\alpha\,, \tag{1.16}$$

where $\partial_t(\cdot)$ stands for the partial derivative of its argument with respect to t. The acceleration of the mixture is indicated by $\boldsymbol{a}$ and is defined as the convective derivative of $\boldsymbol{v}$ with respect to the motion of the mixture as a whole, i.e.

$$\boldsymbol{a} := \partial_t \boldsymbol{v} + \text{grad}\,(\boldsymbol{v})\boldsymbol{v}. \tag{1.17}$$

1.1.3 Balance laws

Balance laws relate physical quantities that govern the mechanics of materials. Balance principles can be expressed either in integral (global) form or in differential (local) form [21]. In regions of space where physical quantities vary sufficiently smoothly, balance laws are equivalent to differential field equations; on the other hand, in the presence of surfaces of discontinuity, balance laws in a strong form have to be supplemented by jump conditions. In the following, the notion of conservation of mass and linear momentum, that will be used throughout this thesis, are presented. In the case of mixtures, when we consider balance laws, we have to refer to the balance of both each constituent and the mixture as a whole.

1.1.3.1 Balance of Mass

If a mass exchange occurs among the phases, associated with each constituent of the mixture, there is the *mass supply* term, $\Gamma_\alpha(t,\mathbf{x})$, which represents the rate of production/depletion of the α-component per unit volume at time t in the position $\mathbf{x}$. The integral formulation of the mass

balance for each constituent in a fixed spatial volume, $\mathscr{V}$ is

$$\frac{\partial}{\partial t}\int_{\mathscr{V}} \rho_\alpha dV = -\int_{\partial\mathscr{V}} \rho_\alpha \boldsymbol{v}_\alpha \cdot \mathbf{n} dS + \int_{\mathscr{V}} \rho_\alpha \Gamma_\alpha dV\,, \tag{1.18}$$

where $\mathbf{n}$ is the outward vector of the element of area dS, $\mathscr{V}$ is the volume in which the balance is written, whereas $\partial\mathscr{V}$ is the boundary of this volume.
For what concerns the mixture, the balance of mass reads

$$\frac{\partial}{\partial t}\int_{\mathscr{V}} \rho dV = -\int_{\partial\mathscr{V}} \rho \boldsymbol{v} \cdot \mathbf{n} dS\,, \tag{1.19}$$

provided that there's no net production of mass inside the mixture, i.e.,

$$\sum_{\alpha=1}^{N} \int_{\mathscr{V}} \rho_\alpha \Gamma_\alpha dV = 0\,. \tag{1.20}$$

By means of the divergence theorem (1.18) leads to

$$\int_{\mathscr{V}} \frac{\partial}{\partial t}\rho_\alpha dV = -\int_{\mathscr{V}} \mathrm{div}(\rho_\alpha \boldsymbol{v}_\alpha) dV + \int_{\mathscr{V}} \rho_\alpha \Gamma_\alpha dV\,. \tag{1.21}$$

Requiring that (1.21) holds for every spatial volumes, we can localize the mass balance for the α-constituent and obtain the Eulerian, local form of the balance of mass for each component of the mixture

$$\frac{\partial}{\partial t}\rho_\alpha + \mathrm{div}(\rho_\alpha \boldsymbol{v}_\alpha) = \rho_\alpha \Gamma_\alpha\,. \tag{1.22}$$

In the same way it is possible to write the local form of (1.19)

$$\frac{\partial}{\partial t}\rho + \mathrm{div}(\rho \boldsymbol{v}) = 0\,, \tag{1.23}$$

which is valid if $\sum_{\alpha=1}^{N} \rho_\alpha \Gamma_\alpha = 0$. Equivalent forms of (1.22) and (1.23) are

$$\dot{\rho}_\alpha + \rho_\alpha \mathrm{div}(\boldsymbol{v}_\alpha) = \rho_\alpha \Gamma_\alpha\,, \tag{1.24}$$

$$\dot{\rho} + \rho \mathrm{div}(\boldsymbol{v}) = 0\,, \tag{1.25}$$

where material derivatives are defined as in (1.14) and (1.15).
In particular, referring to biphasic mixtures, it is useful to rewrite (1.24) with respect to the motion of the solid phase, for both constituents. Thus, the mass balance (1.22), for the solid and

the fluid phase specify to

$$D_s\rho_s + \rho_s \mathrm{div}(\boldsymbol{v}_s) = \rho_s \Gamma_s, \tag{1.26}$$

$$D_s\rho_\ell + \rho_\ell \mathrm{div}(\boldsymbol{v}_s) + \mathrm{div}(\rho_\ell \boldsymbol{w}_{\ell s}) = \rho_\ell \Gamma_\ell, \tag{1.27}$$

Multiplying (1.26) and (1.27) by $J = J_s$, and passing to the material description lead to the following form of the mass balance laws

$$\dot{\overline{(J\rho_s)}} = J\rho_s \Gamma_s, \tag{1.28}$$

$$\dot{\overline{(J\rho_\ell)}} + \mathrm{Div}(J\rho_\ell \mathbb{F}^{-1}\boldsymbol{w}_{\ell s}) = J\rho_\ell \Gamma_\ell\,, \tag{1.29}$$

that follow from the identity $\dot{J}_\alpha = J_\alpha \,\mathrm{div}\boldsymbol{v}_\alpha$. The operators "Div" and "Grad" are the divergence and gradient operators computed with respect to the material coordinates. They are related to "div" and "grad" by the formulae $\mathrm{grad}(\boldsymbol{A}) = \mathrm{Grad}(\boldsymbol{A}_\chi)\mathbb{F}^{-1}$ and $\mathrm{div}(\boldsymbol{A}) = \mathrm{Grad}(\boldsymbol{A}_\chi) : \mathbb{F}^{-T}$, where $\boldsymbol{A}$ is a given vector field, the symbol ":" denotes the inner product between tensors, and the index "χ", which will be dropped from here on, means $\boldsymbol{A}_\chi(t,\cdot) = \boldsymbol{A}(t,\cdot)\circ\chi_s(t,\cdot)$.

A simplification of the mass balance presented before, follows from requiring that the true mass density of the constituent in the mixture, $\hat{\rho}_\alpha$, is constant, so that $\mathscr{P}_\alpha$ is incompressible. For a mixture, with incompressible components, eq. (1.22) can be rephrased in terms of ϕ_α, giving

$$\frac{\partial}{\partial t}\phi_\alpha + \mathrm{div}(\phi_\alpha \boldsymbol{v}_\alpha) = \phi_\alpha \Gamma_\alpha\,. \tag{1.30}$$

Eq. (1.26) and (1.27), for an incompressible biphasic mixture read

$$D_s\phi_s + \phi_s \mathrm{div}(\boldsymbol{v}_s) = \phi_s \Gamma_s\,, \tag{1.31}$$

$$D_s\phi_\ell + \phi_\ell \mathrm{div}(\boldsymbol{v}_s) + \mathrm{div}(\phi_\ell \boldsymbol{w}_{\ell s}) = \phi_\ell \Gamma_\ell\,. \tag{1.32}$$

Also in this case, passing to the material description, we have

$$\dot{\overline{(J\phi_s)}} = J\phi_s \Gamma_s, \tag{1.33}$$

$$\dot{\overline{(J\phi_\ell)}} + \mathrm{Div}(J\phi_\ell \mathbb{F}^{-1}\boldsymbol{w}_{\ell s}) = J\phi_\ell \Gamma_\ell\,. \tag{1.34}$$

Moreover, if we assume that the void spaces of the porous medium are completely filled with the fluid, the medium is said to be *saturated*, and the condition $\phi_s + \phi_\ell = 1$ applies at all times in every point. Granted the incompressibility condition and the saturation constraint, (1.29) takes

the simpler form

$$\mathrm{Div}[J\mathbb{F}^{-1}\boldsymbol{q}_{\ell s}] = -\dot{J} + J(\phi_s\Gamma_s + \phi_\ell\Gamma_\ell)\,, \tag{1.35}$$

with $\boldsymbol{q}_{\ell s} := \phi_\ell \boldsymbol{w}_{\ell s}$.

1.1.3.2 Balance of Linear Momentum

Together with mass balance, also the balance of momentum has to be studied. As done for the mass balance, also in this case we present both the balance of momentum of the single constituents and of the mixture as a whole.
The linear momentum balance for the α-constituent in a fixed volume $\mathscr{V}$ is

$$\frac{\partial}{\partial t}\int_{\mathscr{V}} \rho_\alpha \boldsymbol{v}_\alpha dV = -\int_{\partial\mathscr{V}} \rho_\alpha \boldsymbol{v}_\alpha (\boldsymbol{v}_\alpha \cdot \mathbf{n}) dS + \int_{\partial\mathscr{V}} \mathbb{T}_\alpha \mathbf{n} dS + \int_{\mathscr{V}} (\rho_\alpha \mathbf{b}_\alpha + \mathbf{m}_\alpha + \rho_\alpha \Gamma_\alpha \boldsymbol{v}_\alpha) dV\,, \tag{1.36}$$

where $\mathbb{T}_\alpha$ is the Cauchy stress tensor of the α-constituent [21]. The term containing $\mathbb{T}_\alpha$ represents contact forces on the α-constituent in $\mathscr{V}$ resulting from the contact on $\partial\mathscr{V}$ with the α-constituent outside $\mathscr{V}$. The term $\mathbf{m}_\alpha$ represents the momentum supply [21, 148], also called local or internal body force, since it accounts for the local interactions of the constituent with each other, whereas $\mathbf{b}_\alpha$ is the external body forces density and thus $\int_{\mathscr{V}} \rho_\alpha \mathbf{b}_\alpha dV$ stands for external forces acting on the α-constituent. The Eulerian local form of (1.36) is given by

$$\frac{\partial}{\partial t}(\rho_\alpha \boldsymbol{v}_\alpha) + \mathrm{div}(\rho_\alpha \boldsymbol{v}_\alpha \otimes \boldsymbol{v}_\alpha) = \mathrm{div}\mathbb{T}_\alpha + \rho_\alpha \mathbf{b}_\alpha + \mathbf{m}_\alpha + \rho_\alpha \Gamma_\alpha \boldsymbol{v}_\alpha\,. \tag{1.37}$$

By differentiating the l.h.s and imposing (1.22), eq. (1.37) can be rewritten as

$$\rho_\alpha \boldsymbol{a}_\alpha = \mathrm{div}\mathbb{T}_\alpha + \rho_\alpha \mathbf{b}_\alpha + \mathbf{m}_\alpha\,, \tag{1.38}$$

which is the most common formulation of the local version of the α-constituent momentum balance.
Then we shall consider the axioms of balance of linear momentum for the mixture. The external body force for the mixture is defined by

$$\mathbf{b} = \frac{1}{\rho}\sum_{\alpha=1}^{N} \rho_\alpha \mathbf{b}_\alpha\,.$$

Truesdall and Toupin [148] introduces the *inner part* of the stress tensor for the mixture, which is defined by

$$\tilde{\mathbb{T}} = \sum_{\alpha=1}^{N} \mathbb{T}_\alpha \,,$$

while the Cauchy stress tensor of the mixture is

$$\mathbb{T} = \tilde{\mathbb{T}} - \sum_{\alpha=1}^{N} \rho_\alpha \tilde{\boldsymbol{v}}_\alpha \otimes \tilde{\boldsymbol{v}}_\alpha \,, \tag{1.39}$$

where $\tilde{\boldsymbol{v}}_\alpha = \boldsymbol{v}_\alpha - \boldsymbol{v}$.

Adding together (1.37) for every constituent in the mixture and applying the definitions just introduced, as well as those of the accelerations $\boldsymbol{a}$ and $\boldsymbol{a}_\alpha$, the local form of linear momentum balance for the mixture reads

$$\rho \boldsymbol{a} = \mathrm{div}\mathbb{T} + \rho \mathbf{b} \,, \tag{1.40}$$

enforcing the condition

$$\sum_{\alpha=1}^{N} \mathbf{m}_\alpha + \rho_\alpha \Gamma_\alpha \boldsymbol{v}_\alpha = 0 \,. \tag{1.41}$$

An explanation of the physical meaning of (1.41) in terms of pore scale considerations can be found, for example, in [80].

Finally, neglecting the inertial forces of every phases, the balances of momentum (1.37) and (1.40) become

$$\mathrm{div}(\mathbb{T}_\alpha) + \rho_\alpha \mathbf{b}_\alpha + \mathbf{m}_\alpha = 0 \tag{1.42}$$

$$\mathrm{div}(\mathbb{T}) + \rho \mathbf{b} = \mathrm{div}\left(\tilde{\mathbb{T}}\right) + \rho \mathbf{b} = 0,. \tag{1.43}$$

By means of the Piola transformations of (1.42) an (1.43), the momentum balance laws of the mixture can be written with respect to the material placement, i.e.,

$$\mathrm{Div}(\mathbb{P}_\alpha) + J\rho_\alpha \mathbf{b}_\alpha + J\mathbf{m}_\alpha = 0 \,, \tag{1.44}$$

$$\mathrm{Div}(\mathbb{P}) + J\rho \boldsymbol{b} = 0 \,, \tag{1.45}$$

where

$$\mathbb{P}_\alpha := J\mathbb{T}_\alpha\mathbb{F}^{-T}, \tag{1.46}$$

$$\mathbb{P} \equiv \tilde{\mathbb{P}} := \sum_{\alpha=1}^{N} \mathbb{P}_\alpha \tag{1.47}$$

denote, respectively, the first Piola-Kirchhoff stress tensors of the α-constituent and of the mixture.
We remark that, when the saturation constraint holds, a Lagrange multiplier, that we will name p (because it has the meaning of pressure), shows up in the Cauchy stress tensor. In this dissertation, we will call $\mathbb{T}_\alpha$ the total Cauchy stress tensor of the α-constituent, whereas, $\mathbb{T}^*_\alpha$ denotes its constitutive part, i.e.

$$\mathbb{T}^*_\alpha = \mathbb{T}_\alpha + \phi_\alpha p\mathbb{I}.$$

In order to close the mathematical problem resulting from (1.21), (1.22), (1.37) and (1.40) it is necessary to provide constitutive laws on the stresses $\mathbb{T}_\alpha$ of every constituent in the mixture and the force densities $\rho_\alpha\mathbf{b}_\alpha$ and $\mathbf{m}_\alpha$.

1.1.4 Elements of the Theory of Constitutive Law

As it should be clear form Section 1.1.3, balance laws relate physical quantities, providing a set of necessary conditions that dependent variables must fulfil. However, balance laws are not sufficient to formulate the mechanical problem in a self-consistent form since they involve a number of unknowns which is bigger than the number of equations. Therefore, a certain number of additional non-redundant conditions have to be imposed. These conditions must be consistent with phenomenological observations and experimental results, and must be able to predict the mechanical behaviour of the body. In particular, referring to the classical theory of Continuum Mechanics, these conditions must be consistent with the Clausius - Duhem inequality [38].
These conditions are the so-called *Constitutive Laws*.
We will not present the theory of constitutive laws and the interested reader should refer to the principal books in Continuum Mechanics (e.g. [21, 77, 105]).
In the following, when a particular constitutive law is required, a short explanation of the different terms involved is presented. Moreover some details on the requirements that constitutive laws should satisfy are presented in Section 1.2.4, in a framework suitable to describe living systems.

1.2 Living tissues in the framework of Continuum Mechanics

Cells and biological tissues are complex materials, made of multiple elements [153]: each cell is bounded by the plasma membrane to form a closed object containing the nucleus and a fluid, the cytosol (made of water, soluble proteins, sugar and salt), where numerous organelles are immersed. An important intracellular structure, that plays a key role in many biological process (e.g. maintaining cell shape, enabling movement, aiding cellular division) and that strongly affects cell mechanical behavior, is the cytoskeleton, a complex meshwork of polymers crossing through the cytosol. Each subcellular element is different from the other and mechanical properties are non-homogenously localized inside each of them [155]. For instance, cytoplasm properties strongly depend on the amount of actin or tubulin and on the degree of polymerisation of these filaments. Similarly, the membrane has a bending modulus which is dependent on the number and the type of proteins embedded in it [155]. This high heterogeneity in cell composition and in subcellular properties makes mechanical response difficult to be modelled even for a single cell. In addition, cellular materials are different from usual materials because they can develop an active response when subjected to stresses. This response is due to mechanotransduction, which is the ability of cells to transform mechanical external stresses into biochemical signals (and vice versa) in order to transfer information to and from the nucleus [34, 111, 155]. This ability of cells to deform and generate forces in an active manner, coupled with their extreme complexity and their non linear response to mechanical stimuli, outlines the need of a specific mathematical model to describe cellular dynamics.

Furthermore, cells are able to interact with each other to form tissues and multicellular aggregates in some stages of their life. The rheological properties of such materials are quite uncommon, because they contain both cells and fluids embedded inside each cell and in the extracellular matrix (ECM) among them. It is then known that not only the intrinsic properties of the base components - cells and collagen - but also their relative concentration can affect the rheological properties of multicellular aggregates [35, 132, 154, 155].

Therefore there are big theoretical difficulties in classifying a cell aggregate as a liquid or as a solid [10]. Indeed, treating it like a fluid may bring some simplifications (e.g. to deal with velocities rather than deformations). However, the fact that aggregates are made of both intracellular and extracellular liquid and elastic solid components demonstrates the simplifications introduced by such an hypothesis. On the other hand, it is not correct to consider multicellular spheroids as standard elastic solids, because they are composed of living material: cells forming the aggregates continuously duplicate and die, the ECM is constantly remodelled by the same cells and, even in absence of growth and death, cells can reorganize in response to an external mechanical

stimulus [10]. Therefore it is impossible to define a time-independent "natural" state, towards which the system will naturally evolve.
Due to this complexity, the mechanical behavior of multicellular systems is still far from being understood [10] and most of our knowledge concerning the rheological and mechanical properties of cell aggregates comes from previous studies on soft biological tissues [154, 155], usually corresponding to visco-elastic materials or to non-Newtonian fluids [63].

A biphasic mixture consisting of a solid and a fluid phase is perhaps the most essential model of soft biological tissues and multicellular aggregates [1, 3, 9, 74, 117]. The solid phase that forms the porous structure represents cells and the network of fibers, whereas the fluid phase stands for the interstitial fluid, that completely saturates the pores of the solid and may move throughout it.
In this work, the medium is assumed to be *saturated*, and the condition $\phi_s + \phi_\ell = 1$ applies at all times to all points. It is sometimes assumed that cells and liquid only form a portion of the tissue and that they can occupy a prescribed volume fraction, i.e., $\phi_s + \phi_\ell = \phi_{max}$. All the equations presented in the previous sections hold with $\alpha = s,\ell$.
According to [118], we call $\mathscr{B}_r$ the subset of the three-dimensional Euclidean space $\mathbb{R}^3$ in which the solid skeleton in the mixture is embedded. We denote by $\mathbf{X}$ the coordinates of the centroid of the REV associated with $\mathscr{B}_r$. The set $\mathscr{B}_r$ is also said to be the "reference configuration" and the coordinates $\mathbf{X}$ may be called "material coordinates". A smooth motion of $\mathscr{P}_s$, which is referred to as s-motion in [118], is a sequence of mappings $\chi_s(t,\cdot) : \mathscr{B}_r \mapsto \mathbb{R}^3$, such that $\mathbf{x} = \chi_s(t,\mathbf{X}) \in \mathbb{R}^3$. The material gradient of the map χ_s equals the deformation gradient $\mathbf{F}_s := \mathrm{Grad}(\chi_s)$. In order to describe the kinematics of the fluid phase $\mathscr{P}_\ell$, as done in [118], we introduce the material manifold $\mathscr{B}_\ell$, which consists of fluid particles. A fluid particle, labelled by X_ℓ, is placed in the Euclidean space by means of an embedding that locates the particle at $\mathbf{x}$. A smooth motion of $\mathscr{P}_\ell$, the ℓ-motion, is a sequence of mappings defined by $\chi_\ell(t,\cdot) : \mathscr{B}_\ell \mapsto \mathbb{R}^3$, such that $\mathbf{x} = \chi_\ell(t,X_\ell)$. The definitions of s- and ℓ-motion imply the chain of identities

$$\mathbf{x} = \chi_s(t,\mathbf{X}) = \chi_\ell(t,X_\ell), \tag{1.48}$$

which means that both the solid and the fluid phase co-exist at the same point $\mathbf{x}$ of the Euclidean space.

The main difficulty in describing cell aggregates and biological tissues consists in the fact that even in the absence of growth the ensemble of cells undergoes an internal re-organization

in response to an applied strain or stress, which is macroscopically translated in anelastic deformation. Therefore, when the structural changes of the tissue are considered beside deformation, the picture sketched in the previous sections becomes more complex. With the term *structural changes* we mean processes that contribute to modify the properties of the tissue (e.g., the stiffness, diffusivity and permeability) in response to growth, mass exchange between the fluid and the solid phase, and re-organisation of cells and fibrils. Even though these phenomena are all intermingled, a conceptual classification is usually pointed out in the biomechanical literature (cf., for example, Fung [64] and Taber [143]), where *growth* is said to lead to the variation of mass of a body, while the re-organisation of cells and fibrils is referred to as *remodelling*.
From the point of view of Continuum Mechanics, and in particular in the Theory of Plasticity, the structural changes of the solid phase of a tissue are modelled by means of a class of deformations that describe how the material particles are distributed in the tissue. The mathematical object used to define these deformations is a second-order tensor, which we denote by $\mathbb{F}_a$. With the terminology of [43], $\mathbb{F}_a$ measures the material inhomogeneities triggered by growth, mass exchange processes, and cellular re-organisation. There is a strong conceptual difference between the standard deformations and those described by $\mathbb{F}_a$: whereas the former ones are related to the gradient of displacement of the body, the latter deformations need not to be the gradient of any vector field. Rather, they are primitive entities that define, together with displacements, the parameters that are necessary and sufficient for describing the kinematics of deformable bodies with variable internal structure. When $\mathbb{F}_a$ is not the gradient of any vector field (not integrable), it is said to be incompatible. Physically, this represents the case in which material points lose their geometric compatibility and the reorganization possibly leads to residual stresses [108]. The tensor $\mathbb{F}_a$ represents the anelastic part of the deformation gradient tensor, $\mathbb{F}_s$, which describes the overall change of shape of a solid. The tensor $\mathbb{F}_a$ individuates an evolving relaxed configuration of body elements. The total evolution of the tissue is given through the deformation tensor $\mathbb{F}$, which is a mapping from the tangent space related to the reference configuration, $\mathscr{B}_r$, onto the tangent space related to the current configuration $\mathscr{B}_t$ that represents how the body is deforming locally. Then it is possible to consider the map from $\mathscr{B}_r$ to $\mathscr{B}_t$ as composed of two parts: the first one describes rearrangement of the internal structure, whereas the second one refers to the accomodating part of the deformation. In many cases the first part is related to anelastic processes, whereas the second part refers to elastic deformations. This consideration leads to the introduction of a virtual configurations: the "natural" (or locally stress-free) state $\mathscr{B}_n$, which takes into account cell internal re-organization due to anelastic effects [120].

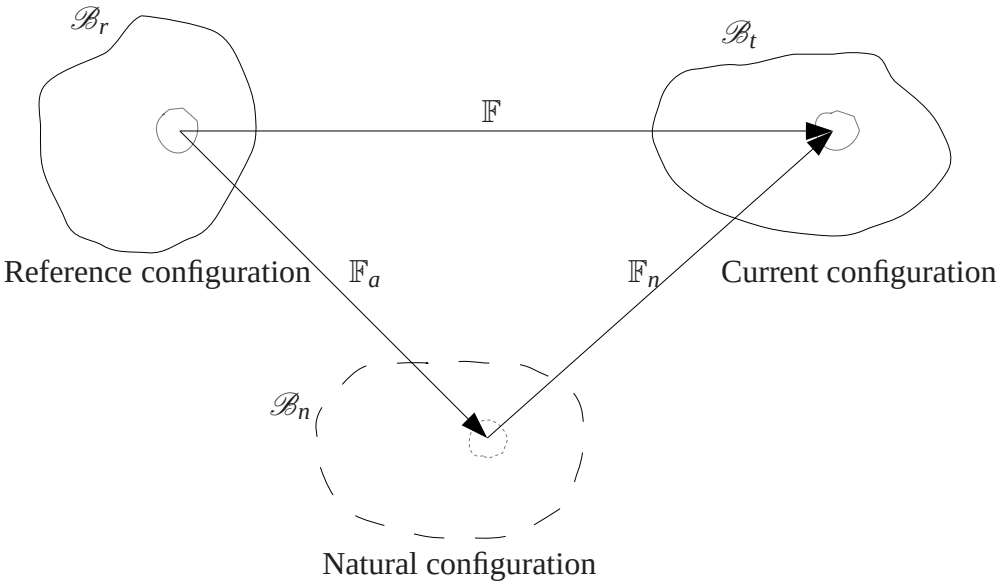

Figure 1.1: Diagram of the states from the original unstressed configuration $\mathscr{B}_r$ to the current configuration $\mathscr{B}_t$, in the framework of multiple natural configurations. $\mathscr{B}_n$ represents the natural state, which takes into account cell internal re-organization.

The accommodating deformation, which determines the actual configuration of the body from the relaxed one, also called *natural configuration*, is denoted by $\mathbb{F}_n$, and obeys the multiplicative decomposition $\mathbb{F}_s = \mathbb{F}_n\mathbb{F}_a$ [98]. In many cases, $\mathbb{F}_n$ is said to be the elastic part of $\mathbb{F}_s$ and it is indicated with $\mathbb{F}_e$.

This setting, introduced in [120] in order to describe non-living materials undergoing structural changes, was then successfully applied [1, 3, 86, 87, 126, 143], to describe the growth and remodelling mechanisms of several tissues, allowing to model separately the contribution due to growth from the one due to deformation alone (see [6] for a review).

The rate of anelastic deformation, $\mathbb{L}_a = \dot{\mathbb{F}}_a(\mathbb{F}_a)^{-1}$, is related to the variation of body mass in such a way that that the mass density of the body is constant when measured with respect to the relaxed configuration [43].

To be more specific, $\mathbb{F}_a$ may be decomposed as the product of tensors, which distinguish the anelastic deformations associated with growth from those associated with the reorganization of cells and fibers, without any mass exchange.

In particular, in Chapter 2 we will consider the simpler case, in which $\mathbb{F}_a$ is prescribed and constant in time. In Chapter 3 the anelastic part of deformation is related to remodelling processes, whereas in Chapter 4, the contribution due to growth is added and therefore $\mathbb{F}_a = \mathbb{F}_p\mathbb{F}_g$, where $\mathbb{F}_g$ is the term related to pure growth, whereas $\mathbb{F}_p$ is the term related to remodelling. In order to make consistent the notation presented in the previous section with the theory for materials with evolving natural configurations, we present a formulation that follows, with some slight differences, the picture put forward by Quiligotti [118].

1.2.1 Kinematics

Referring to the definition introduced in Section 1.1.2, in order to complete the kinematic analysis of the biphasic mixture undergoing structural changes, such as in the biological case, we have to introduce a non-standard descriptor in addition to the standard velocities collected in $\mathscr{V}_{\text{st}} := \{\boldsymbol{v}_s, \boldsymbol{w}_{\ell s}\}$. This descriptor has to model the internal structural change of the solid phase, $\mathscr{P}_s$, in response to interactions that lead to the variation and redistribution of its mass [74]. These types of structural evolution are viewed as anelastic processes, as reported, for example, in [1, 3, 40, 43, 86, 87, 104, 126]. Therefore, the kinematic descriptor of these processes is the tensor of anelastic deformation, $\mathbb{F}_a$, which is related to the rate of anelastic deformation, $\mathbb{L}_a := \dot{\mathbb{F}}_a\mathbb{F}_a^{-1}$.

1.2.2 Mass balance

The variations of volume of the solid phase due to the elastic and the anelastic deformations are denoted by $J_n = \det(\mathbb{F}_n)$ and $J_a = \det(\mathbb{F}_a)$, respectively. The multiplicative decomposition of $\mathbb{F}_s$ implies $J_s = J_nJ_a$. The determinants J_s, J_n and J_a are strictly positive.
In the following, the index "s" associated with $\mathbb{F}_s$ and J_s will be dropped for the sake of simpler notation.
For what concerns the balance of mass, we remark that the product $\rho_{sr} := J\rho_s$ in (1.28) defines the mass of $\mathscr{P}_s$ measured per unit volume of $\mathscr{B}_r$; indeed ρ_s is the mass of $\mathscr{P}_s$ measured per unit volume of $\mathscr{B}_t$ and J represents volumetric changes from $\mathscr{B}_r$ to $\mathscr{B}_t$.
Using the fact that $J = J_nJ_a$, the quantity ρ_{sr} can be rewritten as

$$\rho_{sr} = J_nJ_a\rho_s = J_a\rho_{sn}, \tag{1.49}$$

where $\rho_{sn} := J_n \rho_s$ indicates the mass density of $\mathscr{P}_s$ computed with respect to the natural configuration $\mathscr{B}_n$. Furthermore, substituting (1.49) into (1.28) yields

$$\mathrm{tr}(\mathbb{L}_a)\rho_{sn} + \dot{\rho}_{sn} = \rho_{sn}\Gamma_s\,, \tag{1.50}$$

being $\dot{J}_a = J_a \mathrm{tr}(\mathbb{L}_a)$ [74]. We enforce now the condition that the variation of body mass is compensated by the rate $\mathrm{tr}(\mathbb{L}_a)$, which implies that the mass density ρ_{sn} is constant in time. Thus the following relations hold

$$\Gamma_s = \mathrm{tr}(\mathbb{L}_a), \quad \rho_{sn} = \rho_{s0}\,, \tag{1.51}$$

where ρ_{s0} may be a function of material coordinates only. A consequence of (1.49)–(1.51) is that the solution to (1.28) is given by

$$\rho_s = \frac{\rho_{sr}}{J} = \frac{\rho_{sn}}{J_n} = \rho_{sn}\frac{J_a}{J} = \rho_{s0}\frac{J_a}{J}\,. \tag{1.52}$$

This means that the apparent density of the solid phase, ρ_s, is determined if the constant mass distribution ρ_{sn} is assigned, and the volumetric deformations J and J_a are known.

A simplification may be obtained under the hypothesis that the true mass density $\hat{\rho}_s$ is a given constant. This allows to reformulate (1.52) in terms of the stronger condition

$$\phi_s = \frac{\phi_{sn}}{J_n} = \phi_{sn}\frac{J_a}{J}\,. \tag{1.53}$$

In (1.53), ϕ_{sn} denotes the volumetric fraction of $\mathscr{P}_s$ "seen" by $\mathscr{B}_n$. We remark that ϕ_{sn} is constant and should be regarded as a known quantity of the model.
For the liquid phase, considering a saturated incompressible mixture, eq. (1.35) continues to hold.

1.2.3 Momentum balance

The change of internal structure of the solid phase is a process whose kinematics are described by the tensor map $\mathbb{F}_a$ and the generalised velocity gradient $\mathbb{L}_a = \dot{\mathbb{F}}_a(\mathbb{F}_a)^{-1}$. The set of generalised forces that perform working on $\mathbb{L}_a = \dot{\mathbb{F}}_a(\mathbb{F}_a)^{-1}$ comprises an internal force, $\mathbb{Z}_n$, which drives the structural evolution, and an external force, $\mathbb{Y}_n$, which models the interaction of the system with its surrounding environment. Both forces are second-order tensors. It is postulated [40] that they obey the balance law

$$\mathbb{Z}_n = \mathbb{Y}_n, \tag{1.54}$$

The index "n" means that $\mathbb{Z}_n$ and $\mathbb{Y}_n$ are conceived as forces acting on the natural configuration $\mathscr{B}_n$, although they can be also written with respect to $\mathscr{B}_r$ and $\mathscr{B}_t$ by performing proper transformations. Here, we simply state that, in analogy with the balance laws (1.43) and (1.42) (which describe a balance of forces that perform working on the set of standard velocities), also the forces that perform working on the non-standard descriptor $\mathbb{L}_a$ should satisfy a balance law. Some extensions of the results presented in [40] can be found, for example, in [4, 5, 9, 65, 71, 72, 73].

The internal force-like variables $\boldsymbol{m}_\ell$ and $\mathbb{Z}_n$ are responsible for dissipation, and should thus comply with the dissipation inequality that characterises the system under investigation. In the next Section the main step if the procedure are sketched.

1.2.4 Study of the residual dissipation inequality

We introduce the total internal power density of the system [74]

$$\mathfrak{W}^{in}(\mathscr{B}_t) = \mathfrak{W}^{in}_{\text{st}}(\mathscr{B}_t) + \mathfrak{W}^{in}_{\text{n-st}}(\mathscr{B}_t), \tag{1.55}$$

where $\mathfrak{W}^{in}_{\text{st}}(\mathscr{B}_t)$ and $\mathfrak{W}^{in}_{\text{n-st}}(\mathscr{B}_t)$ describe, respectively, the working performed by the standard and non-standard forces acting on the system. These two contributions are defined by the following expressions

$$\mathfrak{W}^{in}_{\text{n-st}}(\mathscr{B}_t) := \int_{\mathscr{B}_t} (J_n)^{-1}\mathbb{Z}_n : \mathbb{L}_a, \tag{1.56}$$

$$\mathfrak{W}^{in}_{\text{st}}(\mathscr{B}_t) := \int_{\mathscr{B}_t} \big\{ -\boldsymbol{m}_\ell \cdot \boldsymbol{w}_{\ell s} + \mathbb{T}_\ell : \text{grad}(\boldsymbol{w}_{\ell s}) + (\mathbb{T}_s + \mathbb{T}_\ell) : \text{grad}(\boldsymbol{v}_s) \big\}. \tag{1.57}$$

In a purely mechanical context, we call dissipation the quantity

$$\int_{\mathscr{B}_t} \mathscr{D} := -\int_{\mathscr{B}_t} \left[\rho_s D_s \Psi_s + \rho_\ell D_\ell \Psi_\ell\right] + \mathfrak{W}^{in}_{\text{st}}(\mathscr{B}_t) + \mathfrak{W}^{in}_{\text{n-st}}(\mathscr{B}_t) \geq 0, \tag{1.58}$$

where $\rho\Psi := \rho_s\Psi_s + \rho_\ell\Psi_\ell$ is the overall Helmholtz free energy density of the system.
Invoking the saturation constraint, under the hypotheses of hyperelastic solid phase, depending only on the $\mathbb{F}_n$ term of the factorization of the tensor gradient of the deformation, and macroscopically inviscid fluid, the variation of the inequality (1.58) yields the following results for the Cauchy stresses $\mathbb{T}_s$ and $\mathbb{T}_\ell$ [74]

$$\mathbb{T}_s = -\phi_s p\mathbb{I} + \left(\rho_s \frac{\partial \Psi_s}{\partial \mathbb{F}_n}\right)\mathbb{F}_a^{-T}\mathbb{F}^T, \tag{1.59}$$

$$\mathbb{T}_\ell = -\phi_\ell p\mathbb{I}. \tag{1.60}$$

Requiring the invariance of constitutive laws under superimposed rigid motions places further restrictions on the results (1.59) and (1.60). If a rigid motion is impressed, the points $\mathbf{x} \in \mathscr{B}_t$ transform as $\mathbf{x} \mapsto \bar{\mathbf{x}} = \mathbb{R}\,\mathbf{x} + \boldsymbol{c}$, where $\mathbb{R}$ is a proper orthogonal tensor defining a pure rotation, and $\boldsymbol{c}$ is a vector defining a pure rigid translation [77, 107]. Consequently, $\mathbb{F}$, $\mathbb{F}_n$ and $\mathbb{F}_a$ transform as follows

$$\mathbb{F} \mapsto \bar{\mathbb{F}} = \mathbb{R}\mathbb{F}, \quad \mathbb{F}_n \mapsto \bar{\mathbb{F}}_n = \mathbb{R}\mathbb{F}_n, \quad \mathbb{F}_a \mapsto \bar{\mathbb{F}}_a = \mathbb{F}_a. \tag{1.61}$$

However, the Helmholtz free energy density Ψ_s has to remain invariant under these transformations. Therefore, Ψ_s may depend on $\mathbb{F}_n$ only through the Cauchy stretch tensor $\mathbb{C}_n = (\mathbb{F}_n)^T\mathbb{F}_n$, which is independent on $\mathbb{R}$. This yields the relation

$$\left(\rho_s \frac{\partial \Psi_s}{\partial \mathbb{F}_n}\right) = \mathbb{F}_n\left(2\rho_s \frac{\partial \mathscr{W}_s}{\partial \mathbb{C}_n}\right), \tag{1.62}$$

where $\mathscr{W}_s$ is the Helmholtz free energy density of the solid phase written as a function of $\mathbb{C}_n$. On the other hand, the Cauchy stresses $\mathbb{T}_s$ and $\mathbb{T}_\ell$ transform as $\bar{\mathbb{T}}_\alpha = \mathbb{R}\mathbb{T}_\alpha\mathbb{R}^T$, with $\alpha = s,\ell$. Using the definitions (1.53) and (1.46), the first Piola-Kirchhoff stress tensors become

$$\mathbb{P}_s = -J_a\phi_{sn}p\mathbb{F}^{-T} + \mathbb{F}\left[J_a\mathbb{F}_a^{-1}\left(2\frac{\partial \mathscr{W}_{sn}}{\partial \mathbb{C}_n}\right)\mathbb{F}_a^{-T}\right], \tag{1.63}$$

$$\mathbb{P}_\ell = -(J - J_a\phi_{sn})p\mathbb{F}^{-T}, \tag{1.64}$$

where $\mathscr{W}_{sn} = \phi_{sn}\hat{\rho}_s\mathscr{W}_s$. Since $\mathbb{F}^{-T} = \mathbb{F}_n^{-T}\mathbb{F}_a^{-T}$, the stress $\mathbb{P}_s$ can be rewritten as

$$\mathbb{P}_s = J_a\mathbb{P}_{sn}\mathbb{F}_a^{-T}, \quad \mathbb{P}_{sn} := -\phi_{sn}p\mathbb{F}_n^{-T} + \mathbb{F}_n\left(2\frac{\partial \mathscr{W}_{sn}}{\partial \mathbb{C}_n}\right). \tag{1.65}$$

Finally, the Mandel stress tensor is introduced [77]

$$\mathbb{M}_{sn} := J_n\mathbb{F}_n^T\mathbb{T}\mathbb{F}_n^{-T} = \mathbb{F}_n^T\mathbb{P}_{sn} := -\phi_{sn}p + \mathbb{C}_n\left(2\frac{\partial \mathscr{W}_{sn}}{\partial \mathbb{C}_n}\right). \tag{1.66}$$

The constitutive results (1.63) and (1.64) allow for a simplification of the expression of dissipation. After localisation, we obtain

$$\mathscr{D} = -\check{\boldsymbol{m}}_\ell \cdot \boldsymbol{w}_{\ell s} + (J_n)^{-1}\check{\mathbb{Z}}_n : \mathbb{L}_a \geq 0. \tag{1.67}$$

where

$$\check{\boldsymbol{m}}_\ell := \boldsymbol{m}_\ell - p\,\mathrm{grad}(\phi_\ell)\,, \quad \check{\mathbb{Z}}_n := \mathbb{M}_{sn} + \mathbb{Z}_n \tag{1.68}$$

are the dissipative part of the force-like variables $\mathbf{m}_\ell$ and $\mathbb{Z}_n$ respectively.
Substitution of (1.68) into the balance laws (1.42) (with $\alpha = \ell$ and $\mathbf{b}_\alpha = 0$) and (1.54), and use of the constitutive result (1.60) yield

$$\check{\boldsymbol{m}}_\ell = \phi_\ell \mathrm{grad}(p)\,, \tag{1.69}$$

$$\check{\mathbb{Z}}_n = \mathbb{M}_{sn} + \mathbb{Y}_n\,. \tag{1.70}$$

Before proceeding with the determination of the forces $-\check{\boldsymbol{m}}_\ell$ and $(J_n)^{-1}\check{\mathbb{Z}}_n$, a discussion about the study of the dissipation inequality (1.67), and some of its implications, is mandatory.

Let us set $\mathbb{L}_a = 0$ and focus on the pair $(-\check{\boldsymbol{m}}_\ell, \boldsymbol{w}_{\ell s})$. In Biomechanics, it is often assumed that fluid flow obeys Darcy's law [13, 103, 117, 155]. Darcy's model of flow can be retrieved consistently with the study of dissipation by expressing $-\check{\boldsymbol{m}}_\ell$ as a constitutive function of $\boldsymbol{w}_{\ell s}$ that vanishes when $\boldsymbol{w}_{\ell s} = \mathbf{0}$ (see, for example, [80]). This function is then expanded in Taylor series in a neighbourhood of $\boldsymbol{w}_{\ell s} = \mathbf{0}$ and, for small velocities, only the first-order term of the expansion is maintained.

$$-\check{\boldsymbol{m}}_\ell = \mathbb{A}\phi_\ell \boldsymbol{w}_{\ell s}\,. \tag{1.71}$$

Assuming that $\mathbb{A}$ is a positive-definite second-order tensor that represents the resistivity of the medium, substitution of this result into (1.69),

$$\phi_\ell \boldsymbol{w}_{\ell s} = -\frac{1}{\nu}\mathbb{K}\mathrm{grad}(p), \tag{1.72}$$

where $\mathbb{K} = \nu\phi_\ell \mathbb{A}^{-1}$ is the permeability of the porous structure and ν is the dynamic viscosity of the fluid phase. Equation (1.72) is known as Darcy's law.

Let us put now $\boldsymbol{w}_{\ell s} = \mathbf{0}$ and study the pair $((J_n)^{-1}\check{\mathbb{Z}}_n, \mathbb{L}_a)$. In some models of growth mechanics, constitutive laws of the type $\check{\mathbb{Z}}_n = \mathbb{H}_n : \mathbb{L}_a$ have been proposed (cf., for example, [4, 5, 9, 71, 73, 102]), being $\mathbb{H}_n$ a diagonally symmetric, positive-definite fourth-order tensor. The rate of anelastic deformation $\mathbb{L}_a$ is presented in the form $\mathbb{L}_a = \mathbb{G}_n : \check{\mathbb{Z}}_n$, with $\mathbb{G}_n = (\mathbb{H}_n)^{-1}$. Substitution of (1.70) in this relation yields

$$\mathbb{L}_a = \mathbb{G}_n : (\mathbb{M}_{sn} + \mathbb{Y}_n). \tag{1.73}$$

Equation (1.73) follows from the hypothesis that $\check{\mathbb{Z}}_n$ can be assigned as a constitutive function of $\mathbb{L}_a$ that vanishes when $\mathbb{L}_a = 0$. This function is then assumed to be smooth and linearised in a neighbourhood of $\mathbb{L}_a = 0$. For a positive-definite $\mathbb{G}_n$, the formula (1.73) admits the following interpretation: the rate of anelastic deformation, $\mathbb{L}_a$, becomes zero when the external force $\mathbb{Y}_n$ can be tuned in such a way that the sum $(\mathbb{M}_{sn} + \mathbb{Y}_n)$ vanishes. This situation implies that $\mathbb{F}_a$ (which always satisfies the kinematic relation $\dot{\mathbb{F}}_a = \mathbb{L}_a \mathbb{F}_a$) either ceases to evolve in time or remains equal to its initial value. In some biomechanical applications, $\mathbb{Y}_n$ is thought of as the "target stress" that regulates the process with which it is associated (when the target stress is reached, the process ceases). For example, in the model of arterial growth proposed in [108], $\mathbb{Y}_n$ is related to the homeostatic stress. On the other hand, if the tensor $\mathbb{Y}_n$ is zero (or negligibly small), the equality $\mathbb{L}_a = 0$ cannot be recovered in general, since the Mandel stress, $\mathbb{M}_{sn}$, is not compensated by any external force.

Another method for determining evolution laws is given in [29], where rate-independent plasticity is investigated. The dissipation is defined as a function of $\mathbb{L}_a$ and is assumed to be continuous, but generally non-differentiable, at $\mathbb{L}_a = 0$, while the tensor $\check{\mathbb{Z}}_n$ is constitutively indeterminate at $\mathbb{L}_a = 0$. Within this framework, a maximum-dissipation criterion is formulated and it is proven that the dissipation function is everywhere sub-differentiable and, thus, convex with respect to $\mathbb{L}_a$, and that $\check{\mathbb{Z}}_n$ must belong to the sub-differential of the dissipation function. The evolution of $\mathbb{L}_a$ is determined by introducing a scalar yield criterion through the yield function f and showing that $\mathbb{L}_a$ has to be an element of the sub-differential of f. In the case of a smooth yield function f, it is found that $\mathbb{L}_a$ follows the "normality rule"

$$\mathbb{L}_a = \lambda \frac{\partial f}{\partial \check{\mathbb{Z}}_n}, \tag{1.74}$$

where λ is a Kuhn-Tucker multiplier satisfying the conditions $\lambda \geq 0$, $f \leq 0$, $\lambda f = 0$, and determined by the consistency requirement $\lambda \dot{f} = 0$. Many of the mathematical tools for presenting this theory can be found in [121, 122, 125].

We remark that (1.73)–(1.74) are all plausible ways to determine the evolution of $\mathbb{L}_a$.

Chapter 2

Confined compression of a cylindrical sample of cartilage

The scope of this chapter is to study the transport of fluid in a deformable porous medium whose mass and internal structure may vary in time. We formulate our problem with the aid of Mixture Theory and the framework of multiple natural configurations, applying the concept presented in Chapter 1.

Thus, we consider a biphasic mixture consisting of a solid and a fluid phase. The solid phase represents the cellular constituent and the extracellular fibres, whereas the liquid phase stands for the extracellular liquid filling void spaces.

Structural changes occurring inside the sample are described by the second-order tensor $\mathbb{F}_a$. In this first work, the anelastic part of the deformation is taken constant in time and we do not distinguish between anelastic deformation due to proliferation of cells and pure remodelling. Based on this approximation, we study the influence of deviation from sphericity of the anelastic deformation tensor, $\mathbb{F}_a$ (which correspond to different possible ways of changing the internal structure of the solid phase) on the deformation and, thus, the displacement field, as well as the distribution of pressure inside the medium.

The mathematical model is formulated in Section 2.2 and then applied to the compression of a cylindrical sample of biological material in Section 2.2.1. Finally, results are presented in Section 2.3.

2.1 Motivations

Among the factors that assess the health of a tissue, an important role is played by the amount of constituents that supply nutriment to the cells and regulate their metabolism. These chemicals are transported by liquid flowing in the "solid" structure composed of cells and extracellular matrix. Accepting the applicability of Darcy's law to such systems, fluid flow is determined by the hydraulic conductivity, $\mathbb{K}$, and pressure gradient. Therefore, the study of the transport of a fluid in a deformable porous medium with variable mass and internal structure reduces to the determination of the influence of $\mathbb{F}_a$ on $\mathbb{K}$ and pressure, p.
Under the hypothesis of negligible inertial terms and incompressible solid and fluid phases, the unknowns to be determined are the displacement field (whose material gradient is $\mathbb{F}$), the pressure, and $\mathbb{F}_a$. We formulate a boundary value problem for the calculation of pressure and displacements. In this preliminary study, we consider the very particular case in which the tensor of anelastic deformation is kept constant (i.e. $\mathbb{F}_a$ is constant and known from the outset).
In particular, we show that different choices of the initial value $\mathbb{F}_{a0}$ lead to different pressure distributions and displacements. The latter ones, in turn, affect $\mathbb{K}$ and are thus able to influence the capability of the medium of conveying fluid. The alteration of pressure may be relevant for some biomechanical applications in which the health of the cells of a tissue depends on the pressure. For example, this is the case of chondrocytes in articular cartilage. Moreover the most essential model for articular cartilage can be represented by a biphasic mixture, in which specialized cells (chondrocytes), collagen fibres and matrix of proteoglycans form the solid phase. In these soft tissues the flow of the fluid phase, comprising water, ions and various chemical compounds (i.e. nutrients for the cells or products of the cellular metabolic activity), is of fundamental importance in order to preserve its functionality. Furthermore, unlike other connective tissues, cartilage does not contain blood vessels, therefore chondrocytes are supplied by diffusion, helped by the pumping action generated by compression or flexion of the elastic cartilage due to load application.

2.2 Mathematical model

Our purpose is to study how the structural change of the solid phase influences fluid flow through the modulation of the transport properties of the mixture. We use the concepts presented in Chapter 1 and we accept the validity of Darcy's law, so that the fluid flow depends on hydraulic conductivity and pressure gradient. Therefore, to accomplish our task, we have to show how,

for a given type of problem and assigned boundary conditions, different tensors $\mathbb{F}_a$ modulate the hydraulic conductivity of the medium and the pressure field inside it.
We remark that the medium is assumed to be isotropic with respect to both its elastic properties and permeability.
Referring to the concept introduced in Chapter 1, we indicate with ϕ_s the volume ratio of the solid components of the mixture, i.e. cells and fibers, whereas ϕ_ℓ stands for the volume ratio for the extracellular liquid. By substituting (1.72) into (1.35), using the constitutive results (1.63) and (1.64) and writing the pressure gradient in material coordinates, i.e. $\mathrm{grad}(p) = \mathbb{F}^{-T}\mathrm{Grad}(p)$, the equations to solve are

$$-\mathrm{Div}\big[-Jp\mathbb{F}^{-T} + \mathbb{P}_s^*\big] = 0, \tag{2.1}$$

$$\mathrm{Div}\big[\mathbb{K}_r\mathrm{Grad}(p)\big] = \dot{J} - J_a\phi_{sn}\mathrm{tr}(\mathbb{L}_a), \tag{2.2}$$

$$\dot{\mathbb{F}}_a = \mathbb{L}_a\mathbb{F}_a \tag{2.3}$$

where $\mathbb{P}_s^* = J_a\mathbb{F}\mathbb{F}_a^{-1}\mathbb{S}_{sn}^*\mathbb{F}_a^{-T}$ denotes from here on the constitutive part of first Piola-Kirchhoff stress tensor, $\mathbb{P}_s$ (cf. (1.63)). $\mathbb{S}_{sn}^*$ is the constituive part of the second Piola-Kirchhoff stress tensor of the solid phase, measured with respect to $\mathscr{B}_n$, and $\mathbb{K}_r$ is the material form of the tensor of hydraulic conductivity, i.e., $\mathbb{K}_r = J\mathbb{F}^{-1}\mathbb{K}\mathbb{F}^{-T}$. In the following, for sake of simplicity, we will omit the apex $*$ for the constitutive part of the stress tensor. The material is assumed to be hyperelastic and isotropic, and is modelled by the Neo-Hookean elastic energy given below [20], which leads to the following expressions of $\mathbb{S}_{sn}$

$$\mathscr{W}_{sn}(\mathbb{C}_n) = \frac{\mu_n}{2}\big[\mathrm{tr}(\mathbb{C}_n) - 3\big] - \mu_n\ln(J_n) + \frac{\lambda_n}{2}\big[\ln(J_n)\big]^2, \tag{2.4}$$

$$\mathbb{S}_{sn} = 2\frac{\partial\mathscr{W}_{sn}}{\partial\mathbb{C}_n} = \mu_n[\mathbb{I} - (\mathbb{C}_n)^{-1}] + \lambda_n[\ln(J_n)](\mathbb{C}_n)^{-1}. \tag{2.5}$$

The tensor $\mathbb{K}$ is taken from [85] and adapted to our framework, i.e.

$$\mathbb{K} = k_0\left[\frac{\phi_{s0}}{1-\phi_{s0}}\frac{J-\phi_{sn}J_a}{J_a\phi_{sn}}\right]^{m_0}\exp\left\{\frac{m_1}{2}\left[\frac{J^2-J_a^2}{J_a^2}\right]\right\}\mathbb{I} \tag{2.6}$$

where the numbers m_0 and m_1 featuring in (2.6) are material parameters. According to (2.6), the hydraulic conductivity given in (2.6) is an isotropic tensor. However, other forms of hydraulic conductivity, which account for tissue anisotropy, have been recently proposed in [13, 49].
To close the problem, $\mathbb{L}_a$ should be supplied by one of the formulae (1.73)–(1.74).
In the absence of anelasticity, the field equations (2.1) and (2.2) were studied in [42] in the case of

a linear viscoelastic biphasic model for soft tissues. Our analysis wants to focus on how different anelastic deformation tensors, $\mathbb{F}_a$, influence the pressure and flow inside the specimen. In order to reduce the number of equations to solve numerically, we consider the very particular case in which the tensor of anelastic deformation is constant (i.e. $\mathbb{F}_a$ is constant and known from the outset), so that no anelastic evolution occurs. This implies that $\mathbb{L}_a$ is zero. In other words, we assume that anelastic deformations have already taken place, which means that the tissue has already grown and remodelled. Physically, this can be rephrased by saying that the tissue grows and remodels over a time scale much larger than the scale over which fluid flows and elastic deformations take place. This is consistent with the fact that, compared to other connective tissues, cartilage grows and repairs more slowly.

Then, the unknowns of the problem are displacement, $\boldsymbol{u}(t,\mathbf{X}) := \chi(t,\mathbf{X}) - \mathbf{X}$, and pressure, p. Equations (2.1) and (2.2), which hold in the internal points of $\mathscr{B}_r$, are completed with conditions prescribed on the boundary $\partial\mathscr{B}_r$. For each unknown, the boundary $\partial\mathscr{B}_r$ is split into a Dirichlet- and a Neumann-type subset. This means that $\partial\mathscr{B}_r$ admits the representations $\partial\mathscr{B}_r = \Gamma_N^{\boldsymbol{u}} \cup \Gamma_D^{\boldsymbol{u}}$ and $\partial\mathscr{B}_r = \Gamma_N^{p} \cup \Gamma_D^{p}$, where $\Gamma_N^{\boldsymbol{u}}$ and Γ_N^{p} are the subsets of $\partial\mathscr{B}_r$ on which Neumann boundary conditions for the displacement and pressure are prescribed, while $\Gamma_D^{\boldsymbol{u}}$ and Γ_D^{p} are the subsets on which Dirichlet conditions are supplied. Formally, boundary conditions are written as

$$\begin{cases} \boldsymbol{u} = \bar{\boldsymbol{u}}_b, & \text{on } \Gamma_D^{\boldsymbol{u}}, \\ \big[-Jp\mathbb{F}^{-T} + \mathbb{P}_s\big]\boldsymbol{N} = \boldsymbol{f}_{rb}, & \text{on } \Gamma_N^{\boldsymbol{u}}, \\ p = \bar{p}_b, & \text{on } \Gamma_D^{p}, \\ \big[-\mathbb{K}_r \mathrm{Grad}(p)\big]\cdot\boldsymbol{N} = Q_{rb}, & \text{on } \Gamma_N^{p}, \end{cases} \tag{2.7}$$

where $\boldsymbol{N}$ is the unit vector normal to $\partial\mathscr{B}_r$. The surface force $\boldsymbol{f}_{rb}$ is defined per unit area of the reference boundary $\Gamma_N^{\boldsymbol{u}}$ and is generally different from the force $\boldsymbol{f}_b$ associated with the actual configuration $\mathscr{B}_t$. An analogous argument holds true for the quantities Q_{rb} and Q_b, the latter being the flux prescribed per unit area of the boundary $\partial\mathscr{B}_t$ of the actual configuration. The pairs $\boldsymbol{f}_{rb}$-$\boldsymbol{f}_b$ and Q_{rb}-Q_b are related to each other by the formulae [20]

$$\boldsymbol{f}_{rb} = J\sqrt{\boldsymbol{N}\otimes\boldsymbol{N} : \mathbb{C}^{-1}}\,\boldsymbol{f}_b\,, \quad \boldsymbol{Q}_{rb} = J\sqrt{\boldsymbol{N}\otimes\boldsymbol{N} : \mathbb{C}^{-1}}\,\boldsymbol{Q}_b\,. \tag{2.8}$$

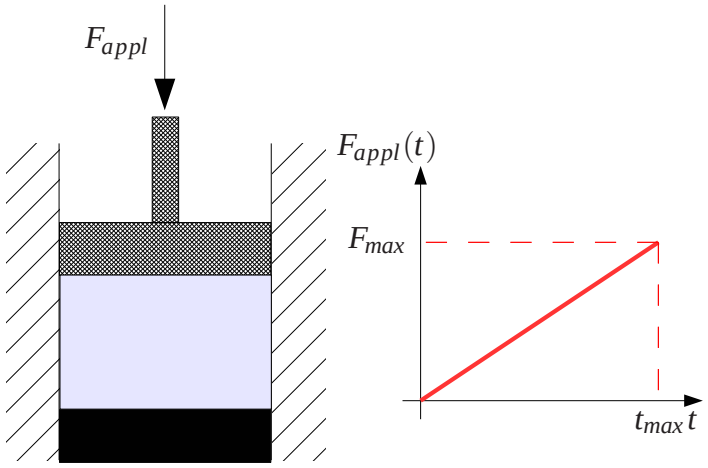

Figure 2.1: Schematic representation of the parallel plate apparatus used in the benchmark problem: the lower plate is impermeable, whereas liquid can flow through the upper plate. Results are reported in the case of an applied load linearly increasing in time.

2.2.1 Compression of a cylindrical sample

We apply the model presented in section 2.2 to describe a confined compression test under given loading conditions. We consider the case in which the biphasic material is positioned inside a rigid cylinder and left free to deform anelastically. In this preliminary study we do not distinguish contributions due to pure growth from those due to the remodelling of bonds among cells and fibers remodelling.
The cylindrical sample is then compressed between two plates: the lower plate is impermeable, whereas the upper plate allows fluid exudation, so that the liquid embedded in the material can escape from the specimen due to compression (see Fig. 2.1).

The formulation of the confined compression is based on the assumption that the matrix representation of the deformation gradient is given a very simple diagonal form. Indeed, since the cylindrical walls of the parallel-plate-apparatus are supposed to be rigid and impervious, it is reasonable to assume deformations and velocities of all constituents to be along the Z-axis.
Therefore, using a cylindrical coordinate system, the deformation generated by a uniaxial force applied along the Z-axis is

$$\chi^r(t,\mathbf{X}) = R, \qquad \chi^\vartheta(t,\mathbf{X}) = \Theta, \qquad \chi^z(t,\mathbf{X}) = z, \tag{2.9}$$

where $\mathbf{X} = (R,\Theta,Z)$. We restrict our investigation to the case in which χ^z depends on Z and t

only, so that the matrix representation of the deformation gradient tensor is diagonal and given by

$$\mathbb{F} = \mathrm{diag}\,\{1,1,\partial_Z \chi^z\}\,. \tag{2.10}$$

We remark that, due to the particular form of $\mathbb{F}$, the identity $J = \partial_Z \chi^z$ holds true.
Then, we assume that $\mathbb{F}_a$, the tensor of anelastic deformation that maps the tangent space of the reference configuration, $T\mathscr{B}_r$, onto the tangent space of the natural configuration, $T\mathscr{B}_n$, has the diagonal form

$$\mathbb{F}_a = \mathrm{diag}\,\{g_1,g_1,g_3\}\,. \tag{2.11}$$

We choose a non-spherical anelastic deformation in order to study the influence of anisotropy on the distribution of load and pressure throughout compression. For the problem under investigation, g_1 and g_3 are assumed to be constant in time and given from the outset. From (2.10) and (2.11), it follows that

$$\mathbb{F}_n = \mathrm{diag}\left\{\frac{1}{g_1},\frac{1}{g_1},\frac{J}{g_3}\right\}. \tag{2.12}$$

The next step is to re-write (2.1) and (2.2) in cylindrical coordinates. For ease of notation, we introduce the symbol

$$\boldsymbol{Q} := -\mathbb{K}_r \mathrm{Grad}(p)\,. \tag{2.13}$$

It follows from (2.2) that

$$\dot{J} = -\mathrm{Div}(\boldsymbol{Q}) = -\frac{1}{R}\frac{\partial}{\partial R}(RQ^R) - \frac{1}{R}\frac{\partial Q^\Theta}{\partial \Theta} - \frac{\partial Q^Z}{\partial Z} = -\frac{\partial Q^Z}{\partial Z}, \tag{2.14}$$

where the last identity holds true by requiring that the derivatives with respect to both the radial and tangential directions vanish identically, and that Q^R is zero. The latter condition amounts to say that there is no fluid flow along the radial direction. It is thus sufficient to determine Q^Z, which is given by

$$Q^Z = -(K_r)^{ZZ}\frac{\partial p}{\partial Z} = -JK\frac{1}{J^2}\frac{\partial p}{\partial Z} = -\frac{K}{J}\frac{\partial p}{\partial Z}. \tag{2.15}$$

By substituting (2.15) into (2.14), we obtain

$$\dot{J} = \frac{\partial}{\partial Z}\left(\frac{K}{J}\frac{\partial p}{\partial Z}\right). \tag{2.16}$$

Taking into account that the Piola-Kirchhoff stress tensor $\mathbb{P}_s$ is diagonal, i.e.

$$\begin{aligned}\mathbb{P}_s &= \operatorname{diag}\left\{P^{rR},P^{\vartheta\Theta},P^{zZ}\right\} \\ &= \mu_n J_a \operatorname{diag}\left\{\frac{1}{g_1^2},\frac{1}{g_1^2},\frac{J}{g_3^2}\right\}+\left[\lambda_n \log\left(\frac{J}{J_a}\right)-\mu_n\right]\operatorname{diag}\left\{J_a,J_a,\frac{J_a}{J}\right\},\end{aligned} \tag{2.17}$$

and that the liquid and the solid phases move along the z-direction only, the balance of momentum (1.45) reduces to

$$\frac{\partial p}{\partial Z}=\frac{\partial P^{zZ}}{\partial Z}. \tag{2.18}$$

By coupling (2.18) with (2.16), we obtain

$$\begin{aligned}\dot{J} &= \frac{\partial}{\partial Z}\left(\frac{K}{J}\frac{\partial P^{zZ}}{\partial Z}\right)= \\ &= \frac{\partial}{\partial Z}\left[\frac{K}{J}\frac{\partial}{\partial Z}\left(\mu_n\frac{g_1^2}{g_3}J+\left(\lambda_n\log\left(\frac{J}{g_1^2g_3}\right)-\mu_n\right)\frac{g_1^2g_3}{J}\right)\right].\end{aligned} \tag{2.19}$$

It can be proven that the partial derivative of P^{zZ} with respect to the axial direction reads

$$\frac{\partial P^{zZ}}{\partial Z}=\left[\frac{J_a\mu_n}{g_3^2}+\frac{J_a\mu_n}{J^2}+\frac{J_a\lambda_n}{J^2}-\frac{J_a\lambda_n}{J^2}\ln\left(\frac{J}{J_a}\right)\right]\frac{\partial J}{\partial Z}. \tag{2.20}$$

Therefore, the mass balance law acquires the form of a nonlinear diffusion equation, in which the "transported" quantity is the volumetric deformation J. Indeed, by substituting (2.20) into (2.19), we obtain

$$\dot{J}=\frac{\partial}{\partial Z}\left[D(J)\frac{\partial J}{\partial Z}\right] \tag{2.21}$$

where $D(J)$ represents a effective diffusion coefficient defined by

$$D(J):=K\left[\frac{J_a\mu_n}{Jg_3^2}+\frac{J_a\mu_n}{J^3}+\frac{J_a\lambda_n}{J^3}-\frac{J_a\lambda_n}{J^3}\ln\left(\frac{J}{J_a}\right)\right]. \tag{2.22}$$

It is important to notice that $D(J)$ is always positive, being $J<J(0,Z)=J_a$ because of compression, which leads to $J_n<1$. Therefore, all the terms on the right-hand-side of (2.22) are positive. This is consistent with the diffusive nature of the problem and it will be important also in defining boundary conditions.

Finally, the diffusion equation (2.21) has to be solved together with the auxiliary equations

$$\frac{\partial \chi^z}{\partial Z} = J, \tag{2.23}$$

$$\frac{\partial p}{\partial Z} = \left[\frac{J_a\mu_n}{g_3^2} + \frac{J_a\mu_n}{J^2} + \frac{J_a\lambda_n}{J^2} - \frac{J_a\lambda_n}{J^2}\ln\left(\frac{J}{J_a}\right)\right]\frac{\partial J}{\partial Z}. \tag{2.24}$$

We remark, however, that (2.23) and (2.24) are decoupled from (2.21), and can thus be solved *a posteriori* once J is known, provided proper boundary conditions are supplied.

2.2.1.1 Boundary and initial conditions.

In order to solve (2.19), (2.23) and (2.24), we have to supply boundary conditions (BCs) and an initial condition (IC). In particular, the mass balance (2.19) requires two BCs and one IC, whereas both (2.23) and (2.24) require one BC only. Boundary conditions have to be provided at the boundary points $Z = 0$ and $Z = L$, which identify the lower and upper boundary of the specimen, respectively.

The boundary conditions have to be consistent with the following requirements:

(i) the axial stress at the upper boundary of the specimen has to be equal to the applied load, $P_{appl}(t)$;

(ii) the velocity of the fluid and of solid phase have to be zero at the bottom because the lower plate is impermeable and fixed;

(iii) the pressure p has to be zero at $Z = L$ since the liquid is in equilibrium with the atmosphere.

These observations are translated in the following set of boundary conditions

$$\chi^z(t,0) = 0, \tag{2.25}$$

$$Q^Z(t,0) = 0 \quad \Rightarrow \quad \frac{\partial p}{\partial Z}(t,0) = 0, \tag{2.26}$$

$$-Jp\left(F^{-T}\right)^{zZ}(t,L) + P^{zZ}(t,L) = P_{appl}(t), \tag{2.27}$$

$$p(t,L) = 0\,. \tag{2.28}$$

We remark that, by virtue of the identity (2.18), we may rephrase (2.26) as follows

$$\frac{\partial P^{zZ}}{\partial Z}(t,0) = \left[\frac{J_a\mu_n}{g_3^2} + \frac{J_a\mu_n}{J^2} + \frac{J_a\lambda_n}{J^2} - \frac{J_a\lambda_n}{J^2}\ln\left(\frac{J}{J_a}\right)\right]_{(t,0)}\frac{\partial J}{\partial Z}(t,0) = 0. \tag{2.29}$$

We recall that the argument in the square brackets is always positive. Therefore, this condition leads to a homogeneous-Neumann BC for J at the lower boundary:

$$\frac{\partial J}{\partial Z}(t,0) = 0\,. \tag{2.30}$$

On the other hand, (4.32) leads to a Dirichlet condition on J at the upper boundary:

$$\mu_n \frac{J_a J(t,L)}{g_3^2} - \mu_n \frac{J_a}{J(t,L)} + \lambda_n \frac{J_a}{J(t,L)} \ln\left(\frac{J(t,L)}{J_a}\right) = P_{appl}(t)\,. \tag{2.31}$$

Since this equation is nonlinear with respect to $J(t,L)$, solutions can be found by applying Newton's method or other techniques.

As initial condition, we take $J(0,Z) = J_a(0,Z)J_n(0,Z) = J_a$. Indeed, at the initial time, there is no elastic deformation, although the anelastic deformation has already occurred. We remark that, for consistency, the condition $\mathbb{F}_n(0,\mathbf{X}) = \mathbb{I}$ entails that $g_1 = 1$.

2.2.2 Discretization

Equation (2.19) can be solved using central differences for space derivatives and then a proper ODE solver to obtain the temporal evolution. In the following we depict the main step of this procedure.

The 1D-domain, represented by the interval $[0,L]$, is divided into $N-1$ subintervals of the same width ΔZ through the introduction of N equispaced nodes

$$0 = Z_1 < Z_2 = Z_1 + \Delta Z < \ldots < Z_j < \ldots < Z_{N-1} < Z_N = L\,.$$

Spaces derivatives are then approximated by finite differences, so that the following system of $N-2$ equations is obtained:

$$\dot{J}_j \;=\; \frac{1}{(\Delta Z)^2}\left(\frac{K_{j+1}}{J_{j+1}}P^{zZ}_{j+1} - \left(\frac{K_{j+1}}{J_{j+1}} + \frac{K_j}{J_j}\right)P^{zZ}_j + \frac{K_j}{J_j}P^{zZ}_{j-1}\right). \tag{2.32}$$

Here, j enumerates the nodes of the grid, i.e. $J_j = J(t,Z_j)$, $K_j = K(t,Z_j)$ and $P^{zZ}_j = P^{zZ}(t,Z_j)$, with $j = 2,\ldots,N-1$. The boundary values J_1 and J_N are given by (2.30) and (4.34). A special treatment is performed for the initial node: in order to preserve the second-order-accuracy of the discretization method, a fictitious node Z_0 is introduced, and the Neumann boundary condition

(2.30) is approximated by the central difference [17]

$$\frac{J_2 - J_0}{2(\Delta Z)} = 0,$$

which implies $J_0 = J_2$. This allows to prolong the validity of the discretization used in (4.67) to the node $j = 1$.

At the upper boundary, we solve (4.34) numerically in order to determine J_N. For this purpose, we implement a standard Newton-Raphson method. According to this procedure, the initial partial differential equation (2.19) is approximated by a system of ordinary differential equations that can be integrated by choosing a stable ODE solver, with the initial condition $J_j(0) = J(0,Z_j) = g_1^2 g_3$, for $j = 1,\ldots,N$.

After computing J, the function χ^z is calculated by invoking (2.23) coupled with (4.30), and using a standard forward Euler method. The variation of pressure inside the specimen can be calculated a posteriori, once P^{zZ} is known. Indeed, integrating the balance of momentum (2.18), with the boundary condition $p(t,L) = 0$ MPa, yields

$$p(t,Z) = P^{zZ}(t,Z) - P^{zZ}(t,L)\,. \tag{2.33}$$

2.3 Results

The model presented in the previous sections is applied to describe the compression of a cylindric specimen of soft biological tissues, which is positioned in a chamber delimited by a rigid cylindric wall and two parallel plates. The wall and the lower plate are impermeable to liquid, whereas the upper plate allows for fluid exudation. An external compressive force is applied at the upper plate, parallel to the symmetry axis of the specimen. The experimental apparatus is schematically shown in Fig. 2.1.

We restrict our analysis to the case in which the external force increases linearly in time until $t_{max} = 30$ s when the maximum force, $F_{max} = -0.2 \cdot 9.81$ N, is reached.

In (2.11), we consider

$$\mathbb{F}_a = \mathrm{diag}\,\{g_1,g_1,g_3\} = \mathrm{diag}\,\{g,g,g+\varepsilon\}\,, \tag{2.34}$$

where ε measures the deviation of $\mathbb{F}_a$ from a spherical anelastic deformation. Therefore, different values of ε stand for different capabilities of the biological sample to change its internal structure.

The numerical results shown in this section are obtained by implementing in Matlab® the procedure described in section 2.2.2. All the parameters are listed in Table I.

TABLE I
PARAMETERS OF THE BENCHMARK PROBLEM

Parameter	Description	Value
L	Height of the specimen	10 mm
$2R$	Diameter of the specimen	5 mm
F_{max}	Maximum applied force	$-0.2 \cdot 9.81$ N
t_{max}	Time of load application	30 s
k_0	Hydraulic conductivity	$3.6454 \cdot 10^{-12}$ m$^4/(\mathrm{N} \cdot \mathrm{s})$
m_0	Material parameter	0.0848
m_1	Material parameter	4.638
ϕ_{s0}	Referential value of solidity.	0.6
ϕ_{sn}	Solidity in the relaxed configuration	0.6
λ_n	Lamé's first modulus	0.3137 MPa
μ_n	Shear modulus	0.3566 MPa

We recall that, for the considered problem, the only possible value of g is unity. This implies that the deviations of $\mathbb{F}_a$ from a referential spherical tensor are actually the deviations from the identity tensor.

Equation (2.19), integrated with the initial condition $J(0,Z) = J_a$ and BCs (2.30) and (4.34), gives origin to the curves in Fig. 2.2-(a), which represent $J(t,Z)$ plotted over space, at different instants of time (every 5 s for 30 s). In this simulation, we set $\varepsilon = 0.1$. The corresponding volumetric fraction of the solid, $\phi_s(t,Z) = \phi_{sn} J_a [J(t,Z)]^{-1}$, is reported in Fig. 2.2-(b).
The characteristic time of the diffusive process described in (2.19) is defined by $t_d := L^2 [D(J)]^{-1}$, which is a function of time and material coordinates through J. For the considered load, $D(J)$ is an increasing function of J. Thus, the maximum characteristic time, t_d^M, corresponds to the minimum value of J, which is reached at the end of the simulation in $Z = L$ (cf. Fig. 2.2-(a)). On the other hand, the minimum characteristic time, t_d^m, is reached at the beginning of the simulation, for $J(0,Z) = J_a$ and $D(J(0,Z)) = k_0(\mu_n g_3^{-2} + \mu_n J_a^{-2} + \lambda_n J_a^{-2}) = k_0(2\mu_n + \lambda_n) J_a^{-2}$. We remark that the factor $(2\mu_n + \lambda_n)$ coincides with the P-wave modulus of the material.
For the parameters listed in Table I, we find $t_d^M \approx 38.26$ s and $t_d^m \approx 32.32$ s. We notice that t_d^M and t_d^m are of the same order as t_{max}.

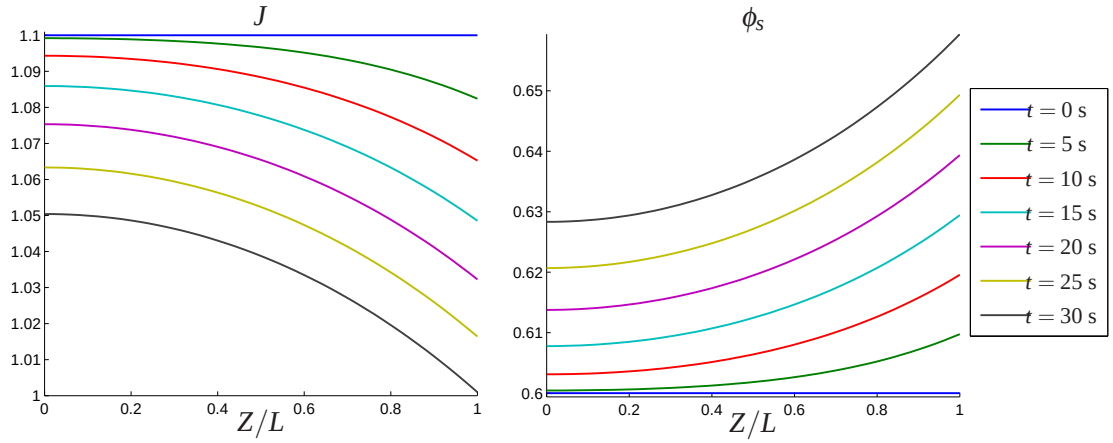

Figure 2.2: Evolution in time and space of $J(t,Z)$ (a) and solid volumetric fraction (b), when $\varepsilon = 0.1$, starting from the initial values $J(0,Z) = J_a$ and $\phi_s = \phi_{sn}$. Solutions are reported every 5 s for 30 s, which correspond to the maximum time of load application. All the parameters used in the simulation are listed in Table I.

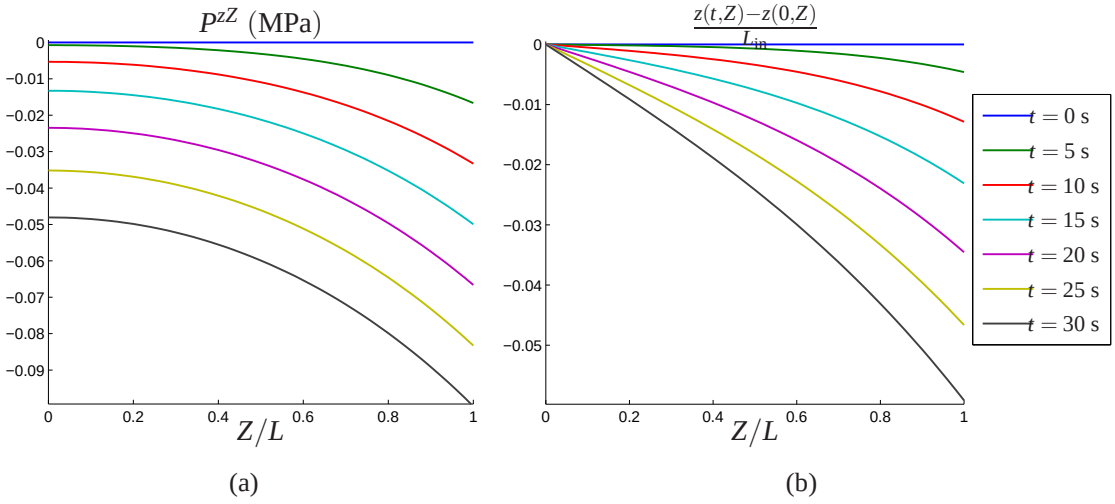

Figure 2.3: Evolution in time and space of $P^{zZ}(t,Z)$ (a) and relative displacement, $[z(t,Z) - z(0,Z)]/L_{\text{in}}$ (b), with $P^{zZ}(0,Z) = 0$ MPa and $z(0,Z) = J_a Z$. Results are plotted every 5 s up to 30 s, in the case of the parameters listed in Table I and $\varepsilon = 0.1$.

The axial component of the constitutive part of the first Piola-Kirchhoff stress tensor, P^{zZ}, and the relative displacement, $[z(t,Z) - z(0,Z)]/L_{\text{in}}$ are plotted in Fig. 2.3-(a) and Fig. 2.3-(b), respectively. Here, L_{in} denotes the length of the specimen at time $t = 0$ s, which is defined by $L_{\text{in}} := \int_0^L \partial_Z \chi^z(0,Z)\mathrm{d}Z = J_a L$ consistently with (2.23).
The value of P^{zZ} at the upper boundary is given by $P^{zZ}(t,L) = \left(F_{appl}(t,L)\right)/S$, where $F_{appl}(t,L) =$

$F_{max}[t/t_{max}]$ and $S = pR^2$, the area of the surface over which the applied load is distributed, coincides with the cross section of the specimen in the reference configuration.
The amplitude of the displacement increases in time with the applied load (cf. Fig. 2.3-(b)). This behaviour is qualitatively the same also for the other values of ε considered in the following. However, the diffusive process tends to become slower as ε gets bigger.

In the following, we run a set of simulations with varying ε in order to highlight the influence of this parameter on the response of the material (e.g., distribution of stress and deformation inside the specimen). Results are presented in Figs. 2.4 and 2.5 for $\varepsilon = \{0, 0.01, 0.1, 0.2\}$. In particular, the volumetric deformation J, which solves (2.19), and the volumetric fraction of the solid phase at $t_{max} = 30$ s are reported in Fig. 2.4-(a) and 2.4-(b), respectively. We remark that the value of the solid volumetric fraction at the upper boundary, $\phi_s(t,L)$, is the same for every value of ε because $J_a[J(t,L)]^{-1}$ is constrained to satisfy (4.34) independently of ε.
Pressure and relative displacements are plotted in Fig. 2.5 at time $t = t_{max}$. Pressure is obtained solving eq. (2.33), consistently with the condition (4.33). The value of the pressure at the lower boundary rises as ε increases, and the pressure distribution tends to become more inhomogeneous for larger deviations of $\mathbb{F}_a$ from sphericity.
For the considered load, the normalised final displacement, $[z(t_{max},Z) - z(0,Z)]/L_{\text{in}}$, which is zero at the bottom of the specimen, diminishes with increasing ε (cf. Fig. 2.5-(b)).

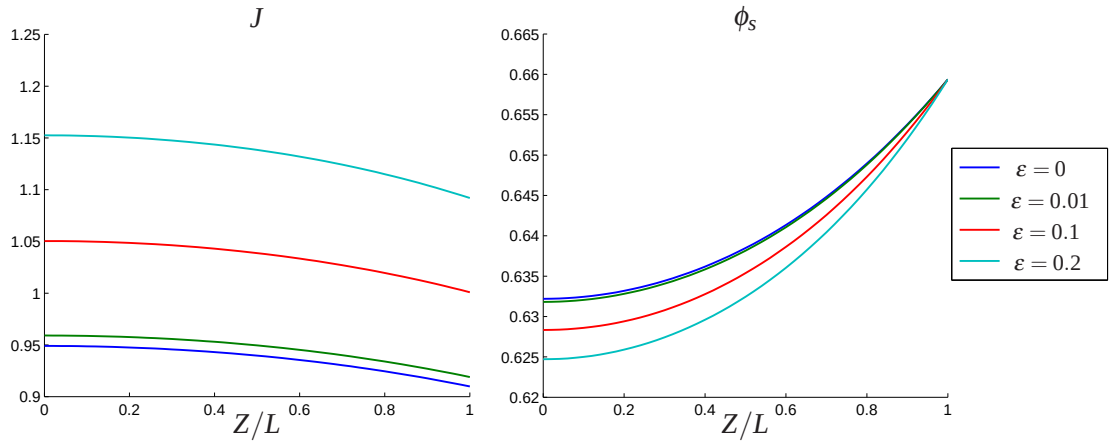

(a) (b)

Figure 2.4: Distribution of J (a) and solid volumetric fraction (b) at the final time of compression $t_{max} = 30$ s, for different values of ε.

The results of the simulations obtained by means of the computational methods outlined in sections 2.2.2 are in good agreement with the results obtained through finite element simulation.

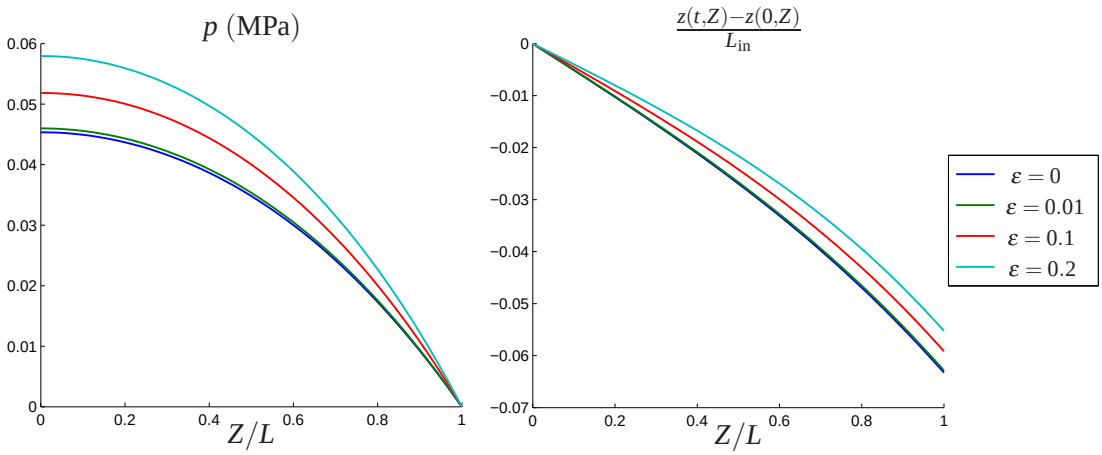

Figure 2.5: Evolution of the pressure over space (a) and relative displacement (b) at the final time of compression $t_{max} = 30$ s, for different values of ε.

Fig. 2.6 and 2.7 show the results for two values of ε, for comparison with the results obtained in Matlab®. The finite element simulations have been developed in collaboration with a group of the Institute of Computational Science at the Universitá della Svizzera Italiana (Lugano, Switzerland) [74].

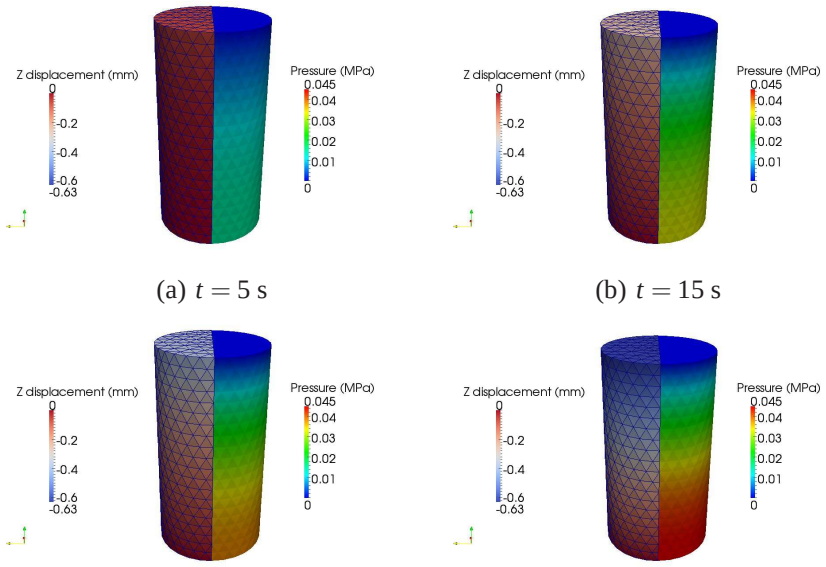

(a) $t = 5$ s (b) $t = 15$ s

(c) $t = 20$ s (d) $t = 30$ s

Figure 2.6: Time evolution of the displacement and the pressure without growth ($\varepsilon = 0$).

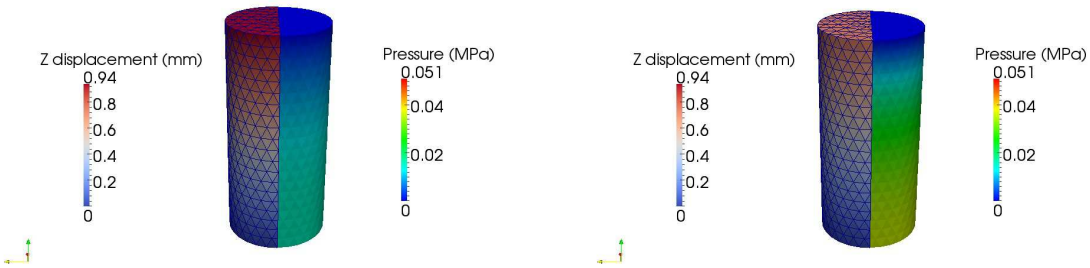

(a) $t = 5$ s

(b) $t = 15$ s

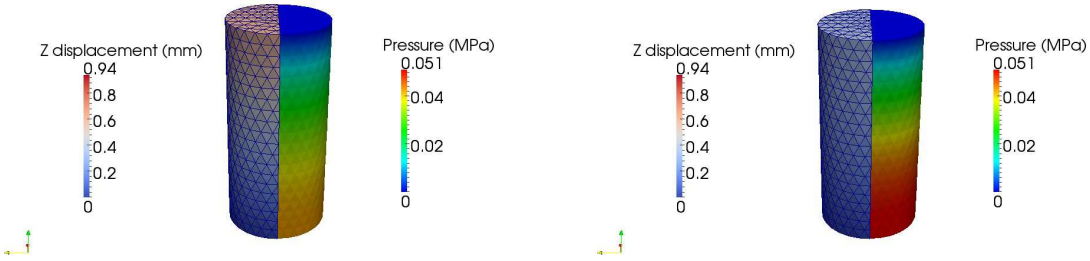

(c) $t = 20$ s

(d) $t = 30$ s

Figure 2.7: Time evolution of the displacement and the pressure with $\varepsilon = 0.1$.

2.4 Discussion

In this chapter, we apply the theory of biphasic materials with variable mass and internal structure to the description of the uniaxial compression of a cylindrical sample of soft biological tissue. The structural change, described by the second-order tensor $\mathbb{F}_a$, and the variation of mass (which is assumed to be due to growth) are connected with each other since the rate at which mass increases (or decreases), γ_s, is related to the rate of anelastic deformation $\mathbb{L}_a$ through $\gamma_s = \mathrm{tr}(\mathbb{L}_a)$. For our purposes, however, we considered a simplified framework in which $\mathbb{L}_a$ is set equal to zero. Consequently, $\mathbb{F}_a$ is taken to be constant. This amounts to study situations in which the biphasic medium evolves under external actions after anelastic re-organization and growth has already occurred. Physically, this means that we are hypothesising that the time scale over which the medium grows and reorganizes is much slower than the scale over which it deforms. Based on this approximation, we study how different choices of $\mathbb{F}_a$ (which correspond to different possible ways of changing the internal structure of the solid phase) influence the deformation and, thus, the displacement field, as well as the distribution of pressure inside the medium.
Our next goal is to consider fully coupled equations, in which the value of $\mathbb{F}_a$ changes in time. Moreover we are also interested in distinguish the contribution due to pure growth from the one due to remodelling. Thus, in Chapter 3 we introduce an evolving equation able to describe anelastic contributions due to the rupture of adhesive bonds, whereas in Chapter 4 we introduce the growth of the cellular constituent.

Chapter 3

Uniaxial compression of spheroids

In this chapter we apply the notion of multiple natural configurations, presented in Chapter 1 to study the mechanical behavior of multicellular aggregates under compression. Cell and aggregate responses to mechanical stimuli have been successfully described using this framework in [7, 115, 116]. However, the viscous contribution of the liquid encapsulated inside the multicellular system has always been neglected, except for the terms modelling the exchange of linear momentum among the phases. In many situations, this simplification leads to unrealistic results when compression is released.
We will treat the system as a deformable porous material, composed of cells and filled with physiological liquid, in order to analyse the non-linear mechanical behavior related to the reorganization of multicellular structures, when a load is applied.
The cellular constituent is responsible for the elastic and the plastic behavior of the material. In particular, the plastic component is due to the rearrangement of adhesion bonds between cells and it is translated into the existence of a yield stress in the macroscopic constitutive equation. On the other hand, the liquid constituent is responsible for the viscous-like response during deformation.
In section 3.1 we present the biological motivation that guides this work and we revised previous work present in literature.

The general mathematical framework is outlined in Section 3.2.1, where the constitutive equation for cellular aggregates is introduces. The model is obtained under the hypothesis of incompressible homogeneous material, with ϕ_s constant in space and time and deformations depending on time only, so that equations presented in Chapter 1 simplifies considerably.
Then the model is applied to describe uniaxial homogeneous compression (3.2.2) in the three following situations

- application of a constant pressure, possibly repeated over time (section 3.3.1),
- compression at constant force and subsequent release (section 3.3.2),
- imposition of a fixed deformation and subsequent release (section 3.3.3).

The qualitative properties of the solution are described in detail, with proofs and the numerical results (in terms of spheroid deformation and applied stress) are compared with the prediction of previous models [115, 116] and mechanical experiments performed in [52].

3.1 Motivations

In recent years, many studies, focused on cell microrheology and mechanical behavior, aim at establishing the constitutive equation of cells and aggregates [1, 3, 7, 115] and at measuring properties like cell interfacial energy, elastic modulus and relaxation times [52, 53, 54, 159]. In particular, in [7, 115] it was shown that the phenomena observed during some compression experiments performed in [52, 53, 54], where a fixed deformation is applied to the cell aggregate, or in [90], where a dense cell suspension is subjected to shear, can be explained using the concept that the natural configuration evolves, due to the rearrangement of adhesion bonds. Then, aggregate mechanical behavior can be modelled coupling the viscoelastic behaviors with a yield condition, generating a plastic reorganization, when the stress becomes too high.

However, pressure controlled experiments (e.g. creep test) and stress-release experiments can not be fully explained with the models in [7, 115], in which the liquid encapsulated in the system is not considered. Indeed experimental evidence [52, 53, 54] suggests that, when an imposed deformation is removed, the shape recovery dynamics of aggregates, requires some time. On the contrary in [1, 3, 7, 115, 116], when the stress is released, the shape recovery is instantaneous. A similar behavior is found when a stress is suddenly applied.
In addition, if the imposed stress is sufficiently high, when the stress is removed, the initial configuration is no longer reached, which can not be described with the models presented in [52, 53, 54], that are based essentially on the existence of a surface tension holding together the cell aggregate. A similar difficulty is encountered when dealing with the description of periodic compressions of spheroids.

Therefore, in this chapter we extend the elasto-visco-plastic model presented in [115] to include the effects described above. On one hand, we take into account the existence of a maximum stress that can be sustained by the cell aggregate before reorganizing and on the other hand,

we consider the fact that the total stress exerted by the specimen is not only due to the cellular component, but also to a further viscous term due to the action of the liquid phase.

3.2 Mathematical Model

3.2.1 The Constitutive Model of Cell Spheroids

Cellular spheroids used in biological experiments [52, 53, 54] have a diameter ranging from 200 and 600 μm, which means $10^4 - 10^5$ cells. Therefore cell aggregates can be modelled as continuum media, presenting elastic, viscous and plastic behaviors:

- the elastic component is mainly due to the cytoskeleton, which is composed of elastic filaments strongly cross-linked,
- the dissipative component, responsible for the viscous behavior, originates primarily from the flow of the cytosol along with and through the cytoskeleton meshwork and from extracellular fluid movements,
- the plastic component is due to the re-organization of adhesion bonds between cells and to actin network remodelling inside cells.

We use the theory for materials with evolving natural configurations [86, 87, 126, 144], presented in Chapter 1, Section 1.2.
In particular, in the case of mechanical testing of multicellular aggregates, it is natural to assume that no growth occurs during stress-induced deformation, since mitosis and apoptosis occur on a much longer time scale (several hours) than the typical time scale of mechanical deformation. Therefore, referring to Fig. 1.1 the anelastic part of the deformation is merely due to the remodelling of the internal structure of aggregates, that we will indicate with $\mathbb{F}_p$. It is therefore possible to introduce the following multiplicative decomposition of the total deformation gradient

$$\mathbb{F} = \mathbb{F}_n \mathbb{F}_p \,, \tag{3.1}$$

where $\mathbb{F}_n$ identifies the deformation without cell reorganization (describing how the body is deforming locally while going from the natural configuration $\mathscr{B}_n$ to $\mathscr{B}_t$), $\mathbb{F}_p$ describes the anelastic component due to the internal re-organization of cells (evolution from $\mathscr{B}_r$ to $\mathscr{B}_n$).
In order to introduce the viscous contribution due to the liquid encapsulated inside cells and among them, we apply the concepts of Mixture Theory, presented in Chapter 1. Cells form the

solid structure, with volume ratio ϕ_s, whereas the liquid phase has volume fraction ϕ_ℓ and obviously the saturation assumption holds: $\phi_s + \phi_\ell = 1$. We will assume that ϕ_s and ϕ_ℓ do not change in time and thus they can be considered given constant of the problem. The total tension of the mixture as a whole, $\mathbb{T}$, is due both to the stress exerted by the cellular constituent, $\mathbb{T}_s$, and to the one exerted by the fluid contained in cells and in which the spheroid is immersed, $\mathbb{T}_\ell$. Hence, neglecting inertial terms, eq. (1.39) yields

$$\mathbb{T} = \mathbb{T}_s + \mathbb{T}_\ell \,. \tag{3.2}$$

Treating the fluid as a linear incompressible Navier-Stokes fluid and assuming that cells and liquid move with the same velocity, the second term in equation (3.2) reads $\mathbb{T}_\ell = -p\phi_\ell \mathbb{I} + 2\nu\phi_\ell \mathbb{D}$, where $\mathbb{D} = (\mathbb{L} + \mathbb{L}^T)/2$ and p is a Lagrangian multiplier due to the volume additivity of the constituents and it represents the interstitial fluid pressure.
Obviously this is only an approximation and a better description of the phenomenon should separate the contribution of the intracellular liquid, from that of the extracellular liquid described, for instance, by Darcy's law (1.72). The introduction of the viscous term is consistent with Saramito's work [130, 131] on elasto-visco-plastic fluids, such as liquid foams, emulsions and blood flows. Indeed in these works the 1D total stress is represented by $\sigma = \tau + \eta\dot{\varepsilon}$, where τ is an extension of the Oldroyd model coupled with the Bingham constitutive equation, whereas the second term takes into account viscous phenomena.

Concerning the tensor $\mathbb{T}_s$ representing the stress of the cellular constituent, a unique representation of the constitutive equation representing living matter behavior is still under investigation. In this work we assume that cells behave elastically, obeying a Neo-Hookean law, with coefficient of the isotropic term $-(p + \Sigma_s(\phi_s))$ and shear modulus μ, the first term of the sum in equation (3.2) is

$$\mathbb{T}_s = -\phi_s \left(p + \Sigma_s(\phi_s)\right) \mathbb{I} + \mu\phi_s \mathbb{B}_n \,, \tag{3.3}$$

where $\mathbb{B}_n = \mathbb{F}_n \mathbb{F}_n^T$.
For what concern the description of the anelastic part, we refer to [115], where plastic effects are included starting from the idea that the rearrangement of adhesion bonds during the deformation of multicellular spheroids is related to the existence of a yield condition in the macroscopic constitutive equation of the stress tensor. The yield stress is a very important quantity in rheology and it is associated with the existence of strong interactions, causing the impossibility for a fluid

to flow when small shear stresses are applied.
Indeed experimental evidence suggest that when a cell aggregate undergoes compression:

1. for moderate values of applied stress, cell aggregates deform elastically;

2. above a limit value, the cell aggregate undergoes internal re-organization which can be modelled at a macroscopic level as a visco-plastic deformation.

The so-called yield stress, denoted by $\tau(\phi_s)$, depends on the number of cells per unit volume because the threshold of the onset of cell re-organization is proportional to the area of the cell membranes in contact times the bond energy, that represents the work needed to break cell-to-cell bonds. This is related to the experimental observation that adhesion bonds between cells have a finite strength and might break or build up during the evolution [15, 27, 139].

To translate this idea into formal terms, we propose a modification of the model presented in [115]. Using the virtual-power formulation and considering that the Cauchy tensor, $\mathbb{T}_s$, is work-conjugate with the elastic deformation rate $\mathbb{L}_n = \dot{\mathbb{F}}_n \mathbb{F}_n^{-1}$ whereas the plastic tensor, $\mathbb{T}_p$, is work-conjugate with $\mathbb{L}_p = \dot{\mathbb{F}}_p \mathbb{F}_p^{-1}$ and it should be deviatoric being $\mathrm{tr}\mathbb{L}_p = 0$, it can be proved [77] that

$$\mathbb{T}_p = \mathrm{dev}\mathbb{M}_{sn} = J\mathbb{F}_n^T \mathbb{T}'_s \mathbb{F}_n^{-T}\,, \tag{3.4}$$

where $\mathbb{M}_{sn}$ is defined in (1.66) and we use the fact that $J_p = 1$ so that $J_n \equiv J$. We remark that $\mathbb{T}'_s$ is the deviatoric part of $\mathbb{T}_s$, i.e., $\mathbb{T}'_s = \mathbb{T}_s - \frac{1}{3}(\mathrm{tr}\mathbb{T}_s)\mathbb{I}$.

Recalling Chapter 1, Section 1.2, we introduce the constitutive free energy ψ and we postulate a dissipation principle, such that we can postulate the following inequality for the solid constituent [77]

$$\phi_s \dot{\psi}_s - \mathbb{T}_s : \mathbb{L}_n - J_n^{-1} \mathbb{T}_p : \mathbb{D}_p \leq 0\,. \tag{3.5}$$

Then taking $\psi_s = \hat{\psi}_s(\mathbb{F}_n)$ and using the classical Coleman-Noll procedure for the exploitation of second law of thermodynamics, we obtain

$$\mathbb{T}_s = \phi_s \frac{\partial \hat{\psi}}{\partial \mathbb{F}_n} \mathbb{F}_{\mathrm{n}}^{\mathrm{T}} \tag{3.6}$$

$$\mathbb{T}_p : \mathbb{D}_p \geq 0\,. \tag{3.7}$$

Therefore $\mathbb{L}_p = G(\mathbb{T}_p)$ satisfies the previous relations, given any positive linear operator G.
Taking into account the mechanical observations on the existence of a yield criterion and the fact that the material can be considered isotropic, we can choose

$$G(\cdot) = \frac{1}{2\eta(\phi_s)} \left[1 - \left(\frac{\tau(\phi_s)}{f(\mathbb{T}'_s)} \right)^{\alpha} \right]_+ \mathrm{sym}(\cdot)\,, \tag{3.8}$$

where $f(\mathbb{T}'_s)$ is a suitable frame invariant measure of the stress of the cellular constituent and $[\cdot]_+$ and $\mathrm{sym}(\cdot)$ stand for the positive and symmetric part of their arguments respectively. The parameter α is in the range $[0,1]$ and determines the viscous behavior at high shear rates. In the following, the particular case $\alpha = 1$ will be considered, to obtain the following constitutive equation

$$\mathbb{L}_p = \mathbb{D}_p = \frac{J}{2\eta(\phi_s)} \left[1 - \frac{\tau(\phi_s)}{f(\mathbb{T}'_s)} \right]_+ \mathrm{sym}\left(\mathbb{F}_n^T \mathbb{T}'_s \mathbb{F}_n^{-T} \right)\,. \tag{3.9}$$

Assuming isochoric transformations, $J = 1$, and thus (3.9) becomes

$$\mathbb{L}_p = \mathbb{D}_p = \frac{1}{2\eta(\phi_s)} \left[1 - \frac{\tau(\phi_s)}{f(\mathbb{T}'_s)} \right]_+ \mathrm{sym}\left(\mathbb{F}_n^T \mathbb{T}'_s \mathbb{F}_n^{-T} \right)\,. \tag{3.10}$$

Equation (3.10) can be interpreted, considering that a crucial role in the reorganization of cells is played by the shear $\mathbf{t} \cdot \mathbb{T}'_s \mathbf{n}$ that can be mapped back to the natural configuration taking into account that a material vector transforms like $\mathbf{t} = \mathbb{F}_n \mathbf{t}_n$ whereas the normal to a material surface like $\mathbf{n} = \det(\mathbb{F}_n)\mathbb{F}_n^{-T}\mathbf{n}_n = \mathbb{F}_n^{-T}\mathbf{n}_n$, since $\mathbb{F}_n$ is an isochoric transformation. Then, one has that $\mathbf{t} \cdot \mathbb{T}'_s \mathbf{n} = \mathbf{t}_n \cdot \mathbb{F}_n^T \mathbb{T}'_s \mathbb{F}_n^{-T} \mathbf{n}_n$. Therefore a crucial role in determining whether the material reorganizes is the tensor $\mathbb{T}_p = \mathbb{F}_n^T \mathbb{T}'_s \mathbb{F}_n^{-T}$.
We observe that in (3.10), the term containing the yield stress switches on just when the stress overcomes the yield stress in terms of the set measure. In this case the energy is no longer elastically stored but it is spent in cell unbinding and cytoskeleton reorganization at the microscopic scale, which produces the spheroid rearrangement at the macroscopic scale.
Referring back to equation (3.10), we explicitly observe that

$$\mathrm{tr}(\mathbb{T}'_s) = \mathrm{tr}(\mathbb{F}_n^T \mathbb{T}'_s \mathbb{F}_n^{-T}) = \mathrm{tr}(\mathbb{D}_p) = 0, \tag{3.11}$$

and that the eigenvalues of $\mathbb{F}_n^{-T} \mathbb{T}'_s \mathbb{F}_n^T$ are the same as those of $\mathbb{T}'_s$.
Furthermore being $\mathbb{T}'_s$ objective, we have to study how the quantities in equation (3.10) transform

under an euclidean change of frame. Denoting with a bar $\overline{(\cdot)}$ the value of a field after the change of frame and with $\mathbb{R}$ an orthogonal tensor, thanks to the relations (1.61) introduced in chapter 1, one has

$$\overline{\mathbb{D}}_p = \mathbb{D}_p \tag{3.12}$$

if and only if

$$G\left(\overline{\mathbb{F}_n^T \mathbb{T}_s' \mathbb{F}_n^{-T}}\right) = G\left(\mathbb{F}_n^T \mathbb{R}^T \overline{\mathbb{T}}_s' \mathbb{R} \mathbb{F}_n^{-T}\right) = G\left(\mathbb{F}_n^T \mathbb{T}_s' \mathbb{F}_n^{-T}\right), \tag{3.13}$$

which implies the frame indifference of $\mathbb{T}_s'$.

3.2.2 Uniaxial compression

In this section we will study in more detail the response of a material satisfying (3.2) - (3.3) (3.10) subject to a uniaxial compression test. Though the results of this section also apply to an elongation test, we focus on compressive forces, because they are the more relevant from the biological point of view.
Typical experiments can be performed under the following conditions:

- a constant pressure is imposed to the specimen and the corresponding deformation is recorded upon time. Possibly the compression is released after some time allowing a stress-free evolution of the specimen. Then, the process of compression with the same constant load can be re-iterated. We will call the first experiment *stress-controlled test* or *creep test* and we will denote the last process as *cyclic stress-controlled test* (or *cyclic creep test*).

- a constant force is imposed to the specimen and the corresponding deformation is measured (*force-controlled test*). Also in this case, the compression is released after some time and the process with the same constant force is reiterated (*cyclic force-controlled test*). We remark that, considering the increase in the transverse section of the aggregate, the applied stress is no more constant.

- a fixed deformation is applied and the evolution of the stress inside the body is monitored (*stress relaxation test*). Finally the same deformation is applied periodically, letting

spheroids to freely expand between two subsequent compressions. In the following we will refer to this process as *cyclic deformation test*.

We will assume that the deformation, generated by a uniaxial force or strain applied along the z-axis, is homogeneous inside the body, keeping a constant volume ratio ϕ_s, and is given by

$$x = \frac{X}{\sqrt{\varphi(t)}}, \quad y = \frac{Y}{\sqrt{\varphi(t)}}, \quad z = \varphi(t)Z\,. \tag{3.14}$$

Then the deformation gradient from the initial to the final configuration is given by

$$\mathbb{F} = \mathrm{diag}\left\{\frac{1}{\sqrt{\varphi(t)}}, \frac{1}{\sqrt{\varphi(t)}}, \varphi(t)\right\}. \tag{3.15}$$

The deformation gradient due to the internal reorganization of the cytoskeleton can be represented by

$$\mathbb{F}_p = \mathrm{diag}\left\{\frac{1}{\sqrt{\Psi_p(t)}}, \frac{1}{\sqrt{\Psi_p(t)}}, \Psi_p(t)\right\}, \tag{3.16}$$

where $\Psi_p(t)$ is a measure of how much the aggregate has reorganized and the natural configuration has evolved. For $\Psi_p(t) = 1$ we have no contribution due to rearrangement of bonds inside the body.

From equations (3.15) and (3.16), being $\mathbb{F} = \mathbb{F}_n\mathbb{F}_p$ it is clear that

$$\mathbb{F}_n = \mathrm{diag}\left\{\sqrt{\frac{\Psi_p(t)}{\varphi(t)}}, \sqrt{\frac{\Psi_p(t)}{\varphi(t)}}, \frac{\varphi(t)}{\Psi_p(t)}\right\}. \tag{3.17}$$

Therefore, considering that in the uniaxial compression test the total force is applied in the z-direction, eq. (3.2) and (3.3) lead to

$$\mathbb{T} = -\left(p + \phi_s\Sigma_s(\phi_s)\right)\mathbb{I} + \mu\phi_s\mathbb{B}_n + 2(1-\phi_s)\nu\mathbb{D} = \mathrm{diag}\left\{0, 0, -P_{appl}(t)\right\}, \tag{3.18}$$

where we consider P_{appl} to be positive for a compressive load.
In a stress-controlled test, P_{appl} is a known constant and it vanishes in the stress release phase, whereas it is a function of time, when we consider that the applied force, F_{appl}, is kept constant, i.e., $P_{appl} = \dfrac{F_{appl}}{S_{appl}}$. Indeed, in this case the stress decreases in time as the area over which the force is applied increases. Finally in a stress-relaxation experiment under constant deformation,

the applied force is one of the unknown of the problem.

Considering that the liquid and the cellular component move with the same velocity,

$$\mathbb{D} = \text{diag}\left\{-\frac{1}{2},-\frac{1}{2},1\right\}\frac{\dot{\varphi}(t)}{\varphi(t)},$$

being

$$\mathbb{B}_n = \text{diag}\left\{\frac{\Psi_p(t)}{\varphi(t)},\frac{\Psi_p(t)}{\varphi(t)},\frac{\varphi^2(t)}{\Psi_p^2(t)}\right\},$$

we obtain the following equation for the stress exerted by the mixture

$$\begin{aligned}\mathbb{T} &= -\Sigma\mathbb{I}+\mu\phi_s\,\text{diag}\left\{\frac{\Psi_p(t)}{\varphi(t)},\frac{\Psi_p(t)}{\varphi(t)},\frac{\varphi^2(t)}{\Psi_p^2(t)}\right\}+\\ &\quad +2\nu(1-\phi_s)\text{diag}\left\{-\frac{1}{2},-\frac{1}{2},1\right\}\frac{\dot{\varphi}(t)}{\varphi(t)},\end{aligned} \tag{3.19}$$

where we call $\Sigma = p+\phi_s\Sigma_s(\phi_s)$.
Imposing the condition on the r.h.s. of (3.18), we have

$$\Sigma(t) = \mu\phi_s\frac{\Psi_p(t)}{\varphi(t)}-\nu(1-\phi_s)\frac{\dot{\varphi}(t)}{\varphi(t)}, \tag{3.20}$$

$$P_{appl}(t) = \mu\phi_s\frac{\Psi_p^3(t)-\varphi^3(t)}{\Psi_p^2(t)\varphi(t)}-3\nu(1-\phi_s)\frac{\dot{\varphi}(t)}{\varphi(t)}. \tag{3.21}$$

The first term in the r.h.s. of both (3.20) and (3.21) is the same obtained in [115], taking account the cellular constituent only, whereas the second terms arise from the introduction of the viscous phase in the model. Equation (3.21) can provide the stress exerted by the aggregate when a deformation is imposed along the z-axis (e.g. a fixed deformation, φ_0), or it can be used to derive the evolution of $\varphi(t)$ when, for instance, a constant load is applied

$$\frac{\dot{\varphi}}{\varphi} = -\frac{P_{appl}}{3\nu(1-\phi_s)}+\frac{\mu\phi_s}{3\nu(1-\phi_s)}\frac{\Psi_p^3-\varphi^3}{\varphi\Psi_p^2}, \tag{3.22}$$

where we omit the dependence from t for sake of simplicity. As a particular case, equation (3.22) can be used to model the stress-free evolution of the system, imposing $P_{appl}=0$.
We observe that, when no load is imposed in eq. (3.22), the ratio $\dfrac{\nu(1-\phi_s)}{\mu\phi_s}$ plays the role of a

characteristic time in the shape recovery process. Considering the fact that we are compressing a multicellular aggregate, this characteristic time can be related to the consolidation time of a saturated porous material filled with fluid, $\frac{\mu_w L^2}{kE}$, where μ_w is the dynamic viscosity of the physiological liquid, L the multicellular aggregate height, k the permeability of the porous structure and E its elastic modulus. In this way it is possible to derive the parameter ν from physical quantities measurable in experiments and by means of known estimates of k, e.g. the Kozeny-Carman relation. Therefore, it is important to remark that, in (3.22), the viscous coefficient, ν, is proportional to the viscosity of the fluid encapsulated in the cellular specimen, but it is not simply the viscosity of the physiological liquid.

Equation (3.22) needs to be joined with equation (3.10), taking into account that

$$\mathbb{T}'_s = \mu\phi_s \,\mathrm{diag}\left\{-\frac{1}{3}, -\frac{1}{3}, \frac{2}{3}\right\} \frac{\varphi^3 - \Psi_p^3}{\Psi_p^2 \varphi}\,. \tag{3.23}$$

and postulating an equation for $f(\mathbb{T}'_s)$.
Here we consider that the frame invariant measure of the stress is the maximum shear stress magnitude, given by half of the difference between the maximum and the minimum stress in the principal directions (Tresca's criterion)

$$f(\mathbb{T}'_s) = \frac{|T'^{zz}_s - T'^{xx}_s|}{2} = \frac{\mu\phi_s}{2}\frac{|\Psi_p^3 - \varphi^3|}{\varphi\Psi_p^2}\,, \tag{3.24}$$

which means that cell unbinding is primarily caused by the slippage of cells along the maximum shear stress surface, which seems reasonable in a cellular aggregate under compression. In a more general case, in which the principal stresses are not trivially known, it is possible to use the von Mises criterion, taking into account that Tresca's criterion is more conservative and, therefore, it predicts plastic reorganization for stresses that are still elastic according to the von Mises criterion.
The evolution for the internal reorganization is therefore

$$\frac{\dot{\Psi}_p}{\Psi_p} = -\frac{1}{3\lambda}\left[1 - \frac{2\tau}{\mu\phi_s}\frac{\varphi\Psi_p^2}{|\Psi_p^3 - \varphi^3|}\right]_+ \frac{\Psi_p^3 - \varphi^3}{\varphi\Psi_p^2}\,. \tag{3.25}$$

where $\lambda = \dfrac{\eta(\phi_s)}{\mu\phi_s}$ is the *cell-reorganization time* (or plastic rearrangement time) and $\tau = \tau(\phi_s)$.
Equation (3.25) states that when the quantity inside the square parenthesis is positive, then Ψ_p

will evolve. In the following we will call $\varphi_y(\Psi_{p,0})$ the unique value of φ that switches on the square brackets for fixed $\Psi_p = \Psi_{p,0}$, i.e.,

$$\frac{\Psi_{p,0}^3 - \varphi_y^3(\Psi_{p,0})}{\Psi_{p,0}^2 \varphi_y(\Psi_{p,0})} = \frac{2\tau}{\mu\phi_s}. \tag{3.26}$$

when the imposed deformation is known, only values of $\varphi_0 < \varphi_y(1)$ are able to trigger the internal reorganization of the aggregates. Moreover, as we will see more in detail in Section 3.3.3, in a stress relaxation experiment with constant deformation equal to $\varphi_0 < \varphi_y(1)$ the equilibrium of (3.25) is reached when $\dfrac{\Psi_p^3 - \varphi_0^3}{\varphi_0 \Psi_p^2} = \dfrac{2\tau}{\mu\phi_s}$, i.e., from (3.22) at $P_{appl} = 2\tau$, independently of φ_0 as in [115].

3.3 Results

The model presented in Section 3.2.2 can provide some useful information on the mechanical behavior of aggregates both when they are compressed with a constant force and when they are released. In Section 3.3.1 and 3.3.2 we present the results obtained in the case of a cyclic creep test and a cyclic force-controlled test, respectively. Section 3.3.3 is devoted to the the cyclic deformation test, as performed in the experiments in [52].
The following proposition will be useful.

Proposition 1. *When the aggregate is compressed according to the following imposed deformation and stress histories:*

a) any given compressive deformation, $\varphi(t)$ with $\dot{\varphi}(t) \leq 0$

b) any sequence of given $\varphi(t)$ with $\dot{\varphi}(t) \leq 0$ for $t \in [t_{2i}, t_{2i+1}]$ followed by a stress release for $t \in [t_{2i+1}, t_{2(i+1)})$ with $i = 0, \ldots, n$

c) any compressive load, $P_{appl}(t) > 0$

d) any sequence of compressive load, $P_{appl}(t) > 0$, for $t \in [t_{2i}, t_{2i+1}]$ followed by stress release for $t \in [t_{2i+1}, t_{2(i+1)})$, with $i = 1, \ldots, n$.

if $\Psi_p(0) \geq \varphi(0)$, then

$$\Psi_p(t) \geq \varphi(t) \qquad \forall t > 0\,.$$

This proposition allows to get rid of the modulus in (3.25) and rewrite (3.22) and (3.25) as

$$\dot{\Psi}_p(t) = -\frac{1}{3\lambda}\left[\frac{\Psi_p^3(t)-\varphi(t)^3}{\varphi(t)\Psi_p^2(t)}-\frac{2\tau}{\mu\phi_s}\right]_+ \Psi_p(t)\,, \tag{3.27}$$

$$\dot{\varphi}(t) = -\frac{P_{appl}(t)}{3\nu(1-\phi_s)}\varphi(t)+\frac{\mu\phi_s}{3\nu(1-\phi_s)}\frac{\Psi_p^3(t)-\varphi(t)^3}{\Psi_p^2(t)}\,. \tag{3.28}$$

Proof. Case a)
We first prove the proposition in the case of a given deformation $\varphi(t)<1$ with $\dot{\varphi}(t)\leq 0$ applied to the cellular aggregate for $t\in[0,t_1]$, where t_1 is the time when the upper plate is possibly lifted up. The same proof holds for $t_1\to\infty$.

Considering that $\Psi_p(0)=1$, if the imposed deformation $\varphi(t)$ is so small that $\varphi(t)<\varphi_y(1)$, where $\varphi_y(1)$ satisfies the yield condition (3.26), from (3.25) the quantity in the square parenthesis is always negative and $\Psi_p(t)=1>\varphi(t)$.

On the other hand, if the imposed deformation is not so small and the yield condition is overcome, then we can rewrite equation (3.25) regulating the evolution of the internal reorganization, as

$$\dot{\Psi}_p = -\frac{1}{3\lambda}\left[\frac{|\Psi_p^3-\varphi^3|}{\varphi\Psi_p^2}-\frac{2\tau}{\mu\phi_s}\right]_+ \operatorname{sgn}(\Psi_p-\varphi)\Psi_p\,. \tag{3.29}$$

It is trivial to check that starting from $\Psi_p(0)=1$, $\Psi_p(t)$ is always positive. For the thesis, we then define $w(t)=\Psi_p(t)-\varphi(t)$ and consider the positive part, w_+, given by

$$w_+(t)=\max\{w(t),0\}=\begin{cases} w(t) & w(t)>0;\\ 0 & w(t)\leq 0;\end{cases}$$

and the negative part w_- defined as

$$w_-=\max\{-w(t),0\}=\begin{cases} -w(t) & w(t)<0;\\ 0 & w(t)\geq 0\,.\end{cases}$$

Therefore the function w can be expressed in terms of w_+ and w_-, as $w=w_+-w_-$.

Then w evolves according to

$$\dot{w} = -\frac{1}{3\lambda}\left[\frac{|\Psi_p^3-\varphi^3|}{\varphi\Psi_p^2}-\frac{2\tau}{\mu\phi_s}\right]_+ \operatorname{sgn}(w)\Psi_p-\dot{\varphi}\,. \tag{3.30}$$

starting from $w(0) > 0$, since at the initial time $\Psi_p(0) = 1 \geq \varphi(0)$.
We multiply each side of (3.30) by w_- and integrate from 0 to an arbitrary time $\tilde{t} \in (0,t_1]$ to get

$$\begin{aligned}\int_0^{\tilde{t}} \dot{w} w_- dt &= -\frac{1}{3\lambda}\int_0^{\tilde{t}} \left[\frac{|\Psi_p^3 - \varphi^3|}{\varphi\Psi_p^2} - \frac{2\tau}{\mu\phi_s}\right]_+ \mathrm{sgn}(w) w_- \Psi_p dt - \int_0^{\tilde{t}} \dot{\varphi} w_- dt = \\ &= \frac{1}{3\lambda}\int_0^{\tilde{t}} \left[\frac{|\Psi_p^3 - \varphi^3|}{\varphi\Psi_p^2} - \frac{2\tau}{\mu\phi_s}\right]_+ w_- \Psi_p dt + \int_0^{\tilde{t}} -\dot{\varphi} w_- dt \geq 0\,, \qquad (3.31)\end{aligned}$$

being both integrands non negative $\forall \tilde{t} \in (0,t_1]$. Hence

$$0 \leq \int_0^{\tilde{t}} \dot{w} w_- dt = -\int_0^{\tilde{t}} \dot{w}_- w_- dt = -\frac{1}{2} w_-^2(\tilde{t}) \leq 0\,,$$

where we used the condition $w(0) \geq 0$, i.e $w_-(0) = 0$.
Therefore

$$w_-^2(\tilde{t}) = 0 \Longrightarrow w(\tilde{t}) \geq 0 \Longrightarrow \Psi_p(\tilde{t}) \geq \varphi(\tilde{t}) \quad \forall \tilde{t} \in (0,t_1]\,.$$

Case b)
If at any time, $t = t_1$, the upper plate is lifted up, then, the equations regulating the evolution of the system, from $t = t_1$ on, are (3.22) and (3.25), that can be rewritten as

$$\dot{\Psi}_p = -\frac{1}{3\lambda}\left[\frac{|\Psi_p^3 - \varphi^3|}{\varphi\Psi_p^2} - \frac{2\tau}{\mu\phi_s}\right]_+ \mathrm{sgn}(\Psi_p - \varphi)\Psi_p \qquad (3.32)$$

$$\dot{\varphi} = \frac{\mu\phi_s}{3\nu(1-\phi_s)}\frac{\Psi_p^3 - \varphi^3}{\Psi_p^2}\,. \qquad (3.33)$$

We apply the same method presented above, computing for an arbitrary time $\tilde{t} \in (t_1,t_2]$, where t_2 is the time when the compression is possibly restored (obviously the same proof holds for $t_2 \to \infty$)

$$\begin{aligned}\int_{t_1}^{\tilde{t}} \dot{w} w_- dt &= -\frac{\mu\phi_s}{3\eta}\int_{t_1}^{\tilde{t}} \left[\frac{|\Psi_p^3 - \varphi^3|}{\varphi\Psi_p^2} - \frac{2\tau}{\mu\phi_s}\right]_+ \mathrm{sgn}(w) w_- \Psi_p dt + \\ &\quad - \frac{\mu\phi_s}{3\nu(1-\phi_s)}\int_{t_1}^{\tilde{t}} \frac{\Psi_p^2 + \varphi\Psi_p + \varphi^2}{\Psi_p^2} w w_- dt\,. \qquad (3.34)\end{aligned}$$

We observe that also in this case, $w_-(t_1) = 0$, being $w(t_1) = \Psi_p(t_1) - \varphi(t_1) \geq 0$ (as demonstrated before) and then $\int_{t_1}^{\tilde{t}} \dot{w} w_- dt = -\frac{1}{2} w_-^2$. On the other hand, both terms on the left hand side are always greater or equal to zero, being $\mathrm{sgn}(w) w_- = -w_- \leq 0$ and $w w_- = -w_-^2 \leq 0$.
Then also in this case, we can conclude that

$$w(\tilde{t}) = w_+(\tilde{t}) \geq 0 \Longrightarrow \Psi_p(\tilde{t}) \geq \varphi(\tilde{t}) \quad \forall \tilde{t} \in (t_1, t_2] \,.$$

Then it is possible to reiterate the process, together with the one in case *a)* to demonstrate the thesis.

Case c)
In the case of the application of a compressive stress, $P_{appl}(t) > 0$, along the negative z-axis

$$\dot{\Psi}_p = -\frac{1}{3\lambda} \left[\frac{|\Psi_p^3 - \varphi^3|}{\varphi \Psi_p^2} - \frac{2\tau}{\mu \phi_s} \right]_+ \mathrm{sgn}(\Psi_p - \varphi) \Psi_p \tag{3.35}$$

$$\dot{\varphi} = -\frac{P_{appl}}{3\nu(1-\phi_s)} \varphi + \frac{\mu \phi_s}{3\nu(1-\phi_s)} \frac{\Psi_p^3 - \varphi^3}{\Psi_p^2} \,. \tag{3.36}$$

Using the same definition for $w(t)$ we have that

$$\begin{aligned} \int_0^{\tilde{t}} \dot{w} w_- dt = & -\frac{\mu \phi_s}{3\eta} \int_0^{\tilde{t}} \left[\frac{|\Psi_p^3 - \varphi^3|}{\varphi \Psi_p^2} - \frac{2\tau}{\mu \phi_s} \right]_+ \mathrm{sgn}(w) w_- \Psi_p dt + \\ & - \frac{\mu \phi_s}{3\nu(1-\phi_s)} \int_0^{\tilde{t}} \frac{\Psi_p^2 + \varphi \Psi_p + \varphi^2}{\Psi_p^2} w w_- dt + \\ & + \int_0^{\tilde{t}} \frac{P_{appl}}{3\nu(1-\phi_s)} \varphi w_- dt \end{aligned} \tag{3.37}$$

The last integral in equation (3.37) is obviously non negative and therefore also in this case $\Psi_p(t) \geq \varphi(t)$.

Case d)
If at any time $t = t_1$ the plate compressing the aggregate is lifted up, the equation regulation the evolution are the same presented in case b) and the condition being $w(t_1) = \Psi_p(t_1) - \varphi(t_1) \geq 0$ continues to hold thanks to case c). Thus adopting the same reasoning of case b), the thesis is easily demonstrated.

□

3.3.1 Cyclic creep test

In a cyclic creep test a constant pressure is applied while the strain induced on the spheroids is measured over a period of time and then the stress on the upper plate is removed. Considering only forces directed along the negative z-axis, it was shown in Proposition 1 (case c) that $\Psi_p(t) \geq \varphi(t)$ and therefore equations (3.27)-(3.28) hold. Obviously, when the upper plate is lifted-up $P_{appl} = 0$ in equation (3.28).

Using Proposition 1, scaling times with 3λ and introducing the dimensionless quantities

$$\tilde{\tau} = \frac{2\tau}{\mu\phi_s}, \qquad \tilde{\mu} = \frac{\mu\lambda\phi_s}{\nu(1-\phi_s)}, \qquad \tilde{P}(t) = \frac{P_{appl}}{\mu\phi_s},$$

the system (3.27)-(3.28) can be written in dimensionless form as

$$\begin{cases} \dot{\Psi}_p = -[g(\Psi_p,\varphi) - \tilde{\tau}]_+ \Psi_p, & \text{(3.38a)} \\ \dot{\varphi} = \tilde{\mu}[g(\Psi_p,\varphi) - \tilde{P}(t)]\varphi, & \text{(3.38b)} \end{cases}$$

where $g(\Psi_p,\varphi) = \dfrac{\Psi_p^3 - \varphi^3}{\Psi_p^2\varphi}$. It can be readily noticed that g is a decreasing function of φ for fixed Ψ_p and an increasing functions of Ψ_p for fixed φ.

The system (3.38) admits non trivial steady state only if $\tilde{P} \leq \tilde{\tau}$, as it is stated in the following proposition.

Proposition 2. *In creep tests*

a) if $\tilde{P} \leq \tilde{\tau}$, then $\Psi_p(t) = 1$ and $\varphi(t) \geq \varphi_c : g(1,\varphi_c) = \dfrac{1}{\varphi_c} - \varphi_c^2 = \tilde{P}$ are solutions of the system (3.38), with initial conditions $\Psi_p(0) = 1$ and $\varphi(0) = 1$.

b) if $\tilde{P}(t) > \tilde{\tau}, \forall t$, then equations (3.27) and (3.28) admit only the trivial steady state.

Proof. Case a)
If $\tilde{P}(t) \leq \tilde{\tau}, \forall t$, from equations (3.38), being $\Psi_p(0) = 1$ and $\varphi(0) = 1$ the right hand side of (3.38a) is initially null, that means $\dot{\Psi}_p(0) = 0$, whereas from (3.38b) $\dot{\varphi}(0) < 0$. Moreover $\Psi_p = 1$

and $\varphi \geq \varphi_c$ makes $[\cdot]_+$ of (3.38a) equal to 0. Indeed, being $g(1,\varphi)$ a decreasing function of φ,

$$g(1,\varphi) - \tilde{\tau} \leq g(1,\varphi) - \tilde{P} \leq g(1,\varphi_c) - \tilde{P} = 0\,, \tag{3.39}$$

which holds for all $t \geq 0$.

From (3.38b) it is then clear that $\varphi = \varphi_c$ and $\Psi_p = 1$ makes $\dot{\varphi} = 0$ and that $\varphi > \varphi_c$ and $\Psi_p = 1$ makes $\dot{\varphi} < 0$. We will then show that $\varphi(t) \geq \varphi_c \forall t > 0$, using the same argument as in Proposition 1. We define $w = \varphi - \varphi_c$ and hence

$$\int_0^{\tilde{t}} \dot{w} w_-\, dt \;\; = \;\; \tilde{\mu} \int_0^{\tilde{t}} \left(g(1,\varphi) - \tilde{P}\right) \varphi\, w_-\, dt \geq 0\,, \tag{3.40}$$

where we used the fact that when $w_- \neq 0$, $\varphi < \varphi_c$ and the parenthesis in the integral is positive.

Therefore

$$0 \leq \int_0^{\tilde{t}} \dot{w} w_-\, dt = -\frac{1}{2} w_-^2(\tilde{t}) \leq 0\,,$$

thanks to the condition $w(0) \geq 0$, i.e $w_-(0) = 0$.
For the arbitrariness of $\tilde{t}$, this means that $\varphi(t) \geq \varphi_c \forall t > 0$.

Case b)
The stationary condition for equation (3.38a) is reached either if $\Psi_p(t) = 0$ or if the expression in square brackets is negative (i.e. the region above the red line in Fig. 3.1 on the right).

If $\tilde{P}(t) > \tilde{\tau}$, this second condition corresponding to $g(\Psi_p,\varphi) \leq \tilde{\tau}$, would make the right hand side of (3.38b) always strictly negative.
Therefore the only possible stationary point for (3.38) is $\Psi_{p,\infty} = 0$, $\varphi_\infty = 0$

□

In the particular case of constant $\tilde{P}$, the right hand side of (3.38b) vanishes for non null Ψ_p only if $g(\Psi_p,\varphi) = \tilde{P}$ that makes the r.h.s. of (3.38a) vanishing only if $\tilde{P} \leq \tilde{\tau}$. As it is evident plotting the vector field corresponding to (3.38), if $\tilde{P} \leq \tilde{\tau}$ the solution starting from $\Psi_p(0) = \varphi(0) = 1$ will keep $\Psi_p = 1$ while φ will tend to $\varphi_c : g(1,\varphi_c) = \tilde{P}$ (see Fig. 3.1, left). On the other hand, if $\tilde{P} > \tilde{\tau}$, solutions of (3.38) will tend to the trivial equilibria (Fig. 3.1, right).

Hence in a certain range of stress, i.e. for $\tilde{P} \leq \tilde{\tau}$, or equivalently $P_{appl} \leq 2\tau$, the cellular aggregate does not undergo an internal reorganization, then $\Psi_p(t) = 1$, whereas $\varphi(t)$ decreases until the value φ_c is reached. In this case, if after some time the load is removed, the specimen will go back to the initial configuration, $\varphi_r = 1$, following the classical visco-elastic response, due to the elastic response of cells and the viscous term of the liquid component (see Fig. 3.2).

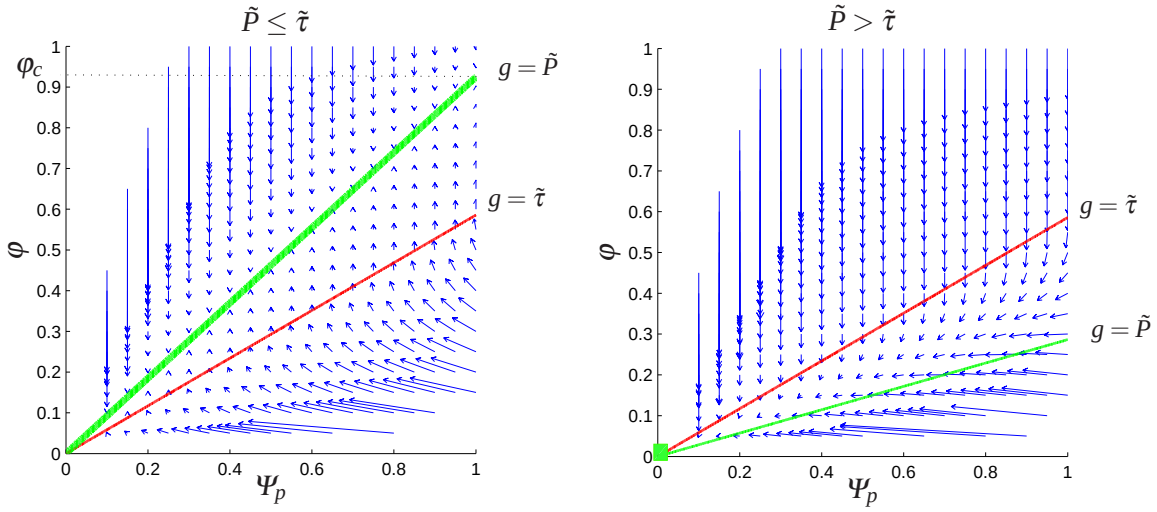

Figure 3.1: Vector field (blue arrows) corresponding to (3.38), if $\tilde{P} \leq \tilde{\tau}$ (on the left) and $\tilde{P} > \tilde{\tau}$ (on the right). The red curve corresponds to $g(\Psi_p,\varphi) = \tilde{\tau}$, whereas the green curve to $g(\Psi_p,\varphi) = \tilde{P}$. It is clear that if $\tilde{P} \leq \tilde{\tau}$, φ and Ψ will tend to the green curve. On the other hand if $\tilde{P} > \tilde{\tau}$, $\Psi_p \to 0$ and $\varphi \to 0$.

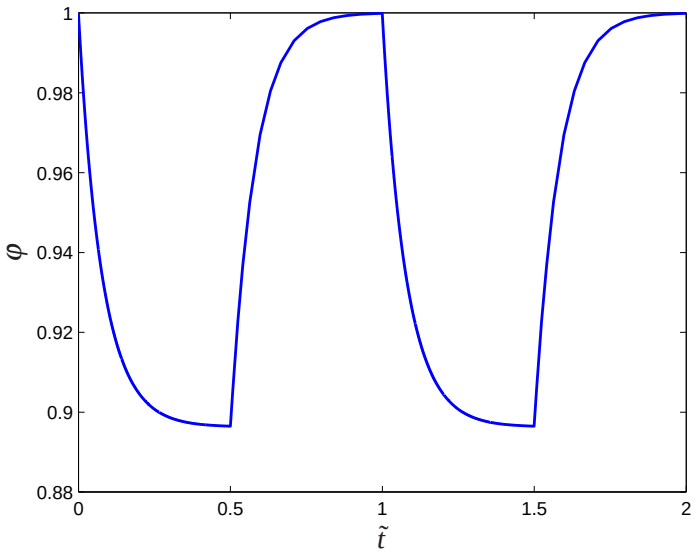

Figure 3.2: Cycle of compressions when $\tilde{P} < \tilde{\tau}$ is applied and then removed. The simulation is performed setting the yield stress $\tau = 0.2Pa$ and $P_{appl} = 0.25Pa$, according to the yield condition. The cellular volume ratio, ϕ_s is set equal to 0.8, which is consistent with biological observations [149] and the cell-reorganization time is $\lambda = 22s$. The other parameters can be scaled according to the chosen τ (here: $\mu = 1Pa$ and $\nu = 20Pa \cdot s$). The compression and release times are both equal to $3/2\lambda = 33s$. The applied stress being under the yield condition, there is no internal reorganization of bonds ($\Psi_p(t) = 1$), therefore when the compression is removed aggregates progressively go back to the initial configuration, $\varphi_r = 1$. The liquid component in the mixture is responsible of the delay introduced in the recovery dynamics of spheroids when the upper plate is lifted up.

We observe that if the stress is not constant, but smaller than $2\tau\ \forall t$, $\Psi_p(t) = 1$ is still a solution of (3.27).

In order to trigger spheroid internal reorganization $\tilde{P}$ must be larger than $\tilde{\tau}$. In this case Ψ_p will decrease from $\Psi_p(0) = 1$ according to (3.38a), causing a macroscopic remodelling of the multicellular body. Therefore when the upper plate is removed a plastic deformation of the aggregate can be observed. The internal reorganization rate depends on the intensity of the load applied to the aggregate, compared to the yield stress (see Fig. 3.3) and, if $\tilde{P}(t) > \tilde{\tau}\ \forall t$, it continues until the stationary condition is reached, then $\Psi_p \to 0$ and $\varphi \to 0$. This physically means that the aggregate is totally squeezed out between the upper and lower plates of the apparatus. These results are intuitively reasonable and analytically correct, however they need to be verified with experimental tests, that unfortunately are not present in literature yet. It is important to observe that standard creep tests used for the measurement of mechanical properties of inert material, eventually need to be modified to be suitable for the application to living cell aggregates, that must be kept in healthy conditions during measurements.

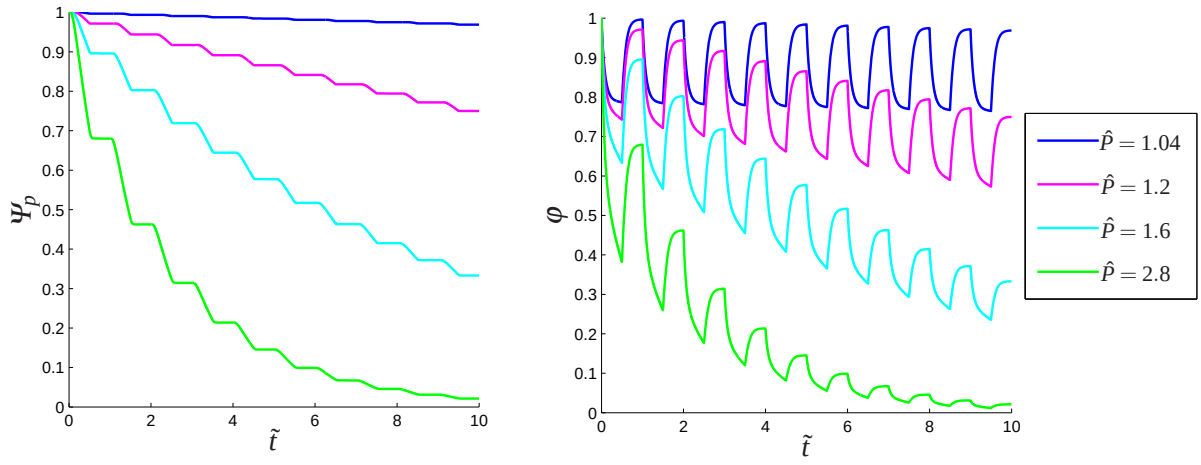

Figure 3.3: Creep test and release for values of P_{appl} above the yield condition, i.e. $\hat{P} = \tilde{P}/\tilde{\tau} > 1$. The other parameters are the same specified in Figure 3.2. It is possible to see that, because of the internal reorganization that occurs within the spheroid under compression (Ψ_p dynamics), the natural configuration of the aggregate changes and when the upper plate is removed the multicellular body does not recover its original shape and a macroscopic deformation can be seen. The process that leads to the plastic deformation of aggregates is faster as P_{appl} increases and, independently of P_{appl}, $\Psi_p \to 0$ and $\varphi \to 0$, which physically means the rupture of the aggregate.

3.3.2 Cyclic force-controlled test

In the previous section, a description of creep tests, i.e., mechanical experiments at constant stress, is proposed. The assumption of constant stress leads to the total disruption of the aggregate when the imposed pressure is above the threshold that induces the internal reorganization. However, in many cases, experimental machines works under controlled force conditions. Therefore in this case, the stress is no longer constant, since the transverse section of the sample increases as the aggregate is compressed and therefore the constant force is distributed over a larger area.

In this Section, we aim to study the influence of the increasing transverse section on the capability of aggregates to reorganize in order to bear the external load. We assume a cylindrical sample of soft biological material under a homogeneous compressive constant force directed along the z-axis, $F_{appl}(t)$. Some properties of the solution are proved and numerical results are presented for a cycle of constant compressive forces and subsequent releases, making a comparison with the results obtained in the previous section for a creep test under constant stress.
We remark that eq. (3.27)-(3.28) continue to hold, defining $P_{appl}(t) = F_{appl}(t)/S_{appl}(t)$ where $S_{appl}(t)$ is the surface on which the load is applied. In order to define the external applied stress we need to do some hypothesis on the geometry of the biological sample. In this case we assume a cylindrical sample of soft biological material, thus, due to the definition of $\mathbf{F}$, we have $P_{appl}(t) = F_{appl}(t)\psi(t)/\pi$.
As done before, we use Proposition 1 and we scale times with 3λ. Introducing the new dimensionless quantities

$$\tilde{F}(t) = \frac{F_{appl}}{\pi\mu\phi_s},$$

and the function $h(\Psi_p,\varphi) = \dfrac{\Psi_p^3 - \varphi^3}{\Psi_p^2\varphi^2}$, the system (3.27)-(3.28) can be written in dimensionless form as

$$\begin{cases} \dot{\Psi}_p = -[g(\Psi_p,\varphi) - \tilde{\tau}]_+\Psi_p, & \text{(3.41a)} \\ \dot{\varphi} = \tilde{\mu}[h(\Psi_p,\varphi) - \tilde{F}(t)]\varphi^2, & \text{(3.41b)} \end{cases}$$

where, as before, $g(\Psi_p,\varphi) = \dfrac{\Psi_p^3 - \varphi^3}{\Psi_p^2\varphi} = h(\Psi_p,\varphi)\varphi$. It can be readily noticed that both g and h are decreasing functions of φ for fixed Ψ_p and increasing functions of Ψ_p for fixed φ. We recall

that $\varphi_y(\Psi_{p,0})$ stands for the unique value that inverts $g = \tilde{\tau}$ for fixed $\Psi_p = \Psi_{p,0}$, i.e., such that

$$g(\Psi_{p,0},\varphi_y(\Psi_{p,0})) = \frac{\Psi_{p,0}^3 - \varphi_y^3(\Psi_{p,0})}{\Psi_{p,0}^2\varphi_y(\Psi_{p,0})} = \tilde{\tau}\,.$$

Similarly, we define by $\varphi_{c,F}(\Psi_{p,0})$ the unique value that inverts $h = F_M = \max_t\{\tilde{F}(t)\}$ with respect to φ for fixed $\Psi_p = \Psi_{p,0}$, i.e., such that

$$h(\Psi_{p,0},\varphi_{c,F}(\Psi_{p,0})) = \frac{\Psi_{p,0}^3 - \varphi_{c,F}^3(\Psi_{p,0})}{\Psi_{p,0}^2\varphi_{c,F}^2(\Psi_{p,0})} = F_M\,, \tag{3.42}$$

where of course we assume that the applied force is bounded.

We first derive, also in this case, the yield condition that trigger the internal reorganization of cellular aggregates.

Proposition 3. *For any given* $\Psi_{p,0}$

$$\varphi_y(\Psi_{p,0}) \le \varphi_{c,F}(\Psi_{p,0}) \quad \Longleftrightarrow \quad F_M \le \frac{\tilde{\tau}}{\varphi_y(\Psi_{p,0})}\,. \tag{3.43}$$

If $F_M > \dfrac{\tilde{\tau}}{\varphi_y(1)}$ *the unique solution of the system*

$$\begin{cases} g(\Psi_p,\varphi) = \tilde{\tau}\,, \\ h(\Psi_p,\varphi) = F_M\,, \end{cases} \tag{3.44}$$

in $(0,1]^2$ *is* $\varphi = \tilde{\tau}/F_M$ *and* Ψ_p *such that*

$$h\left(\Psi_p, \frac{\tilde{\tau}}{F_M}\right) = F_M\,. \tag{3.45}$$

Proof. Since h is a decreasing function of φ, if $\varphi_y(\Psi_{p,0}) \le \varphi_{c,F}(\Psi_{p,0})$,

$$F_M = h(\Psi_{p,0},\varphi_{c,F}(\Psi_{p,0})) \le h(\Psi_{p,0},\varphi_y(\Psi_{p,0})) = \frac{g(\Psi_{p,0},\varphi_y(\Psi_{p,0}))}{\varphi_y(\Psi_{p,0})} = \frac{\tilde{\tau}}{\varphi_y(\Psi_{p,0})}\,.$$

Viceversa, if $F_M \leq \dfrac{\tilde{\tau}}{\varphi_y(\Psi_{p,0})}$, we have

$$h(\Psi_{p,0},\varphi_y(\Psi_{p,0})) = \frac{g(\Psi_{p,0},\varphi_y(\Psi_{p,0}))}{\varphi_y(\Psi_{p,0})} = \frac{\tilde{\tau}}{\varphi_y(\Psi_{p,0})} \geq F_M = h(\Psi_{p,0},\varphi_{c,F}(\Psi_{p,0}))$$

and because of the fact that h is a decreasing function of φ, we can conclude that $\varphi_y(\Psi_{p,0}) \leq \varphi_{c,F}(\Psi_{p,0})$. On the other hand, for small φ and Ψ_p it is possible to prove that the curve $h(\Psi_p,\varphi) = F_M$ behaves like

$$\varphi = \Psi_p - \frac{F_M}{3}\Psi_p^2\,,$$

while $g(\Psi_p,\varphi) = \tilde{\tau}$ behaves like

$$\varphi = \alpha\Psi_p\,, \quad \text{with} \quad \alpha < 1\,, \quad \text{solution of} \quad \alpha^3 + \tilde{\tau}\alpha - 1 = 0\,.$$

This means that in the square $(0,1]^2$ of the plane (Ψ_p,φ), for small Ψ_p, the implicit curve $g(\Psi_p,\varphi) = \tilde{\tau}$ always starts below $h(\Psi_p,\varphi) = F_M$ and ends (at $\Psi_p = 1$) below or above according to the criterium (3.43) (see Fig. 3.4). Hence, if $F_M > \dfrac{\tilde{\tau}}{\varphi_y(1)}$ there is at least a solution of (3.44). Uniqueness can be readily realized by observing that $g = h\varphi$ and thus, substituting in the equations (3.41) the value $\varphi = \tilde{\tau}/F_M$, Ψ_p is given by the solution of

$$h\left(\Psi_p, \frac{\tilde{\tau}}{F_M}\right) = F_M\,,$$

which is unique due to the monotonicity of h. □

We first consider a specimen subject to a controlled constant force $F(t) = F_M$. We will then generalize the results for the case in which a bounded force is imposed to the specimen and the corresponding deformation is recorded upon time. Depending on the imposed load, internal reorganization can be triggered during cell aggregate deformation (see the previous proposition). We observe that initially in the experiments $\varphi(0) = \Psi_p(0) = 1$. However, we will generalize the following statement to any $\Psi_p(0) = \Psi_{p,0} \geq \varphi_0$, because the result will be useful for the discussion after the Corollary.

Proposition 4. *If $\varphi(0) = \varphi_0 > \varphi_{c,F}(\Psi_{p,0})$ and $\Psi_p(0) = \Psi_{p,0} \geq \varphi_0$, applying a constant force $\tilde{F}(t) = F_M \leq \tilde{\tau}/\varphi_y(\Psi_{p,0}), \forall t$, then $\Psi_p(t) = \Psi_{p,0}$, $\forall t$ and the solution of eq. (3.38b), is such that $\varphi(t) \geq \varphi_{c,F}(\Psi_{p,0}) \geq \varphi_y(\Psi_{p,0})$.*

Proof. First of all, being $F_M \leq \tilde{\tau}/\varphi_y(\Psi_{p,0})$, from (3.43), we have $\varphi_0 > \varphi_{c,F}(\Psi_{p,0}) \geq \varphi_y(\Psi_{p,0})$.

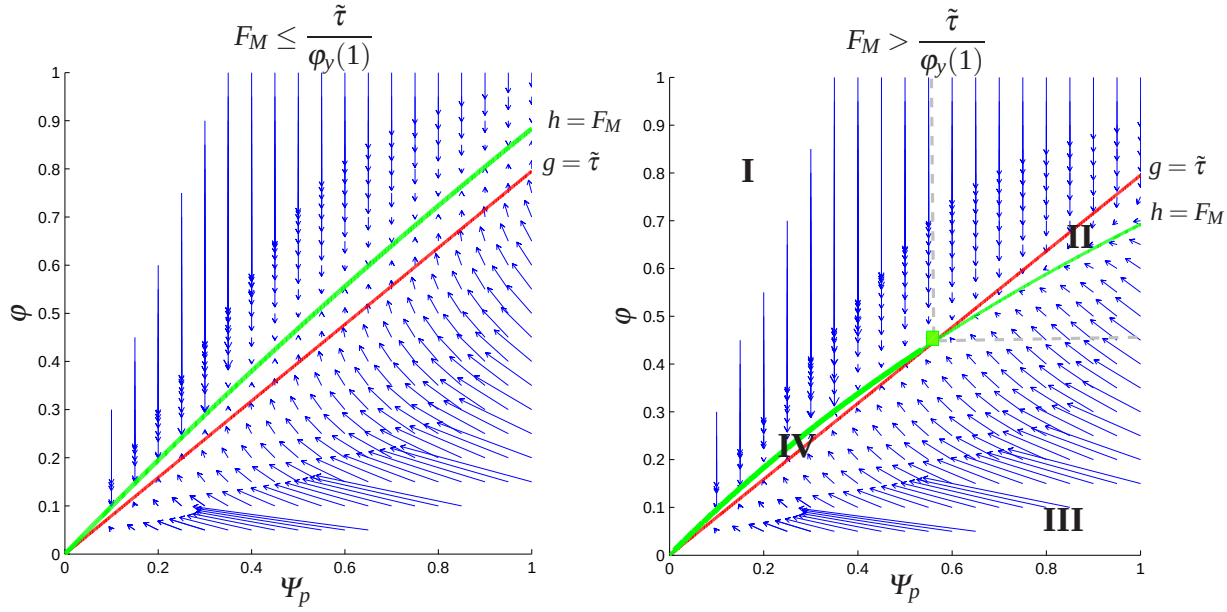

Figure 3.4: Vector field (blue arrows) corresponding to (3.41), if $F_M \leq \tilde{\tau}/\varphi_y(1)$ (on the left) and $F_M > \tilde{\tau}/\varphi_y(1)$ (on the right). The red curve corresponds to $g(\Psi_p,\varphi) = \tilde{\tau}$, whereas the green curve to $h(\Psi_p,\varphi) = F_M$. If $F_{appl}(t) \leq F_M \leq \tilde{\tau}/\varphi_y(1)$, the trajectories will tend toward the green curve. On the other hand, if $F_M > \tilde{\tau}/\varphi_y(1)$, trajectories starting from $\varphi = \Psi_p = 1$ will tend to the intersection of the two curves (square green mark), which represents the solution of the system (3.41). The green curve delimiting region IV is thicker because is composed of non-isolated stationary points.

We have

$$h(\Psi_{p,0},\varphi_0) - \tilde{F}(0) < h(\Psi_{p,0},\varphi_{c,F}(\Psi_{p,0})) - F_M = 0\,,$$

and

$$g(\Psi_{p,0},\varphi_0) - \tilde{\tau} < g(\Psi_{p,0},\varphi_y(\Psi_{p,0})) - \tilde{\tau} = 0\,,$$

because both g and h are decreasing functions of φ for fixed Ψ_p. Then $\dot{\Psi}_p(0) = 0$, while φ initially decreases. Actually $\Psi_p(t) = \Psi_{p,0}$ until φ eventually reaches $\varphi_y(\Psi_{p,0})$. If this value is overcome, then the material yields and Ψ_p can only decrease (see region II in Fig. 3.4, right panel).
However, we will now prove that $\varphi(t)$ does not decrease below $\varphi_{c,F}(\Psi_{p,0}) > \varphi_y(\Psi_{p,0})$, so the material never yields and $\Psi_p(t) = \Psi_{p,0}$, $\forall t$.
To demonstrate that $\varphi(t) \geq \varphi_{c,F}(\Psi_{p,0})\,, \forall t > 0$, we define $w = \varphi - \varphi_{c,F}(\Psi_{p,0})$ and recalling that $\varphi_0 > \varphi_{c,F}(\Psi_{p,0})$, so that $w_-(0) = 0$, we have

$$0 \geq -\frac{w_-^2(\tilde{t})}{2} = \int_0^{\tilde{t}} \dot{w} w_- dt = \int_0^{\tilde{t}} \tilde{\mu}\left[h(\Psi_{p,0},\varphi) - h(\Psi_{p,0},\varphi_{c,F}(\Psi_{p,0}))\right]\varphi^2 w_- dt\,.$$

Then the r.h.s. either vanishes if $\varphi > \varphi_{c,F}(\Psi_{p,0})$ (because $w > 0$), or is positive if $\varphi < \varphi_{c,F}(\Psi_{p,0})$, because h is a decreasing function of φ for fixed Ψ_p. Hence, because of the arbitrariness of $\tilde{t}$,

$w_-(t) = 0 \forall t$ and thus

$$\varphi(t) \geq \varphi_{c,F}(\Psi_{p,0}) \geq \varphi_y(\Psi_{p,0}), \qquad \forall t\,.$$

□

The condition on the constancy of $\tilde{F}(t)$ can be relaxed, if we assume that $\Psi_{p,0} = \varphi_0 = 1$, as stated in the following Corollary.

Corollary 5. *If $\varphi(0) = 1$ and $\Psi_{p,0} = 1$ and $\tilde{F}(t) \leq \tilde{\tau}/\varphi_y(1)$, then $\Psi_p(t) = 1$, $\forall t$ and the solution of eq. (3.38b) is such that $\varphi(t) \geq \varphi_{c,F}(1) \geq \varphi_y(1)$.*

Proposition 4 implies, for instance, that in the case of pre-stressed aggregates that have already deformed plastically, during cyclic compression tests at constant load, being $\Psi_{p,0} \geq \varphi_0$ at the beginning of every interval of compression (see Proposition 1), then remodelling is not triggered if $F_M \leq \tilde{\tau}/\varphi_y(\Psi_{p,0})$ and $\varphi(t) \geq \varphi_{c,F}(\Psi_{p,0}) \geq \varphi_y(\Psi_{p,0}), \forall t$.
The corollary 5 states that if an undeformed aggregate is subjected to compression with bounded force $F(t)$, with maximum below the critical value $\tilde{\tau}/\varphi_y(1)$, then the deformation of the aggregate occurs without any plastic effect and $\varphi(t) \geq \varphi_{c,F}(1) \geq \varphi_y(1)$. This result can be applied to the description of a cyclic creep test and release in which the force is maintained constant, $F(t) = F_M$, during compression and it is equal to zero during releases. Therefore, when a constant external force F_M is periodically applied and then removed, if $F_M \leq \tilde{\tau}/\varphi_y(1)$, no reorganization occurs and the unloaded specimen will go back to the initial configuration, $\varphi = 1$, following the classical visco-elastic response, due to the elastic response of cells and the viscous term of the liquid component (see Fig. 3.5, top curve).
On the other hand, as we shall see, when a constant force $F_M > \tilde{\tau}/\varphi_y(1)$ is applied, trajectories enter in the region II identified in Fig. 3.4, right panel, and the natural configuration of the aggregate changes, so that the solution tends to the intersection between the two curves in Fig. 3.4, right panel. In this case, when the upper plate is removed the multicellular body does not recover its original shape and a macroscopic deformation can be seen (lower curves in Fig. 3.5, right panel). The internal reorganization rate depends on the intensity of the load applied to the aggregate, compared to the yield stress and, in particular, it is faster and more intense as F_M increases, as shown in Fig. 3.5, left panel. In particular we demonstrate the following proposition.

Proposition 6. *If $F_M > \tilde{\tau}/\varphi_y(1)$, solutions of (3.41) starting from $\varphi(0) > \dfrac{\tilde{\tau}}{F_M}$ and $\Psi_{p,0} > \varphi(0)$, are such that $\varphi(t) \in \left[\dfrac{\tilde{\tau}}{F_M}, 1\right]$ and $\Psi_p(t) \in [\Psi_{p,\infty}, 1]$, where $\Psi_{p,\infty}$ is the solution of (3.45).*

Proof. To prove the thesis we proceed by absurd assuming that there exists a first $\bar{t}$ with

$$\Psi_p(\bar{t}) = \Psi_{p,\infty}\,, \qquad \dot{\Psi}_p(\bar{t}) < 0\,, \qquad \text{and} \quad \varphi(\bar{t}) \geq \frac{\tilde{\tau}}{F_M}\,,$$

$$\text{or} \quad \varphi(\bar{t}) = \frac{\tilde{\tau}}{F_M}\,, \qquad \dot{\varphi}(\bar{t}) < 0\,, \qquad \text{and} \quad \Psi_p(\bar{t}) > \Psi_{p,\infty}\,.$$

In the former case, since $\varphi_y(\Psi_{p,\infty}) = \varphi_{c,F}(\Psi_{p,\infty}) = \dfrac{\tilde{\tau}}{F_M}$, the same reasoning of the previous proposition can be used. If the line $\Psi_p = \Psi_{p,\infty}$ is reached, then the solution will always stay there. In fact,

$$g(\Psi_p(\bar{t}),\varphi(\bar{t})) = g(\Psi_{p,\infty},\varphi(\bar{t})) \leq g\left(\Psi_{p,\infty},\frac{\tilde{\tau}}{F_M}\right) = \tilde{\tau}\,,$$

which implies that $[g(\Psi_p(\bar{t}),\varphi(\bar{t})) - \tilde{\tau}]_+ = 0$ and therefore $\dot{\Psi}_p = 0$, against what assumed.

In the latter case,

$$h(\Psi_p(\bar{t}),\varphi(\bar{t})) = h\left(\Psi_p(\bar{t}),\frac{\tilde{\tau}}{F_M}\right) > h\left(\Psi_{p,\infty},\frac{\tilde{\tau}}{F_M}\right) = F_M \geq \tilde{F}(t)\,,$$

which implies that $\dot{\varphi} > 0$, against what assumed.

□

Corollary 7. *If $\tilde{F}(t) = F_M$, being the r.h.s of (3.41) continuous and locally Lipschitz for φ and Ψ_p belonging to the compact invariant set $\left[\dfrac{\tilde{\tau}}{F_M},1\right] \times [\Psi_{p,\infty},1]$, then solutions of (3.41) will tends to the stationary point $\left(\dfrac{\tilde{\tau}}{F_M},\Psi_{p,\infty}\right)$, where $\Psi_{p,\infty}$ is the solution of (3.45).*

The results demonstrated in Proposition 5 and 7 are also evident plotting the vector field corresponding to (3.41). Indeed, if $\tilde{F} \leq \tilde{\tau}/\varphi_y$ (see Fig. 3.4, left panel), φ and Ψ_p will tend to the green curve, which corresponds to the condition $h(\Psi_p,\varphi) = F_M$. Then the solutions of the system (3.41) starting from $\varphi(0) = 1$ and $\Psi_p(0) = 1$, will keep $\Psi_p = 1$ while φ will tend to $\varphi_{c,F}(1)$. On the other hand if $F_M > \tilde{\tau}/\varphi_y(1)$ (see Fig. 3.4, right panel), φ and Ψ_p will tend to the the intersection of the green and red curve, which represents the solution of the system (3.44).
We remark that the condition $F_M > \tilde{\tau}/\varphi_y(1)$ is coherent with the one found in the previous section for creep tests at constant stress. Indeed, defining the yield stress $P^*_{appl} = F_M\varphi_y/\pi$, the creep test yield condition becomes $P^*_{appl} = 2\tau$.
However, in this case also the steady state deformation and the maximum internal reorganization that can be induced depend on the intensity of imposed loads and do not necessary tend to the trivial state, i.e., $\Psi_p \to 0$ and $\varphi \to 0$, if the compression is maintained, in contrast with what

shown in Fig. 3.3. This means that, as remodelling takes place, cellular aggregates reorganize (i.e., Ψ_p decreases) in order to bear the load. Moreover being φ decreasing, the external stress P_{appl} generated by a constant force, decreases in time.

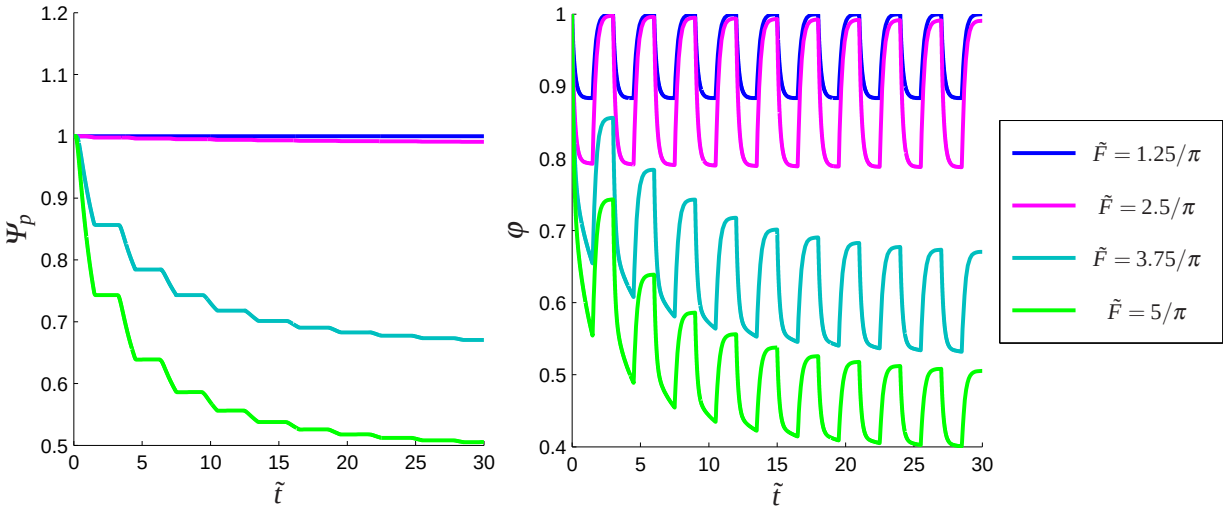

Figure 3.5: Cycle of compressions, when a constant external force F_M is periodically applied and then removed: reorganization (on the left) and deformation (on the right). The simulations are performed setting $\tilde{\tau} = 0.625$ and $\tilde{\mu} = 1.6$. The compression and release times are both equal to $\tilde{t}_c = \tilde{t}_r = 3/2$. From top to bottom the applied force increases.

3.3.3 Cyclic deformation test

In the compression experiments, like those performed in [52, 53, 54], a fixed deformation is applied to cellular spheroids, using a thermostated parallel plate apparatus, immersed in a chamber, filled with pre-warmed tissue culture medium. The specimens used in [52, 53, 54] were obtained from 5 to 6 day old chick embryos, whose cells were dissociated in a solution of trypsin and then placed in a tissue culture medium, to allow them to reorganize. When cultured for about a day, in a $37°C$ shaker bath, these multicellular aggregates adopted an almost perfect spherical shape, with a diameter ranging from 200μm to 500μm.

Recording the force exerted by aggregates upon the upper compression plate, it is possible to observe that living structures undergoing constant deformation, are able to relax the internal stress until an asymptotic value is reached [52, 54].

A variation of this experiment is the cyclic deformation test, like those performed in [52, 53], in which multicellular bodies are forced to periodic compressions at controlled deformation and

the compressive force is briefly interrupted at intervals during the approach to shape equilibrium. When compression is interrupted early in this process (as compared to the reorganization time, λ), aggregates can be observed to almost retrieve their initial shape, over the course of a few seconds, whereas after some releases from compressions, a macroscopic deformation can be measured. The process is reiterated until the attainment of an asymptotic behavior, described in the following.

The force relaxation curve and the presence of a plastic deformation are consistent with the visco-elastic model combined with the existence of a yield stress, described in [115], where the experimental stress-relaxation curves are reproduced qualitatively (a direct comparison is not possible due to the lack of some fundamental data as the imposed deformation or the contact area where the force is applied). Indeed the internal reorganization (due to the presence of τ), leads to the relaxation of a part of the stress, $P_{appl}(t)$ to the yield value, $P_{appl,\infty} = 2\tau$, regardless of the magnitude of the applied strain φ_0, as long as $\varphi_0 < \varphi_y(1)$, where $\varphi_y(1)$ is defined by (3.26). Indeed (3.26) determines the critical value of φ that makes the square bracket in (3.25) positive and thus it switches on the evolution of Ψ_p. For $\varphi \in (0,1]$, being $g(\Psi_p,\varphi)$ a positive and decreasing function of φ, only values of φ sufficiently small, so that the yield condition is satisfied, are able to trigger the internal reorganization inside spheroids.
For such values of φ_0, if the deformation is released, then the spheroid will not recover its initial shape, because in the meantime the natural configuration has changed. As pointed out in the motivation, the model proposed in [115] is not able to reproduce the stress-release dynamic, predicting an instantaneous shape recovery: if at any instant t_1 the compression is released, then $\Psi_p(t) = \Psi_p(t_1), \forall t \geq t_1$ and φ will suddenly adjust to the value $\varphi(t) = \Psi_p(t_1), \forall t \geq t_1$ so that $P_{appl} = 0$ (see top curve in Fig. 3.6). This result does not couple well with biological experiments [52, 53, 54], where aggregates progressively expand in height trying to recover their previous shapes, in a process that takes few seconds (e.g. in the specific case of 5-day-old chick embryonic liver cells, 11 s were allowed for this) [52].

The introduction of the viscous component in (3.2), due to the aqueous constituents of aggregates is able to take into account of this phenomenon. To show the behavior of the model described in Section 3.2.2 and in order to compare the results obtained with mechanical data in [52], we simulate cycles of compressions at constant deformation.
We know that $\Psi_p(t) \geq \varphi(t)$ during the entire process thanks to Proposition 1 (case *b*). Hence during the compression stage, the deformation is imposed and equation (3.27) holds, with $\varphi(t) = \varphi_0$, whereas when the upper plate is removed, equation (3.27) combined with (3.28) and the condition $P_{appl} = 0$ (stress-free evolution) can describe the shape recovery stage.

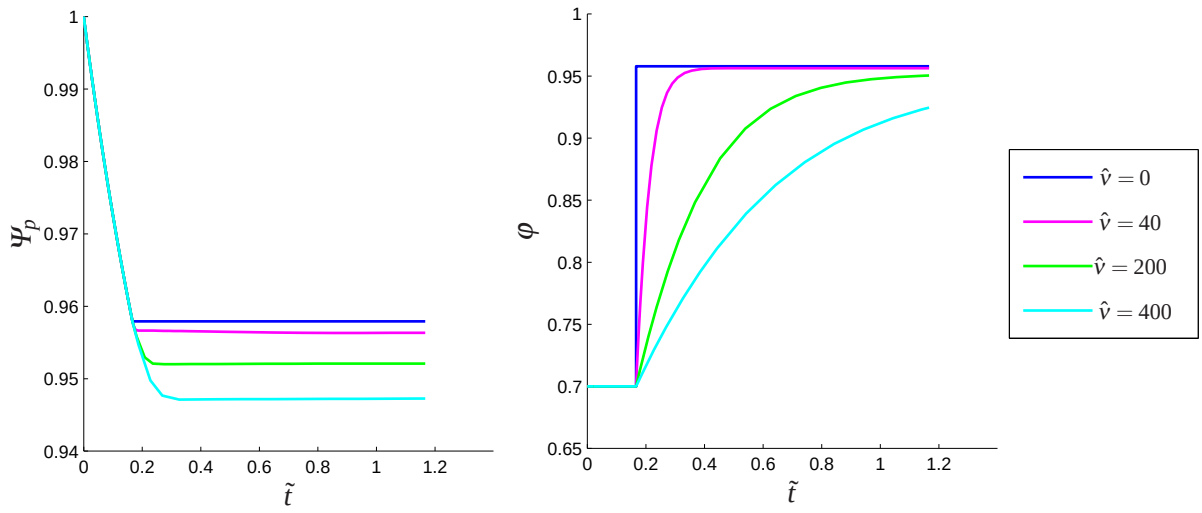

Figure 3.6: Shape dynamics of cell aggregates when the imposed deformation ($\varphi_0 = 0.7$), above the yield value, is released at a given time t_2 (here $t_2 = \lambda/2$, where $\lambda = 22s$). All the simulations are performed with the fixed value of $\tau = 0.25Pa$ and $\phi_s = 0.8$, whereas $\mu = 1Pa$. The blue curves represent the model with no viscous effect, $\nu = 0$ corresponding to the model in [115]. It is possible to observe the influence of the viscous parameter, $\hat{\nu} = \nu/\tau$, on the internal reorganization and shape recovery dynamics. According to the experiments in [52] the shape recovery requires tens of seconds, which can be reproduced in our simulations (see magenta curve) setting $\hat{\nu} = 40s$ (i.e. $\nu = 10Pa \cdot s$).

The results of the integration of these two systems is plotted in Fig. 3.6, where it is clear that the shape recovery is not instantaneous and its dynamics is controlled by the viscous coefficient: as ν increases the shape recovery will require more time.

Indeed the characteristic time for the shape recovery is given by $\nu/(\mu\phi_s)$. Moreover, the body will not recover the original height, Z, but it presents some plastic deformation. Keeping the mechanical properties of the spheroid fixed, the amplitude of the remodelling and hence the shape recovery depend on the time under compression. In Fig. 3.7, it is possible to see that in our simulations, with a reorganization time of 22 seconds, a compression of 1 second will be recovered up to 98% while a 10 second compression up to 95%. These results are consistent with biological observations, in fact in Figure 4 of [54] the spheroid aggregate compressed for few seconds almost recovers the original shape, showing a little flattening of the top.

It is also important to remark that even for very long compression times, $t_1 \gg \lambda$, the body will still recover an amount of the deformation, corresponding to the elastic component. Indeed, keeping the compression for times much larger than the reorganization time, spheroids will still experience an elastic recovery that can be considerably smaller (almost 75% in our case, see the leftmost curve in Fig. 3.7), consistently with Figure 5 of [54]. In other words, aggregates will not keep the imposed deformation, φ_0 even if the upper plate is removed after a very long time.

It is also interesting to see that during the stress-free evolution of spheroids, the internal reorganization continues following equation (3.27) until the stationary situation is reached, corresponding to the new natural configuration of the remodelled body.

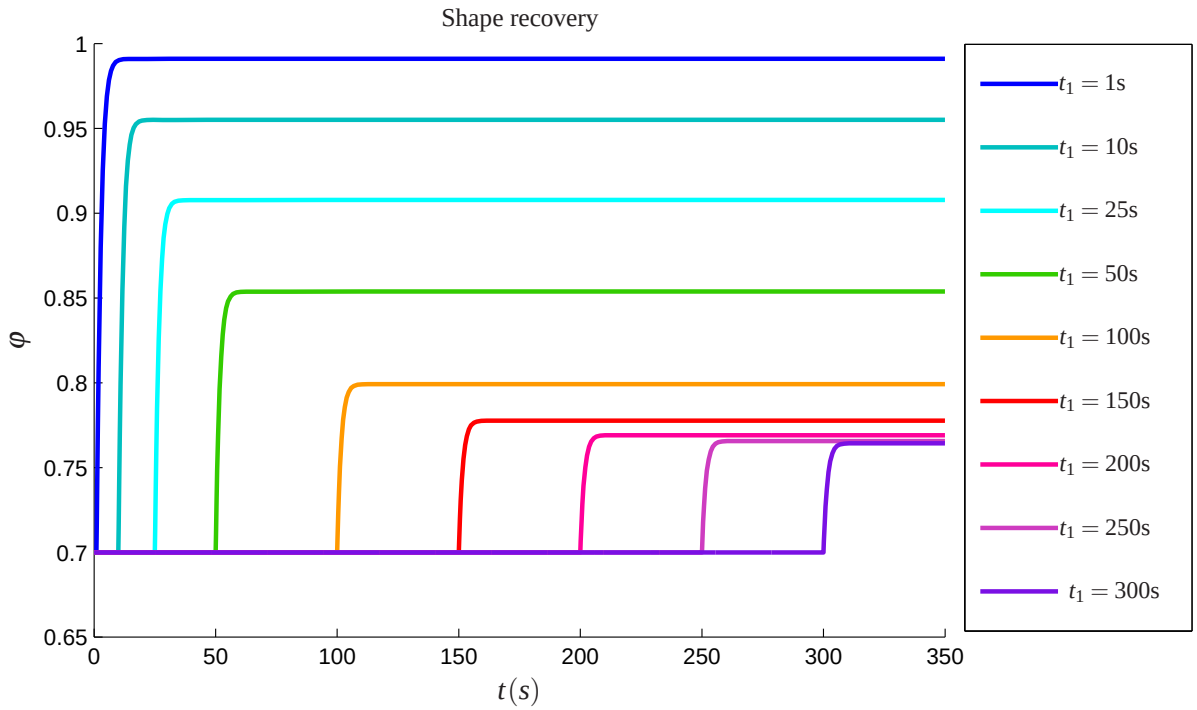

Figure 3.7: Uniaxial compression test for different values of compression time, t_1 (measured in seconds). The viscosity is chosen in order to reach the stationary shape in a period of 11 seconds (i.e. $\nu = 10\text{Pa}\cdot\text{s}$, see Fig. 3.6). The shape recovery gets smaller and smaller as the compression time increases, approaching a limit value.

Turning to cycles of compressions at constant deformation and releases, as in [52], a typical result for a twenty-cycle compression/release test is shown in Fig. 3.8. It is possible to see that, at the end of the simulation, the aggregate reaches the maximum of internal reorganization corresponding to the imposed deformation φ_0 and therefore an asymptotic behavior in the shape recovery is attained. An interesting parameter in the model is μ, which affect the recovery dynamics, along with ν: for small values of this parameter, we have no internal reorganization, because $\varphi_0 > \varphi_y(1)$, with $\varphi_y(1)$ satisfying the yield condition (3.26) and therefore we have no changes in aggregate shapes; on the other hand, as μ increases, the plastic reorganization of aggregates is more pronounced (see Fig. 3.9).

In [52] measurements are presented in terms of height/width ratio over time under compression. We try to report the results of our simulations in a similar way, observing that in our model

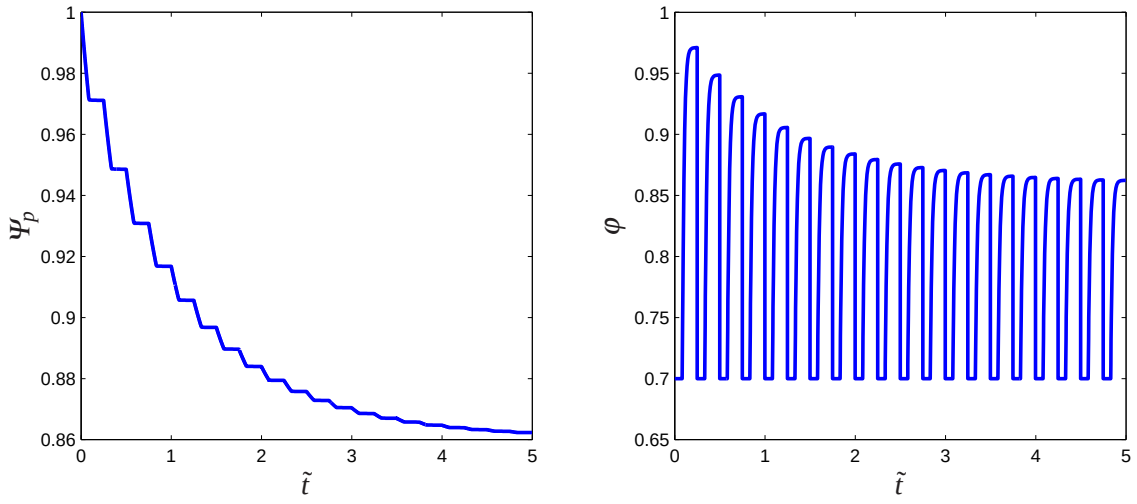

Figure 3.8: Spheroid behavior under a cycle of 20 compressions at constant deformation and subsequent stress releases. The figures report the internal reorganization Ψ_p (left) and the deformation gradient along the z-axis, φ (right). The simulation is performed letting the aggregate reorganize under compression for a time $t_c = \lambda/4$ and then remove the upper plate for $11s$ (corresponding to $\lambda/2$).

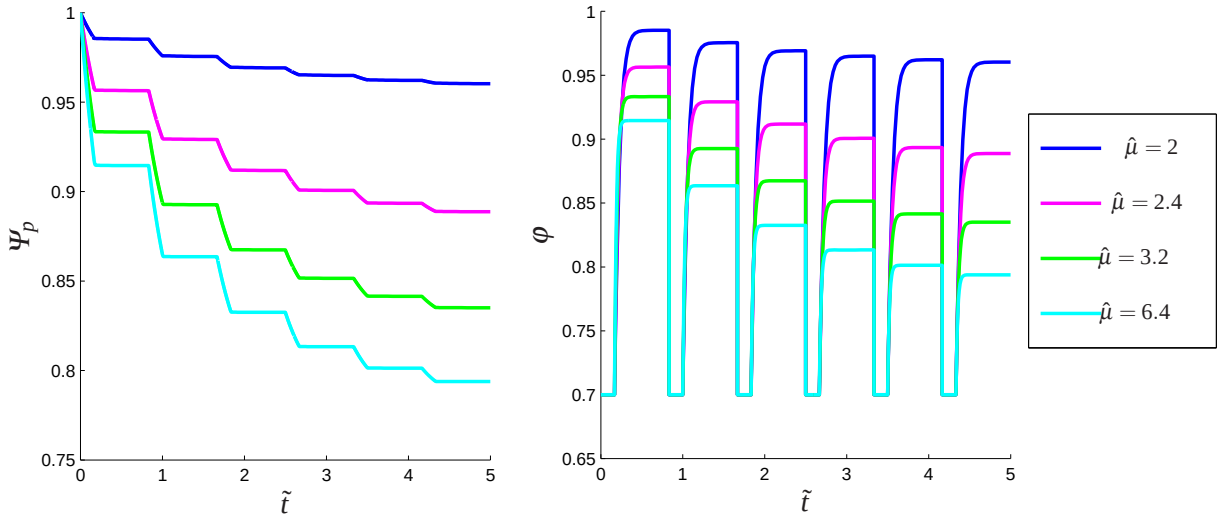

Figure 3.9: Influence of $\hat{\mu} = \mu\phi_s/\tau$ on spheroid behavior under a compression cycle test ($n = 6$). Aggregates are compressed for $t_c = \lambda/2$ and are let free to expand for $t_r = 2\lambda$ (in order to allow the fulfilment of shape recovery). For the imposed deformation, $\varphi_0 = 0.7$, value of $\hat{\mu} < 2.1309$ are not able to induce the internal reorganization of cells, because $\varphi_0 > \varphi_y(1)$. Therefore $\Psi_p = 1$ (blue curve) and when the compression is released the multicellular body comes back to the original shape in few seconds.

this quantity is represented by $\varphi^{3/2}(t)$, from equation (3.14). The results are presented in Fig. 3.10 for different values of the parameter μ and in Fig. 3.11 for different values of reorganization time (keeping μ fixed). The best fit is obtained for a reorganization time equal to $66s$, whereas

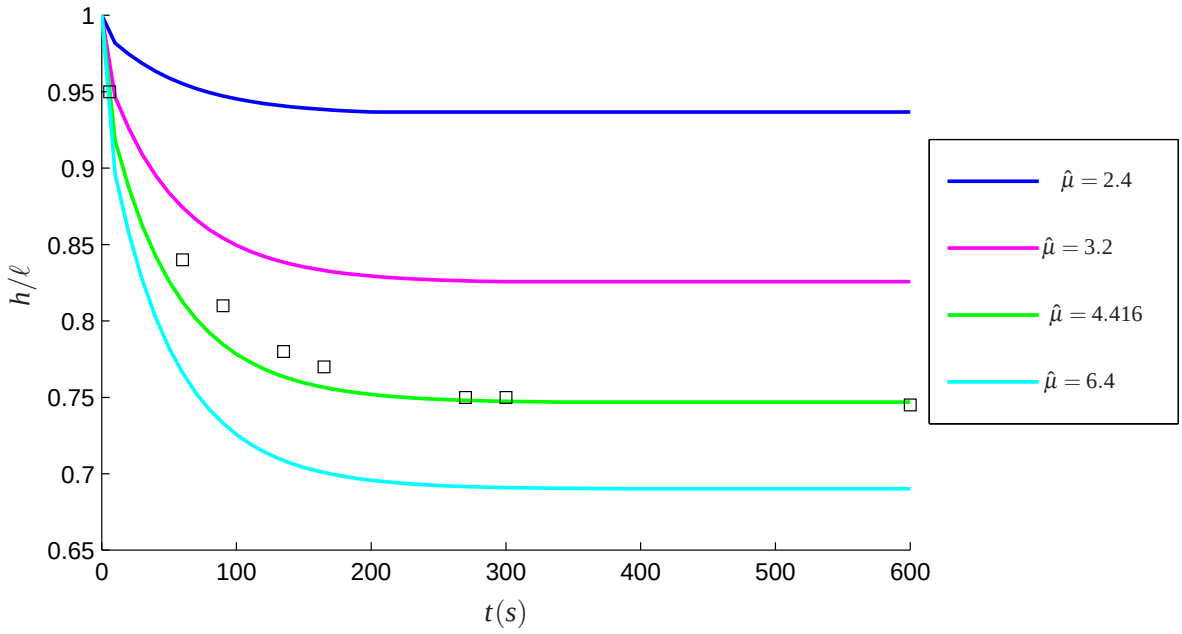

Figure 3.10: Height/width ratio chart for a cubic multicellular aggregate. The height and width are computed through equation (3.14) and therefore the ratio h/ℓ is represented by the quantity $\varphi^{3/2}$ that is plotted for different value of $\hat{\mu} = \mu\phi_s/\tau$, considering the same imposed deformation $\varphi_0 = 0.7$ and $\lambda = 50s$. Experimental data obtained by Forgacs et al. [52] are marked with squares.

the best-fitting values of μ depends on the imposed deformation. Indeed it is possible to observe that the equilibrium of (3.22) and (3.25) is reached when $\varphi(t) = \Psi_p(t) = \Psi_{p,\infty}$, satisfying the condition indicated in the following proposition.

Proposition 8. *During the cyclic deformation test at constant deformation, $\varphi_0 > \varphi_y(1)$, such that $\varphi_y(1)$ satisfies the yield condition (3.26), Ψ_p is non increasing, tending to the asymptotic value $\Psi_{p,\infty}$ satisfying*

$$g(\Psi_{p,\infty},\varphi_0) = \tilde{\tau} \tag{3.46}$$

Asymptotically, $\varphi(t) \in [\varphi_0,\Psi_{p,\infty})$.

Proof. During each compression phase at constant deformation above the yield condition, equation (3.27) states that Ψ_p is non increasing and that $\dot{\Psi}_p = 0$ when $g(\Psi_{p,\infty},\varphi_0) = \tilde{\tau}$, that corresponds, recalling equation (3.21), to $P_{appl} = 2\tau$.

Considering the system (3.27) and (3.28), with the limit condition $\Psi_p(t_1) = \Psi_{p,\infty}$ and $\varphi(t_1) = \varphi_0$, we have that $\dot{\Psi}_p(t_1) = 0$ whereas $\dot{\varphi}(t_1) > 0$. Actually, being $\varphi(t) \leq \Psi_p \ \forall t \geq t_1$ (Proposition

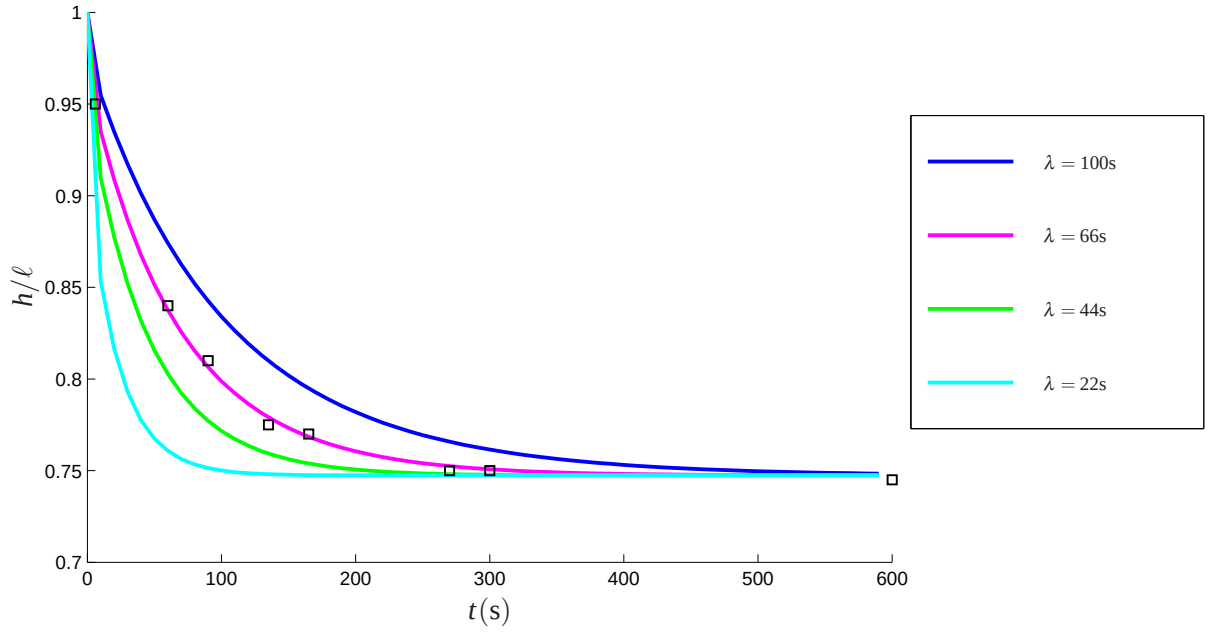

Figure 3.11: Height/width ratio chart for a cubic multicellular aggregate, for different value of λ (s). The parameter μ is fixed, in order to obtain the right asymptotic value (see Fig. 3.10), whereas η changes. The best fit with experimental data (square mark) is obtained for $\lambda = 66$ s.

1), $\dot{\varphi}(t) > 0$ and then φ increases until the limit value of $\varphi = \Psi_p$ is reached, which corresponds to the equilibrium of (3.28). From the physical point of view this means that the aggregate expands when the compressive force is removed. At the same time, as $\varphi(t)$ increases, $g(\Psi_p, \varphi)$ decreases, so that square brackets in (3.27) is still equal to zero and therefore $\dot{\Psi}_p(t) = 0 \forall t \geq t_1$, then $\Psi_p(t) = \Psi_{p,\infty}$.

Thus at the stationary condition we have $\varphi_\infty = \Psi_{p,\infty} \; : \; g(\Psi_{p,\infty}, \varphi_0) = \tilde{\tau}$.

□

The physical interpretation of the result presented in Proposition 8 is straightforward. In the stress release process, the deformation gradient between the deformed configuration (where $\varphi(t) = \varphi_0$) and the final configuration (where $\varphi(t) = \varphi_\infty$) is

$$\mathbb{F}_n = \text{diag}\left\{\sqrt{\frac{\varphi_0}{\varphi_\infty}}, \sqrt{\frac{\varphi_0}{\varphi_\infty}}, \frac{\varphi_\infty}{\varphi_0}\right\}$$

then

$$\mathbb{B}_n = \text{diag}\left\{\frac{\varphi_0}{\varphi_\infty}, \frac{\varphi_0}{\varphi_\infty}, \frac{\varphi_\infty^2}{\varphi_0^2}\right\}.$$

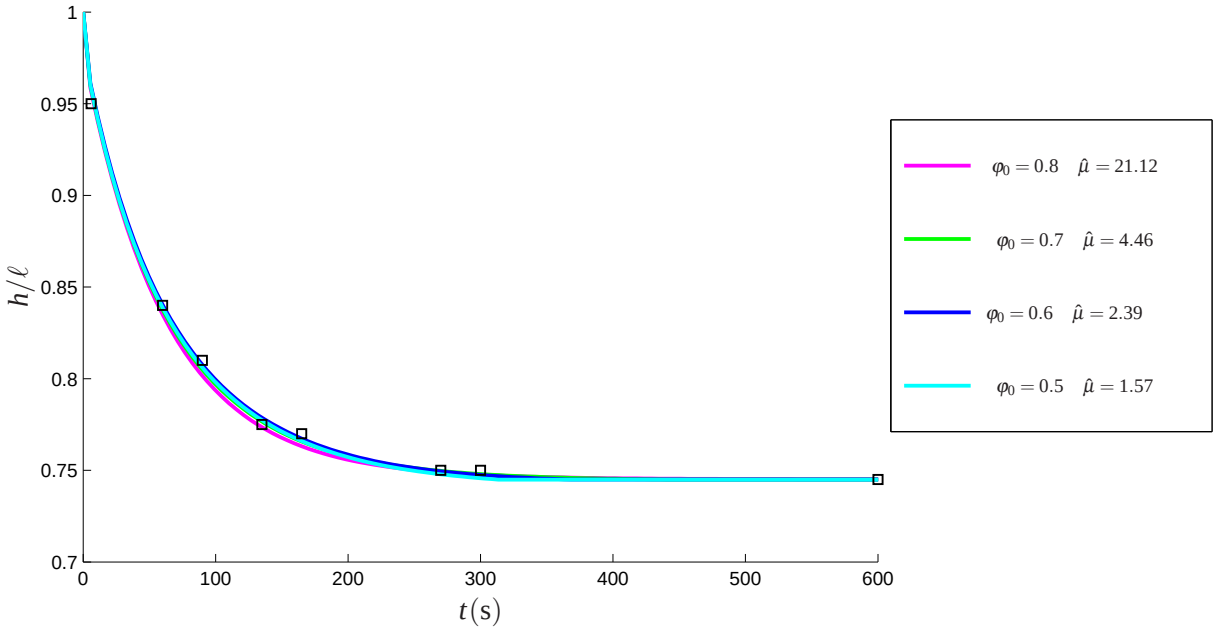

Figure 3.12: Height/width ratio chart for a cubic multicellular aggregate, for different value of initial deformation φ_0. To obtain the best fit with experimental data (squares) [52], μ is computed according to equation (3.46).

If we consider the asymptotic state $\Psi_p = \varphi = \Psi_{p,\infty}$ as the reference configuration, a deformation $\dfrac{\varphi_0}{\varphi_\infty}$ will not trigger further reorganization and the energy is elastically stored, as

$$\mathbb{T}_m = -\Sigma\mathbb{I} + \mu\phi_s\mathbb{B}_n = \mathrm{diag}\{0,0,2\tau\}\ ,$$

where we consider that, when the remodelling inside the spheroid has attained the maximum, the internal stress is equal to 2τ.
We obtain

$$\Sigma = \mu\phi_s\frac{\varphi_0}{\varphi_\infty}\,, \tag{3.47}$$

$$-\frac{\varphi_0}{\varphi_\infty} + \frac{\varphi_\infty^2}{\varphi_0^2} = \frac{2\tau}{\mu\phi_s}\,. \tag{3.48}$$

Taking into account that $\varphi_\infty = \Psi_{p,\infty}$ this is the same result we have obtained only with analytical considerations.

Therefore $\varphi_\infty^{3/2}$ is the asymptotic value in Fig. 3.10 and 3.11, and it is a function of $\varphi_0, \tau, \mu, \phi_s$.

Thanks to this result, it is possible to find for each φ_0 a value of μ (see Fig. 3.12), fitting experimental data from [52], where the imposed deformation is unfortunately not known. As shown in Fig. 3.12, knowing this datum it would be possible to get the best fitting value of $\hat{\mu} = \frac{\mu\phi_s}{\tau}$.

3.4 Discussion

The 3D elasto-visco-plastic model provided here is based on the existence of a yield criterion, above which cells reorganize.
Indeed, the cyclic deformation test presented in [52] cannot be described only resorting on a surface tension model, while the model characterized by a yield condition, as the one presented here, is able to qualitatively reproduce the deformation dynamic observed during biological experiments.
With the introduction of the liquid component, we have improved the model presented in [115], to take into account the viscous component of cell aggregates. Though the constitutive model is kept as simple as possible, we have shown how it can reproduce compression tests performed by [52, 53, 54] and how it can explain creeping phenomena.
In particular, results presented in Section 3.3.1 refer to an experiment in which the external stress is preserved constant in time and it is always above the threshold that induces the ruptures of bonds. The internal reorganization continues until all bonds are totally broken, i.e., the aggregates is disrupted. On the other hand, the results presented in section 3.3.2, highlight that, when the force (and not the stress) is maintained constant, even if the load is initially able to trigger the rupture of adhesive bonds, cells re-allocate in order to increase the transverse section and to reach a new internal configuration that does not undergo reorganization under the same imposed load.
Unfortunately, in both cases only a partial comparison with biological experiment is possible.
In Section 3.3.3 we show that, thanks to the the introduction of the viscous term, the model is able to reproduce aggregate release dynamics observed during biological experiments.

Of course, the model can be improved in several directions in order to reproduce more closely the behavior of cell aggregates. An extension can be represented by the inclusion of more cell re-arrangement times, that can be related, for instance, to the detachment of different adhesion proteins inside the cell membrane or to the response occurring inside the cell itself with the rearrangement of the actin cytoskeleton. The introduction of more relaxation times would certainly lead to a better understanding of the mechanics and a better fit of experimental data. Indeed in

the experiments in [52] it is evident the existence of at least two relaxation times in the cellular matter (one of the order of few seconds and the other of the order of tens of seconds). Moreover eq. (3.10) is based on empirical observations and it does not take into account the microscopic mechanisms that leads to the rupture of bonds between cells. A more detailed description of the reorganization mechanism should incorporate information deriving from the subcellular scale. Furthermore, more realistic 2D and 3D simulations of aggregates deformation have to be performed, in order to obtain a more precise calculation of the height/width ratio, which is of relevant importance for comparing computational data to experimental ones.

Chapter 4

Growth and remodelling of cancer spheroids

In this Chapter, we present a theoretical and numerical study of growth and remodelling of a cancer spheroid, surrounded by healthy tissue, considering both the cellular constituent and the fluid phase. In order to consider separately the contribution of pure growth from the one due to pure remodelling, a new virtual configuration is added, the “grown configuration". Thus, the anelastic part of the deformation $\mathbb{F}_a$, introduced in Chapter 1, Section 1.2 is further decomposed in $\mathbb{F}_g$, which describes deformations due to growth, and $\mathbb{F}_p$, which refers to internal reorganization. Thus, by means of the multiplicative decomposition, we have $\mathbb{F}_a = \mathbb{F}_p\mathbb{F}_g$.

Section 4.1 is devoted to the presentation of the biological problem and a brief review of some existing papers on spheroid growth is provided. We do not claim to be exhaustive, because the literature on the growth of cellular aggregates is widespread, so that we will focus only on those contributions that were fundamental for this work. Balance laws and constitutive equations are summarized in Section 4.2.1. For more details on the derivation of equations, please refer to Chapter 1. Equations are then set in spherical coordinates in Section 4.2.2 and some details on the dimensionless formulation of the problem and on the discretization are discussed in Section 4.2.3 and 4.2.4, respectively. Results are presented in Section 4.3, considering different situations. As a first step, the effect of the surrounding tissue is modelled as a known stress exerted at the outer boundary of the spheroid: both the case of quiescent aggregates undergoing pure remodelling (Section 4.3.1) and the case of growing aggregates, with and without remodelling (Section 4.3.2) are considered. For what concerns the growth term, we first consider that cell proliferation depends on the volume fraction only (4.3.2.1). Then, we introduce the diffusion of nutrients

inside the cellular structure, so that cell growth is limited by the availability of these chemical substances (Section 4.3.2.2). Finally, in (Section 4.3.3) we model the surrounding tissue as an ensemble of cells in which growth is balanced by physiological death, i.e., the net growth is equal to zero.

4.1 Motivations

The formulation of a mathematical model able to simulate the process of cell growth in vitro and in vivo is of great interest both from the biological and the mathematical point of view. Indeed modelling the proliferation of tumors has the potential of shedding light on the biological mechanisms involved and on their interactions, becoming a fundamental tool in cancer research.
From the mathematical point of view, due to the high complexity of living structures, this problem is a really challenging task, that has risen more and more attention in the mathematical community. However, the attempt to give a unified description of tumor progression is still hopeless, both because there are several tumors with different origin and characteristics and because there are many concurrent causes on tumor development and evolution [12].
Solid tumours develop initially as a single mass of cells, that proliferate more rapidly than the healthy cells around them. Tumors are known to progress through two distinct phases of growth [50, 51]:

- the avascular phase, so called because it is not associated with the formation of new blood vessels;
- the vascular phase, which sets up with tumor ability to induce new blood vessels from the surrounding tissue, that sprout towards the cancer cells, surround the tumor mass and gradually penetrate into it, providing an adequate blood supply.

The very early stages of tumour growth are rarely seen clinically because of the small size of the cell masses and the absence of symptoms. However, the initial avascular growth phase can be easily studied in vitro, by culturing cancer cells in the form of 3D multicellular spheroids in a liquid medium containing appropriate nutrients [41, 106]. This assay, introduced by Sutherland and coworkers in the early 1970s [140, 141], has been used extensively to study properties of tumor spheroids, to investigate subsequent stages of tumour progression, and to predict the response to therapeutic treatments (see [78, 95] for reviews). This in vitro multicellular system can be of great value in understanding the progression of tumors, because it possess growth kinetics which are very similar to the one shown by tumors in vivo.

Multicellular spheroids have a well-established characteristic structure: tipically the avascular mass grows up to several millimetres in diameter [30, 135], then, cell towards the centre, being deprived of vital nutrients, die forming the central necrotic core [69]. Proliferative cells can be found in a thin layer (a few hundred μm thick) at the outer boundary of the tumor mass. Between these regions there is a layer of quiescent cells, which are not dividing but are alive, and can begin dividing again if environmental conditions change. At the same time, a portion of the quiescent cells can be recruited by the proliferative ring or they can undergo apoptosis, i.e., programmed death, increasing the size of the necrotic region. The reason for cells in a multicellular spheroid becoming quiescent and then undergoing necrosis has been studied extensively, but there is still no definitive answer [135]. Levels of oxygen and glucose play an important role, but several other factors can be involved (e.g. growth factors, reduced mitochondrial function,...).
From the biological point of view, the study of multicellular spheroid is well set, and many experimental data on the internal architecture of spheroids and on the distribution of nutrients [41, 56, 57, 75, 142, 158] are available in literature. However, the introduction of this huge amount of data in mathematical modelling is still missing.
Indeed, even though mathematical modelling of avascular tumour growth has a long history, dating back to the middle '50s [146], a reliable complete model able to predict the growth of multicellular spheroids in vivo is still needed.
The description of solid tumors as a multiphasic mixtures date back to the late-1990s [113, 114]. In the last years several multiphase models have been developed and applied with success to describe tumor growth [2, 22, 23, 24, 25, 31, 55]. For a more detailed review of mathematical modelling of solid tumor growth, refer to [11, 18, 68, 103].

We formulate our model using the tools provided by mixture theory. Indeed, as we saw in Chapter 1, Section 1.2, in a first approximation, one can say that cells, forming a compact tumor, live in a watery environment full of proteins, including nutrients, that cells need to survive and duplicate, and chemical factors, in particular chemotactic factor, growth promoting and inhibitory factors, which trigger sub-cellular chemical pathways determining the behavior of cells [12].
Therefore, we study the growth and remodelling of a spheroid, modelled as a porous medium composed of a "solid" fraction, ϕ_s, representing cells, and a liquid phase, ϕ_ℓ, representing the interstitial fluid. We assume that the saturation condition for the aggregate is $\phi_s + \phi_\ell = \phi_{max}$, where ϕ_{max} is a given constant.
Then, we adopt the theory for materials with evolving natural configurations (see Chapter 1,

Section 1.2), in order to distinguish the plastic component of the deformation, from the elastic response of the material to stresses and strains. The plastic component refers both to growth and to the internal reorganization of cells, that are modelled separately. Therefore, we consider the deformation gradient, $\mathbb{F}$, as composed of three parts:

- the first one related to pure growth/death (therefore accompanied with cell mass variation),
- the second one due to internal rearrangement of cells
- the third one due to stress-induced deformation

Growth and remodelling are responsible of the plastic deformation of the tissue. Elastic deformations and internal reorganization are assumed to occur without changes of mass.
These considerations leads to the introduction of one more virtual configuration, between $\mathscr{B}_r$ and $\mathscr{B}_t$, besides the "natural state" $\mathscr{B}_n$ (introduced in Chapter 1, Section 1.2 and exploited in Chapter 2 and 3): the "grown configuration", $\mathscr{B}_g$ that represents cells that have undergone pure growth, without undergoing either remodelling or stress-induced deformation (see Fig. 4.1).
Therefore tensor $\mathbb{F}_g$ represents the growth of the material, mapping vectors attached to $\mathscr{B}_r$ into vectors attached to $\mathscr{B}_g$, whereas the tensor $\mathbb{F}_p$ is a mapping from the tangent space related to the grown configuration $\mathscr{B}_g$ onto the tangent space related to the relaxed configuration $\mathscr{B}_n$ and thus it represents anelastic deformations due to remodelling. Finally $\mathbb{F}_n$, which gives the evolution from the natural configuration to the actual state, refers to the elastic component of the deformation, as in Chapter 2 and 3. Hence,

$$\mathbb{F} = \mathbb{F}_n \mathbb{F}_p \mathbb{F}_g \,. \tag{4.1}$$

The variations of volume of the solid phase due to the deformation when no growth and remodelling take place is denoted by $J_n = \det(\mathbb{F}_n)$, whereas the volume increase due to growth is represented by $J_g = \det(\mathbb{F}_g)$. We assume that deformations due to remodelling takes place, without changes in volume, i.e. $J_p = \det(\mathbb{F}_p) = 1$. Thus, the multiplicative decomposition of $\mathbb{F}$ implies $J = J_n J_p J_g = J_n J_g$.

The model presented follows the work done by Ambrosi and Mollica [1, 3], in which the response of tumor spheroids undergoing growth is studied, and by Preziosi and Ambrosi [7, 115] in which the role of remodelling in tumor response is introduced. In [1, 3], spheroids are considered as a monophasic elastic material, undergoing growth depending on the external loading and the availability of nutrients, without considering the role of remodelling. On the other hand

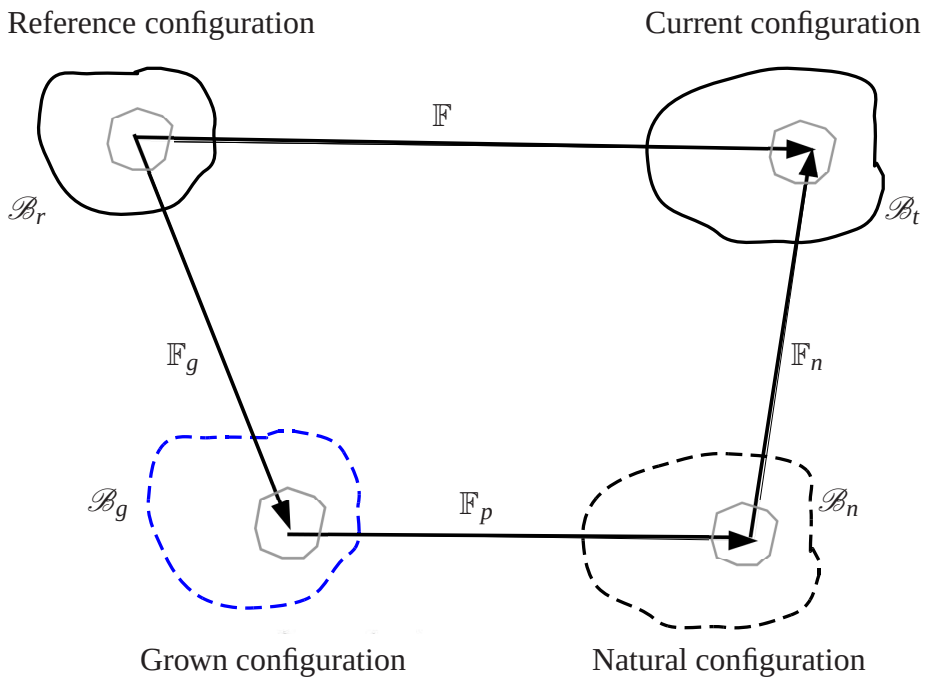

Figure 4.1: Diagram of the states from the original unstressed configuration $\mathscr{B}_r$ to the current configuration $\mathscr{B}_t$, in the framework of multiple natural configurations. $\mathbb{F}_n$ identifies the deformation without anelastic deformations, $\mathbb{F}_p$ describes the internal reorganization of cells and $\mathbb{F}_g$ the growth of the aggregate.

in [115] a remodelling equation is introduced, but the process of growth inside spheroidal aggregates is not exploited. In [7] a similar model, with different remodelling equation, is presented and applied to the description of tumor growth inside cylindrical duct (with rigid wall). Moreover, in these works the presence of the surrounding host tissue and the diffusion and transport of nutrients are not exploited. Nutrient availability controls the duplication of cells and its depletion limits the expansion of the tumor spheroids. In order to properly describe the flow of nutrients inside multicellular spheroids, the introduction of the liquid phase is fundamental.

We start considering a simple setting, composed of a necrotic core and a quiescent ring, undergoing radial compression (Section 4.3.1). We then consider the interplay between growth and remodelling in a tumor composed of a necrotic core and a proliferative ring (Section 4.3.2). In these models we consider both the case in which the central necrotic core is composed by calcified debris resulting from the death of cells (i.e., rigid necrotic core) and the case in which debris have been removed and the spheroid is left with a liquid necrotic core. Both morphologies have been observed in biological experiments.

In these first models the presence of the blood vessels is not considered and nutrients are assumed

to penetrate in the whole spheroid. Indeed mathematical modelling of avascular tumours is the first step in building models for tumour growth in later stages. Finally, we introduce the diffusion of nutrients, from vessels surrounding the tumor mass, so that cell growth is limited by the availability of these chemical substances (Section 4.3.2.2). Then, in (Section 4.3.3) we model the surrounding tissue, an an ensemble of cells in which growth is balanced by physiological death, i.e., the net growth is equal to zero.

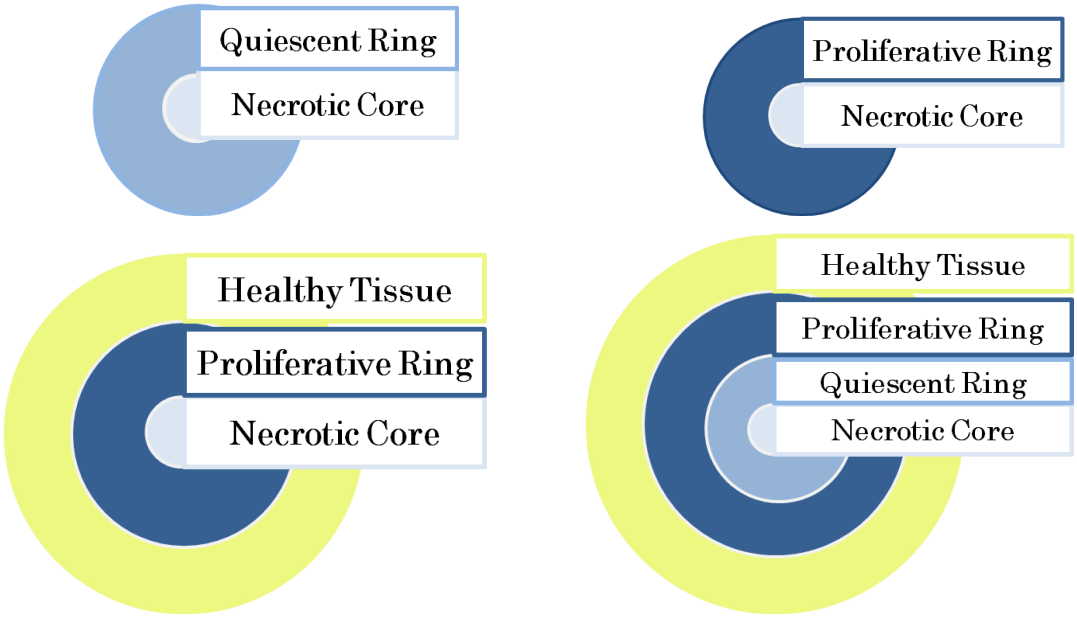

Figure 4.2: Schematic representation of the different spheroid configurations that we consider in this Chapter. First we look at the mechanical response of quiescent aggregates with a necrotic core. Then we consider the case of proliferative aggregates: in a first assumption we can consider that all cells in the tumor mass can proliferate until the maximum cell volume fraction is reached, then nutrients are included in order to model the quiescent region. We then implement the comprehensive model in which also the surrounding healthy tissue is described.

4.2 Mathematical model

4.2.1 Balance laws

Referring to Chapter 1, we consider the balance law in their Lagrangian local form, in order to have all the quantities expressed in the reference configuration which is fixed in time. For a biphasic mixture, composed by incompressible solid and liquid phases (i.e. the true densities $\hat{\rho}_s$ and $\hat{\rho}_\ell$ are constant), eq. (1.28) and (1.29) hold. Enforcing the saturation assumption and

assuming that $\hat{\rho}_s = \hat{\rho}_\ell$ (which is reasonable being cells mainly composed of water) and that $\phi_s \Gamma_s = -\phi_\ell \Gamma_\ell$ (i.e., growth of cells occurs with liquid absorption from the outside), eq. (1.28) and (1.35) become

$$\dot{\overline{(J\phi_s)}} = J\phi_s \Gamma_s, \tag{4.2}$$

$$\dot{J} + \mathrm{Div}\left(J\phi_\ell \mathbb{F}^{-1}(\boldsymbol{v}_\ell - \boldsymbol{v}_s)\right) = 0\,, \tag{4.3}$$

where the operator Div is the divergence computed with respect to the material coordinates.
As observed in Chapter 1, Section 1.2.2 the solution of (4.2) is given by (1.53), i.e., $\phi_s = \phi_{sn}\dfrac{J_g}{J}$. This means that the volumetric fraction of the solid phase, ρ_s, is determined if the constant mass distribution ϕ_{sn} is assigned, and the volumetric deformations J and J_g are known. We remark that ϕ_{sn} is constant and should be regarded as a known quantity of the model.

Together with mass balance, we have to provide also the balances of momentum of the cellular and liquid phases.
We accept the validity of Darcy's law, so that the fluid flow depends on the permeability of the medium ($\mathbb{K}$) and on the gradient of the interstitial pressure, p

$$\nu\phi_\ell(\boldsymbol{v}_\ell - \boldsymbol{v}_s) = -\mathbb{K}\mathrm{grad}(p), \tag{4.4}$$

where ν is the dynamic viscosity of the fluid. Substitution of this result into (4.3) yields

$$\dot{J} = \frac{1}{\nu}\mathrm{Div}\left(J\mathbb{F}^{-1}\mathbb{K}\mathbb{F}^{-T}\mathrm{Grad}(p)\right), \tag{4.5}$$

where we wrote the pressure gradient in material coordinates, i.e., $\mathrm{grad}(p) = \mathbb{F}^{-T}\mathrm{Grad}(p)$.

The material, local form of the momentum balance law for the mixture, written with respect to the reference placement $\mathscr{B}_r$ and neglecting inertial terms, is given by (1.45). assuming that the external body force density is null, we have

$$\mathrm{Div}(\mathbb{P}) = 0, \tag{4.6}$$

where $\mathbb{P}$ is the first Piola-Kirchhoff stress tensor of the mixture, given by (1.47), i.e., it can be approximated with the sum of the stress tensors of the solid and liquid phase, $\mathbb{P} = \mathbb{P}_s + \mathbb{P}_\ell$ where

$\mathbb{P}_s$ and $\mathbb{P}_\ell$ are defined through the Piola transformations (1.46)

$$\mathbb{P}_s := J\mathbb{T}_s\mathbb{F}^{-T} \tag{4.7}$$

$$\mathbb{P}_\ell := J\mathbb{T}_\ell\mathbb{F}^{-T}. \tag{4.8}$$

where $\mathbb{T}_s$ and $\mathbb{T}_\ell$ denote the Cauchy stress tensors of the solid and fluid phase. We remark that in (4.7) and (4.8), J and $\mathbb{F}$ refers to the solid phase. In order to close the mathematical problem resulting from (4.5) and (4.6), it is necessary to provide information about the stresses $\mathbb{T}_s$ and $\mathbb{T}_\ell$.

The cellular component is assumed to be a hyperelastic and isotropic material, and it is modelled by the following constitutive relation [7]:

$$\mathbb{T}_s = -\phi_s\left(p + \Sigma(\phi_s) + \frac{1}{3}\mathrm{tr}(\mu\mathbb{B}_n)\right)\mathbb{I} + \mu\phi_s\mathbb{B}_n\,, \tag{4.9}$$

where $\mathbb{B}_n = \mathbb{F}_n\mathbb{F}_n^T$ and $\Sigma(\phi_s)$ is a stress function that in the following we will assume to have the form $\Sigma(\phi_s) = E\dfrac{\phi_s - \phi_0}{\phi_{max} - \phi_s}$. We will use the apex $'$ to indicate the deviatoric part of the stress tensor of the solid phase, whereas the apex $*$ stands for the constitutive part, i.e.,

$$\mathbb{T}'_s = \mathbb{T}_s - \frac{1}{3}\mathrm{tr}(\mathbb{T}_s)\mathbb{I}\,, \quad \mathbb{T}^*_s = \mathbb{T}_s + \phi_s p\mathbb{I}\,.$$

Once it is known how the material behaves from the natural configuration to the actual state, we need to describe how the natural configuration evolves, through remodelling and growth.
For the evolution of the internal reorganization, we use the relation (3.10), introduced in Chapter 3, i.e.,

$$\mathbb{L}_p = \frac{J}{2\eta(\phi_s)}\left[1 - \frac{\tau(\phi_s)}{f(\mathbb{T}'_s)}\right]_+ \mathbb{F}_n^T\mathbb{T}'_s\mathbb{F}_n^{-T}\,,$$

where the different terms have the meaning explained in Chapter 3.
We then have to set an equation representing the growth of the cellular constituent. In [7], it was shown that

$$\frac{\dot{J}_g}{J_g} = \Gamma_s\,, \tag{4.10}$$

that can be rephrased as

$$\mathrm{tr}\left(\dot{\mathbb{G}}\mathbb{G}^{-1}\right) = \Gamma_s\,. \tag{4.11}$$

The term Γ_s is the source term in the mass balance equation and it can assume different forms, depending on the assumption we use. The simplest equation for this term is $\Gamma_s = \gamma(\phi_{max} - \phi_s)$ which states that the proliferation of cells continues until the maximum cell volume fraction is

reached. Of course, more complicated relation can be chosen. In particular we will also consider the case in which Γ_s depends on nutrient concentration.

4.2.2 Spherical symmetry

We apply the model presented in section (4.2.1) to describe the growth of tumor spheroids. Since all processes are considered homogeneous and isotropic, the initial spherical geometry is preserved. Therefore it is reasonable to rewrite equations (4.5) and (4.6) in material spherical coordinates, (R,Θ,Φ). We assume deformations and velocities of all constituents to be along the R-axis.
We restrict our investigation to the case in which the radial deformation depends on R and t only. Therefore we have

$$r(t,\boldsymbol{X}) = \chi(t,R), \qquad \vartheta(t,\boldsymbol{X}) = \Theta, \qquad \varphi(t,\boldsymbol{X}) = \Phi, \tag{4.12}$$

so that the matrix representation of the deformation gradient tensor is diagonal and given by

$$\mathbb{F} = \operatorname{diag}\left\{\partial_R\chi, \frac{\chi}{R}, \frac{\chi}{R}\right\}. \tag{4.13}$$

We remark that $J = \partial_R\chi\frac{\chi^2}{R^2}$ holds true. Then, being $J_p = 1$ and enforcing spherical symmetry, we take

$$\mathbb{F}_p = \operatorname{diag}\left\{\frac{R^2}{\Psi_p^2}, \frac{\Psi_p}{R}, \frac{\Psi_p}{R}\right\}, \tag{4.14}$$

where $\Psi_p = \Psi_p(t,R)$ is a measure of the internal remodelling of the spheroid. We then assume a spherical growth

$$\mathbb{F}_g = \operatorname{diag}\{g,g,g\}, \tag{4.15}$$

where $g = g(t,R)$. The next step is to re-write (4.5) and (4.6) in spherical coordinates.
We assume that the medium is isotropic with respect to both its elastic properties and permeability. Thus the permeability tensor is diagonal $\mathbb{K} = K(\phi_s)\mathbb{I}$. It follows, from (4.5), that

$$\dot{J} = \frac{1}{\nu R^2}\frac{\partial}{\partial R}(\chi^2 K(\phi_s)\Pi^R), \tag{4.16}$$

which leads to

$$\dot{J} = \frac{1}{\nu}\frac{\chi^2}{R^2}\frac{\partial}{\partial R}(K(\phi_s)\Pi^R) + 2\frac{K(\phi_s)}{\nu}\frac{J}{\chi}\Pi^R, \tag{4.17}$$

where Π^R is the radial component of the material gradient of the interstitial pressure pulled-forward to the actual configuration and it can be computed through (4.6), as

$$\mathbb{F}^{-T}\mathrm{Grad}\, p = \frac{1}{J}\mathrm{Div}(\mathbb{P}_s^*) = (\Pi^R, 0, 0)^T, \tag{4.18}$$

where $\mathbb{P}_s^* = \mathrm{diag}\left((P_s^*)^{rR}, (P_s^*)^{\vartheta\Theta}, (P_s^*)^{\varphi\Phi}\right)$ is the constitutive part of the first Piola-Kirchoff stress tensor of the cellular component. Writing (4.18) in spherical coordinates we obtain

$$\Pi^R = \frac{1}{J}\left[\frac{\partial}{\partial R}(P_s^*)^{rR} + \frac{2}{R}\left((P_s^*)^{rR} - (P_s^*)^{\vartheta\Theta}\right)\right]. \tag{4.19}$$

Using the constitutive equation (4.9) and the Piola transformation, we have

$$(P_s^*)^{rR} = -J\phi_s\left(\Sigma(\phi_s) + \frac{1}{3}\mu\frac{J^2\Psi_p^6 + 2\chi^6}{g^2\Psi_p^2\chi^4}\right)\frac{\chi^2}{JR^2} + J\phi_s\mu\frac{J\Psi_p^4}{\chi^2 g^2 R^2}, \tag{4.20}$$

$$(P_s^*)^{\vartheta\Theta} = (P_s^*)^{\varphi\Phi} = -J\phi_s\left(\Sigma(\phi_s) + \frac{1}{3}\mu\frac{J^2\Psi_p^6 + 2\chi^6}{g^2\Psi_p^2\chi^4}\right)\frac{R}{\chi} + J\phi_s\mu\frac{\chi R}{g^2\Psi_p^2}. \tag{4.21}$$

Equation (4.17) needs to be coupled with equations (4.11) and (3.10), representing the evolution in time of g and Ψ_p respectively, i.e.,

$$\dot{g} = \frac{\Gamma_s}{3}g \tag{4.22}$$

$$\dot{\Psi}_p = -\frac{J\phi_s\mu}{6\eta}\left[1 - \frac{2\tau}{\mu\phi_s\left|\dfrac{J^2\Psi_p^6 - \chi^6}{g^2\Psi_p^2\chi^4}\right|}\right]_+ \frac{J^2\Psi_p^6 - \chi^6}{g^2\Psi_p\chi^4}. \tag{4.23}$$

In (4.23), as done in Chapter 3, we use the Tresca criterion in order to give a representation of frame invariant measure of the stress in (3.10), i.e., $f(\mathbb{T}_s') = |(T_s^{rr})' - (T_s^{\vartheta\vartheta})'|/2$. Moreover it is possible to rewrite (4.23) as

$$\dot{\Psi}_p = -\frac{J\mu\phi_s}{6\lambda}\left[\left|\frac{J^2\Psi_p^6 - \chi^6}{g^2\Psi_p^2\chi^4}\right| - \frac{2\tau}{\mu\phi_s}\right]_+ \mathrm{sign}\left(J^2\Psi_p^6 - \chi^6\right)\Psi_p, \tag{4.24}$$

where $\lambda = \eta/\mu$. Equations (4.17)-(4.22)-(4.24) should be solved together with the auxiliary equation

$$\frac{\partial}{\partial R}\chi = J\frac{R^2}{\chi^2}. \tag{4.25}$$

We remark that, eq. (4.18) leads to

$$\frac{\partial}{\partial R}p(t,R) = J\frac{R^2}{\chi^2}\Pi^R, \tag{4.26}$$

that can be solved a posteriori, once the other unknowns have been determined.

In order to solve (4.17)-(4.22)-(4.24)-(4.25), we have to supply proper boundary conditions (BCs) and initial conditions (ICs) for the unknowns. In particular, the mixture mass balance (4.17) requires two BCs and the value of J at the initial time, whereas eq. (4.25) is well defined provided that one BC is given. In order to solve eq. (4.22) and (4.24) the initial conditions on g and Ψ_p are required.
As initial condition, we set

$$J(0,R) = 1, \tag{4.27}$$

$$\Psi_p(0,R) = R, \tag{4.28}$$

$$g(0,R) = 1. \tag{4.29}$$

Indeed, at the initial time, there are no elastic and plastic deformations and we assume that also the deformation due to growth is null.

For what concerns boundary conditions, we have to distinguish between internal calcified core and liquid core. We consider a spheroid of initial radius, $R = R_{out}$ with an internal calcified core of radius R_0. Therefore equations (4.17)-(4.25) hold for $R_0 < R < R_{out}$.
For what concerns the calcified core case, boundary conditions have to be consistent with the following requirements:

(i) the radial stress at the external boundary of the specimen has to be equal to the applied stress, $P_{appl}(t)$;

(ii) the velocities of the fluid and of solid phases have to be zero at the inner boundary because we assume that the necrotic core is impermeable and fixed;

(iii) the pressure p has to be zero at $R = R_{out}$ since the liquid is in equilibrium with the liquid outside the spheroid.

These observations are translated in the following set of boundary conditions

$$\chi(t,R_0) = R_0, \tag{4.30}$$
$$\Pi^R(t,R_0) = 0 \tag{4.31}$$
$$(T_s^*)^{rr}(t,\chi(R_{out})) = P_{appl}(t), \tag{4.32}$$
$$p(t,\chi(t,R_{out})) = 0\,. \tag{4.33}$$

Indeed (4.30) guaranties that the interface between the necrotic calcified core and the surrounding living cells is fixed, whereas (4.31) states that the flux at the inner boundary is null, being velocities null. Eq. (4.32) and (4.33) arise directly from conditions (i) and (iii), respectively.
We remark that (4.31) is a Robin BC for J at the inner boundary, whereas (4.32) looks like a Dirichlet condition on J at the external boundary, even though J depends on the derivative of χ. Indeed, for the particular form of $\Sigma(\phi_s)$ that we chose,

$$\left[-\phi_s\left(E\frac{\phi_s-\phi_0}{\phi_{max}-\phi_s}+\mu\frac{1}{3}\frac{J^2\Psi_p^6+2\chi^6}{g^2\Psi_p^2\chi^4}\right)+\mu\phi_s\frac{J^2\Psi_p^4}{\chi^4 g^2}\right]_{\chi(t,R_{out})} = P_{appl}(t)\,. \tag{4.34}$$

Since this equation is nonlinear with respect to $J(t,R_{out})$, solutions can be found by applying Newton's method or other techniques.

On the other hand, when we consider the case of spheroids with necrotic liquid core, we cannot assume that the inner boundary of the spheroid is impermeable and fixed. Initial conditions are still valid and equations (4.17)-(4.25) still hold for $R_0 < R < R_{out}$, with the conditions (4.32)-(4.33) at $R = R_{out}$, whereas at the inner boundary, BCs have to be consistent with the following requirements:

(i) the radial stress exerted by the mixture equals the liquid core radial stress, T_ℓ^{rr};

(ii) the flux at the inner boundary is preserved and the inner boundary moves with the solid phase.

These observations are translated in the following set of boundary conditions

$$\dot{\chi}(t,R_0) = \boldsymbol{v}_s, \tag{4.35}$$

$$T_m^{rr}(t,\chi(t,R_0)) = T_\ell^{rr}(t,\chi(t,R_0))\,, \tag{4.36}$$

that replace eq. (4.30)-(4.31). Eq. (4.36) entails that

$$(T_s^*)^{rr}(t,\chi(t,R_0)) = 0\,. \tag{4.37}$$

Looking at the mass-balance equation of the liquid and the cellular phase for an incompressible mixture, (1.30), we can write

$$\frac{\partial}{\partial t}\phi_s + \mathrm{div}(\phi_s \boldsymbol{v}_s) = \phi_s \Gamma_s\,, \tag{4.38}$$

$$\frac{\partial}{\partial t}\phi_\ell + \mathrm{div}(\phi_\ell \boldsymbol{v}_\ell) = \phi_\ell \Gamma_\ell\,. \tag{4.39}$$

$$\tag{4.40}$$

As already observed, the global mass balance implies $\phi_\ell \Gamma_\ell = -\phi_s \Gamma_s$, so that

$$\mathrm{div}(\phi_s \boldsymbol{v}_s + \phi_\ell \boldsymbol{v}_\ell) = 0 \tag{4.41}$$

holds, thanks to the saturation assumption. Enforcing spherical symmetry and assuming that the velocities of the components are directed along the r-axis, the previous relation can be rephrased as

$$\frac{\partial}{\partial r}\left(r^2(\phi_s \boldsymbol{v}_s + \phi_\ell \boldsymbol{v}_\ell)\right) = 0\,, \tag{4.42}$$

which entails

$$r^2(\phi_s \boldsymbol{v}_s + \phi_\ell \boldsymbol{v}_\ell) = \text{constant}\,. \tag{4.43}$$

Being $\boldsymbol{v} = \phi_s \boldsymbol{v}_s + \phi_\ell \boldsymbol{v}_\ell$ continues across the interface,

$$(\phi_s \boldsymbol{v}_s + \phi_\ell \boldsymbol{v}_\ell)|_{\chi(R_0)} = 0\,,$$

because $\boldsymbol{v} = 0$ in the liquid core. Thus, in (4.43), constant $= 0$ and

$$\boldsymbol{v}_\ell = -\frac{\phi_s}{\phi_\ell}\boldsymbol{v}_s \tag{4.44}$$

in the whole spheroid domain.
Substituting the previous relation in the Darcy's equation and coming back to the Lagrangian formulation, we have

$$\boldsymbol{v}_s = \frac{K(\phi_s)}{\nu}\Pi^R\,. \tag{4.45}$$

Observing that $\mathbb{T}_\ell = -p\mathbb{I}$, conditions (4.35) and (4.37) can be rephrased, thanks to (4.45), giving the following set of BCs

$$\dot{\chi}(t,R_0) = \frac{K(\phi_s)}{\nu}\Pi^R(t,R_0), \tag{4.46}$$

$$\left[-\phi_s\left(E\frac{\phi_s-\phi_0}{\phi_{max}-\phi_s}+\frac{1}{3}\mu\frac{J^2\Psi_p^6+2\chi^6}{g^2\Psi_p^2\chi^4}\right)+\mu\phi_s\frac{J^2\Psi_p^4}{\chi^4 g^2}\right]_{\chi(t,R_0)} = 0 \tag{4.47}$$

$$\left[-\phi_s\left(E\frac{\phi_s-\phi_0}{\phi_{max}-\phi_s}+\frac{1}{3}\mu\frac{J^2\Psi_p^6+2\chi^6}{g^2\Psi_p^2\chi^4}\right)+\mu\phi_s\frac{J^2\Psi_p^4}{\chi^4 g^2}\right]_{\chi(t,R_{out})} = P_{appl}(t)\,, \tag{4.48}$$

$$p(t,\chi(t,R_{out})) = 0\,. \tag{4.49}$$

We remark that in this case we have Dirichlet conditions on J both at the internal and at the external boundary, whose solutions can be found by applying Newton's method or other techniques. Both in the liquid and in the calcified core case, eq. (4.18) requires the condition (4.33), in order to be solved, once the other variables are known.

4.2.3 Dimensionless system

Results in Section 4.3 are presented in terms of dimensionless quantities. We report here the dimensionless system. Spatial quantities are scaled with respect to the initial external radius of the spheroid, R_{out}, whereas temporal quantities scale with the typical cell proliferation time, $t_r = \dfrac{1}{\phi_{max}\gamma_s}$, where γ_s is the coefficient weighting the growth term (i.e., $\Gamma_s = \gamma_s(\phi_{max}-\phi_s)$). Tension and material parameters scale with respect to the shear modulus of the material, μ and the

volume fraction are compared to the maximum cellular volume fraction, ϕ_{max}. Thus, introducing

$$\tilde{R} = \frac{R}{R_{out}}, \quad \tilde{r} = \tilde{\chi} = \frac{\chi}{R_{out}}, \quad \tilde{\Psi}_p = \frac{\Psi_p}{R_{out}},$$

$$\tilde{t} = \frac{t}{t_r}, \quad \tilde{\phi}_s = \frac{\phi_s}{\phi_{max}},$$

$$\tilde{E} = \frac{E}{\mu}, \quad \tilde{\tau}(\tilde{\phi}_s) = \frac{\tau(\phi_s)}{\mu\phi_{max}}, \quad \tilde{P}_{appl} = \frac{P_{appl}}{\mu\phi_{max}}, \quad \tilde{\lambda} = \frac{\lambda}{t_r},$$

the system of equations (4.17)-(4.22)-(4.24) becomes

$$\frac{dJ}{d\tilde{t}} = \tilde{k}_p \frac{\tilde{\chi}^2}{\tilde{R}^2}\frac{\partial}{\partial\tilde{R}}(\tilde{K}(\tilde{\phi}_s)\tilde{\Pi}^R) + 2\tilde{k}_p \frac{J}{\tilde{\chi}}\tilde{K}(\tilde{\phi}_s)\tilde{\Pi}^R \qquad \tilde{R}_0 < \tilde{R} < 1, \quad (4.50)$$

$$\tilde{\Pi}^R = \frac{1}{J}\left[\frac{\partial}{\partial\tilde{R}}(\tilde{P}_s^*)^{rR} + \frac{2}{\tilde{R}}\left((\tilde{P}_s^*)^{rR} - (\tilde{P}_s^*)^{\vartheta\Theta}\right)\right] \qquad \tilde{R}_0 < \tilde{R} < 1, \quad (4.51)$$

$$\frac{\partial\tilde{\chi}}{\partial\tilde{R}} = J\frac{\tilde{R}^2}{\tilde{\chi}^2} \qquad \tilde{R}_0 < \tilde{R} \leq 1 \quad (4.52)$$

$$\frac{dg}{d\tilde{t}} = \frac{1}{3}\tilde{\Gamma}_s g = \frac{1}{3}(1-\tilde{\phi}_s)g \qquad \tilde{R}_0 \leq \tilde{R} \leq 1, \quad (4.53)$$

$$\frac{d\tilde{\Psi}_p}{d\tilde{t}} = -\frac{J\tilde{\phi}_s}{6\tilde{\lambda}}\left[\left|\frac{J^2\tilde{\Psi}_p^6 - \tilde{\chi}^6}{g^2\tilde{\Psi}_p^2\tilde{\chi}^4}\right| - \frac{2\tilde{\tau}(\tilde{\phi}_s)}{\tilde{\phi}_s}\right]_+ \operatorname{sign}\left(J^2\tilde{\Psi}_p^6 - \tilde{\chi}^6\right)\tilde{\Psi}_p \quad \tilde{R}_0 \leq \tilde{R} \leq 1, \quad (4.54)$$

where $\tilde{k}_p = \dfrac{k_0\mu\phi_{max}t_r}{\nu R_{out}^2}$ and $(\tilde{P}_s^*)^{rR} = (P_s^*)^{rR}/(\mu\phi_{max})$, $(\tilde{P}_s^*)^{\vartheta\Theta} = (P_s^*)^{\vartheta\Theta}/(\mu\phi_{max})$ are given by

$$(\tilde{P}_s^*)^{rR} = -J\tilde{\phi}_s\left(\tilde{E}\frac{\tilde{\phi}_s - \tilde{\phi}_0}{1-\tilde{\phi}_s} + \frac{1}{3}\frac{J^2\tilde{\Psi}_p^6 + 2\tilde{\chi}^6}{g^2\tilde{\Psi}_p^2\tilde{\chi}^4}\right)\frac{\tilde{\chi}^2}{J\tilde{R}^2} + J\tilde{\phi}_s\frac{J\tilde{\Psi}_p^4}{\tilde{\chi}^2 g^2\tilde{R}^2} \quad (4.55)$$

$$(\tilde{P}_s^*)^{\vartheta\Theta} = -J\tilde{\phi}_s\left(\tilde{E}\frac{\tilde{\phi}_s - \tilde{\phi}_0}{1-\tilde{\phi}_s} + \frac{1}{3}\frac{J^2\tilde{\Psi}_p^6 + 2\tilde{\chi}^6}{g^2\tilde{\Psi}_p^2\tilde{\chi}^4}\right)\frac{\tilde{R}}{\tilde{\chi}} + J\tilde{\phi}_s\frac{\tilde{\chi}\tilde{R}}{g^2\tilde{\Psi}_p^2}. \quad (4.56)$$

The frame invariant measure of the stress is defined, as in Chapter 2, through the Tresca criterion and thus

$$\tilde{f}(\mathbb{T}'_s) = \frac{\tilde{\phi}_s}{2}\left|\frac{J^2\tilde{\Psi}_p^6 - \tilde{\chi}^6}{g^2\tilde{\Psi}_p^2\tilde{\chi}^4}\right| \quad (4.57)$$

The tensor $\mathbb{K}$ is taken from [85] and adapted to our framework, i.e.,

$$\tilde{K}(\phi_s) = \left[\frac{\tilde{\phi}_{s0}}{1-\tilde{\phi}_{s0}}\frac{J-\phi_{sn}J_g}{J_g\tilde{\phi}_{sn}}\right]^{m_0}\exp\left\{\frac{m_1}{2}\left[\frac{J^2-J_g^2}{J_g^2}\right]\right\}. \quad (4.58)$$

The dimensionless form of (4.26) is

$$\frac{\partial}{\partial \tilde{R}}\tilde{p}(\tilde{t},\tilde{R}) = J\frac{\tilde{R}^2}{\tilde{\chi}^2}\tilde{\Pi}^R, \tag{4.59}$$

with $\tilde{p} = p/(\mu\phi_{max})$.
Initial conditions (4.27) and (4.29) continues to hold, whereas (4.28) rephrases as

$$\tilde{\Psi}_p(0,\tilde{R}) = \tilde{R} \tag{4.60}$$

For what concerns boundary conditions, in the case of a calcified core we have

$$\tilde{\chi}(\tilde{t},\tilde{R}_0) = \tilde{R}_0, \tag{4.61}$$

$$\tilde{\Pi}^R(\tilde{t},\tilde{R}_0) = 0 \tag{4.62}$$

$$\tilde{p}(\tilde{t},\tilde{\chi}(1)) = 0, \tag{4.63}$$

$$\left[-\tilde{\phi}_s\left(\tilde{E}\frac{\tilde{\phi}_s-\tilde{\phi}_0}{1-\tilde{\phi}_s}+\frac{1}{3}\frac{J^2\tilde{\Psi}_p^6+2\tilde{\chi}^6}{g^2\tilde{\Psi}_p^2\tilde{\chi}^4}\right)+\tilde{\phi}_s\frac{J^2\tilde{\Psi}_p^4}{\tilde{\chi}^4 g^2}\right]_{\tilde{\chi}(1)} = \tilde{P}_{appl}(\tilde{t})\,. \tag{4.64}$$

On the other hand, when we consider the case of spheroid with necrotic liquid core, we have

$$\frac{\partial\tilde{\chi}}{\partial\tilde{t}}(\tilde{t},\tilde{R}_0) = \tilde{k}_p\tilde{K}(\phi_s)\tilde{\Pi}^R(\tilde{t},\tilde{R}_0)\,, \tag{4.65}$$

$$\left[-\tilde{\phi}_s\left(\tilde{E}\frac{\tilde{\phi}_s-\tilde{\phi}_0}{1-\tilde{\phi}_s}+\frac{1}{3}\frac{J^2\tilde{\Psi}_p^6+2\tilde{\chi}^6}{g^2\tilde{\Psi}_p^2\tilde{\chi}^4}\right)+\tilde{\phi}_s\frac{J^2\tilde{\Psi}_p^4}{\tilde{\chi}^4 g^2}\right]_{\tilde{\chi}(\tilde{R}_0)} = 0 \tag{4.66}$$

and conditions (4.63) and (4.64) continue to hold.
In the following for sake of simplicity in the notation, we will drop the $\tilde{(\cdot)}$ and all the quantities reported are dimensionless.

4.2.4 Discretization

We solve the system of equations (4.50)-(4.52)-(4.53)-(4.54) using central differences for space derivatives and then a proper ODE solver to obtain the temporal evolution [17]. In the following we depict the main steps of this procedure. The 1D-domain, represented by the interval $[R_0,1]$, is divided into $N+1$ subintervals of width $\Delta R_j = R_{j+1} - R_j$ through the introduction of

N Chebyshev nodes in $(R_0,1)$

$$R_j = \frac{1}{2}(1+R_0) + \frac{1}{2}(1-R_0)\cos\left(\frac{2j-1}{2n}\pi\right)$$

with $j = 1,...,N$. Spaces derivatives are then approximated by finite differences, so that the following system of $3N+4$ equations is obtained:

$$\dot{J}_j = k_p \frac{\chi_j^2}{R_j^2} \frac{K_{j+1}(\phi_{s,j+1})\Pi_{j+1}^R - K_j(\phi_{s,j})\Pi_j^R}{(\Delta R_j)} + 2k_p \frac{J_j}{\chi_j} K_j(\phi_s)\Pi_j^R, \quad j = 1,...,N, \quad (4.67)$$

$$\dot{g}_j = \frac{\Gamma_{s,j}}{3} g_j, \qquad j = 0,...,N+1, \quad (4.68)$$

$$\dot{\Psi}_{p,j} = -\frac{J_j \phi_{s,j}}{6\lambda} \left[\left| \frac{J_j^2 \Psi_{p,j}^6 - \chi_j^6}{g_j^2 \Psi_{p,j} \chi_j^4} \right| - \frac{2\tau}{\phi_{s,j}} \right]_+ \operatorname{sign}\left(J_j^2 \Psi_{p,j}^6 - \chi_j^6\right) \Psi_{p,j}, \quad j = 0,...,N+1 \quad (4.69)$$

Here, j enumerates the nodes of the grid, i.e. $J_j(t) = J(t,R_j)$, $\Psi_{p,j}(t) = \Psi_p(t,R_j)$ and $g_j(t) = g(t,R_j)$, $\phi_{s,j}(t) = \phi_s(t,R_j) = \phi_{sn} g(t,R_j)^3 J(t,R_j)^{-1}$ and $K_j(t) = K(t,R_j)$.
In eq. (4.67) Π^R is given by (4.51), that, approximated with finite differences, gives

$$\Pi_j^R = \frac{1}{J_j} \frac{(P^*)_j^{rR} - (P^*)_{j-1}^{rR}}{(\Delta R_{j-1})} + 2\frac{(P^*)_j^{rR} - (P^*)_j^{\vartheta\Theta}}{J_j R_j}. \quad (4.70)$$

The function χ is calculated by invoking (4.52) and using a standard forward Euler method.

$$\chi_{j+1}(t) = \chi_j(t) + J_j(t) \frac{R_j^2(t)}{\chi_j^2(t)} \Delta R_j, \quad (4.71)$$

coupled with (4.30) for the calcified core and (4.35) for the liquid core. Condition (4.30) gives $\chi_0(t) = R_0$, whereas (4.35) can be rephrased as

$$\chi_0^{i+1} = \chi_0^i + \Delta t k_p K_0^i (\Pi_0^R)^i, \quad (4.72)$$

where the apex i enumerates the discretized instant in time. The boundary values J_0 and J_{N+1} are computed imposing boundary conditions (4.31)-(4.34) for the calcified core and (4.37)-(4.34) for the liquid core.

The boundary values J_{N+1}, both for the calcified core and the liquid core, is given by (4.34), which is solved numerically, by means of a Newton-Raphson method.

In the case of liquid core simulations (4.37) gives the value of J_0, always using the Newton-Raphson method, whereas in the case of the first node, we impose $\Pi_0^R = 0$, according to (4.31), in eq. (4.67) prolonged to node $j = 0$.

According to this procedure, the initial system of partial differential equations (4.50)-(4.53)-(4.54) is approximated by a system of ordinary differential equations that can be integrated by choosing a stable ODE solver, with the initial conditions $J_j(0) = J(0,R_j) = 1$, $g_j(0) = g(0,R_j) = 1$, $\Psi_{p,j}(0) = \Psi_p(0,R_j) = R_j$, for $j = 1,\ldots,N$.

The variation of pressure inside the specimen can be calculated a posteriori, once Π^R is known, using (4.59), that can be solved with the boundary condition (4.33) with an explicit Euler scheme.

4.3 Results

In this section we first present the results of a quiescent spheroid undergoing pure remodelling due to the application of an external load at the outer boundary (Section 4.3.1). We then consider the case of a proliferative spheroid with a necrotic core (Section 4.3.2.1). Nutrients are included in Section 4.3.2.2 in order to model the presence of a quiescent region in which cells do not proliferate because of the lack of nutrients. The presence of the healthy tissue is modelled in Section 4.3.3.

4.3.1 Remodelling without growth

We first consider the case of a spheroid composed of a necrotic core (that can be either composed of calcified debris, i.e., rigid, or filled with liquid) and a quiescent shell, in which cell proliferation is compensated by death. Therefore in this case we do not have any net production of the cellular phase, i.e., $\Gamma_s = 0$ in (4.53), which implies $g(t,R) = 1\,, \forall t$ and $\forall R$. The evolution of the system is represented by (4.50)-(4.52)-(4.54), coupled with the initial conditions (4.27) and (4.60) and the boundary conditions (4.61)-(4.62)-(4.64) for the rigid necrotic core and (4.64)-(4.65)-(4.66) for the liquid core. We remark that if no stress is applied at the outer boundary, the stationary case corresponds to the initial condition, i.e. we do not have any evolution of the system.

The external stress can represent a controlled stress exerted in vitro by the gel in which cancer cells are plated or the stress exerted by the external tissue. In this case the stress exerted at the outer boundary is known.

Applying an external compressive load, J decreases, which means that the volume of the spheroid

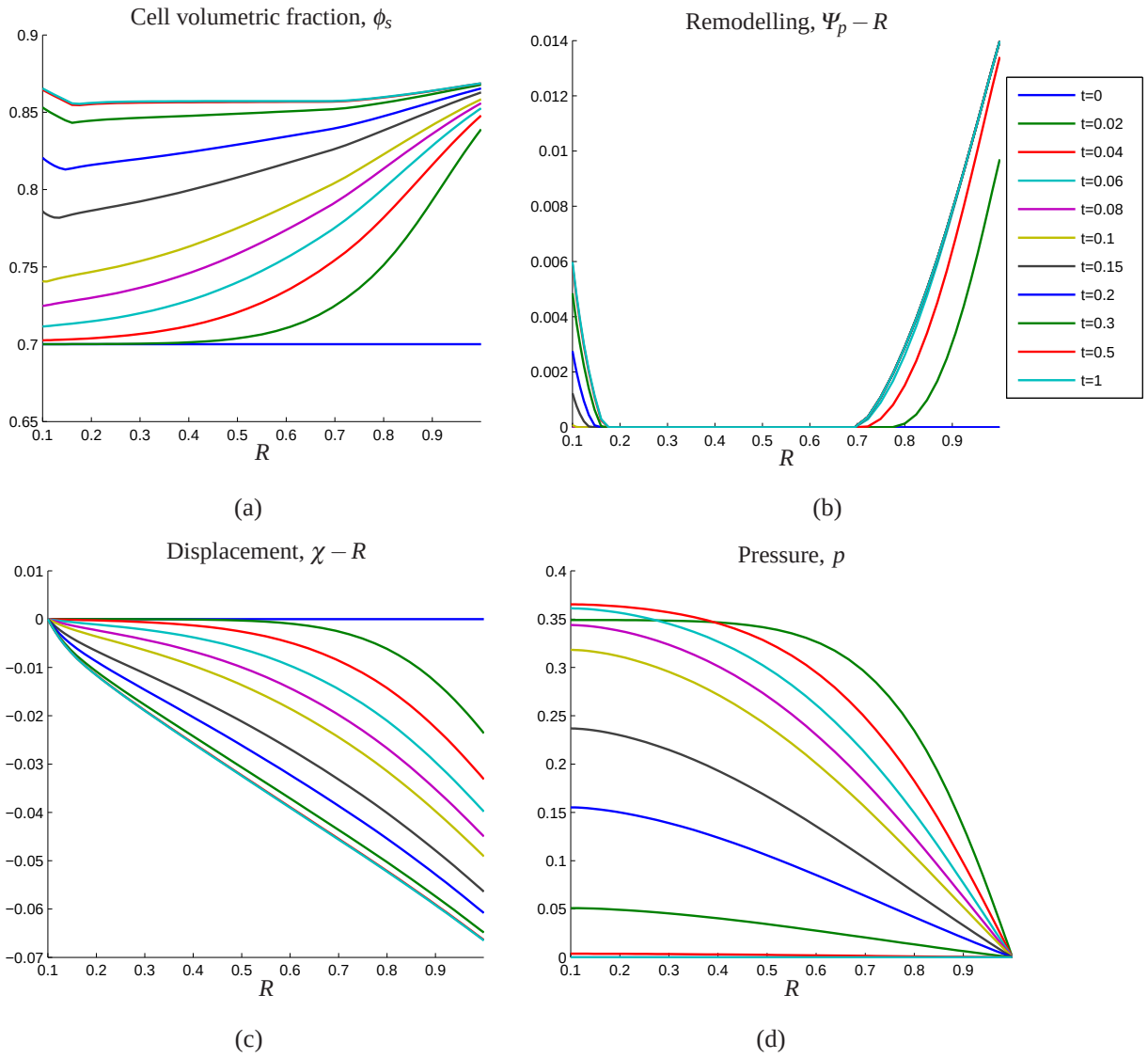

Figure 4.3: Calcified core without growth: simulations for dimensionless parameters $P_{appl} = -0.2809$, $k_p = 0.7745$, $m_0 = 0.0848$, $m_1 = 4.638$, $\tau = 0.0281$, $\lambda = 0.0281$, $E = 0.2809$. Lines report the evolution in space of the variable at the instant of time specified. For the final time reported the system is at the stationary condition.

diminishes, and, if the applied load is sufficiently high, the internal reorganization of the spheroid is triggered.

Fig. 4.3 shows the evolution in time and space of $\phi_s(t,R) = \phi_{sn}/J(t,R)$, $\Psi_p(t,R) - R$, $\chi(t,R) - R$ and $p(t,R)$ for a spheroid subjected to a constant stress at the outer boundary. Every curve represents the trend over R of the different quantities at a fixed time step (see legend). It is possible to see that, in the first time steps, the cell volumetric fraction strongly increases at the

outer boundary where the load is applied. Then the whole aggregate is strongly compressed (see Fig. 4.3-(a)). We remark that after $t \approx 0.1$ the trend in the curves changes in proximity of the internal boundary. This change corresponds to the activation of the internal reorganization (see Fig. 4.3-(b)). For what concerns remodelling, we remark that $F_p^{rR} = \dfrac{R^2}{\Psi_p^2}$, whereas $F_p^{\theta\Theta} = F_p^{\phi\Phi} = \dfrac{\Psi_p}{R}$, thus

- $\Psi_p - R < 0 \iff F_p^{rR} > 1$ and $F_p^{\theta\Theta} = F_p^{\phi\Phi} < 1$, which means that remodelling occurs through extensions along the radial direction and compression in the transverse directions;
- $\Psi_p - R > 0 \iff F_p^{rR} < 1$ and $F_p^{\theta\Theta} = F_p^{\phi\Phi} > 1$, which means that remodelling occurs through compression along the R-axis and extensions along the Θ and Φ directions.

Fig. 4.4 intuitively explains the biological meaning of the remodelling term.

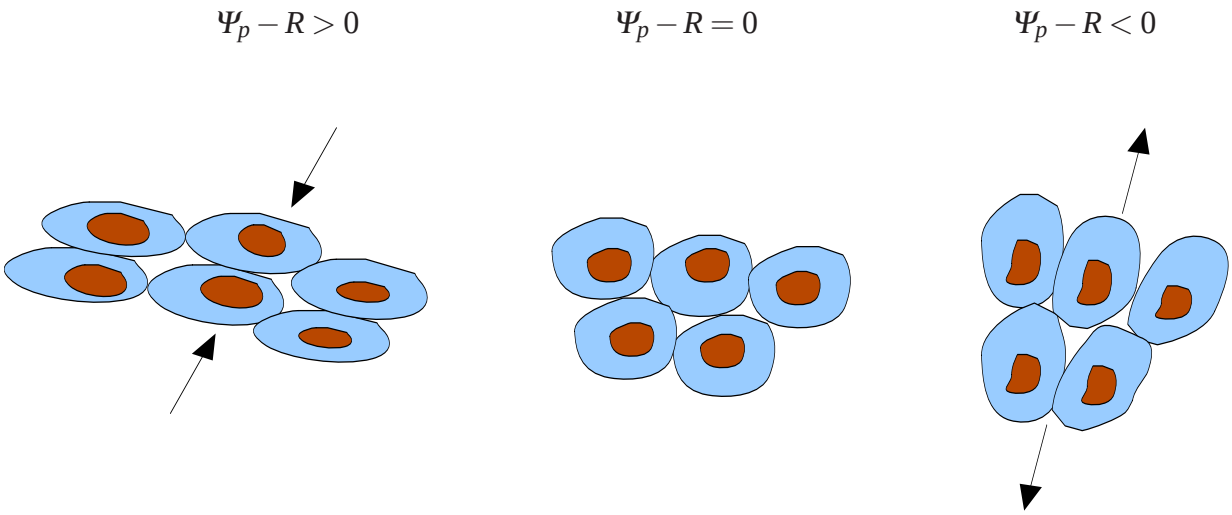

Figure 4.4: Diagram of the possible internal reorganization occurring inside a spheroid: remodelling through compression (on the left), physiological condition (centre), remodelling through extension (on the right).

In Fig. 4.3-(b), it is possible to see that, in the first instants of time, consistent remodelling occurs at the external boundary due to compression along the R direction and extension along the Θ and Φ directions, as a consequence of the external compressive load application. Then remodelling at the external boundary reaches the steady state condition (indeed, for the specific parameters used in Fig. 4.3, after $t \approx 0.06$ the curves at the external boundary almost overlap), while remodelling starts at the internal boundary where cells are constrained not to penetrate the

necrotic core. Close to the internal boundary, $\Psi_p - R > 0$, being cell compressed towards the necrotic core. Also in this case, remodelling continues until a stationary condition is reached (after $t \approx 0.5$). We remark that, thanks to the remodelling occurring in the region near the calcified core and in the outer region, ϕ_s is higher than in the central region, where remodelling is not triggered. Therefore the effect of bonds rupture, when the aggregate is constrained on both sides, leads to a closer packaging of cells.
Moreover we observe that, for the parameters setted in this simulations, remodelling occurs only in some region of the aggregate, therefore we have that the mechanical behaviour of the aggregate changes in space: in the central region it behaves elastically, whereas close to the inner and the outer boundary it behaves as an elasto-plastic material. This difference in the mechanical response of cells leads to the non-homogeneous distribution of variables inside the domain.
For what concerns displacement it is possible to see that the spheroid radius decreases until the stationary condition is reached and due to the BC (4.61) the displacement is null in proximity of the necrotic core. Moreover at the end of the simulation the pressure in homogeneously distributed in the whole domain, which implies that fluxes are null and thus the stationary condition is reached (after $t \approx 0.5$).

On the other hand, looking at the liquid core case, in Fig. 4.5 we observe that, also in this case, in the first instants of time, cells are more compressed at the outer boundary (Fig. 4.5-(a)), then, as the deformation of the aggregate increases (see Fig. 4.5-(c)), cells volumetric fraction increases in the whole domain. However, in this case, the solid volumetric fraction in the region near the necrotic core is less influenced by the application of an external load, being cells not compressed towards a rigid wall. Indeed in this case, cells can move toward the liquid core, as fluid encapsulated inside the central core flows inside the aggregate, leading to the decrease of the central liquid core radius ($\chi(t,R_0) - R_0 < 0$ in Fig. 4.5-(c)). Moreover, consistent remodelling initially occurs at the external boundary, due to compression along the R direction and extension along the transverse directions. In order to reach the steady state condition, in proximity of the external boundary where load is applied, remodelling slightly decreases until the condition $f(\mathbb{T}'_s) = \tau$ is reached. Then, remodelling starts at the internal boundary. We remark that in this case, at the internal boundary, $\Psi_p - R$ is negative which means that remodelling occurs through extension along the R-axis. Indeed the effect of bond rupture, in this case, is to allow cells to move more freely towards the central liquid core, as long as the necrotic region is all filled by cells. For what concerns displacement it is possible to see that the spheroid radius decreases and intense negative displacements are recorded also at the inner boundary, where cells move toward

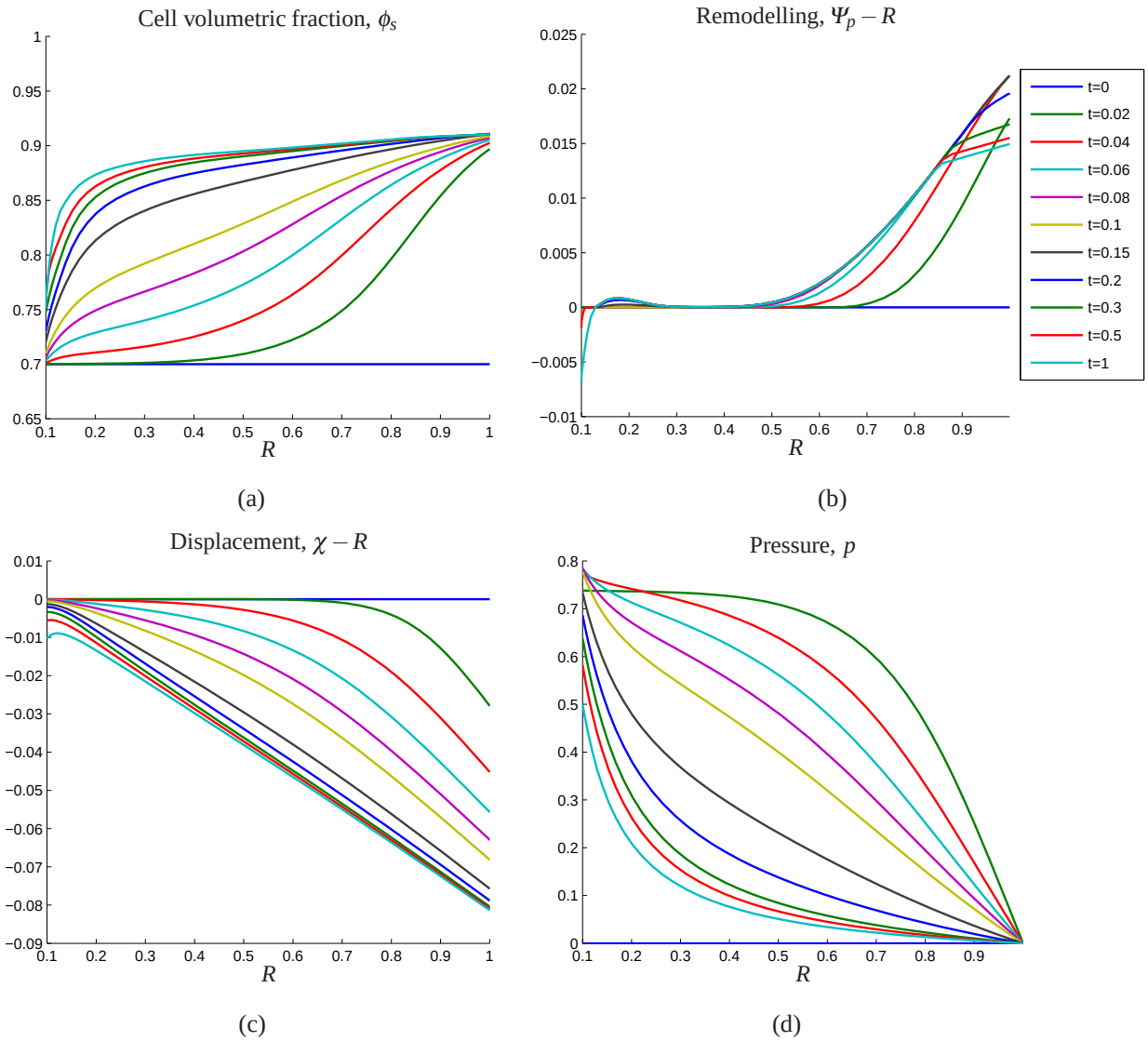

Figure 4.5: Liquid core without growth: simulations for the same value used in the simulation of the calcified core. Lines report the evolution in space of the variable at the instant of time specified. We remark that in this case at time $T = 1$ the steady state is not yet reached. Indeed, for the liquid core undergoing remodelling the internal boundary continues to move until cells fill all the internal gap.

the necrotic liquid core. In this case, for $t = 1$ the steady state condition is not reached yet.

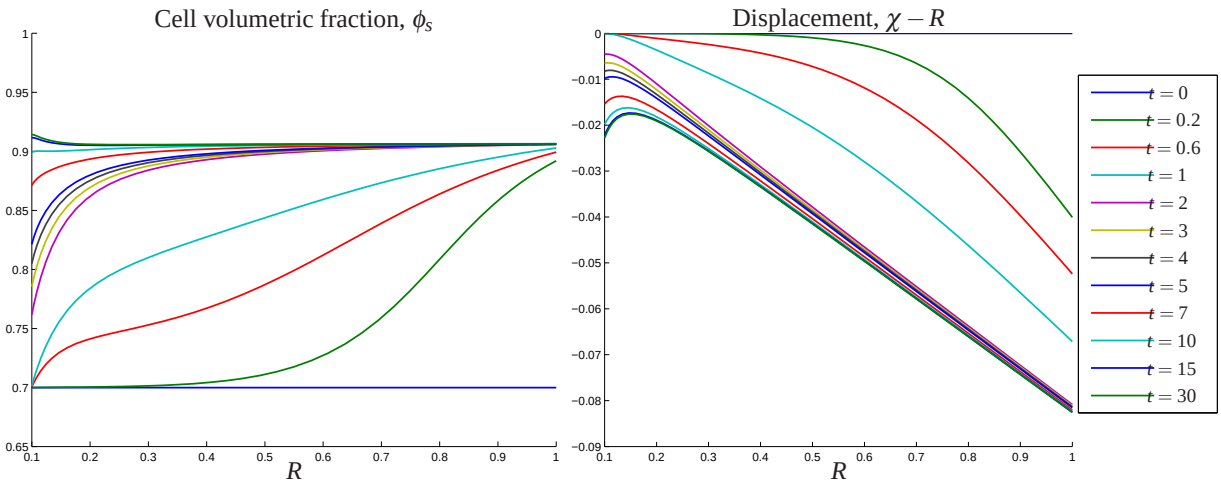

(a) (b)

Figure 4.6: Liquid core without growth and without remodelling: simulations for the same value used in the simulation of the calcified core, but for a value of τ for which no remodelling occurs. Lines report the evolution in space of the variable at the instant of time specified. We remark that at the stationary state (after $t \approx 15$) there's still some liquid in the central necrotic core.

Fig. 4.6 reports the value of $\phi_s(t,R)$ and $\chi(t,R) - R$ in the case in which a quiescent aggregate with a liquid necrotic core is compressed, without experiencing remodelling. Differently from what observe in the case in which the internal reorganization is triggered, in this case, at the steady state condition (which is reached after 15 unit of time), the internal liquid core is not fully filled by cells.

Fig. 4.7 reports the values of $\phi_s(t,R)$, $\Psi_p(t,R) - R$ and $\chi(t,R) - R$ at the reference time $t = 5$, both for the calcified core with and without remodelling (red and blue curves, respectively) and the liquid core with and without remodelling (purple and light-blue curves, respectively). From Fig. 4.7 it is clear that, for the calcified core, where remodelling is triggered, cells are closer-packed than in the region in which remodelling does not occurs. Thus, at the internal and external boundaries, the cell volumetric fraction is higher than in the central region. On the other hand, remodelling in the liquid core strives to maintain the cell volumetric fraction closer to the physiological value and thus, when it is triggered, less intense volumetric changes are perceived in proximity of the necrotic region. Indeed, in this case, the rupture of bonds leads to more intense cell movements toward the central necrotic region and thus more intense displacement are recorded at the interface between the necrotic and the quiescent regions. When no remodelling is triggered, the displacement of the solid phase at the interior boundary is smaller and so ϕ_s is bigger, compared to case in which remodelling occurs.

We remark that in the case in which the solid volumetric fraction changes consistently, due to growth or the application of an external load, the assumption that the permeability $\mathbb{K}$ is a function of ϕ_s is fundamental. As ϕ_s increases (i.e. J decreases), being $K(\phi_s)$ an increasing function of J in the interval $(\phi_{sn},1)$, the velocity of the fluid and the solid phases decreases consistently, leading to a slowing-down of the overall process.

4.3.2 Growth and remodelling

We consider the growth of a cancer spheroid with a given applied load at the outer boundary. We consider both the case in which the central core is composed of calcified cells debris, i.e., the tumor has a central rigid necrotic core, and the case in which the central core is filled with water.

In a first assumption we consider that growth depends only on the cellular volume fraction (Section 4.3.2.1). This condition represents a cellular aggregate composed of a necrotic core and a proliferative shell in which growth is limited only by contact inhibition. We then include nutrients (Section 4.3.2.2), in order to model the presence of a quiescent ring between the necrotic core and the proliferative ring, in which the concentration of nutrients is not enough in order to support the anomalous growth of cancer cells.

4.3.2.1 Growth depending only on the cell volumetric fraction

Fig. 4.8 shows the evolution of the dependent variables $J(t,R)$, $g(t,R)$, $\Psi_p(t,R)-R$, $\phi_s(t,r)=\phi_{sn}g^3/J(t,r)$, $\chi(t,R)-R$ and $T_m^{*rr}(t,r)$ along R at different time steps (different lines) for a spheroid with a necrotic rigid core, whose growth is limited only by geometrical constraints, i.e., cells duplicate until the maximum cell volume fraction is reached. Therefore $\Gamma_s=(1-\phi_s)$, which biologically means that the growth of cells is governed only by contact inhibition. Thus $g(t,R)>1$ in all the domain (see Fig. 4.8-(b)). This situation represents the case in which nutrients are available in all the domain and thus it is suitable to describe only tumors in the first stages. When remodelling occurs, consistent volumetric changes are experienced both at the internal and the external boundary of the tumor (see Fig. 4.8-(a)). Indeed, at the external boundary, the spheroid is let free to expand and thus volume increases ($P_{appl}=0$). Cells at the interior of the spheroid are pulled from the cells at the outer boundary that can freely move and so the aggregate expands. However in living cells closed to the calcified core are forced to stay attached to the central necrotic core. If remodelling occurs (see Fig. 4.8-(c)), bonds breaks and cells detach one from the others. In this case Ψ_p-R is highly negative in the region close to the necrotic

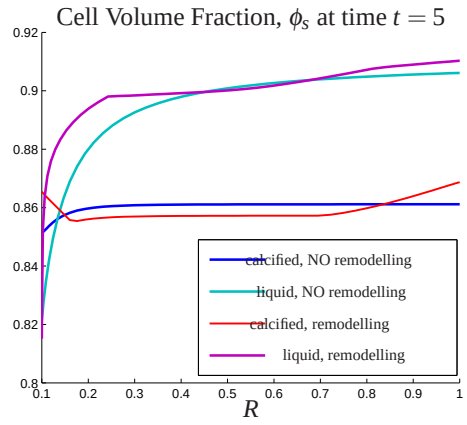

(a)

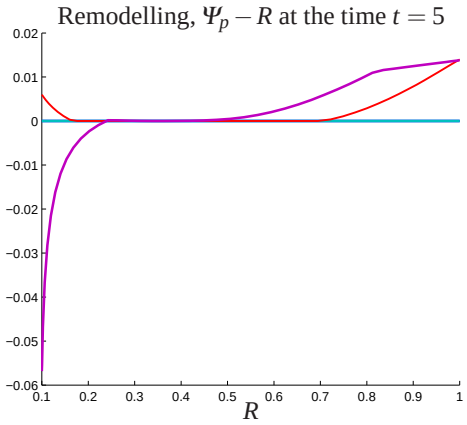

(b)

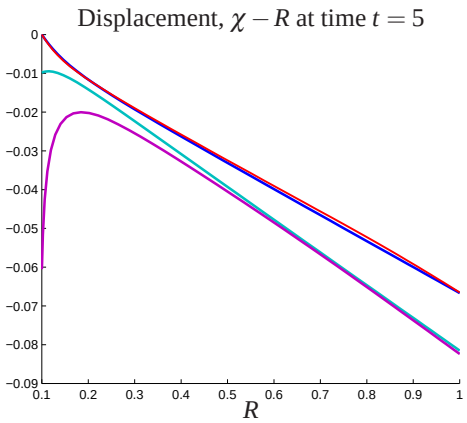

(c)

Figure 4.7: Comparison between liquid core and calcified core without growth: results at time $t = 5$.

core, because remodelling occurs through extension along the R-axis and compression along the Θ and Φ directions, as explained in Section 4.3.1. Moreover, also at the external boundary, where cells can move, $\Psi_p - R$ is negative. We remark that, being the growth terms dependent only by the cellular volumetric fraction, where J increases also g increases (see Fig.4.8-(b)). The action of remodelling on an expanding cellular spheroid is to maintain the solid volumetric fraction, $\phi_s = \dfrac{\phi_{sn} J}{g^3}$ close to the physiological value: where remodelling does not occur ϕ_s is higher than in those region in which bonds break and cells are more motile. We remark that intense displacements are experienced also in proximity of the central necrotic core (Fig. 4.8-(e)).

We observe that in our model, we do not fix the volumetric fraction of the cellular constituent to be equal to ϕ_0, but the boundary condition on J is obtained imposing the free stress condition at the outer boundary and, thus, it is in general different from ϕ_0 even when $P_{appl} = 0$.
Fig. 4.8-(f) reports the radial component of the constitutive Cauchy stress tensor of the mixture, T_m^{*rr}. We remark that at the external boundary T_m^{rr} equals the imposed load, which is zero in this case.

In Fig. 4.9 we reports the results of the growth of a spheroid with calcified liquid core, without remodelling. Parameters are the same used in Fig. 4.8, except for τ that we choose in order not to have remodelling.
In this case, being the mechanical behaviour of the aggregate the same in the whole domain, the curves are smoother. In particular we observe that, when remodelling does not occur, cells at the interior of the spheroid, being attached to the central necrotic core, are less motile (indeed in this case, we do not have any reorganization).

Therefore, volumetric changes are less consistent in proximity of the inner boundary (see Fig. 4.9-(a)), and the growth of cells is less intense (see Fig. 4.9-(b)), because cells are more packed (see Fig. 4.9-(c)). In this case, displacements in proximity of the necrotic core are less intense (cf. Fig. 4.9-(d) with 4.8-(e)). The total mass is preserved because of the higher ϕ_s.

We then look at the growth of a spheroid under compressive loads (see Fig. 4.10). In the first instants of time the aggregate is compressed due to external load, then cells duplication becomes high enough in order to make the spheroid expands (after $t \approx 1.6$). Indeed, if we look at the evolution of $\chi(t,R) - R$ it is possible to see that when an external load is imposed, the aggregate size decreases, $\chi(t,R) - R < 0$ until $t < 1.6$. Then growth predominate and the spheroid expands, $\chi(t,R) - R > 0$. Consistently, $J(t,R) > 1$ in the first instants of time in the whole domain. Looking at remodelling it is possible to see that $\Psi_p - R$ is positive at the outer boundary

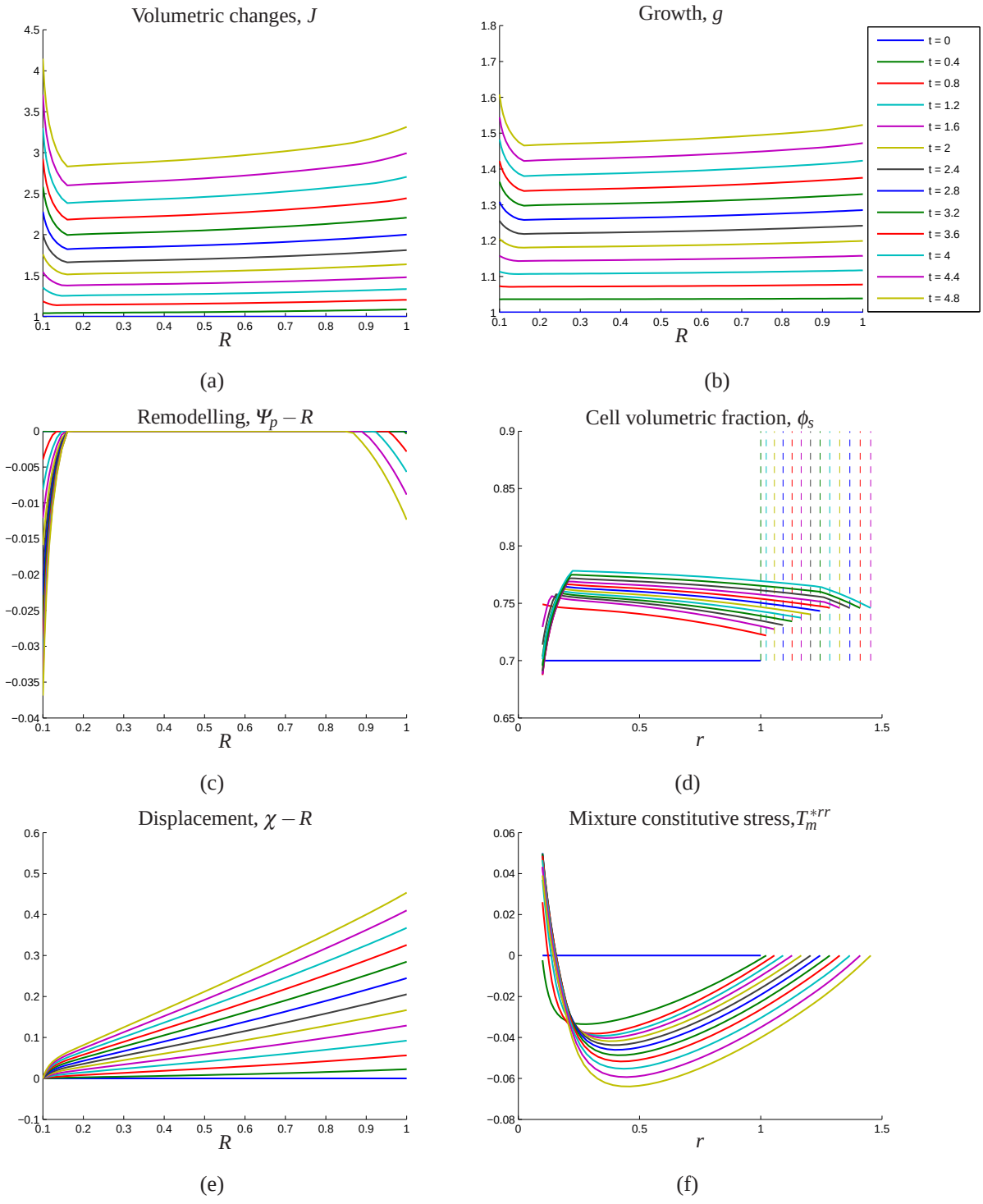

Figure 4.8: Free growth of a spheroid composed of a calcified core surrounded by a proliferative shell. All the other parameters are the same used for the simulation without growth.

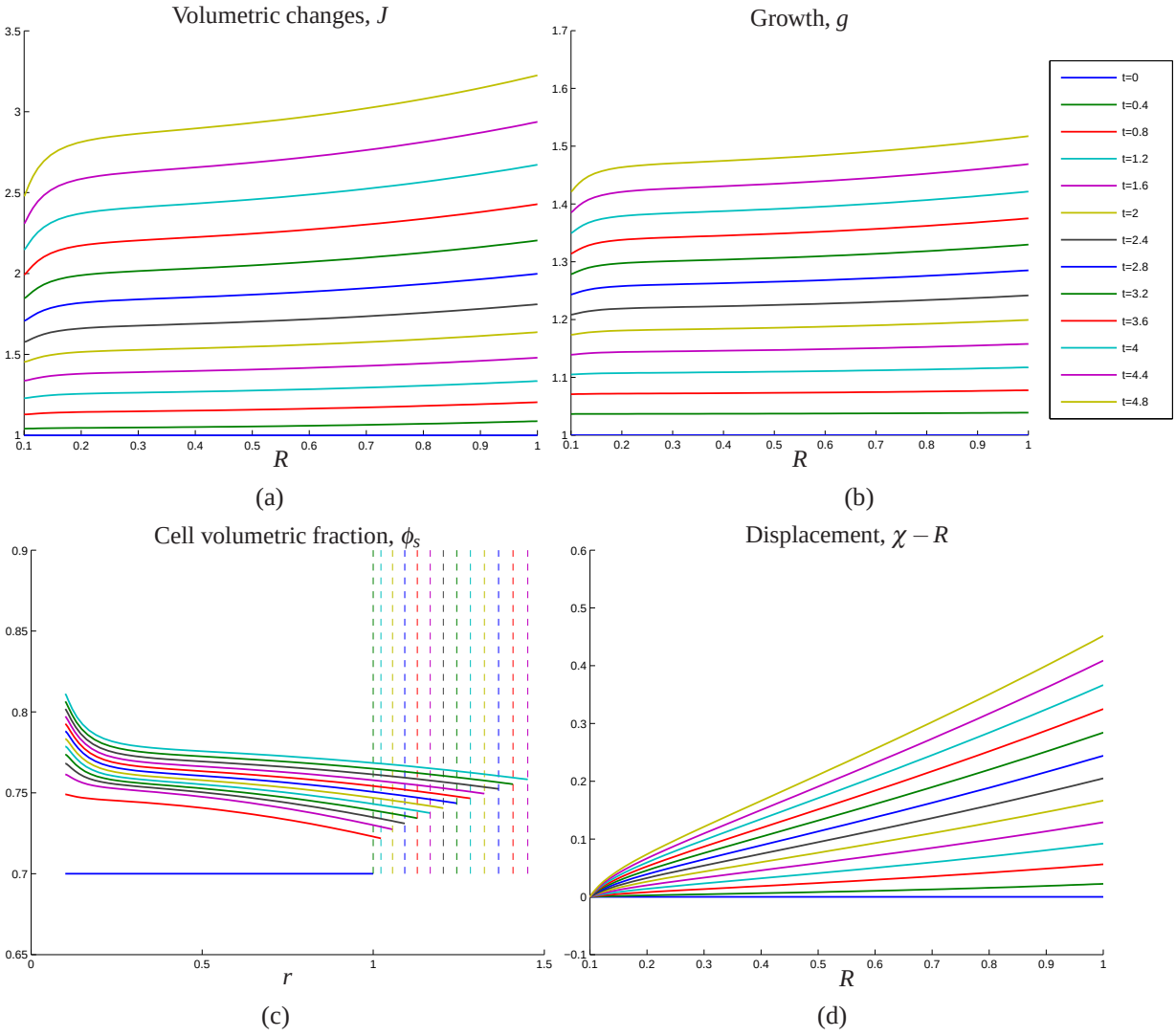

Figure 4.9: Free growth without remodelling of a spheroid composed of a calcified core surrounded by a proliferative shell. In this simulation τ is chosen in order not to have internal reorganization of the multicellular aggregate. All the parameters are the same used for the simulation with growth and remodelling.

of the tumor, indeed while expanding, cells at the outer boundary are compressed because of the application of the external stress. On the other hand, at the inner boundary, $\Psi_p - R$ is initially positive, which means that remodelling occurs through compression along the R-axis, as in the case of the compression of a quiescent aggregate, then, as proliferation increases, $\Psi_p - R < 0$ because proliferative cells expand.

Fig. 4.11 shows the typical results for the stress free growth of an aggregate with a necrotic

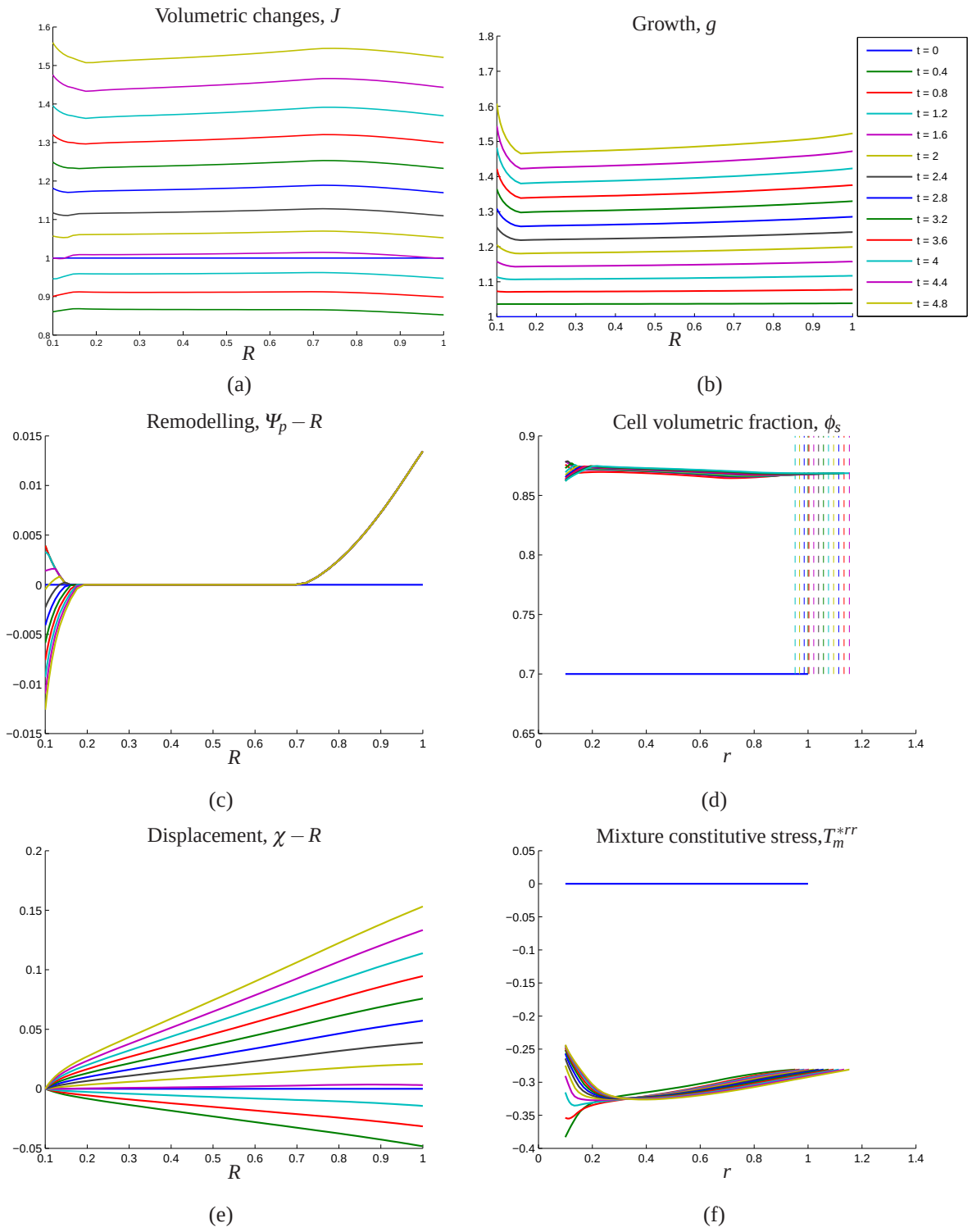

Figure 4.10: Calcified core simulation under compressive load at the external boundary, $P_{appl} = -0.1$. All the other parameters are the same used for the simulation without growth.

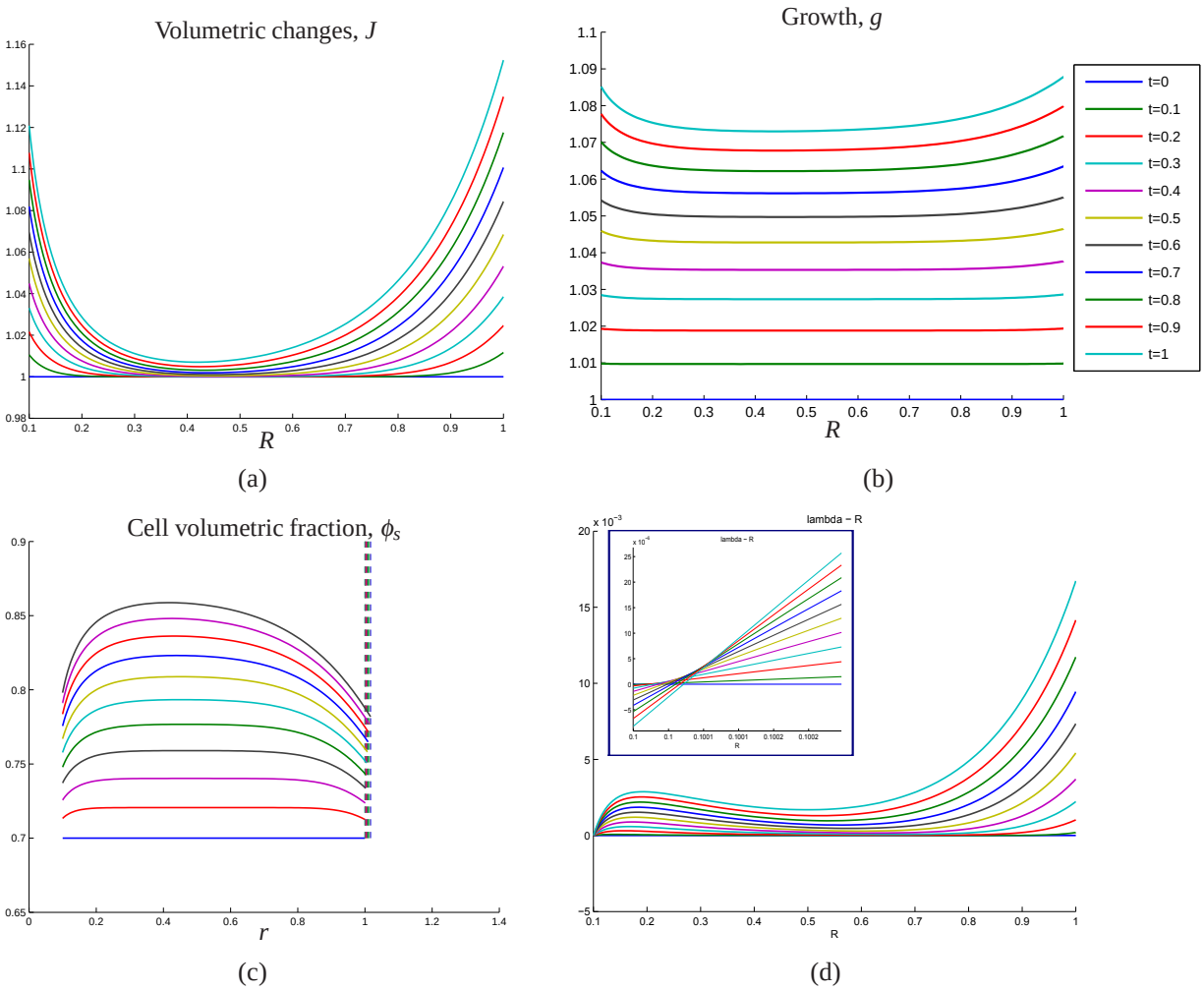

Figure 4.11: Free growth of a spheroid with a necrotic liquid core. Growth is limited only by contact inhibition, so that the internal boundary expands towards the central necrotic core. Simulations are performed setting $k_p = 0.0333$, $m_0 = 0.0848$, $m_1 = 4.638$, $\tau = 3$, $\lambda = 0.03$, $E = 0.33$.

liquid core. It is possible to see that in this case we have consistent volumetric changes also in proximity of the necrotic core of the spheroid. Indeed in this case the spheroid is not constrained by a rigid wall; therefore cells can proliferate also in proximity of the necrotic region (Fig. 4.11-(b)) and proliferative cells moves towards the liquid core (Fig. 4.11-(d)). We remark that for the particular Γ_s chosen, the production of new cells is limited only by the availability of space. This simulation corresponds, for instance, to the case in which a spheroid is left free to grow inside an environment in which nutrients are not sufficient. Thus the necrotic core is formed. Then, after some time the spheroid is positioned in an environment full of nutrients and the quiescent cells

in the central region can re-start to grow, filling the central void space.
However, considering the growth of a spheroid inside a tissue it is unlikely that cell growth can occur in proximity of a necrotic region. It is therefore fundamental to introduce nutrients diffusion in order to consider the dependency of growth from these chemical factors.

4.3.2.2 Inclusion of nutrients

Results presented in the previous subsection are strictly linked to the assumption we made on the expression of the growth term, Γ_s, which depends only on the volume fraction of the cellular constituent, i.e., in the dimensionless formulation, $\Gamma_s = (1-\phi_s)$. This assumption means that cell can grow until the saturation condition is reached, without any other constraints. This assumption leads to the unrealistic growth of cells even in proximity of a necrotic region, as seen in Fig.4.8-(b), 4.9-(b) and 4.11-(b).
In reality, cell growth is limited by different factors. In particular the availability of nutrients, that diffuse inside the tissue and are transported by the liquid moving in the interstitial space, strongly affects cells capability to duplicate.
In this section, we include nutrients, in order to differentiate the proliferative region from the quiescent region of the spheroid. In particular we fix a minimum threshold of nutrients concentration, c_{n0} above which cells can proliferate. It can be postulated that $\Gamma_s = \gamma_s(\phi_{max}-\phi_s)(c_n - c_{n0})_+$.
In this way we have the introduction of a quiescent zone in which the amount of nutrients is not sufficient to maintain cell proliferation.
In order to insert the dependency on nutrients in the growth term, it is necessary to give the evolution of these chemicals inside the spheroid.
The mass balance for nutrients dissolved in the liquid phase, in Lagrangian coordinates, reads [73]

$$\dot{c}_n = \frac{1}{\nu\phi_\ell}\left(\mathbb{F}^{-1}\mathbb{K}(\phi_s)\mathbb{F}^{-T}\mathrm{Grad}p\right)\cdot\mathrm{Grad}c_n + \frac{1}{J\phi_\ell}\mathrm{Div}\left(J\mathbb{F}^{-1}D_n\mathbb{F}^{-T}\mathrm{Grad}c_n\right) - \zeta\frac{\phi_s}{\phi_\ell}c_n\,, \quad (4.73)$$

where $c_n = m_n/m_\ell$ is the mass concentration of the nutrients, ζ is the rate of consumption of nutrients for cell biological functions and D_n is the diffusion coefficient of nutrients.
Eq. (4.73) is obtained from the mass balance of nutrients

$$\frac{d}{dt}\int_V \phi_\ell c_n dV = \int_{\partial V}\phi_\ell c_n \mathbf{v}_\ell\cdot\mathbf{n}dS - \int_{\partial V}\phi_\ell\mathbf{j}_\ell\cdot\mathbf{n}dS + \int_V \Gamma_\ell\phi_\ell c_n dV + \int_V G_n dV\,, \quad (4.74)$$

where $\mathbf{j}_\ell = -D_n \text{grad} c_n$ is given by the Fick's law and G_n represents the production/decay of nutrients. The local form of (4.74) is

$$\frac{\partial}{\partial t}(\phi_\ell c_n) + \text{div}(\phi_\ell c_n \boldsymbol{v}_\ell) = \text{div}(\phi_\ell D_n \text{grad} c_n) + \Gamma_\ell \phi_\ell c_n + G_n \,, \tag{4.75}$$

which in the Lagrangian formulation, reads

$$\dot{\overline{(J\phi_\ell c_n)}} + \text{Div}(J\phi_\ell c_n \mathbb{F}^{-1} \boldsymbol{w}_{\ell s}) = \text{Div}(J\phi_\ell \mathbb{F}^{-1} D_n \mathbb{F}^{-T} \text{grad} c_n) + J\Gamma_\ell \phi_\ell c_n + J G_n \,, \tag{4.76}$$

Recalling the mass balance of the liquid phase (1.34) and the Darcy's Law (1.72), eq. (4.73) is easily obtained, setting $G_n = -\zeta \phi_s c_n$.
Eq. (4.73) in spherical coordinates reads

$$\begin{aligned} \dot{c}_n &= \frac{1}{\nu} \frac{\chi^2}{J\phi_\ell R^2} K(\phi_s) \Pi^R \frac{\partial c_n}{\partial R} + \\ &+ \frac{D_n}{J(1-\phi_s)R^2} \frac{\partial}{\partial R} \left(\frac{\chi^4}{JR^2} \frac{\partial c_n}{\partial R} \right) - \zeta \frac{\phi_s}{\phi_\ell} c_n \,. \end{aligned} \tag{4.77}$$

Writing eq. (4.77) with respect to the dimensionless quantities presented in Section 4.2.3 and the quantity $\tilde{c}_n = c_n / c_b$, where c_b is the mass concentration of the nutrients in the blood , we have

$$\begin{aligned} \dot{\tilde{c}}_n &= \frac{\tilde{k}_p}{\phi_{max}} \frac{\tilde{\chi}^2}{J(1-\tilde{\phi}_s)\tilde{R}^2} \tilde{K}(\tilde{\phi}_s) \tilde{\Pi}^R \frac{\partial \tilde{c}_n}{\partial \tilde{R}} + \\ &+ \tilde{D}_n \frac{1}{J(1-\tilde{\phi}_s)\tilde{R}^2} \frac{\partial}{\partial \tilde{R}} \left(\frac{\tilde{\chi}^4}{J\tilde{R}^2} \frac{\partial \tilde{c}_n}{\partial \tilde{R}} \right) - \zeta \frac{\tilde{\phi}_s}{(1-\tilde{\phi}_s)} \tilde{c}_n \,, \end{aligned} \tag{4.78}$$

where $\tilde{D}_n = \dfrac{D_n t_r}{\phi_{max} R_{out}^2}$. We remark that, in this case, for the particular expression of Γ_s, we have that $t_r = 1/(\gamma_s \phi_{max} c_b)$, so that eq. (4.53) holds. Eq. (4.78), coupled with (4.50)-(4.52)-(4.53)-(4.54) and the new growth term

$$\tilde{\Gamma}_s = (1-\tilde{\phi}_s)(\tilde{c}_n - \tilde{c}_0)_+ \,, \tag{4.79}$$

represents the evolution of a spheroid, whose growth is limited by the availability of nutrients. Indeed $\tilde{c}_0$ represents the threshold of nutrients concentration, above which cells can duplicate. For what concerns boundary conditions, we can assume that, when all the domain is composed

by tumor cells, both in the case of a calcified core and in the case of a liquid core, we have that

$$\tilde{c}_n(\tilde{t},1) = 1\,, \tag{4.80}$$

which corresponds to the presence of a vessel in proximity of $\tilde{R}_{out} = 1$ with a wall perfectly permeable to nutrients.
On the other hand for what concerns the internal boundary, we can assume that the rigid necrotic core is impermeable to nutrients, which leads to the condition

$$\frac{\partial \tilde{c}_n}{\partial \tilde{R}}(\tilde{t},\tilde{R}_0) = 0\,. \tag{4.81}$$

In the liquid core case, we can consider that the concentration of nutrients in the central liquid region is homogeneous, which leads also in this case to the condition

$$\frac{\partial \tilde{c}_n}{\partial \tilde{R}}(\tilde{t},\tilde{R}_0) = 0\,. \tag{4.82}$$

In the following, in order to simplify the notation, we will omit the tilde, as done for the other dimensionless variables.
Results are shown in Fig. 4.12 for the rigid necrotic core and 4.13 for the liquid necrotic core. We remark that, in the free growth case, i.e. with $P_{appl} = 0$, the condition at the inner boundary does not affect significantly the results of the simulations, being the growth concentrated at the external boundary that can freely move. Both in the calcified and in the liquid core case, it is possible to see that the more intense volumetric changes are focused at the external boundary (see Fig. 4.12-(a) and 4.13-(a)), where nutrients concentration is above the threshold (Fig. 4.12-(d) and 4.13-(d)) that guarantee the proliferation of cells (Fig. 4.12-(b) and 4.13-(b)). In this case remodelling is due to deformations occurring for the proliferation of cells and not to the application of an external load.

Therefore in the first instants of time proliferation of cells occurs without remodelling (up to $t \approx 0.9$). Then remodelling due to extension along the R-direction starts at the external boundary (see Fig. 4.12-(c) and 4.13-(c)). The solid volumetric fraction highly increases in the proliferative region. In the first instants of time cells in the quiescent region are pulled by proliferative cells and thus ϕ_s slightly decreases in the proliferative region. Then, as the proliferative process goes on, ϕ_s increases in the whole domain (Fig. 4.12-(e) and 4.13-(e)). From the displacement plot (Fig. 4.12-(f) and 4.13-(f)) it is possible to see that the whole aggregate is expanding.

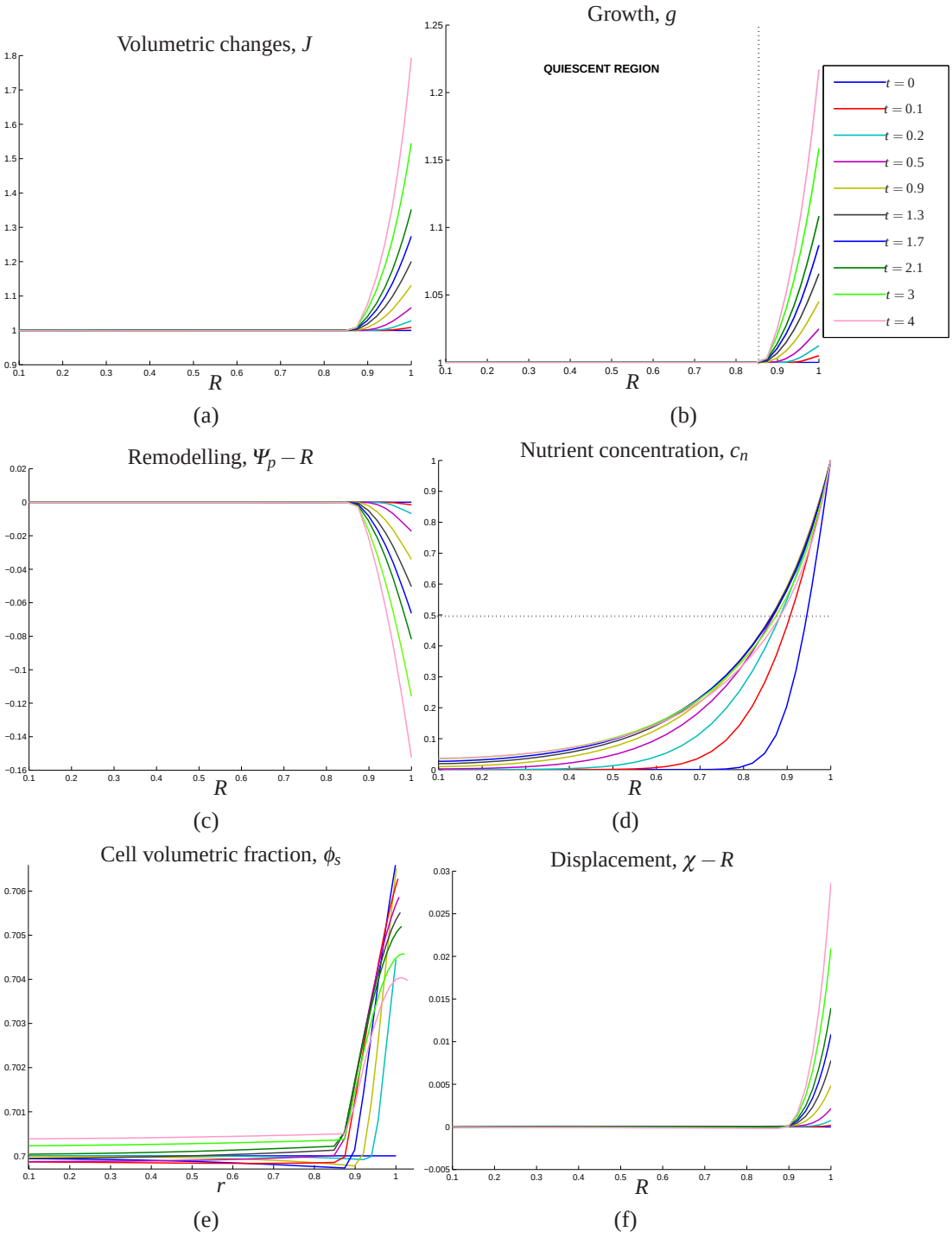

Figure 4.12: Free growth of a spheroid with a calcified core, a quiescent region and an external proliferative ring. The amplitude of the proliferative ring is determined by nutrient diffusion and consumption. Here we set $c_{n0} = 0.5$, $\zeta = 0.5$, $D_n = 0.01$.

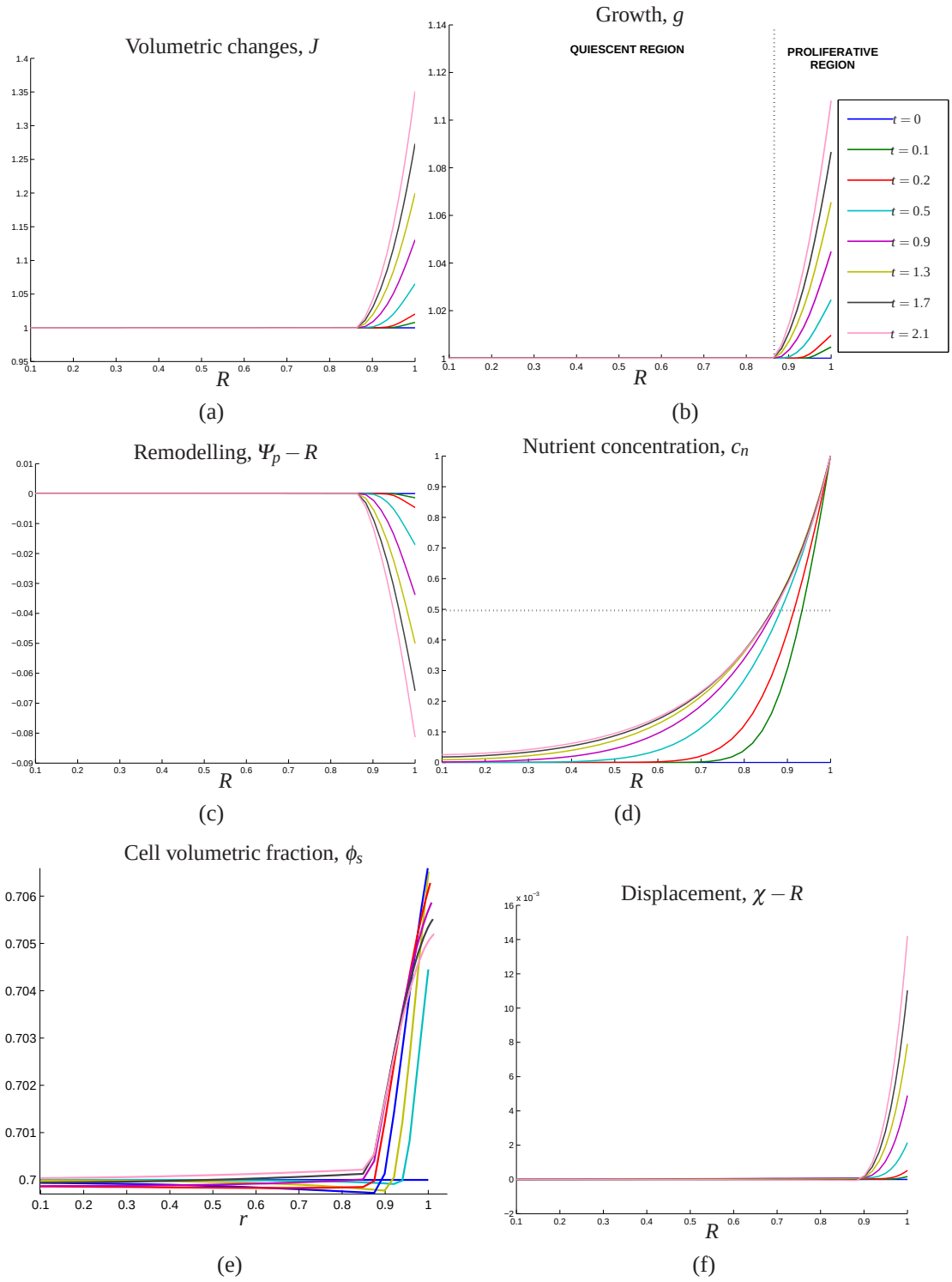

Figure 4.13: Free growth of a spheroid with a liquid core, a quiescent region and an external proliferative ring. The parameters are the same setted in the simulation with a calcified core.

4.3.3 Inclusion of surrounding tissue

Finally, in order to make a step towards a more realistic description of tumor growth in-vivo, we introduce the surrounding healthy tissue.
In order to consider the influence of the surrounding tissue, we have to split our computational 1D-domain into two parts:

- the tumor region, $R_0 \leq R \leq R_T$
- the healthy tissue region $R_T < R \leq 1$

For the moment we will consider that the tumor grows pushing the healthy tissue, without inducing the death of the surrounding cells and we will assume that cell proliferation is balanced by cell death in the healthy region. Therefore in this region we do not have any anomalous proliferation and the Γ_s term in (4.53) is null, whereas cells can proliferate in the central tumor region, for $R_0 \leq R \leq R_T$. We first consider the case in which the growth term depends only on the cell volumetric fraction. Thus, eq. (4.50)-(4.52)-(4.53)-(4.54) hold for $R_0 \leq R \leq R_T$, whereas (4.50)-(4.52)-(4.54), with $\Gamma_s = 0$ and $g(t,R) = 1$ hold in $R_T < R \leq 1$. Being the mathematical model is different in the two domains, the continuity of the dependent variables is no more guaranteed in the whole domain, but only for $R_0 < R < R_T$ and $R_T < R < 1$. In order to solve the problem, we apply the domain decomposition technique [17]. The domain decomposition technique requires to solve the problem separately in the two subdomains and then to transmit the information from one subdomain to the other, imposing additional conditions on the interface, keeping in mind the physical origin of the continuum model used.
We indicate the dependent variables in the tumor domain with the apex (1), whereas the apex (2) refers to quantities in the healthy tissue. Therefore the problem can be formulated as

$$\frac{dJ^{(1)}}{dt} = k_p^{(1)} \frac{{\chi^{(1)}}^2}{R^2} \frac{\partial}{\partial R}(K^{(1)}(\phi_s^{(1)}) \Pi^{R^{(1)}}) + 2k_p^{(1)} \frac{J^{(1)}}{\chi^{(1)}} K^{(1)}(\phi_s^{(1)}) \Pi^{R^{(1)}}, \tag{4.83}$$

$$\Pi^{R^{(1)}} = \frac{1}{J^{(1)}} \left[\frac{\partial}{\partial R}(P_s^{*rR})^{(1)} + \frac{2}{R} \left((P_s^{*rR})^{(1)} - (P_s^{*\vartheta\Theta})^{(1)} \right) \right] \tag{4.84}$$

$$\frac{\partial \chi^{(1)}}{\partial R} = J^{(1)} \frac{R^2}{{\chi^{(1)}}^2} \tag{4.85}$$

$$\frac{dg^{(1)}}{dt} = \frac{1}{3} \Gamma^{(1)} g^{(1)} \tag{4.86}$$

$$\frac{d\Psi_p^{(1)}}{dt} = -\frac{J^{(1)} \phi_s^{(1)}}{6\lambda^{(1)}} \left[\left| \frac{{J^{(1)}}^2 {\Psi_p^{(1)}}^6 - {\chi^{(1)}}^6}{{g^{(1)}}^2 {\Psi_p^{(1)}}^2 {\chi^{(1)}}^4} \right| - \frac{2\tau}{\phi_s^{(1)}} \right]_+ \operatorname{sign}\left({J^{(1)}}^2 {\Psi_p^{(1)}}^6 - {\chi^{(1)}}^6 \right) \Psi_p^{(1)} \tag{4.87}$$

for the tumor domain and

$$\frac{dJ^{(2)}}{dt} = k_p^{(2)}\frac{{\chi^{(2)}}^2}{R^2}\frac{\partial}{\partial R}(K^{(2)}(\phi_s^{(2)})\Pi^{R^{(2)}}) + 2k_p^{(2)}\frac{J^{(2)}}{\chi^{(2)}}K^{(2)}(\phi_s^{(2)})\Pi^{R^{(2)}}, \tag{4.88}$$

$$\Pi^{R^{(2)}} = \frac{1}{J^{(2)}}\left[\frac{\partial}{\partial R}(P_s^{*rR})^{(2)} + \frac{2}{R}\left((P_s^{*rR})^{(2)} - (P_s^{*\vartheta\Theta})^{(2)}\right)\right] \tag{4.89}$$

$$\frac{\partial\chi^{(2)}}{\partial R} = J^{(2)}\frac{R^2}{{\chi^{(2)}}^2} \tag{4.90}$$

$$\frac{d\Psi_p^{(2)}}{dt} = -\frac{J^{(2)}\phi_s^{(2)}}{6\lambda^{(2)}}\left[\left|\frac{{J^{(2)}}^2{\Psi_p^{(2)}}^6 - {\chi^{(2)}}^6}{{\Psi_p^{(2)}}^2{\chi^{(2)}}^4}\right| - \frac{2\tau}{\phi_s^{(2)}}\right]_+ \operatorname{sign}\left({J^{(2)}}^2{\Psi_p^{(2)}}^6 - {\chi^{(2)}}^6\right)\Psi_p^{(2)} \tag{4.91}$$

for the healthy tissue, where $g^{(2)} = 1$.

The material interface between the tumor and the healthy tissue, located at $R = R_T$ moves with tumor cells, with velocity, $\boldsymbol{v}_s$. In particular, we have to guarantee the continuity of displacement, stress and flux in $R = R_T$, i.e.,

$$[\![\chi]\!]|_{R_T} = 0 \tag{4.92}$$

$$[\![p]\!]|_{R_T} = 0 \tag{4.93}$$

$$[\![T_m^{rr}]\!]|_{\chi(R_T)} = 0 \tag{4.94}$$

$$[\![\phi_\ell(\boldsymbol{v}_\ell - \boldsymbol{v}_s)\cdot\mathbf{n}]\!]|_{\chi(R_T)} = 0\,, \tag{4.95}$$

where $[\![(\cdot)]\!]$ indicates the jump of the variable $(\cdot)$ across the boundary located in $R = R_T$. Eq. (4.95) entails that

$$[\![(\mathbb{K}(\phi_s)\mathbb{F}^{-T}\mathrm{Grad}p)\cdot\mathbf{n}]\!]|_{\chi(R_T)} = [\![K(\phi_s)\Pi^R]\!]|_{\chi(R_T)} = 0\,. \tag{4.96}$$

These conditions, coupled with the BCs (4.61)-(4.62)-(4.63)-(4.64) for the necrotic rigid core, fully define the problem in both domains. Indeed boundary conditions are provided at the interior boundary and the outer boundary of the tissue, i.e., on $J^{(1)}(t,R_0)$ and $J^{(2)}(t,R_{out})$, through the conditions (4.62) and (4.64), whereas at the tumor interface, we impose

$$\chi^{(1)}(t,R_T) = \chi^{(2)}(t,R_T) \tag{4.97}$$

$$T_m^{*rr(1)}(t,R_T) = T_m^{*rr(2)}(t,R_T) \tag{4.98}$$

$$K(\phi_s)^{(1)}\Pi^{R^{(1)}}(t,R_T) = K(\phi_s)^{(2)}\Pi^{R^{(2)}}(t,R_T)\,. \tag{4.99}$$

In both domains, the dependent variable χ has a Dirichlet BC prescribed in the first node, which allows to solve (4.85) and (4.90). The value of J in the first node of each domain is determined through a Robin BC, whereas the value of J in the last node is given by a Dirichlet condition. Indeed eq. (4.98) can be seen as a Dirichlet condition on $J^{(1)}(R_T)$, provided that $J^{(2)}(R_T)$ is known, whereas eq. (4.99) gives a Robin BC on $J^{(2)}(R_T)$, given $\Pi^{R^{(1)}}(t,R_T)$. Since the value of $J^{(1)}(R_T)$ and $J^{(2)}(R_T)$ are unknowns, the solution has to be computed via an iterative procedure. At every time step one has to

1. set a guessed value of J at the interface, J_{guess}

2. solve (4.83)-(4.85)-(4.86)-(4.87), with BCs $J^{(1)}(R_T) = J_{guess}$, $\Pi^R(1)(R_0) = 0$ and $\chi^{(1)}(R_0) = R_0$

3. compute the flux through the interface $\mathbf{q}\cdot\mathbf{n} = K^{(1)}\Pi^{(1)}$

4. solve (4.88)-(4.90)-(4.91), with $K^{(2)}\Pi^{(2)} = \mathbf{q}\cdot\mathbf{n}$, $J^{(2)}(R_T)$ given by (4.64) and $\chi^{(2)}(R_T) = \chi^{(1)}(R_T)$

5. compute the stress at the interface, $T^{rr(2)}(R_T)$

6. calculate $J^{(1)}(R_T)$ in order to insure the continuity of stress along the r-axis, $T^{rr(1)}(R_T) = T^{rr(2)}(R_T)$

7. go back to step 2, putting $J_{guess} = (1-\alpha)J^{(1)}(R_T) + \alpha J^{old}_{guess}$ (where α is a relaxation parameter) and iterate until convergence.

Fig. 4.14 reports the results of a spheroid whose growth is limited only by contact inhibition, i.e., $\Gamma_s = (1-\phi_s)$. We remark that in this case, we consider only spheroids with a necrotic core composed by calcified debris.

Finally, we modelled the effects of a nutrient-controlled growth on a spheroid growing inside an healthy tissue. In this case the growth inside the tumor region is controlled by nutrients, whereas in domain 2 nutrients are not considered being the net growth null. Therefore in (4.86) we set

$$\Gamma^{(1)} = (1-\phi_s)(c_n - c_0)_+ .$$

Equations (4.83)-(4.85)-(4.86)-(4.87) are coupled with the dimensionless equation representing the evolution of nutrients

$$\begin{aligned}\dot{c}_n^{(1)} &= \frac{k_p^{(1)}}{\phi_{max}^{(1)}}\frac{{\chi^{(1)}}^2}{J^{(1)}(1-\phi_s^{(1)})R^2}K^{(1)}(\phi_s^{(1)})\Pi^{R^{(1)}}\frac{\partial c_n^{(1)}}{\partial R}+ \\ &+ D_n^{(1)}\frac{1}{J^{(1)}(1-\phi_s^{(1)})R^2}\frac{\partial}{\partial R}\left(\frac{{\chi^{(1)}}^4}{J^{(1)}R^2}\frac{\partial c_n^{(1)}}{\partial R}\right)-\zeta\frac{\phi_s^{(1)}}{(1-\phi_s^{(1)})}c_n^{(1)}, \qquad (4.100)\end{aligned}$$

in domain 1. We assume that vessels are located at the border of the tumor, therefore

$$c_n(t,R_T)=1\,. \qquad (4.101)$$

At the boundary between the tumor and the necrotic calcified core, condition (4.81) holds.
Fig. 4.15 shows the simulations in which the effect of nutrients is considered.

In both cases, the most consistent volumetric changes are experienced in proximity of the interface between the tumor and the healthy tissue (see Fig. 4.14-(a) and 4.15-(a)).

In particular, in the case in which the growth of cells occurs in the whole spheroid (4.14-(b)) because it is limited only by cell volume fraction, $J>1$ in the expanding tumor domain, whereas $J<1$ in the healthy tissue, which is compressed by proliferative cells. Healthy cells are more compressed in proximity of the tumor boundary. Cell volumetric fraction increases in the tumor region due to cell growth, but we can observe also some slight increase, i.e. $\phi_s>\phi_{sn}$, also in the healthy tissue, due to the compression of cells (Fig. 4.14-(c)).
We remark that $J(t,R)$ and $g(t,R)$ are not continuous in the whole domain and that no restriction on ϕ_s are imposed, neither at the interface between the tumor and the healthy tissue nor at the external boundary of the tissue, but the value of ϕ_s is obtained by the continuity of stresses (Fig. 4.14-(f)). Indeed, we observe that pressure (Fig. 4.14-(e)) and stresses (Fig. 4.14-(f)) as well as displacements (Fig. 4.14-(d)) are continuous at the interface, as imposed in the domain decomposition procedure. For the instant of time considered and the parameters used in the simulation, no remodelling is observed inside the spheroid.

With the introduction of nutrients, the model is able to simulate the necrotic core, the quiescent region and the proliferative shell, along with the surrounding healthy tissue (Fig. 4.15).
Nutrients diffuses and are transported by the fluid moving inside the spheroid, from the network

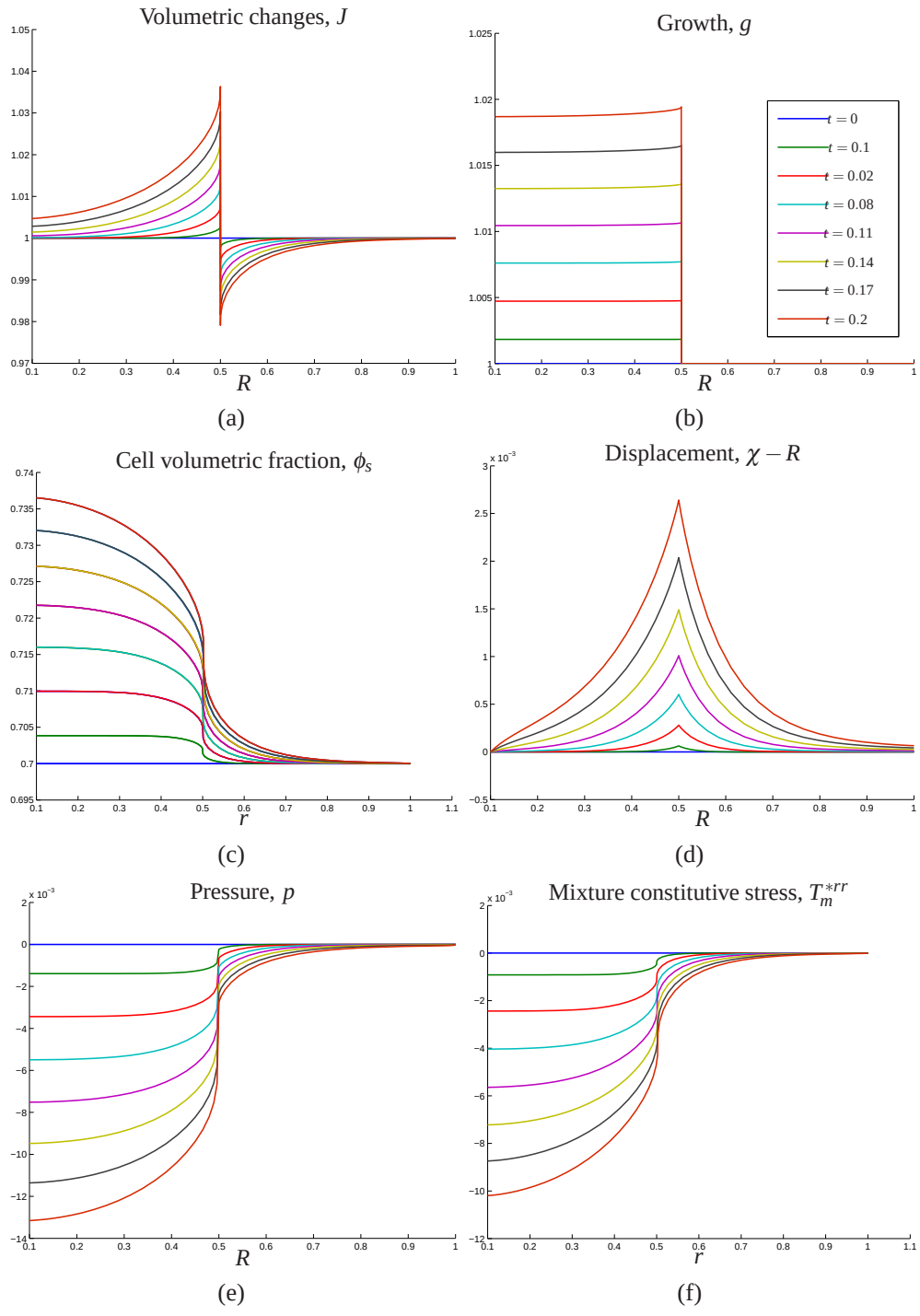

Figure 4.14: Growth of a tumor spheroid with calcified core inside an healthy tissue. The growth of cell here is limited only by contact inhibition, so that cells proliferation is not null in the whole tumor domain.

of vessel in R_T. Only in the region close to the vessel, nutrient concentration is high enough in order to guarantee the proliferation of cells (see Fig. 4.15-(f)). Thus $g > 1$ only in the external portion of the tumor spheroid, which correspond to the proliferative shell (see Fig. 4.15-(b)). In the rest of the tumor $g = 1$ (quiescent region). Volumetric changes occurs at the interface between the tumor and the healthy tissue. As before, where cells proliferate $J > 1$, whereas where cells are compressed $J < 1$. We remark that in this case, not only healthy cells are compressed by proliferative cancer cells, but also quiescent cells in proximity of the proliferative region are compressed (cf. Fig. 4.15-(a) with Fig. 4.14-(a)). Thus ϕ_s increases both in the proliferative region and in the region close to the proliferative one (Fig. 4.15-(e)). From the displacement plot (Fig. 4.15-(d)) it is clear that the proliferative shell expands both toward the healthy tissue and towards the quiescent region. Some remodelling due to extension along the radial directions occurs where cells are proliferating (Fig. 4.15-(c)).

4.4 Discussion

In this Chapter we formulated a mathematical model able to reproduce the growth of a tumor spheroid, described as a biphasic material.
The model is able to take into account anelastic deformations resulting both from growth processes and internal reorganization of cells. At the same time, thanks to the introduction of the liquid phase, the transport of nutrients regulating growth can be properly described. The effect of the surrounding tissue on the overall process can be introduced in this framework, in order to obtain a comprehensive model of tumor growth in-vivo.
Therefore, the model presented is able to simulate different experimental conditions.

In particular, here we show that when an external load is imposed to a quiescent aggregate with liquid necrotic core, if no remodelling occurs, the aggregate is able to bear the load, if it is not too high. On the other hand if remodelling occurs, bonds break and the internal liquid core is filled by cells.
Looking at proliferative aggregate, the introduction of nutrients is fundamental in order to guarantee that no growth occurs at the interior of the spheroid. Depending on nutrients diffusion and transport inside the aggregate, the amplitude of the proliferative region changes.
Finally, the introduction of the surrounding tissue is very important in order to simulate a situation closer to the pathological one, in which tumor cells are surrounded by healthy cells.

However, more simulations should be performed in order to better characterize the effect of

remodelling on the overall process. At the same time, more efficient ways to solve the model can be proposed in order to speed up simulations and to increase the accuracy. From the biological point of view, in order to apply the model to study the real evolution of tumor growth both in vitro and in vivo, simulations need to be fitted to biological experiments, through parameter estimation.

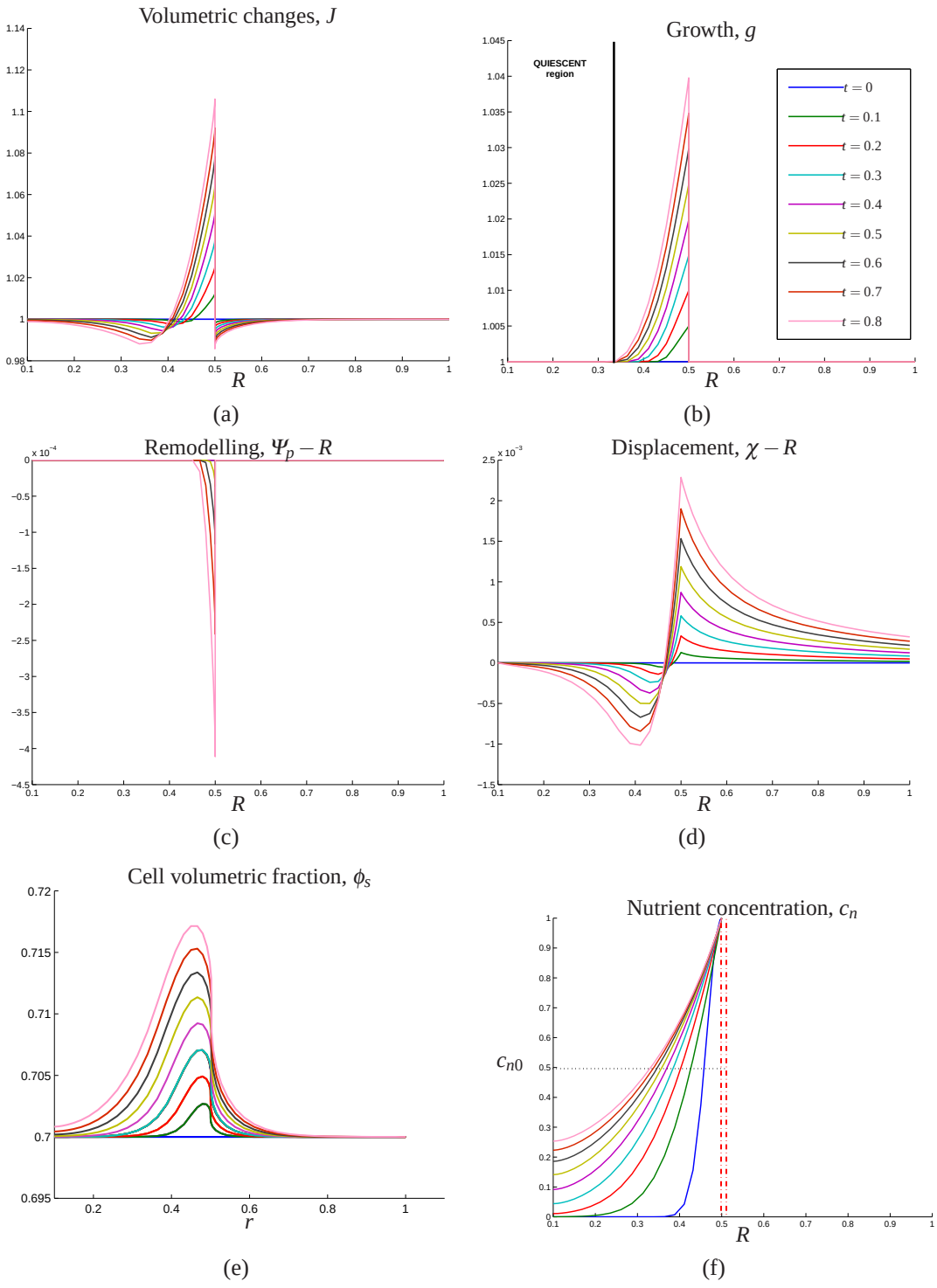

Figure 4.15: Nutrient-controlled growth of a tumor spheroid with calcified core surrounded by tissue. In this case, the proliferation of cells inside the tumor mass is not null only when nutrient concentration is above a fixed threshold (here $c_{n0} = 0.5$).

Chapter 5

Influence of nucleus deformability on cell entry into cylindrical ECM structures

In this Chapter we study the influence of cell mechanical properties on the process of single cell migration inside the surrounding fibrous environment, with the aim to incorporate this information into a macroscopic model describing the movement of an ensemble of cells.
Looking at the process of an ensemble of cell moving in the surrounding tissue, as long as continuum models are concerned, cell movements inside the extracellular matrix (modelled as a porous structure) are described by Darcy's law [103, 117, 155]. In order to properly define this process, it becomes important to determine the permeability of the porous structure in order to quantify its capability of transporting matter. This capability depends on geometrical factors of the porous structure (i.e., geometry of the pore space) but also on mechanical properties of single cells composing the whole cellular aggregate. However, to our knowledge, mechanical properties of cells have always been neglected in the description of cell aggregates migration in porous structures.
We start to tackle this complex problem, looking at the process of a single cell entering inside a cylindrical channel composed of extracellular matrix (ECM) in order to highlight the influence of cell deformability and the capability of cell to generate active forces on the overall process of cell migration.

In Section 5.1 we briefly review the biological experiments done in order to assess cell and cell nucleus mechanical properties. In particular, micropipette experiments and the related classical aspiration criteria are presented in Section 5.2, commenting how they can be applied to the the description of a cell entering an ECM channel, where the force is provided by the active contraction of cell cytoskeleton. Indeed in order to migrate, cells form adhesive sites with the

external environment, though the expression of transmembrane proteins of the integrin family. As a consequence of bond formation, an internal tensile force is generated, through actomyosin contraction. Migrating cells exert traction on the underlying substrate or ECM, where the bond is formed. The active traction force is responsible of cell movement along the ECM fiber and of the deformation of the cell nucleus. Cell traction force is essential for migration in many types of cells, being the way in which cells move along the ECM fiber and deform their nucleus. However, recent findings [96, 124] have highlight that other mechanism of motion, that do not require adhesion, are possible.

A simple mathematical model for active forces, required to accomplish the process, is analysed in Section 3. We focus here only on integrin-dependent migration [160], in which the process of cell adhesion with the substrate is fundamental in order to activate the actomyosin contraction necessary for nucleus deformation and cell movement along the track.

Here, we started from the biological observations that the traction force is related to focal adhesion [156] and we make different hypothesis on the active traction force (acting on the nucleus), generated after the formation of a single bond. In particular, we point out two possible representations of the active force generate after the formation of a single cell-ECM bond (linear vs. constant) and we make some considerations on the extension of the adhesive area (boundedness assumption). The results obtained applying the active force models proposed coupled with the micropipette criteria are presented in Section 5.5.1, showing that they lead to some unrealistic results, because they do not consider the boundedness of cells.

We therefore derive an energetic approach in order to describe the process of cell migration. The mathematical model presented in Section 5.4, based on an energetic approach, is able to describe the deformation of a spherical finite elastic structure (representing the nucleus) into an elongated deformed one, that can move inside the channel. Two different representations for nuclear deformation are implemented (ellipsoidal vs. cigar-shaped). The nucleus is mechanically assimilated either to an elastic membrane (Section 5.4.2) or to an elastic solid (Section 5.4.3). The computational findings are reported and discussed in Section 5.5.2. Results are presented in terms of dimensionless parameters that represent the interplay between active and mechanical properties. With the term active properties we will refer to cell adhesive and contractile skills, which together determine the capability of the cell to actively generate forces.

5.1 Motivations

Cell migration inside extracellular matrix networks plays a critical role in many physiological and pathological processes. For instance, in wound healing the deposition of ECM and the migration of cells through it contribute to repair both epithelial layers and connective tissues, whereas in immune surveillance and inflammation, leukocytes actively migrate towards the site of infection [60]. On the other hand, in pathological conditions, cell migration is involved, for example, in chronic inflammatory diseases and in cancer cell invasion and metastasis formation [129].
Moreover, with the advent of tissue engineering, the process of cell migration is finally exploited in biomedical applications for the regeneration of various tissues, both in vivo and in vitro [28, 163].
From the biological point of view, an increasing number of experimental works has been designed in order to determine cell properties and functions that are involved in the dynamics of motion inside the extracellular microenvironment, and the contribution of this complex network of structural fibrous proteins on the overall process (see, for instance, [76, 97, 127, 160]). In particular, the key factors for cell migration on flat substrates are the dynamic adhesion of cells on it via the expression of adhesive molecules (in particular integrins) and the generation of the force necessary for propulsion by contraction of cytoskeletal elements [61]. These are also the basic “ingredients" in the process of migration inside three-dimensional (3D) porous environments. However, in this case, cells require steering their way throughout steric obstacles. This process can be supported by the production of proteolytic enzymes (e.g. Matrix Metalloproteinases, MMPs) able to degrade matrix components in order to open gaps for cell movement [58, 59, 128, 162]. The migratory and invasive process in three-dimensional environments is generally associated with both significant cell deformation and cytoskeletal force generation while passing through constricted openings of the ECM [127, 160]. The cell body basically consists of the cytoplasm and the nucleus. The cytoplasmatic region is highly adaptable to morphological changes and it can adjust to virtually any shape [62]. On the other hand, the nucleus, is 5-10 times stiffer tha the surrounding cytoskeleton and it can resists to changes in shape [26, 62]. Thus, nucleus deformability is a limiting factor in the process of cell migration [62, 160].
Cell nuclei are exposed are exposed to a variety of mechanical stresses and deformations [93], especially, when the proteolytic machinery is inhibited or during migration inside artificial rigid scaffolds. Cellular and nuclear deformation require substantial reorganization of the cytoskeleton and compression of the keratin envelope of the nuclear region, in order to acquire an elongated configuration, allowing the entire cell to completely squeeze and stretch (see Fig. 5.1(a)). Indeed, it has been observed that inside ECM channels, nucleus shape and keratin network structure

strongly deviate from the normal spatial distribution in the undeformed cell [127].
These biological findings highlight that the geometry of the environment strongly affects cell migratory capabilities and that the deformability of the cell, and in particular of the nucleus, are crucial for cell migration in 3D structures.
The first efforts in describing mechanical behaviour of living cells were aimed at understanding cell response to mechanical stress in the vascular system (e.g., red and white blood cells) [136]. In order to measure the mechanical properties of cells, these must be deformed by a known force or stress and the corresponding deformation must be measured.
In the last years several tests have been developed to this aim. In particular some of the most used mechanical instruments are atomic force microscope (AFM), optical trap (laser tweezers), microcompression method and micropipette suction [83, 84, 101]. Despite the wide range of technological instrument available, the description of mechanical properties of cells is still at a primitive stage and a constitutive theory able to describe cell behaviour is still missing.
Even though the scientific community is becoming aware of the importance of mechanical properties of cells in their process of migration inside porous structures, poor investigations have been carried from the mathematical modelling point of view and mechanical information is generally neglected in the description of cell movements.
Nowadays, if we want to describe the movement of a population of cells inside a region containing extracellular matrix, from the continuum mechanics point of view, Darcy's Law is generally used

$$\boldsymbol{v}_c = -\frac{k(\phi_{ECM})}{\nu(1-\phi_{ECM})}\nabla P\,.$$

Therefore cells are viewed as a liquid continuum with velocity $\boldsymbol{v}_c$ and dynamic viscosity ν that can flow through the static and rigid ECM structure, with porosity $\varepsilon = 1-\phi_{ECM}$ (where ϕ_{ECM} is the volume fraction of the ECM) driven by the gradient of the interstitial pressure, ∇P. The permeability, $k(\phi_{ECM})$, which is a scalar only if the ECM is isotropic (with respect to the flow), is generally a function of porosity (e.g. Kozeny-Carman or Holmes-Mow [85]), but it is often assumed to be a constant [103, 117, 155]. Sometimes the orientation of ECM fibres is considered [32, 33, 109]. However, to our knowledge, mechanical properties of cells are always neglected in the description of cell migration in porous structures. In the Conclusion section we will give some hints on how the model of single cell migration can give some information on the permeability coefficient.
Even when we move towards the length scale at which discrete models are used, the mechanical properties of cells are poorly considered, unless we move towards really detailed models of the

cells. One of them, is the tensegrity model [88, 89], in which loads are supported by struts in compression and cables in tension. Clearly, this description is close to reality, but the high complexity of this model makes it difficult to be used in simulations with a big number of cells and to be up-scaled to the description of macroscopic behaviours.
Some first efforts to include cells mechanical properties inside the description of cell movement on 2D and inside 3D substrates has been done in [133, 134] using Cellular Potts Models (CPM), which allow intuitive representation of cells and their mechanical properties, without requiring too expensive computations.

The introduction of microscopic mechanical properties of cells into continuum macroscopic equations are of fundamental importance in order to make a step towards a more comprehensive representation of cells and tissue. To do that, we study how the nucleus deformability can influence the process of a cell entering a 3D extracellular structure, using a continuum description of the cell nucleus. Even though, in vivo, fibre structures and bundles are arranged into really complex networks of strongly varying local densities [161], that create pores and gaps, we simplify the problem, considering the ECM structured in parallel cylindrical channels composed of fibres and bundles that provide directional guidance cues to cells. This is of course a strong assumption of the far more complex real structure of the extracellular environment, but it can be a good approximation for regular scaffolds used in tissue engineering, for microchannel set-up used to test cell deformability and migration capacity, for packed collagen bundles consisting of multiple aligned fibers, for myofibers and for nerve strands [162]. Moreover it helps to make a first step towards the description of the real phenomenon.

5.2 Mathematical Model of Micropipette Aspiration

A cell can be schematically represented as consisting of two main compartments, the cytoplasm and the nucleus, both surrounded by lipid bilayer membranes. The cytoplasm holds all cell's internal sub-structures (except for the nucleus) immersed in what is called cytosol. The cytosol, which fills much of the volume of the cell, is composed by a complex mixture of cytoskeleton filaments, dissolved macro-molecules and water. The cell cytoskeleton is a network of long filaments interacting with motor proteins, which use the energy deriving from the hydrolysis of ATP

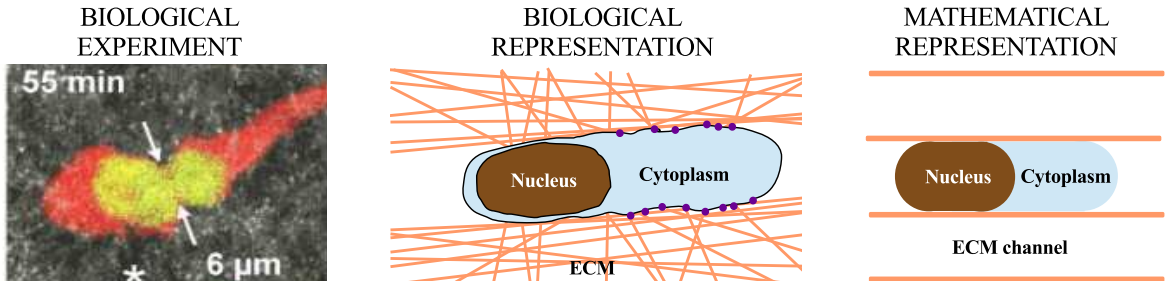

(a) (b) (c)

Figure 5.1: Nuclear deformation during cell migration: biological experiments and schematic representation of the process. (a) Confocal time-lapse snapshot of cell migration inside mid-density collagen (3.3 mg/ml) shows nuclear (in green) and cytoplasmic (in red) shape change (with permission from [62]). (b) Biological sketch of the process of cell migrating through 3D matrix of fibres. Dots denote focal contacts, pink lines stand for ECM fibres (adapted from [62]). (c) Schematic representation of the geometry considered in the model: the cytosol (light blue) can freely move into one of the cylindrical channels composed of ECM bundles, whereas the nucleus stands on the back and progressively deforms in order to enter the channel.

(adenosine triphosphate hydrolysis) to produce active force and deform the network and consequently cell nucleus [81]. The nucleus, however, is less deformable than the cytoplasm [26, 62] and its deformability is mainly regulated by both chromatin structure, and lamin intermediate filaments [62, 66].

When migrating inside a thick 3D fibrous environment made of extracellular matrix, with typical channel size smaller than the cellular diameter, cells need to deform both their cellular body and their nucleus. Being the nucleus the stiffest organelle [26, 62], the nuclear deformability strongly contributes to the migratory efficiency of a cell, whereas it is much easier for the cytosol (and the embedded organelles) to intensively change its shape and to extend into the channel while the nucleus lags behind (see Fig. 5.1(a)).

In order to describe the above complex environment we simplify the geometry considering the motion of a cell in a cylindrical microchannel. In this respect micropipette aspiration is one of the most common way to study the mechanical behavior of living cells and it can help understanding the process of a cell entering inside a channel. In a typical experiment, a cell is aspirated into a small glass tube applying a suction pressure. The leading edge of its surface is tracked with light microscopy. It is observed that, if the suction pressure is sufficiently high, both soft cells (e.g., neutrophils, that normally transmigrate across small pores) and more rigid cells (e.g., chondrocytes and endothelial cells) completely enter pipettes, within a certain range of calibers (see [84] for a review). In both cases the response to an aspiration pressure is similar until a hemispherical

projection is formed inside the pipette. Beyond that point, for cells behaving like a liquid surrounded by a membrane, a further increase in the suction pressure can cause the complete entry of the cell into the channel [48]. On the other hand, when cells behaving like a solid are aspirated, they do not flow into the micropipette when the aspiration length (L_p in Fig. 5.2) exceeds the pipette radius, rather the surface extends until a new equilibrium position is reached [91, 145]. Because of the small suction pressures relative to the osmotic pressure of isotonic saline solution in which cells are positioned, in all these experiments cells usually deform at constant volume [84].

Some simple continuum models, treating the cell either as a liquid droplet surrounded by an elastic cortical shell [164], or as a homogeneous elastic membrane [37], or as a solid [145] have been formulated in order to fit experimental data. Even though these models average out the high heterogeneity in cell composition, they surprisingly make good predictions of the cell deformation response to known suction forces produced by the pipette and they are still used today in the biomechanical community.

In Evans' model [164], cells are described as passive viscous liquid droplet encapsulated by a distinct cortical layer, with cortical tension, T_c. The equilibrium condition comes directly from Laplace law applied to the suction of a cell until a hemispherical projection is formed inside the pipette. Calling L_p the aspired length and R_p the pipette radius, the critical suction pressure drop ΔP_c is obtained for $L_p/R_p = 1$, when the following relation holds

$$\frac{\Delta P_c R_p}{T_c} = 2\left(1 - \frac{R_p}{R_c}\right) \tag{5.1}$$

where R_c is the radius of the cell outside the pipette (when $L_p/R_p = 1$).

This relation can be easily obtained [46], observing that if no friction exists between the pipette wall and the cell membrane, then the membrane tension is uniform over the cell surface and the Laplace Law can be applied, both to the cap of the projection inside the pipette and to the spherical portion outside the pipette (see Fig. 5.2),

$$P_{cell} - P_0 = \frac{2T_c}{R_c}, \tag{5.2}$$

$$P_{cell} - P_p = \frac{2T_c}{R_p}. \tag{5.3}$$

where P_{cell}, P_p, P_0 are respectively the pressure inside the cell, in the pipette and outside the cell. Eliminating the cell cell pressure from (5.2), it is possible to obtain (5.1), defining $\Delta P_c = P_0 - P_p$. The cortical tension creates a threshold pressure drop below which the cell will not enter the

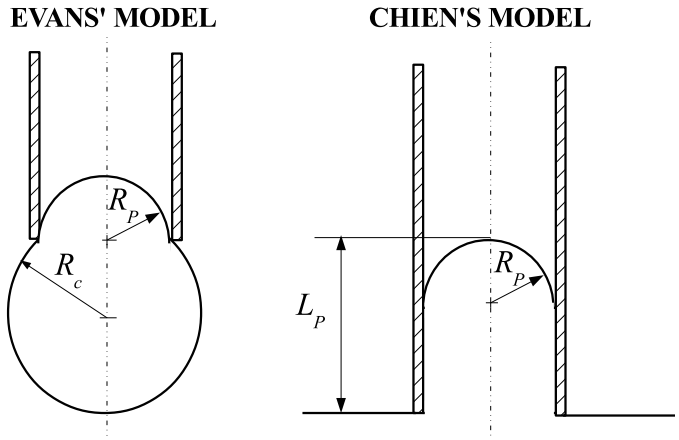

Figure 5.2: Schematic representation of the geometry used to derive Evans' and Chien's equation.

pipette and above which cells can flow into it. Moreover Evans et al. [164] observed that the rate at which a cell flows into a pipette is almost constant, with only a small nonlinearity over time until the cell completely enters the pipette.
When the cell has totally entered the pipette all the microscopic "ruffles" and "folds" have been pulled smooth. However they observed that there exists a lower limit below which cells cannot enter the pipette, that for the specific cells used in their biological experiments (granulocytes) corresponds to a caliber of 2.7μm [47, 48].

For what concerns cells behaving like a solid, many studies have been done on human red blood cell. The biconcave shape of this anucleate cells comes from their membrane. The deformation of such cells has been studied under a constant area assumption [37, 45, 46, 157], to derive the suction pressure ΔP needed to aspire a portion of cell of length L_p inside a cylindrical channel of radius R_p (see Fig. 5.2), which is given by the following relation (that holds for $L_p > R_p$)

$$\frac{\Delta P R_p}{\gamma} = 2\frac{L_p}{R_p} - 1 + \log\left(2\frac{L_p}{R_p}\right), \tag{5.4}$$

where γ is the shear elastic modulus of the membrane.
Eq. (5.4) is obtained as the stationary condition of the dynamic relation

$$\frac{\Delta P R_p}{\gamma} = 2\frac{L_p}{R_p} - 1 + \log\left(2\frac{L_p}{R_p}\right) + 4\frac{\eta}{\gamma}\frac{\dot{L}_p}{R_p}, \tag{5.5}$$

where a viscoelastic stress-strain relation is assumed for the membrane. Therefore in (5.5) γ represents the elastic properties of the membrane, whereas η is its viscosity.
It has been experimentally observed that, when $\frac{L_p}{R_p} > 1$, the relation between $\frac{\Delta P R_p}{\gamma}$ and $\frac{L_p}{R_p}$ is almost linear, with a slope equal to 2.45. This consideration leads to the well known Chien's relation [37]

$$\frac{\Delta P R_p}{\gamma} = 2.45 \frac{L_p}{R_p} \quad \left(\frac{L_p}{R_p} > 1 \right). \tag{5.6}$$

Finally, Theret et al. [145] studied the entry into a channel of a cell treated as a homogeneous elastic solid, with Young's modulus equal to E. Their analysis for an infinite, homogeneous half-space drawn into a micropipette can be summarized by the following relation

$$\frac{\Delta P}{E} = \frac{2\pi}{3} \Phi \frac{L_p}{R_p}, \tag{5.7}$$

where Φ is a factor linking the external and internal radius of the pipette, which is assumed to be equal to 2.1 in many works [84].

The process of a cell entering a glass tube has some similarities with the process of a cell entering a channel composed of ECM fibres. Of course in the biological movement of cell migration across matrix channels, we do not have any aspiring pressure, but what makes the cell deform and enter the channel is the capability of the cell to form adhesive bonds with the ECM and translate this "adhesive information" into the contraction of the internal cytoskeletal structure, that actively pull the cell and deform the nucleus. This migratory mechanism is strictly linked to cell capability to establish bonds (integrin-dependent migration) and it is the preferential way of moving of those kind of cells which are highly adhesive (e.g. smooth muscle cells and fibroblasts). Recent works [96, 124] show that integrin-independent mechanisms of motion are possible in confined environment. However in this paper we will refer only to adhesion-driven motion. Therefore, trying to apply these classical model to the description of a cell entering a channel, the ΔP in eq. (5.4)-(5.7) should be related to the active force generated through cytoskeleton contraction as a consequence of cell-ECM bond formation, $\pi R_p^2 \Delta P \approx F^Z_{ad-trac}$, where $F^Z_{ad-trac}$ is the component on the long axis of the cell. We will give more details about this force in Section 5.3
Moreover, we can assume that only the nucleus of the cell behaves as an elastic material, applying eq. (5.4)-(5.7) to the deformation of the cellular nucleus only. Even though results obtained under these hypothesis seem promising (see Section 5.5.1), we have to be aware that we are pushing the criteria away from their limit of validity. In fact, Chien's and Theret's models have been

obtained assuming, respectively, an infinite 2D membrane and a 3D half space aspired inside a pipette. Moreover, the pipettes used in Chien's biological experiments ranged from $0.3\,\mu$m up to $0.8\,\mu$m and the volumes aspired into the pipettes were always $< 5\%$ of the cell volume [37]. At the same time, even though the pipettes used by Theret et al. [145] were bigger (with an internal diameter ranging between 2 μm and 3 μm), the portion of the cell aspired was two-to-four times R_p. Therefore both validations stay away from the complete entry of the cell. Actually, all these studies were designed in order to determine the mechanical properties of cells in the first stages of the deformation and they better apply to problems in which deformations are quite small (normally L_p/R_p up to 5 [145]), whereas micropipette experiments account also for the total aspiration of the cell.

5.3 Active forces in integrin-dependent motion

To describe cell entry into ECM channels, a fundamental step is the definition of active forces, that lead to cell deformation and migration inside the channel.
Cell migration into 3D environments consists of different steps, cyclically reiterated by the cell [62]. In integrin-mediated locomotion, first the cell polarizes, assembling actin at the cell front into filaments which push the plasma membrane outward and form protrusions. Then these protrusions interact with the ECM, building strong adhesion points with the substrate, through the expression and activation of transmembrane receptors of the integrin family [81, 96]. At this stage, cell eventually activate the proteolytic degradation and realignment of ECM fibers, forming tracks for cell motion. Then actomyosin contracts the actin networks, generating local traction and the force necessary for nucleus deformation and cell movement along the track [62]. For most cell types, adhesion and migration is so intimately linked that regulation of substrate adhesiveness is the main factor guiding the locomotion (haptokinetic). In this type of cells, the internal cytoskeleton is strictly linked to the ECM, through transmembrane receptors (primarily integrins), on one side, and to the cellular nucleus, on the other side, through the lamin intermediate filaments forming a part of the nuclear envelope [62, 66]. This adhesiveness largely determines cell shape and nuclear deformation [160]. Moreover, it has been experimentally observed [156] that the traction force generated through myosin contraction depends on the focal adhesion area of the cell.
Even though recent works [96, 124] shows that, at least for some kind of cells (e.g. leukocytes and some metastatic tumor cells), the migration in confined environment is sustained by integrin-independent mechanisms, here, we consider only adhesion-dependent movements, in which the

deformation of the nucleus during cell movement is driven by the generation of an active force in the cytoskeleton meshwork, as a consequence of bond formation. We do not give an explicit model of active force generation, but we postulate different constitutive forms for the force exerted after the formation of a bond.

Then, the active force related to adhesive processes can be, thought as the resultant of all forces generated by cytoskeleton contraction after single cell-ECM bond formation on the surface of adhesion. Cell-matrix adhesion is mainly mediated by integrins on the cell surface that connect ECM to the cytoskeleton. The adhesion can be modulated by the density of expressed and activated integrins, $\rho_b = N_{integrin}/S_{cell-ECM}$ (where $N_{integrin}$ is the number of integrins over the surface of contact between the cell and the ECM, $S_{cell-ECM}$), and by the density of substratum ligands (ECM adhesive sites), here represented by the ECM surface ratio, $\alpha_{ECM} = S_{ECM}/S_{channel}$. We will assume that the cytoplasm can easily penetrate inside the channel, acquiring an elongated shape with an hemispherical cap (see Fig. 5.3), so that the traction will cause on one hand the displacement of the cytosolic region (keeping the same shape with a tip that will be modelled as a spherical cap) and on the other hand the advancement of the nucleus, that, being at the entrance of the microchannel, will deform to penetrate into it. We assume that the length of the region on which bonds are formed is constant in time and it corresponds to the portion of the cell in contact with the channel wall and in front of the nucleus. Therefore, referring to Fig. 5.3 and defining $S = \left\{(X,Y,Z) : X^2+Y^2 = R_p^2, \bar{Z}_{low}(t) < Z < \bar{Z}_{up}(t)\right\}$ the surface for which ECM-bonds are expressed, we can say that the length for which bonds are formed, $L_b = \bar{Z}_{up}(t) - \bar{Z}_{low}(t)$ remains constant in time during cell deformation.

Accepting that the density of bonds on cell surface, ρ_b, and the portion of the channel wall composed of ECM adhesive sites, α_{ECM}, do not depend on time, the total integrin-dependent active force is

$$\mathbf{F}_{active} = \int_S \rho_b(\mathbf{X})\alpha_{ECM}(\mathbf{X})\mathbf{F}_{bond}(\mathbf{X})dS, \tag{5.8}$$

where $\mathbf{F}_{bond}(\mathbf{X})$ is the traction force exerted on the nucleus through cytoskeleton contraction, as a consequence of bond formation. Though ρ_b and α_{ECM} may be generally functions of the space, in the homogeneous case, eq. (5.8) simplifies into

$$\mathbf{F}_{active} = \rho_b\alpha_{ECM}\int_S \mathbf{F}_{bond}(\mathbf{X})dS. \tag{5.9}$$

Considering only the Z-component of this force, we have

$$F^Z_{active} = 2\pi\rho_b\alpha_{ECM}R_p\int_0^{L_b} F^Z_{bond}dZ. \tag{5.10}$$

The total active force pulling the cell is therefore a function of the radius of the pipette, the density of bonds ρ_b, the surface fraction of the channel composed of extracellular matrix, α_{ECM}, and the integral of the single bond forces over the contact surface. In particular, under the assumption that the bonds are formed only on the portion of the cell in front of the nucleus in contact with the channel (see Fig. 5.3), we have

$$L_b = L^0_{cell} - R_p - L^0_n \tag{5.11}$$

where L^0_{cell} is the initial length of the cell inside the channel (which corresponds to the length of the region filled by the deformed cytoplasm) and L^0_n is the portion of the nucleus that can enter the pipette without any deformation. To obtain (5.11), we have assumed that the cytoplasm forms an hemispherical projection inside the channel. Imposing the conservation of the volume for the cytosol (before and after the entrance in the channel) we have

$$\frac{4}{3}\pi(R_c^3 - R_n^3) = \pi R_p^2 \left(L^0_{cell} - R_p\right) - \left(L^0_n\right)^2 \left(R_n - \frac{1}{3}L^0_n\right) + \frac{2}{3}\pi R_p^3, \tag{5.12}$$

where R_p is the radius of the cylindrical channel, R_n the radius of the nucleus and R_c the radius of the spherical cell. Thus, the left-hand-side of (5.12) represents the volume of the cytosol in the spherical cell, whereas the left-hand-side stands for the volume of the cytosol totally inside the channel (see Fig. 5.3). Eq. (5.12) leads to

$$L^0_{cell} = R_p \left[\frac{4}{3}\frac{R_c^3 - R_n^3}{R_p^3} + \frac{1}{3} + \frac{1}{R_p^3}\left(L^0_n\right)^2 \left(R_n - \frac{1}{3}L^0_n\right)\right] ,, \tag{5.13}$$

where $L^0_n = R_n - \sqrt{R_n^2 - R_p^2}$. Once that a proper function representing bond forces is provided, the description of active force is accomplished. In particular, we will consider the following simple forms of F^Z_{bond}, which is the Z-component of the force transmitted to the nucleus when a bond is established.

Linear bond force

We assume that, as a consequence of a single bond formation, a force proportional to the distance between the nucleus and the site in which the bond is formed is exerted on the nucleus, through

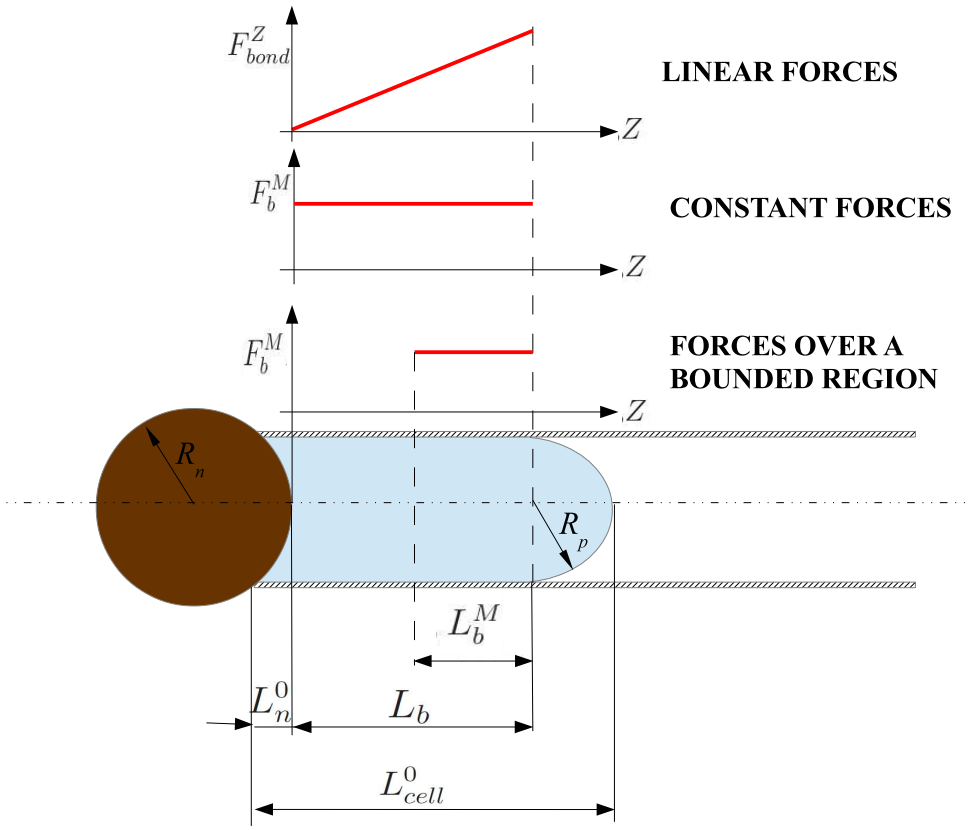

Figure 5.3: Schematic representation of the length of the adhesive region and of the types of forces considered.

actomyosin contraction, i.e.,

$$F^Z_{bond} = k_b Z\,, \tag{5.14}$$

where k_b is the elastic constant of a virtual spring linking the bond site to the nucleus Substituting (5.14) into (5.9) we obtain

$$F^Z_{active} = \pi R_p \rho_b \alpha_{ECM} k_b L_b^2\,. \tag{5.15}$$

This relation takes into account the biological observation that the biggest traction forces are expressed at the apical portion of the cell [8, 39, 99, 112]. However, it has the disadvantage that there is no upper limit to the force that can be exerted, which is not true. This may become important when the size of the channel is very small causing long cell extensions (see Section 5.5.2 and 5.5.2).

Constant bond force

We assume that the traction force acting on the nucleus, generated by a single bond activation, is constant, $F^Z_{bond} = F^M_b$, which implies that

$$F^Z_{active} = 2\pi R_p \rho_b \alpha_{ECM} F^M_b L_b \,. \tag{5.16}$$

This relation represents the fact that there is a mean force that can be exerted and a maximum traction force above which bonds break [15, 110, 112, 139] and thus the cytoskeleton no more contracts, because the cell looses adhesion to the substrate.

Force over a bounded region

We consider the case in which cells are able to form bonds only over a certain area of the contact region, e.g. the apical portion of the deformed cell. Therefore, taking a constant force assumption, we have $F^Z_{bond} = F^M_b \chi_{L^M_b}(Z)$, where L^M_b represents the length of the maximal area of contact for which bonds are formed (adhesive region) and

$$\chi_{L^M_b}(Z) = \begin{cases} 1 & \text{if} \quad (L_b - L^M_b)_+ < Z < L_b \\ 0 & \text{if} \quad 0 \le Z \le (L_b - L^M_b)_+ \vee Z \ge L_b \end{cases}$$

where $(\cdot)_+$ stands for the positive part of $(\cdot)$, to take into account that for protrusions smaller than L^M_b all the cytoplasmic membrane participates in the adhesion process. Therefore, the total active force is represented by the following relation

$$F^Z_{active} = 2\pi R_p \rho_b \alpha_{ECM} F^M_b L^*_b \,, \tag{5.17}$$

where $L^*_b = \min\left\{L_b, L^M_b\right\}$. This relation prevents active forces to growth dramatically for $R_p \to 0$ and it represents the fact that for very small pipette radius the cell cannot extend his protrusion over too large areas.

A similar relation would be achieved if the interval over Z is substituted by several disconnected intervals. In this case χ is the sum of the sizes of the intervals. Also the localization of these "adhesive sites" does not affect the final result, provided that the overall length is the same.

Analogously, it is possible to use the linear force assumption, taking $F^Z_{bond} = k_b Z \chi_{L^M_{b,el}}(Z)$, that leads to

$$F^Z_{active} = 2\pi R_p \rho_b \alpha_{ECM} k_b L^*_{b,el} \left(L_b - \frac{1}{2} L^*_{b,el}\right) , \tag{5.18}$$

where $L^*_{b,el} = \min\left\{L_b, L^M_{b,el}\right\}$. However with a proper re-definition of $L^M_{b,el}$ as a function of L^M_b, eq. (5.18) leads to the same results as (5.17), when $L_b > L^M_b$.

5.4 Energy Balance Models

In order to overcome the limits of models present in literature, in which the finite size of the cell is not considered, we tackle the problem of a cell entering into a cylindrical structure by an energetic approach. Always working under constant volume assumption, we develop two models to analyse the total energy required to deform the initial spherical nucleus (see Fig. 5.4-(a)) into a nucleus that is totally inside a cylindrical channel. As observed in [156] the central nucleus takes an elongated shape when the cell is forced to cross channels of different radius. Experimental evidence [92, 156] suggests that, when the cell elongates, the initially spherical nucleus significantly deforms, orienting with respect to the cell long-axis direction. Cell elongation is associated with the formation on either sides of the nucleus of actin bundles parallel to the channel wall, that are responsible of the nuclear deformation and help maintaining the deformed configuration. Indeed, during cell elongation, the tension in actin filaments grows and generates compressive forces acting laterally on both sides of the nucleus [156].
The shape of the deformed cell, when it is totally inside the channel can be approximated either The shape of the deformed cell can be approximated either

- by a prolate ellipsoid [156, 162], with smaller axis R_p (see Fig. 5.4(b)) or
- by a cigar-like shape (see Fig. 5.4(c)), with cylindrical central region of radius R_p and hemispherical caps [62].

Both morphologies have been observed in vivo and in vitro experiments [26, 62, 156]. Of course the morphology acquired in vivo by the nuclear shape, especially if the geometry of the channel is not so regular, can be more complex.

Concerning the calculation of the energy required to deform the nucleus, we consider the two cases in which:

- all the energy is spent to increase the membrane area of the nucleus, whereas the material inside is treated as an inviscid liquid that freely rearranges according the geometry of the channel (see subsection 5.4.2);

- all the energy is spent to deform the internal solid nucleus of the cell, treated as an elastic material (see subsection 5.4.3).

Of course, these hypotheses can be considered extreme cases and intermediate situations should be studied (i.e., energy of membrane plus bulk energy). We recall once again that, in both cases, the cytoplasm can freely move inside the channel.

The energy required to deform the initial spherical shape will then be compared to the work done by active forces, described in section 5.3, to make the cell advance in the microchannel. We will give more details on the work done by adhesive-mediated traction in subsection 5.4.1.

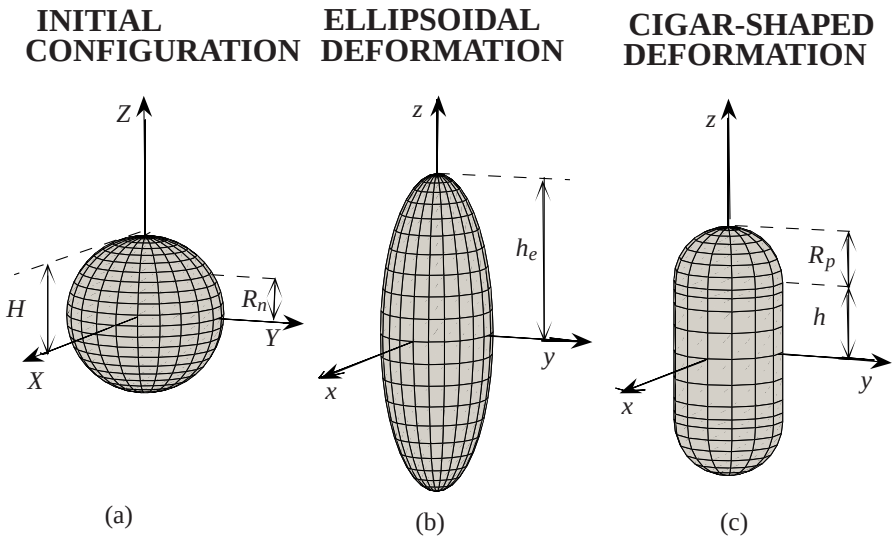

Figure 5.4: Deformation from (a) the initial spherical configuration to the final one, considering (b) an ellipsoidal and (c) a cigar-shaped deformed nucleus

5.4.1 Active force work

The work required to have the cell completely inside the channel should be provided by active forces. We can express this work as

$$\mathscr{W}_{active} = F^{Z}_{active} \Delta L \,, \tag{5.19}$$

where ΔL is the total displacement of the cell nucleus inside the channel, and F^Z_{active} is the resultant directed along the Z-axis of all bond forces developed after cell-ECM bond formation, described in Section 5.3. In the following we will assume that $\Delta L = L_n^{fin} - L_n^0$, where L_n^{fin} is the final length of the nucleus when it is totally inside the channel and it varies depending on the representation chosen for the deformation of the nucleus. Indeed, for the ellipsoidal shape we have that $L^{fin}_{n,ellips} = 2h_e$, where

$$h_e = \frac{R_n^3}{R_p^2} \tag{5.20}$$

is the longer semi-axis of the prolate ellipsoid that preserves the initial volume, whereas considering the cigar nucleus $L^{fin}_{n,cigar} = 2(h + R_p)$, where h can be easily computed, assuming the conservation of the nuclear volume

$$h = \frac{2}{3} R_p \frac{R_n^3 - R_p^3}{R_p^3}. \tag{5.21}$$

On the other hand L_n^0 is the initial length of the nucleus that can freely enter the channel without any deformation and it is given by eq. (5.13).

5.4.2 Membrane Energy Model

As a first example, we consider the case in which the volume of the nucleus is treated as a liquid droplet surrounded by an elastic shell. The energy required to increase the surface area, $\mathscr{W}^S_{tot}$, can be approximated by the following relation [46]

$$\mathscr{W}^S_{tot} = \lambda (\Delta S)^2 \tag{5.22}$$

where ΔS is the increase in the surface area of the cell passing from an initial spherical shape to its final conformation.

More complex formulae can be applied to describe the energy required to increase shell area, such as those proposed in [82, 137, 150, 151], however eq. (5.22) can be used to make easy analytical computations and it has been shown to well represent cell behaviour at least in a certain range of deformations [46].

The increment in the surface area, ΔS, can be easily calculated, assuming that the volume is preserved and computing the new surface area of the deformed nucleus. Using the ellipsoidal

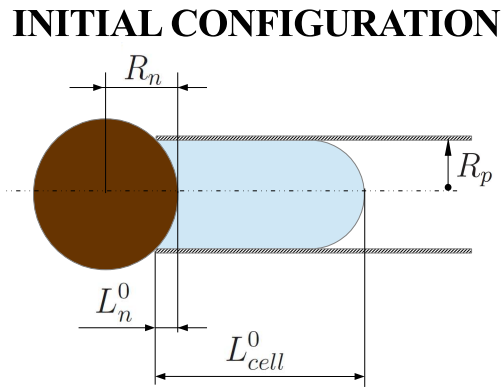

(a)

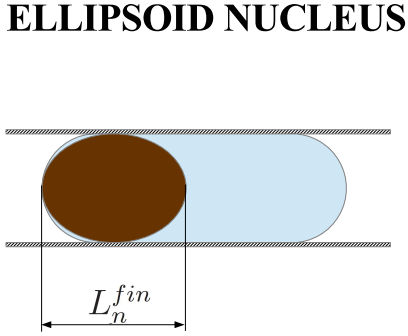

(b)

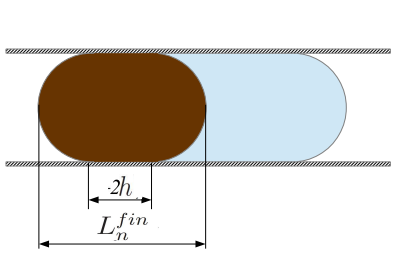

(c)

Figure 5.5: Schematic representation of cell displacement and nucleus deformation.

deformation assumption, the increment in the surface area is given by

$$\begin{aligned}\Delta S_{ellips} &= S_{ellips} - S_{sphere} = 2\pi R_p^2 \left(1 + \frac{h_e}{R_p e}\sin^{-1}(e)\right) - 4\pi R_n^2 = \\ &= 4\pi R_n^2 \left[\frac{1}{2}\tilde{R}_p^2 \left(1 + \frac{1}{\tilde{R}_p^3\sqrt{1-\tilde{R}_p^6}}\sin^{-1}\left(\sqrt{1-\tilde{R}_p^6}\right)\right) - 1\right]. \end{aligned} \tag{5.23}$$

where $e = \sqrt{1 - \dfrac{R_p^2}{h_e^2}}$ and h_e is given by (5.20) and all distances have been conveniently scaled with the nucleus radius, defining the dimensionless quantity $\tilde{R}_p = R_p/R_n$. Therefore $\dfrac{\mathscr{W}^S}{(4\pi R_n^2)^2}$ is a function of $\tilde{R}_p$. Actually, in the following all the quantities with a tilde represent the corresponding distance scaled with R_n.
On the other hand, using the cigar-shaped deformation hypothesis we have

$$\begin{aligned}\Delta S_{cigar} &= S_{cigar} - S_{sphere} = 4\pi R_p^2 + 2\pi R_p(2h) - 4\pi R_n^2 = \\ &= 4\pi R_n^2 \left(\frac{1}{3}\tilde{R}_p^2 + \frac{2}{3\tilde{R}_p} - 1\right) \end{aligned} \tag{5.24}$$

where the height of the cylindrical portion of the cigar, $2h$, is given by (5.21).

5.4.3 Solid Nucleus Model

To compute the energy required to deform the nucleus of the cell treated as a simple solid, we have to assume a proper constitutive equation, representing the response of the material to deformations, and calculate the deformation gradient, $\mathbb{F}$.
Nowadays, a representation of the Cauchy stress tensor for cellular components is still under investigation. For sake of simplicity, we assume an incompressible neo-Hookean constitutive law for the nucleus of the cell, therefore the elastic stored energy per unit volume is given by

$$\mathscr{W}^V = \frac{\mu}{2}\left[\mathrm{tr}(\overline{\mathbb{C}}) - 3\right], \tag{5.25}$$

where $\overline{\mathbb{C}} = J^{-2/3}\mathbb{F}^T\mathbb{F}$, $J = \det(\mathbb{F})$ and μ is the shear modulus of the nucleus [20]. We observe that being the nucleus incompressible, $J = 1$.
In both the cases in which the deformed nucleus has an ellipsoidal shape and the case in which

it takes a cigar-shaped conformation, we assume that parallel planes perpendicular to the axis of the cylinder in the undeformed configuration, $Z = \mathrm{c}$, are mapped into parallel planes in the final deformed geometry, $z = \mathrm{c}'$, with $\mathrm{c},\mathrm{c}' \in \mathbb{R}$. Using the standard notation of continuum mechanics, capital letters refers to quantities in the initial configuration whereas lower cases refer to quantities in the deformed configuration. Therefore with (X,Y,Z) we indicate the cartesian coordinates in the undeformed configuration and with (x,y,z) the corresponding cartesian spatial coordinates. Sometimes cylindrical coordinates are used, denoted with (ρ,Φ,Z) and with (r,ϕ,z) in the undeformed and deformed configuration, respectively. The calculation shown in the following are based on merely geometrical considerations.

5.4.3.1 Ellipsoidal deformed nucleus

The deformation of a sphere in a prolate ellipsoid with the same volume is simply given by a uniaxial deformation

$$\mathbb{F} = \mathrm{diag}\left\{\frac{R_p}{R_n},\frac{R_p}{R_n},\frac{R_n^2}{R_p^2}\right\} = \mathrm{diag}\left\{\tilde{R}_p,\tilde{R}_p,\frac{1}{\tilde{R}_p^2}\right\}. \tag{5.26}$$

For the particular $\mathbb{F}$ given by (5.26), we can rewrite eq. (5.25) as

$$\mathscr{W}^V = \frac{\mu}{2}\left(2\tilde{R}_p^2 + \frac{1}{\tilde{R}_p^4} - 3\right), \tag{5.27}$$

which integrated over the total volume of the initial sphere gives the total energy required to pass from the initial to the final configuration, i.e.,

$$\mathscr{W}^V_{tot} = \int_{V_r} \mathscr{W}^V dV = \frac{2}{3}\mu\pi R_n^3\left(2\tilde{R}_p^2 + \frac{1}{\tilde{R}_p^4} - 3\right), \tag{5.28}$$

where V_r is the volume of the cell in the reference configuration.
Eq. (5.28) links the elastic energy of deformation to the mechanical properties of the nucleus, μ, the morphological properties of the nucleus R_n and the radius of the channel, R_p.

5.4.3.2 Cigar-shaped nucleus

Another slightly different possibility is that the solid sphere (representing the nucleus), deforms into a cigar-shaped nucleus, composed of a cylinder of radius $\tilde{R}_p$ and height $\tilde{h} = \dfrac{h}{R_n}$ and two

hemispherical caps (see Fig. 5.4-(c)).
In order to obtain the deformation gradient we subdivide the initial spherical nucleus into three regions: the central one, of scaled height $\tilde{H} = \dfrac{H}{R_n}$, is mapped into the cylindrical portion of dimensionless radius $\tilde{R}_p$ and scaled height $\tilde{h}$ defined by (5.21), whereas the upper and lower poles of the nucleus are mapped into the apical and basal hemispheres of the cigar-shaped nucleus.
Therefore the deformation gradient can be described as

$$\mathbb{F} = \begin{cases} \mathbb{F}_{N-pole} & \text{for} \quad \tilde{H} \leq Z \leq 1\,; \\ \mathbb{F}_c & \text{for} \quad -\tilde{H} < Z < \tilde{H}\,; \\ \mathbb{F}_{S-pole} & \text{for} \quad -1 \leq Z \leq -\tilde{H}\,. \end{cases} \tag{5.29}$$

Assuming symmetry, we can restrict our analysis to the upper half of the nucleus, i.e., $0 \leq Z \leq 1$. To derive the deformation gradient of the central region, $\mathbb{F}_c$, we consider a reference slice of height ε and volume $V_r(\varepsilon)$, which is mapped into the final volume $V_f(\varepsilon)$ (see Fig. 5.6). Assuming that the volume is conserved and passing to the infinitesimal limit, we obtain

$$1 = \lim_{\varepsilon\to 0} \frac{V_f(\varepsilon)}{V_r(\varepsilon)} = \lim_{\varepsilon\to 0} \frac{\pi\tilde{R}_p^2\,(z(Z+\varepsilon)-z(Z))}{\pi\,(1-Z^2)\,\varepsilon - \pi\left(Z\varepsilon^2 + \dfrac{\varepsilon^3}{3}\right)} = \frac{\tilde{R}_p^2}{1-Z^2}\frac{\partial z}{\partial Z}\,, \tag{5.30}$$

which leads to

$$\frac{\partial z}{\partial Z} = \frac{1-Z^2}{\tilde{R}_p^2}\,. \tag{5.31}$$

We assume that all the slices of the reference “barrel" remain parallel while deforming, i.e., $x = x(X,Y,Z)$, $y = y(X,Y,Z)$ and $z = z(Z)$. We then consider an internal volume of the reference spherical region of height ε and volume $V_r(\varepsilon) = \pi\rho^2\varepsilon + o(\varepsilon)$ (for $\varepsilon \to 0$), which is deformed into a volume $V_f = \pi r^2\,(z(Z+\varepsilon)-z(Z))$. Keeping in mind the relation (5.31) we obtain

$$r = \frac{\rho}{\sqrt{1-Z^2}}\tilde{R}_p\,. \tag{5.32}$$

Assuming that $\phi = \Phi$, for the central volume of the sphere, one then has the following matrix representation of the deformation gradient in normalized bases of cylindrical coordinates (for

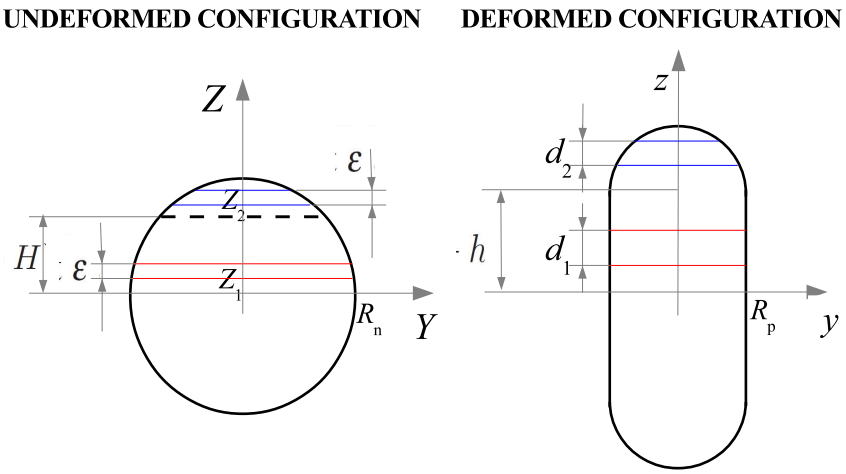

Figure 5.6: To derive the deformation gradient of a sphere deforming in a cigar, we consider a reference slice of height ε in the central region of the sphere which is mapped into a cylinder of radius R_p and height $d_1 = z(Z_1+\varepsilon) - z(Z_1)$ and a slice of height ε in the upper portion of the sphere which is mapped in the spherical segment of height $d_2 = z(Z_2+\varepsilon) - z(Z_2)$.

both configurations)

$$\mathbb{F}_c = \begin{bmatrix} \dfrac{\tilde{R}_p}{\sqrt{1-Z^2}} & 0 & \dfrac{\tilde{R}_p Z\rho}{(1-Z^2)^{3/2}} \\ 0 & \dfrac{\tilde{R}_p}{\sqrt{1-Z^2}} & 0 \\ 0 & 0 & \dfrac{1-Z^2}{\tilde{R}_p^2} \end{bmatrix}. \tag{5.33}$$

To fulfil the problem of describing the total deformation gradient, we have to consider the upper and lower portion of the sphere, which are mapped into the two hemispheres of the cigar-shaped nucleus. Considering a slice in these region (see Fig. 5.6), in analogy with the central region case, we have the following zZ-component of the deformation gradient

$$\frac{\partial z}{\partial Z} = \frac{1-Z^2}{\tilde{R}_p^2 - (z-\tilde{h})^2}, \tag{5.34}$$

where $z = z(Z)$. An explicit relation between z and Z will be derived in the following. We remark that (5.34) holds for $\tilde{H} \leq Z \leq 1$ and $\tilde{h} \leq z \leq \tilde{h} + \tilde{R}_p$.
Also in this case, assuming that undeformed parallel planes remain parallel in the deformed

configuration, we obtain

$$r = \frac{\sqrt{\tilde{R}_p^2 - (z-\tilde{h})^2}}{\sqrt{1-Z^2}}\rho\,, \tag{5.35}$$

that coupled with the hypothesis $\phi = \Phi$ gives the following deformation gradient in cylindrical coordinates, for the upper pole of the sphere

$$\mathbb{F}_{N-pole} = \begin{bmatrix} \dfrac{\sqrt{\tilde{R}_p^2 - (z-\tilde{h})^2}}{\sqrt{1-Z^2}} & 0 & \Gamma(Z)\rho \\ 0 & \dfrac{\sqrt{\tilde{R}_p^2 - (z-\tilde{h})^2}}{\sqrt{1-Z^2}} & 0 \\ 0 & 0 & \dfrac{1-Z^2}{\tilde{R}_p^2 - (z-\tilde{h})^2}\,, \end{bmatrix} \tag{5.36}$$

where

$$\Gamma(Z) = \left(\frac{Z\sqrt{\tilde{R}_p^2 - (z-\tilde{h})^2}}{(1-Z^2)^{3/2}} - \frac{(z-\tilde{h})\sqrt{1-Z^2}}{\left(\tilde{R}_p^2 - (z-\tilde{h})^2\right)^{3/2}} \right).$$

We observe that, for the particular form of $\mathbb{F}_c$ and $\mathbb{F}_{N-pole}$ the deformation gradient, $\mathbb{F}$ is continuous. Indeed $\mathbb{F}_{N-pole}(Z=\tilde{H}) = \mathbb{F}_c(Z=\tilde{H})$, being $z(H) = \tilde{h}$.
In order to express all the quantities in the material frame, we integrate eq. (5.34), which gives the implicit relation between the eulerian coordinate z and the corresponding material one, Z

$$(z-\tilde{h})^3 - 3\tilde{R}_p^2(z-\tilde{h}) + 3(Z-\tilde{H}) - (Z^3 - \tilde{H}^3) = 0\,. \tag{5.37}$$

Eq. (5.37) is a cubic function in z and it has three real solutions, but only the root

$$z(Z) = \tilde{h} + 2\tilde{R}_p \cos\left[\frac{1}{3}\cos^{-1}\left(\frac{(Z-\tilde{H})(Z^2+\tilde{H}^2+Z\tilde{H}-3)}{2\tilde{R}_p^3}\right) + \frac{4}{3}\pi\right] \tag{5.38}$$

is acceptable, in order to satisfy the condition $h < z < h + R_p$, and can be substituted in (5.36) to have the deformation gradient in terms of the Lagrangian coordinates.
Eq. (5.37) can also be used to derive $\tilde{H}$, given $\tilde{h}$. Indeed substituting $z = \tilde{h} + \tilde{R}_p$, with $\tilde{h}$ given by eq. (5.21), and $Z = 1$ in (5.37) we have a cubic function of the new unknown $\tilde{H}$, which gives the only acceptable solution

$$\tilde{H} = 2\cos\left[\frac{1}{3}\cos^{-1}\left(\tilde{R}_p^3 - 1\right) + \frac{4}{3}\pi\right]. \tag{5.39}$$

As for the ellipsoidal deformation, once that the deformation gradient is known it is possible to compute the total energy required to pass from the initial configuration to the final configuration. Still assuming an incompressible neo-Hookean constitutive law (5.25) for the nucleus of the cell, the elastic energy stored per unit volume in the central portion of the sphere is

$$\mathscr{W}_c^V = \frac{\mu}{2}\left[2\frac{\tilde{R}_p^2}{1-Z^2} + \frac{\tilde{R}_p^2 Z^2 \rho^2}{\left(1-Z^2\right)^3} + \frac{\left(1-Z^2\right)^2}{\tilde{R}_p^4} - 3\right], \tag{5.40}$$

whereas the energy for the upper and lower poles of the spheres is

$$\begin{aligned}\mathscr{W}_{N-pole}^V = \mathscr{W}_{S-pole}^V &= \frac{\mu}{2}\left[2\frac{\tilde{R}_p^2 - (z-\tilde{h})^2}{1-Z^2}\right] + \\ &+ \frac{\mu}{2}\left[\left(\frac{Z\sqrt{\tilde{R}_p^2-(z-\tilde{h})^2}}{\left(1-Z^2\right)^{3/2}} + \frac{(z-\tilde{h})\sqrt{1-Z^2}}{\left(\tilde{R}_p^2-(z-\tilde{h})^2\right)^{3/2}}\right)^2 \rho^2\right] + \\ &+ \frac{\mu}{2}\left[\frac{\left(1-Z^2\right)^2}{\left(\tilde{R}_p^2-(z-\tilde{h})^2\right)^2} - 3\right],\end{aligned} \tag{5.41}$$

where $z = z(Z)$ is given by (5.38). To obtain the total energy required to pass from the initial spherical configuration to the cell totally deformed inside the channel, we have to integrate over the corresponding domains in the undeformed body, i.e.,

$$\begin{aligned}\mathscr{W}_{tot}^V &= \int_{V_r^c} \mathscr{W}_c^V dV + \int_{V_r^{N-pole}} \mathscr{W}_{N-pole}^V dV + \int_{V_r^{S-pole}} \mathscr{W}_{S-pole}^V dV = \\ &= 2\left(\int_{V_r^{c+}} \mathscr{W}^V dV + \int_{V_r^{N-pole}} \mathscr{W}_{N-pole}^V dV\right),\end{aligned} \tag{5.42}$$

where V_r^c is the volume of the central zone in the reference configuration, V_r^{N-pole} and V_r^{S-pole} are the volume of the north and south pole of the sphere and V_r^{c+} is the volume of the upper-half central part of the sphere, i.e.,

$$V_r^{c+} = \left\{(\rho,\Theta,Z) \in \mathbb{R}^3 : 0 \le \rho \le \sqrt{1-Z^2}, 0 < \Theta \le 2\pi, 0 \le Z < \tilde{H}\right\},$$

whereas

$$V_r^{N-pole} = \left\{(\rho,\Theta,Z) \in \mathbb{R}^3 : 0 \le \rho \le \sqrt{1-Z^2}, 0 < \Theta \le 2\pi, \tilde{H} \le Z \le 1\right\},$$

The previous integral can be easily computed in the central region

$$\begin{aligned} \mathscr{W}_c^{tot} &= \mu\pi R_n^3 \left[2\tilde{R}_p^2\tilde{H} + \frac{1}{2}\tilde{R}_p^2 \left(\tanh^{-1}\tilde{H} - \tilde{H} \right) \right] + \\ &+ \mu\pi R_n^3 \left[\frac{1}{\tilde{R}_p^4} \left(\tilde{H} - \tilde{H}^3 + \frac{3}{5}\tilde{H}^5 - \frac{1}{7}\tilde{H}^7 \right) - 3\left(\tilde{H} - \frac{\tilde{H}^3}{3} \right) \right] . \end{aligned} \tag{5.43}$$

We observe that since $\tilde{H}$ is a function of $\tilde{R}_p$ through (5.39), $\dfrac{\mathscr{W}_c^{tot}}{\mu R_n^3}$ is a function of $\tilde{R}_p$.
On the other hand, for what concerns $\int_{V_r^{N-pole}} \mathscr{W}_{N-pole}^V dV$, using the fact that the domain of integration is normal with respect to the XY-plane, we can express the triple integral as a simple integral

$$\begin{aligned} \mathscr{W}_{N-pole}^{tot} &= \frac{\pi\mu}{2} R_n^3 \left[2\int_{\tilde{H}}^1 \left[\tilde{R}_p^2 - (z-\tilde{h})^2 \right] dZ \right] + \\ &+ \frac{\pi\mu}{2} R_n^3 \left[\frac{1}{2}\int_{\tilde{H}}^1 \left(\frac{Z\sqrt{\tilde{R}_p^2 - (z-\tilde{h})^2}}{(1-Z^2)^{3/2}} + \frac{(z-\tilde{h})\sqrt{1-Z^2}}{\left(\tilde{R}_p^2 - (z-\tilde{h})^2\right)^{3/2}} \right)^2 \left(1-Z^2\right)^2 dZ \right] + \\ &+ \frac{\pi\mu}{2} R_n^3 \left[\int_{\tilde{H}}^1 \frac{\left(1-Z^2\right)^3}{\left(\tilde{R}_p^2 - (z-\tilde{h})^2\right)^2} dZ - 2 + \left(2+\tilde{R}_p^2\right)\sqrt{1-\tilde{R}_p^2} \right] , \end{aligned} \tag{5.44}$$

that needs to be evaluated numerically, in order to obtain an estimate of the total energy required to deform the nucleus.

5.5 Results

In subsection 5.5.1 we present results obtained adapting models from the literature for micropipette aspiration of a cell through a cylindrical channel, conscious that we are pushing Chien's and Theret's criteria far from their limit of validity. In subsections 5.5.2 we show results obtained with our energetic approach, both under the elastic membrane and the elastic solid nucleus assumptions.

5.5.1 Micropipette models applied to cell migration inside channels

We consider here the case in which nucleus entry obeys the classical relations (5.4) or (5.7), deforming the initial spherical nucleus into a cigar-like shape, with the assumption that L_p in (5.4)

and (5.7) represents the length of the deformed nucleus, i.e. $L_p = L_{n,cigar}^{fin} = 2(h+R_p)$ with h given by eq. (5.21). We define the critical pressure as the value of ΔP for which $L_p = L_{n,cigar}^{fin}$ and we assume that a proper representation for ΔP in eq. (5.4) and (5.7) is $\frac{F_{active}^Z}{\pi R_p^2}$, where F_{active}^Z is the Z-component of the active traction force given either by eq. (5.15) or (5.16) or (5.17). Then, for a pressure above the critical one, the cell moves inside the pipette. This way we obtain the yield value of the ratio between mechanical and active parameters that a cell should have in order to enter the channel, depending on the geometrical properties (i.e. R_n, R_c and R_p).
The inequalities that should be satisfied in each case are summarized in Table 5.1, as a function of the diameter ratio $\tilde{R}_p = \frac{R_p}{R_n}$. On the left-hand-side of each relation we have characteristic parameters representing the ratio between cell active properties and nuclear mechanical properties of cell nucleus. In particular, we identify

$$G_\gamma^k = \frac{\rho_b \alpha_{ECM} k_b R_n^2}{\gamma}, \quad G_\gamma^F = \frac{\rho_b \alpha_{ECM} F_b^M R_n}{\gamma},$$

$$G_E^k = \frac{\rho_b \alpha_{ECM} k_b R_n}{E}, \quad G_E^F = \frac{\rho_b \alpha_{ECM} F_b^M}{E}.$$

Table 5.1: Entry criteria

Model	Linear Force	Constant (bounded) Force
Chien	$G_\gamma^k \geq \frac{2\frac{\tilde{L}_p}{\tilde{R}_p} - 1 + \log\left(2\frac{\tilde{L}_p}{\tilde{R}_p}\right)}{\tilde{L}_b^2}$	$G_\gamma^F \geq \frac{2\frac{\tilde{L}_p}{\tilde{R}_p} - 1 + \log\left(2\frac{\tilde{L}_p}{\tilde{R}_p}\right)}{2\tilde{L}_b^{(*)}}$
Theret	$G_E^k \geq \frac{2\pi}{3}\Phi\frac{\tilde{L}_p}{\tilde{L}_b^2}$	$G_E^F \geq \frac{2\pi}{3}\Phi\frac{\tilde{L}_p}{2\tilde{L}_b^{(*)}}$

On the right-hand-side of each relation we have the critical value of the characteristic number (indicated with $\overline{G}_i^j$, with with $i = \{\gamma, E\}$, $j = \{k, F\}$), which is a function of the diameter ratio, being

$$\tilde{L}_p = \frac{L_p}{R_n} = \frac{2}{3}\tilde{R}_p\left[1 + 2\left(\frac{1}{\tilde{R}_p}\right)^3\right],$$

$$\tilde{L}_b = \frac{L_b}{R_n} = \tilde{R}_p\left[\frac{4}{3}\left(\frac{\tilde{R}_c}{\tilde{R}_p}\right)^3 - \frac{1}{\tilde{R}_p^3} + \frac{1}{3} + \frac{\left(\tilde{L}_n^0\right)^2}{\tilde{R}_p^3}\left(1 - \frac{1}{3}\tilde{L}_n^0\right)\right]$$

with $\tilde{L}_n^0 = 1 - \sqrt{1-\tilde{R}_p^2}$ and $\tilde{R}_c = R_c/R_n$. The notation $\tilde{L}_b^{(*)}$ means that the value of $\tilde{L}_b = L_b/R_n$ is

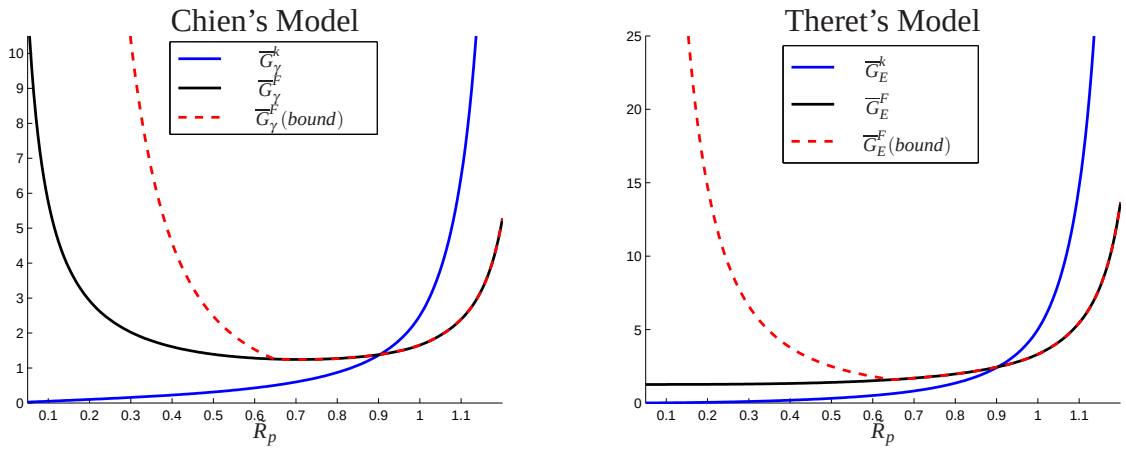

(a) (b)

Figure 5.7: Critical value of the characteristic numbers obtained applying (a) Chien's model and (b) Theret's model, under the assumption of a linear force (blue), a constant force (black) or a constant force over a bounded region (red dashed). We remark that Φ is a factor linking the external and internal radius of the pipette, which is assumed to be equal to 2.1 in many works [84].

used in the case of the constant force assumption whereas the value of $\tilde{L}_b^* = L_b^*/R_n$ is considered for the bounded adhesive region case.

The critical characteristic numbers are plotted in Fig. 5.7 as a function of the diameter ratio of the channel. The graphs represent the minimum value that each dimensionless parameter should assume in order to have the cell totally inside the channel, according to Chien's criterion (Fig. 5.7(a)) and Theret's one (Fig. 5.7(b)). Results obtained with the linearized Chien's equation (5.6) are comparable with the ones obtained with the more complex formula (5.4). In Fig. 5.7 the dashed line represents results obtained using constant forces over a bounded domain (where we set $\tilde{L}_b^M = 5$). It is possible to see that for big $\tilde{R}_p$, $\overline{G}_\gamma^F$ and $\overline{G}_E^F$ are obviously not influenced by the assumption on the boundedness of the contact region in which integrins are expressed (i.e., the red-dashed curve and the black-solid one overlap). Indeed, it exists an $\tilde{R}_p^*$ such that $L_b^* = L_b$ for $\tilde{R}_p \geq \tilde{R}_p^*$, whereas $L_b^* = L_b^M$ for $\tilde{R}_p < \tilde{R}_p^*$. Therefore the work of active forces is influenced by the boundedness assumption only for $\tilde{R}_p < \tilde{R}_p^*$.

For instance, Fig. 5.8 explains how these graphs can be interpreted (for the particular case of Chien model): the bar charts below the graph represent the range of $\tilde{R}_p$ for which a cell characterized by a given G_γ^k or a given G_γ^F can enter the channel.

In the figure, 'cell 1' (orange) is characterized by higher G_γ^k or G_γ^F than 'cell 2' (violet). This means that 'cell 1' is either a softer cell (i.e., small γ) or a cell that is able to establish

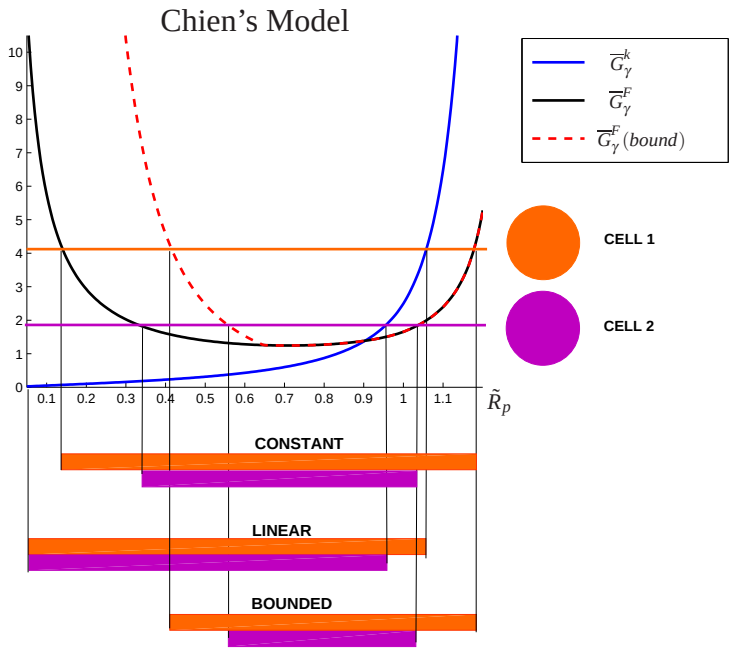

Figure 5.8: Interpretation of the results: bar charts represents the range for which a cell, with a given G_γ^k or G_γ^F can enter the channel, for the different hypothesis of bond forces.

a higher number (i.e., higher $\rho_b \alpha_{ECM}$) of stronger (i.e., bigger k_b or F_b^M) adhesive bonds. In any case, the range for which 'cell 1' can enter the pipette is bigger than for 'cell 2' (orange bars vs. violet bars), according to what we expect from biological observations. Moreover, using the constant force assumption it is possible to see that the range for which cells can enter the pipette is bounded both from below and from above. On the other hand, using the linear force assumption, we do not have any inferior limit, in contrast with biological observation. This contradictory result is due to the hypothesis used in the representation of forces. Indeed in this case the more the cytoplasm of the cell spread inside the channel (small $\tilde{R}_p$), the more bonds can pull the nucleus inside. In particular, even though the force required to deform the nucleus grows as $\tilde{R}_p^{-3}$, as $\tilde{R}_p \to 0$, the bond force raises faster, since $\tilde{L}_b^2 = \mathscr{O}\left(\tilde{R}_p^{-4}\right)$. On the other hand, when a constant force assumption is used, for small $\tilde{R}_p$, the length for which bonds are formed augments $\left(\tilde{L}_b = \mathscr{O}\left(\tilde{R}_p^{-2}\right) \text{for} \tilde{R}_p \to 0\right)$. Thus, the total active force increases, but it is not sufficient to compensate the greater deformation required to the nucleus, which goes like $\tilde{R}_p^{-3} \text{for} \tilde{R}_p \to 0$. Conversely, introducing the boundedness assumption on L_b, the active force is limited.

In particular, we have that for $\tilde{R}_p \to 0$, $\overline{G}_F^\gamma$ goes like $\tilde{R}_p^{-\alpha}$ (with $\alpha = 1$ for unbounded L_b and $\alpha = 3$ when the adhesive region is limited) and $\overline{G}_K^\gamma$ grows linearly.

On the other hand, when the radius of the pipette is very big, the entry of the cell into the channel is limited due to the decrease in the contact area between the cell and the channel wall, where adhesive bonds are formed. It is likely that, in this case, the bond force is not equal to the maximum applicable force. Thus, a linear force can better describe the physiological behaviour. Therefore, a good choice for the bond force relation could be a ramp force on a bounded adhesive region, which is also the most conservative case.

In Theret's model it is possible to see that, for $\tilde{R}_p \to 0$, $\overline{G}_E^k = \mathscr{O}\left(\tilde{R}_p^2\right)$ and $\overline{G}_E^F = \mathscr{O}(1)$ when the constant force assumption with unbounded adhesive region is implemented. Thus neither the constant force assumption nor the linear force one can account for the inferior limit in pipette calibers. Only enforcing the boundedness of the adhesive region, the capability of cells to enter very small channels is prevented.
Both Chien's and Theret's models, with the assumption of constant bond forces over a bounded region, provide evidence for a biphasic cell migratory behavior that reveals most optimal migration at channel sizes at nuclear and subnuclear diameters and diminishes at gaps greatly bigger or smaller than the cell nucleus diameter.
However, even though results obtained applying the classical models above seem promising, especially when adhesion is active on a bounded domain, they cannot account for the finite boundaries of the nucleus. Indeed Chien's model refers to an infinite 2D membrane, whereas Theret's one was derived for a 3D half space aspired inside a pipette, only for a small portion. Therefore these criteria cannot be applied to describe the total entry of the cell into a pipette. The consequence of this assumption are evident in Fig. 5.7, where, for $\tilde{R}_p = 1$, the force needed to deform the nucleus does not vanish.

Table 5.2: Behaviours of $\overline{G}_\gamma$ and $\overline{G}_E$ for $\tilde{R}_p \to 0$

Model	Linear Force	Constant Force	Bounded adhesive region
Chien	$\overline{G}_\gamma^k = \mathscr{O}\left(\tilde{R}_p\right)$	$\overline{G}_\gamma^F = \mathscr{O}\left(\frac{1}{\tilde{R}_p}\right)$	$\overline{G}_\gamma^F = \mathscr{O}\left(\frac{1}{\tilde{R}_p^3}\right)$
Theret	$\overline{G}_E^k = \mathscr{O}\left(\tilde{R}_p^2\right)$	$\overline{G}_E^F = \mathscr{O}(1)$	$\overline{G}_E^F = \mathscr{O}\left(\frac{1}{\tilde{R}_p^2}\right)$

5.5.2 Energetic models

In this subsection we present the results obtained with the energy balance model, presented in Section 5.4. When the elastic membrane model (subsection 5.4.2) is used, we consider that the cell can enter the channel if

$$\mathscr{W}_{active} \geq \mathscr{W}_{tot}^{S}, \tag{5.45}$$

where $\mathscr{W}_{active}$ is given by (5.19) and $\mathscr{W}_{tot}^{S}$ has the form presented in eq. (5.22). On the other hand, when the elastic solid nucleus model (subsection 5.4.3) is applied, the nucleus can enter the cylindrical structure if

$$\mathscr{W}_{active} \geq \mathscr{W}_{tot}^{V}, \tag{5.46}$$

where $\mathscr{W}_{tot}^{V}$ has the form presented in either eq. (5.28) for the ellipsoidal deformation or eq. (5.42) for the cigar-shaped one. Depending on the hypothesis used to describe the adhesive-dependent active force (linear vs. constant vs. bounded) and the geometry chosen for the deformed nucleus (ellipsoid vs. cigar-shaped), inequalities (5.45) and (5.46) lead to the results presented in Table 5.3, with respect to the diameter ratio $\tilde{R}_p$. As before, $\tilde{L}_b^{(*)}$ stands either for $\tilde{L}_b = L_b/R_n$ in the case of the constant force assumption or $\tilde{L}_b^* = L_b^*/R_n$ for the bounded adhesive region case. By scaling all distances with R_n and writing all material parameters on the right-hand-side, we identify four dimensionless numbers that represent the ratio between active properties and nuclear mechanical parameters. In particular, for the elastic membrane model we name

$$G_\lambda^k = \frac{\rho_b \alpha_{ECM} k_b}{\lambda} \qquad \text{and} \qquad G_\lambda^F = \frac{\rho_b \alpha_{ECM} F_b^M / R_n}{\lambda},$$

whereas, when the elastic nucleus model is used, we introduce

$$G_\mu^k = \frac{\rho_b \alpha_{ECM} k_b R_n}{\mu} \qquad \text{and} \qquad G_\mu^F = \frac{\rho_b \alpha_{ECM} F_b^M}{\mu}.$$

At the numerator we have all the parameters that characterize bonds forces (densities of bonds, surface ratio of ECM, elasticity or maximum executable force) whereas at the denominator we have the parameter describing the mechanical properties of the cell nucleus (λ in the case of an elastic membrane, μ in the case of an elastic solid).
In Table 5.3,

$$\mathscr{I}(\tilde{R}_p) = \frac{\mathscr{W}_c^{tot}}{\frac{4}{3}\pi\mu R_n^3} + 2\frac{\mathscr{W}_{N-pole}^{tot}}{\frac{4}{3}\pi\mu R_n^3},$$

Table 5.3: Energy based criteria

Model		Linear Force	Constant (bounded) Force
Elastic membrane	Ellipsoid	$G^k_\lambda \geq 16\pi \dfrac{\left[\frac{1}{2}\tilde{R}_p^2\left(1+\frac{\sin^{-1}(e)}{\tilde{R}_p^3 e}\right)-1\right]^2}{\tilde{R}_p\tilde{L}_b^2\Delta\tilde{L}_{ellips}}$	$G^F_\lambda \geq 8\pi \dfrac{\left[\frac{1}{2}\tilde{R}_p^2\left(1+\frac{\sin^{-1}(e)}{\tilde{R}_p^3 e}\right)-1\right]^2}{\tilde{R}_p\tilde{L}_b^{(*)}\Delta\tilde{L}_{ellips}}$
	Cigar	$G^k_\lambda \geq 16\pi \dfrac{\left(\frac{1}{3}\tilde{R}_p^2+\frac{2}{3\tilde{R}_p}-1\right)^2}{\tilde{R}_p\tilde{L}_b^2\Delta\tilde{L}_{cigar}}$	$G^F_\lambda \geq 8\pi \dfrac{\left(\frac{1}{3}\tilde{R}_p^2+\frac{2}{3\tilde{R}_p}-1\right)^2}{\tilde{R}_p\tilde{L}_b^{(*)}\Delta\tilde{L}_{cigar}}$
Elastic nucleus	Ellipsoid	$G^k_\mu \geq \frac{2}{3}\dfrac{2\tilde{R}_p^2+\frac{1}{\tilde{R}_p^4}-3}{\tilde{R}_p\tilde{L}_b^2\Delta\tilde{L}_{ellips}}$	$G^F_\mu \geq \frac{2}{3}\dfrac{2\tilde{R}_p^2+\frac{1}{\tilde{R}_p^4}-3}{\tilde{R}_p\tilde{L}_b^{(*)}\Delta\tilde{L}_{ellips}}$
	Cigar	$G^k_\mu \geq \frac{4}{3}\dfrac{\mathscr{I}(\tilde{R}_p)}{\tilde{R}_p\tilde{L}_b^2\Delta\tilde{L}_{cigar}}$	$G^F_\mu \geq \frac{2}{3}\dfrac{\mathscr{I}(\tilde{R}_p)}{\tilde{R}_p\tilde{L}_b^{(*)}\Delta\tilde{L}_{cigar}}$

where $\mathscr{W}_c^{tot}$ and $\mathscr{W}_{N-pole}^{tot}$ are defined in (5.43) and (5.44) respectively. The right-hand-side of each relation identifies the critical value of the characteristic number and it is indicated in the following with $\overline{G}_i^j$ (with $i=\{\lambda,\mu\}$, $j=\{k,F\}$). Therefore, once a proper model is chosen, for every diameter ratio $\tilde{R}_p$, it is possible to define the value of $\overline{G}_i^j$, above which a cell, with a nucleus of dimension R_n can enter a channel of radius $\tilde{R}_p R_n$.
We remark that this model, taking into account the finiteness of the nuclear dimensions, is valid only for $\tilde{R}_p \leq 1$. Indeed, when $\tilde{R}_p \to 1$, the elastic energy required to deform the nucleus is almost null, whereas, allowing the cytoskeleton to enter the channel, the work done by active forces is not null and it can easily pull the nucleus inside the channel.

Fig. 5.9 shows the value of (a) $\overline{G}^k_\lambda$ in the case of linear forces, (b) $\overline{G}^F_\lambda$ in the case of constant forces and (c) $\overline{G}^F_\lambda$ for constant force over a bounded adhesive region, above which the cell can enter a channel of scaled radius $\tilde{R}_p$, when the elastic membrane model is used. On the other hand, Fig. 5.10 reports the ratios (a) $\overline{G}^k_\mu$ and (b-c) $\overline{G}^F_\mu$ obtained applying the elastic nucleus model, under the same hypothesis of active traction forces.
Both in Fig. 5.9 and 5.10 solid lines represent ellipsoidal deformations, whereas dashed lines stand for cigar-shaped final configurations. In any case, the assumption on the geometry acquired by the deformed nucleus does not affect the qualitative behaviour of the solutions.
We remark that in Fig. 5.9-(a) and (b), for very small radius, the energy required to increase the area of the nuclear membrane increases but the active force increases faster and therefore, for $\tilde{R}_p \to 0$, the critical G^k_λ and G^F_λ go to zero when the unbounded L_b is used, giving rise to the contradiction that cell can enter pipettes of very small diameters.

Indeed, when the radius of the channel is small, the length of the cytoplasm inside it grows considerably, leading, in the linear case, to active traction forces that are unrealistically high. In particular, for $\tilde{R}_p \to 0$, we have that the energy required to deform the elastic membrane increases as $\tilde{R}_p^{-2}$, given that the increase in the surface area grows as $\tilde{R}_p^{-1}$. On the other hand, at the denominator of G_i^j, we have $\Delta L = \mathscr{O}\left(\tilde{R}_p^{-2}\right)$ and $L_b = \mathscr{O}\left(\tilde{R}_p^{-2}\right)$. Therefore, when the linear force assumption is used, $\overline{G}_\lambda^k = \mathscr{O}\left(\tilde{R}_p^3\right)$ for $\tilde{R}_p \to 0$, whereas, when the bond force is assumed constant, $\overline{G}_\lambda^F = \mathscr{O}\left(\tilde{R}_p\right)$ for $\tilde{R}_p \to 0$. In order to avoid the unphysical result, we more realistically assume that bonds are formed on the surface of the channel until the maximum length, L_b^M is reached. Restricting the extent for which bonds are formed to a certain length ($L_b = L_b^*$), will dramatically limit the work done by active forces for very small $\tilde{R}_p$. In this case, for $\tilde{R}_p \to 0$, $L_b = \mathscr{O}(1)$ and thus the critical G_λ^F goes to infinity like $\tilde{R}_p^{-1}$ (see Fig. 5.9-(c)).
The same unrealistic result is obtained using the linear force model coupled with the elastic solid nucleus model (see Fig. 5.10-(a)). In this case, for very small radii, the energy required to deform the elastic nucleus grows as $\tilde{R}_p^{-4}$ and hence, under the linear force assumption, the critical G_μ^k goes linearly for $\tilde{R}_p \to 0$. On the other hand, when a constant force assumption is used, we have that $\overline{G}_\mu^F$ goes to infinity as $\tilde{R}_p^{-1}$, whereas limiting the adhesive region, it goes like $\tilde{R}_p^{-3}$, for $\tilde{R}_p \to 0$.
Fig. 5.10-(b) reports the results obtained applying the elastic solid nucleus model with the constant force assumption, whereas Fig. 5.10-(c) is obtained under the boundedness assumption. In both cases the relation between $\overline{G}_\mu^F$ and $\tilde{R}_p$ is a bijection. Therefore, for every $\tilde{R}_p$ it is possible to uniquely define a minimum value of G_μ^F above which the nucleus is pulled inside the channel, conversely knowing nuclear mechanical and active properties, the minimum value of R_p that allows the nucleus of radius R_n to enter the channel, is determined.

Table 5.4: Behaviours of $\overline{G}_\lambda$ and $\overline{G}_\mu$ for $\tilde{R}_p \to 0$

Model	Linear Force	Constant Force	Bounded adhesive region
Elastic membrane	$\overline{G}_\lambda^k = \mathscr{O}\left(\tilde{R}_p^3\right)$	$\overline{G}_\lambda^F = \mathscr{O}\left(\tilde{R}_p\right)$	$\overline{G}_\lambda^F = \mathscr{O}\left(\frac{1}{\tilde{R}_p}\right)$
Elastic nucleus	$\overline{G}_\mu^k = \mathscr{O}\left(\tilde{R}_p\right)$	$\overline{G}_\mu^F = \mathscr{O}\left(\frac{1}{\tilde{R}_p}\right)$	$\overline{G}_\mu^F = \mathscr{O}\left(\frac{1}{\tilde{R}_p^3}\right)$

Being the discrepancy between results obtained assuming the cigar-shaped and the ellipsoidal deformation very small, it is possible to use the analytical relation obtained for the ellipsoidal

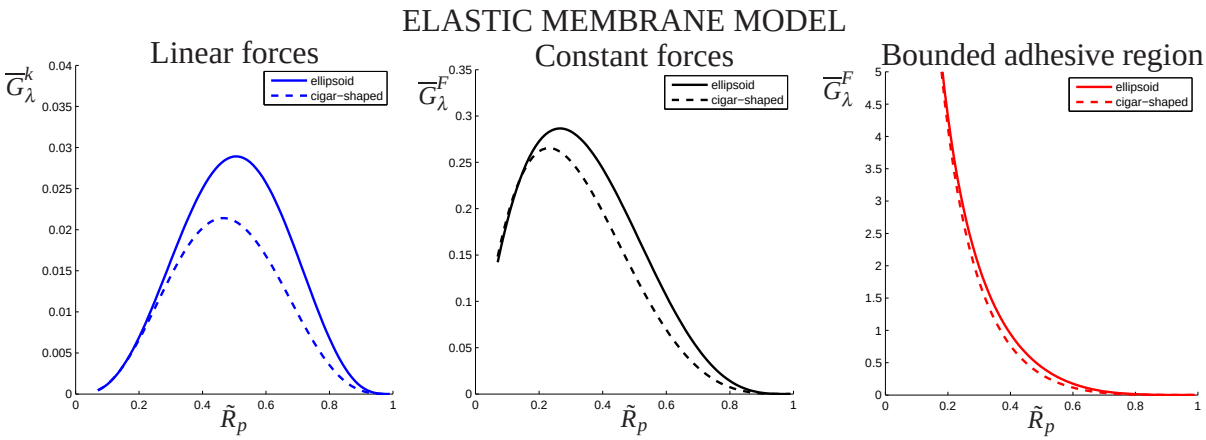

Figure 5.9: Elastic membrane model: (a) $\overline{G}^k_\lambda$ (in the case of linear forces), $\overline{G}^F_\lambda$ in the case of constant forces (b) and in the case of constant forces over a bounded region, with $\tilde{L}^M_b = 5$ (c). The curves indicate the minimum value of the characteristic numbers that need to be overcome in order to have the cell enter a channel of radius $\tilde{R}_p$.

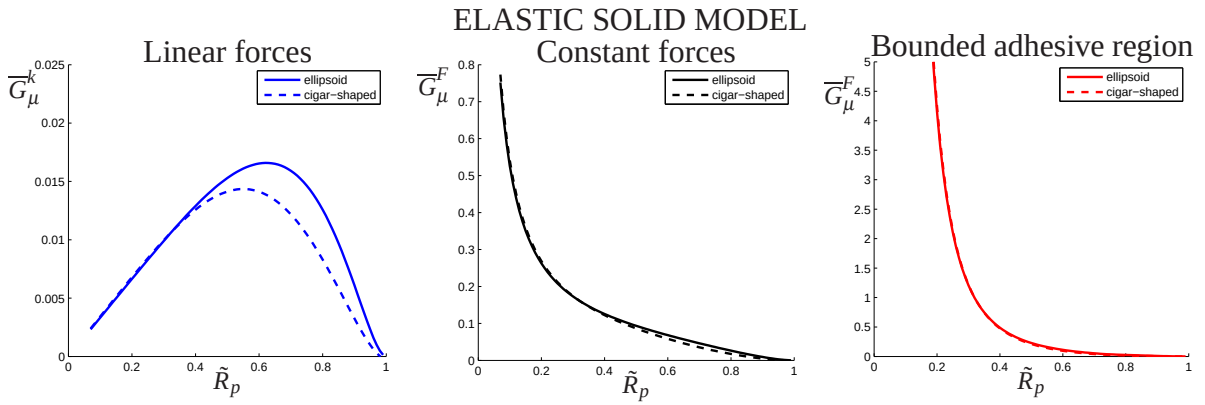

Figure 5.10: Elastic solid nucleus model: (a) $\overline{G}^k_\mu$ in the case of linear forces, (b) $\overline{G}^F_\mu$ in the case of constant forces and (c) $\overline{G}^F_\mu$ in the case of constant forces over a bounded region (with $\tilde{L}^M_b = 5$), above which the cell can enter a channel of radius $\tilde{R}_p$.

case

$$\overline{G}^F_\mu = \frac{2}{3}\frac{\left[2\tilde{R}_p^2 + \dfrac{1}{\tilde{R}_p^4} - 3\right]}{\tilde{R}_p \tilde{L}_b^{(*)} \Delta \tilde{L}_{ellips}}. \tag{5.47}$$

Being G^F_μ the ratio between active and mechanical properties, eq. (5.47) shows that with respect to cells with softer nuclei, in order to enter the same channel, more rigid cells (greater μ) should

either increase the number of adhesive bonds (ρ_b) or the number of focal points in contact with ECM (α_{ECM}) or even force strength (F_b^M). This finding is in qualitative agreement with a number of experimental works, such as [16, 127, 160], where cell migratory capability is associated with nuclear deformations and the existence of critical channel radius above which cell can enter has been observed. Moreover, it is comparable with the results obtained with discrete model [133, 134], confirming that mechanical properties of the nucleus can affect the cell entry into channels.

Eq. (5.47) can be of great value, for instance, in scaffold design. Indeed, assuming that cell mechanical properties and their capabilities to express bonds are known it is possible to evaluate the pore size that allows the cells to penetrate the rigid network.

5.6 Discussion

Due to the increasingly recognized importance of cell migration process in extracellular matrix environments and its exploitations, e.g., in tissue engineering, theoretical models, able to analyse the relative influence of single and interrelated parameters on the overall migratory process, are needed.

We identified some energy-based criteria that take into account the mechanical properties of cell nucleus, the adhesive characteristics of cell membrane, the active force generated through cytoskeleton contraction, the finiteness of the nucleus and the aspect ratio of the structures involved in cell migration, trying to maintain the model as simple as possible in order to obtain easily manageable results.

For the examples presented, some analytical results are obtained, providing the relation between active and mechanical properties that should be satisfied in order to have cells entering a channel of given radius. Therefore, knowing the adhesive, mechanical and contractile properties of the cell, it is possible to derive the minimum channel size and, conversely, observing experimentally the capability of a cell to enter cylindrical channels of different dimensions, it is possible to characterize the interplay between mechanical and active properties.

Results show that cells are able to enter ECM-networks only for pore radii bigger than a critical one, depending on the stiffness of the nucleus of the cell and their capabilities to express adhesion molecules in order to bind to the extracellular matrix. Indeed, a rigid cell body would nullify any attempt of the cell to squeeze through channels and network gaps narrower than the nucleus dimension, as observed in [127, 160].

Therefore the approach described here could be applied to the design of synthetic scaffolds,

with optimal values of pore size and fibre density, that may accelerate cell transport and ingrowth, critical for regenerative treatments (see Fig. 5.11(a)). Moreover results show that applying Darcy's law to describe the motion of a continuum of cells, we have to consider that the permeability depends not only on the geometry and dimensions of the pores, but also on the microscopic mechanical properties of cells nucleus. Indeed there is a region in which the permeability of the structure is null even though the radius of the pore is not null (see Fig. 5.11(b)).

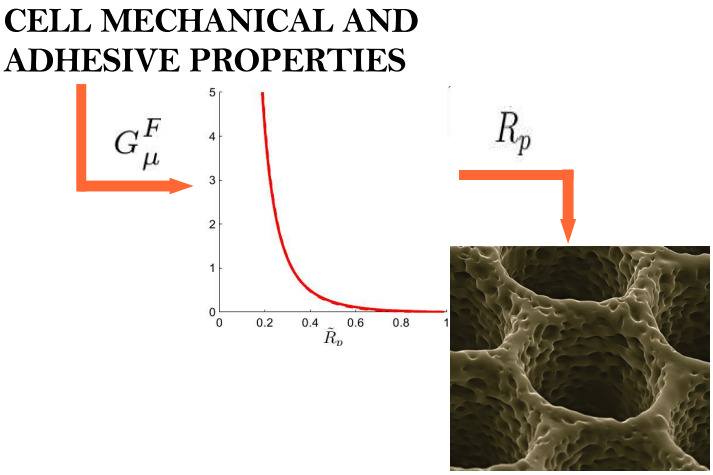

(a)

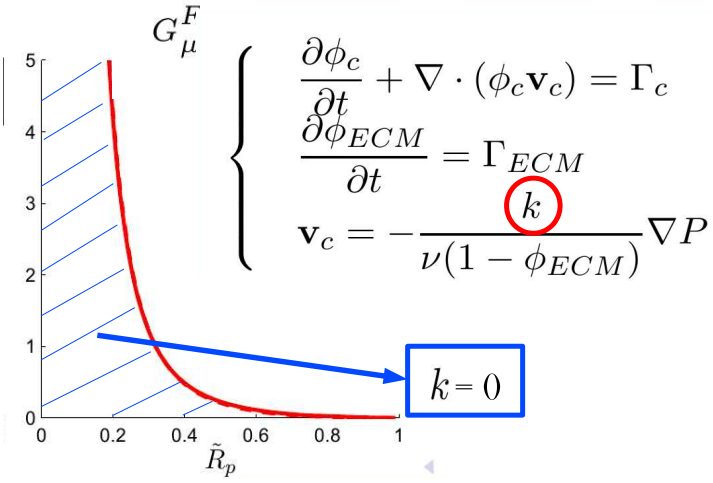

(b)

Figure 5.11: Application of the energetic model proposed: (a) determination of the minimum pore size in the design of scaffold with cylindrical channels; (b) definition of a region with null permeability.

However, in order to obtain reliable quantitative results, more studies are required, both from the biological and from the mathematical point of view. In particular, more experiments are needed in order to characterize cell mechanical response and a proper relation for the integrin-mediated active force. A more comprehensive understanding on the microscopical mechanism regulating nucleus deformation and cytoscheletal reorganization, when the cell is anchored to ECM, can also help to obtain a more realistic description of the process. Indeed, it has been observed that one of the major determinants of cell rigidity is the filamentous cytoskeleton. In particular, microtubules seem to be implicated in cell shape changes and migration, whereas actin filaments are generally considered more important for elastic resistance to deformation [92].
Moreover, biological experiments are necessary to validate the model presented, once the mechanical characterization of cells is accomplished.
From the mathematical point of view, the model can be improved in several directions in order to reproduce more closely the behavior of cells. For instance, in our ongoing work we want to study the whole dynamic process, considering all the steps of the cell entering the channel. Indeed, the model we proposed is based on an “integral" approach, i.e., it considers the total work required to pass from the initial to the final configuration and, thus, it gives an estimate of the “mean" active force required, scaled by the mechanical deformability of the nucleus. However, this method does not take into account the possible existence of intermediate states in which the force exerted by bounds should be greater than the force needed to squeeze the nucleus inside the channel. That is, the integral criterion used here to obtain analytical expressions gives a necessary but not sufficient condition for the passage of the cell inside the channel. Therefore, a criterion able to establish the maximum force needed would be more precise, though it requires 3D time-dependent numerical simulations.
Of course, one could use more realistic constitutive models representing cell response to stress (hopefully supported by experimental tests) and more complex relations for the active force exerted by the cytoskeleton. In order to obtain a model able to reproduce more closely the behaviour of cells, in particular, it seems very promising to study the active component that characterizes living matter response to external stimuli.

In spite of all possible developments, the energetic framework presented here is quite general and continues to be valid even for more complex cell and membrane constitutive assumptions.

Conclusions

This work presents some crucial aspects of cell and cellular aggregates mechanics. All the problems have been addressed in the continuum mechanics framework and referring to specific systems, relevant from the biophysical point of view.
Chapters 2, 3 and 4 are devoted to the macroscopic description of an ensemble of cells, whereas Chapter 5 refers to processes occurring at the cellular scale.
The results exposed in Chapter 2-3 and 4 represents a development of previous models [1, 3, 7, 115, 116]. The mathematical theory stands on known results, while the novelty of this contribution is in the application of such results to a comprehensive multiphase model, in which both the cellular and the liquid phase are considered, along with nutrients diffusion and the presence of the healthy tissue. In particular, the aim of these Chapters is the exploitation of the remodelling equation proposed in [7, 115] and its introduction into a complete model able to simulate a variety of physiological and pathological conditions.

In Chapter 2, we apply the theory of biphasic mixtures to the description of the uniaxial compression of a cylindrical sample of soft biological tissue. In this preliminary work, the internal structural changes are prescribed and constant in time. Therefore we do not have any evolution of the natural configuration. Starting from this approximation, we study how different ways of changing the internal structure of the solid phase (i.e. different choices of $\mathbb{F}_a$) influence the deformation and, thus, the displacement field, as well as the distribution of pressure inside the medium. We show that deviation from the sphericity of the anelastic tensor $\mathbb{F}_a$ affects the distribution of pressure inside the sample of soft biological material, which can be of great interest in all those biological processes in which the transport of substancesis fundamental.
The evolution of the natural configuration is considered in Chapter 3. Here, we propose a modification of the equation introduced in [7, 115], which empirically linked the evolution of internal structural changes to anelastic contributions due to the rupture of adhesive bonds. The new model is based on the existence of a yield criterion, above which cells reorganize. In particular, the

elasto-plastic model proposed in [115] is extended in order to incorporate the viscous contribution due to the fluid encapsulated in the cellular structure. The 3D elasto-visco-plastic model we derived is able to reproduce the dynamic observed during experiments, providing an explanation of the stress-relaxation phenomenon and of the dynamic observed during the stress-free shape recovery procedure. Indeed, the cyclic deformation test presented in [52] cannot be described only resorting on a surface tension model, whereas a model characterized by a yield condition, as the one presented here, can account for the phenomenologies observed during biomechanical experiments.
At the same time, thanks to the introduction of the viscous constituent, the model is able to reproduce aggregate release dynamics observed during biological experiments.
Moreover, in Chapter 4 we introduce into this framework the contribution due to cell proliferation. The model proposed is able to describe the remodelling and growth of a cellular spheroid, under different simulation settings. In particular we look at different stages of tumor progression: we first describe the mechanical response of a quiescent aggregate with a necrotic core. We show that if the imposed load is not able to trigger the internal reorganization of cells, the aggregate is able to bear the load even if the necrotic core is filled by liquid. We then consider the capability of cells to proliferate, when they are not subjected to an external mechanical stress and in the case in which the aggregate is compressed. Then, in order to give a more detailed description of the growth terms, nutrients are introduced. The continuum description of cell aggregates allows to introduce in the framework also the presence of the surrounding tissue, which would be computationally too expensive with a discrete model.
The model provided in Chapter 4 is therefore able to simulate the growth of a tumor spheroid, described as a biphasic material, taking into account anelastic deformations resulting both from growth processes and internal reorganization of cells. At the same time, thanks to the introduction of the liquid phase, the transport of nutrients regulating growth can be properly described. The model also allows to describe the surrounding tissue, in order to obtain a comprehensive model of tumor growth in-vivo.

Finally, in Chapter 5, we focus on the last stage of tumor progression: the detachment and migration of single cells across the surrounding extracellular environment in order to invade the whole organism. In particular, in recent year, it has gained attention the study of different factors involved in cell migration inside 3D structures, because it can be fundamental in order to assess the metastatic potential of cancer cells and it can be exploited in bioengineering studies, e.g., tissue engineering.

Despite the great importance of this subject, a mathematical model able to incorporate the mechanical properties of cells in the description of cell migratory process is still lacking.
We apply the tools provided by continuum mechanics in order to describe the effects of nucleus deformability on the process of cell migration inside cylindrical channels. In particular, we identified some energy-based criteria that take into account the mechanical properties of cell nucleus and the active characteristics of the cell, trying to maintain the model as simple as possible in order to obtain easily manageable results.
Results show that cells are able to enter inside cylindrical channels only if the lumen radius is bigger than a critical one, which depends on the rigidity of the nucleus and its capabilities to express molecules of adhesion in order to bind to the extracellular matrix. The results shown in Chapter 5 can therefore be of great value in the design of synthetic scaffolds, with optimal values of pore size and fiber density, that may accelerate cell in-growth, critical for regenerative treatments. Moreover the results highlight that applying Darcy's law to describe the motion of a continuum of cells, we have to consider that the permeability depends not only on the geometry and dimensions of the pores, but also on the microscopic mechanical properties of cells nucleus.

Even though, we are conscious that a realistic description of the mechanical behaviour of single cells and multicellular aggregates is still far from being achieved, we believe that this work provides the basis for a more detailed understanding of the influence of remodelling phenomena on tumor response to stress and on the interplay between remodelling and growth. Moreover, we provide some new hints on modelling the influence of nucleus deformability and the capability of cells to actively develop a force when anchored to the ECM, during the migratory process.
Of course, we are aware that the models presented in this Dissertation can be improved in several directions in order to reproduce more closely the behavior of cells and multicellular aggregates. In particular, future works, should be addressed to the derivation of the remodelling equation directly from microscopic measurements on the detachment forces of single adhesion bonds. Indeed the inclusion of microscopic information into continuum models and a rigorous mathematical theory to upscale data arising from the subcellular scale are still at their first stage. Moreover the simulation of the whole 3D process, both for the spheroid compression and growth problem, in absence of symmetry, and for the process of cell migration is highly required.
At the same time, from the biological point of view, more experiments are needed in order to characterize cell constitutive response to stress, to find a proper expression of the force arising from cytoskeletal contraction during cell movements into 3D environments and to better understand the microscopical mechanism regulating nucleus deformation and cytoscheletal reorganization. Moreover, biological experiments are necessary to validate the models presented and to

find realistic parameters.

In spite of all the possible improvements, the framework presented in this work is quite general and it continues to be valid even if more complicated relation for cell capability to reorganize, proliferate, adhere to the ECM and respond to stress are provided.

Bibliography

[1] D. Ambrosi, F. Mollica. *On the mechanics of a growing tumour.* Int. J. Engng. Sci., 40: 1297–1316 (2002).

[2] D. Ambrosi, L. Preziosi. *On the closure of mass balance models for tumor growth.* Math. Mod. Meth. Appl. Sci., 12(5): 737–754 (2002).

[3] D. Ambrosi, F. Mollica. *The role of stress in the growth of a multicellular spheroid.* J. Math. Biol., 48: 477–499 (2004).

[4] D. Ambrosi, F. Guana. *Stress modulated growth*. Math. Mech. Solids. 12(3): 319–343 (2007).

[5] D. Ambrosi, A. Guillou and E.S. Di Martino. *Stress-modulated remodelling of a non-homogeneous body*. Biomech. Model. Mechanobiol., 7(1): 63–76 (2008).

[6] D. Ambrosi, K. Garikipati, E. Kuhl. *Mechanics in biology: Cells and tissues*. Phil. Trans. R. Soc. A, 367: 3333–3334 (2009).

[7] D. Ambrosi, L. Preziosi. *Cell adhesion mechanisms and stress relaxation in the mechanics of tumours.* Biomech. Model. Mechanobiol., 8: 397–413 (2009).

[8] D. Ambrosi, A. Duperray, V. Peschetola, C. Verdier. *Traction patterns of tumor cells.* J. Math. Biol., 58: 163–181 (2009).

[9] D. Ambrosi, L. Preziosi, G. Vitale. *The insight of mixtures theory for growth and remodeling*. Z. Angew. Math. Phys., 61: 177–191 (2010).

[10] D. Ambrosi, L. Preziosi, G. Vitale. *The Interplay between Stress and Growth in Solid Tumors.* Mech. Res. Comm., 42: 87-91 (2012).

[11] R.P. Araujo, D.L.S. McElwain. *A History of the Study of Solid Tumour Growth: The Contribution of Mathematical Modelling*. Bulletin of Mathematical Biology., 66: 1039–1091 (2004).

[12] S. Astanin, L. Preziosi. *Multiphase models of tumour growth*. Selected Topics in Cancer Modelling: Genesis-Evolution- Immune Competition- Therapy, N. Bellomo, M. Chaplain, E. De Angelis Eds., Birkhäuser (2008).

[13] G.A. Ateshian, J.A. Weiss. *Anistropic Hydraulic Permeability Under Finite Deformation*. J Biomech Eng., 132 (2010).

[14] R.J. Atkin and R.E. Craine. *Continuum Theories of Mixtures: Basic Theory and Historical Development*. Quart. J. Mech. Appl. Math., 29: 209–244 (1976).

[15] W. Baumgartner, P. Hinterdorfer, W. Ness, A. Raab, D. Vestweber, H.D.D. Schindler. *Cadherin interaction probed by atomic force microscopy.* Proc. Nat. Acad. Sci. USA, 97: 4005–4010 (2000).

[16] C. Beadle, M.C. Assanah, P. Monzo, R. Vallee, S.S. Rosenfeld, P. Canoll. *The role of myosin II in glioma invasion of the brain*. Mol. Biol. Cell., 19: 3357–3368 (2008).

[17] N. Bellomo, L. Preziosi. *Modelling Mathematical Methods and Scientific Computation*. CRC Mathematical Modelling Series. N. Bellomo Eds. (1995).

[18] N. Bellomo, N.K. Li,P.K. Maini. *On the foundations of cancer modelling: Selected topics, speculations and perspectives.* Math. Models Methods Appl. Sci., 18: 593–646 (2008).

[19] L.S. Bennethum, M.A. Murad, J.H. Cushman. *Macroscale Thermodynamics and the Chemical Potential for Swelling Porous Media*. Transport in Porous Media, 39: 187–225 (2000).

[20] J. Bonet, R.D. Wood. *Nonlinear Continuum Mechanics for Finite Element Analysis*, Cambridge University Press, Cambridge, New York, Melbourne (2008).

[21] R.M. Bowen. *Theory of Mixtures*. Academic Press, Inc., New York. A.C. Eringen Ed. Vol. III: 1–127 (1976).

[22] C. Breward, H. Byrne, C. Lewis. *The role of cell-cell interactions in a two-phase model for avascular tumor growth.* J. Math. Biol., 45: 125–152 (2002).

[23] C. Breward, H. Byrne, C. Lewis. *A multiphase model describing vas- cular tumor growth.* Bull. Math. Biol., 65: 609–640 (2003).

[24] H. Byrne, J. King, D. McElwain, L. Preziosi, L. *A two-phase model of solid tumor growth.* Appl. Math. Letters, 16: 567–573 (2003).

[25] H. Byrne, L. Preziosi. *Modelling solid tumor growth using the theory of mixtures.* Math. Med. Biol., 20: 341–360 (2004).

[26] N. Caille, O. Thoumine, Y. Tardy, J.J. Meister. *Contribution of the nucleus to the mechanical properties of endothelial cells.* J Biomech. 35(2): 177–87 (2002).

[27] E. Canetta, A. Duperray, A. Leyrat, C. Verdier. *Measuring cell viscoelastic properties using a force-spectrometer: Influence of the protein-cytoplasm interactions*. Biorheology, 42: 298–303 (2005).

[28] R.M. Capito, M. Spector. *Scaffold-based articular cartilage repair*. IEEE Eng. Med. Biol. Mag., 22: 42–50 (2003).

[29] P. Cermelli, E. Fried, S. Sellers. *Configurational stress, yield and flow in rate-independent plasticity*. Proc. R. Soc. Lond. A., 457: 1447–1467 (2001).

[30] M.A. Chaplain. *Avascular growth, angiogenesis and vascular growth in solid tumors: the mathematical modelling of the stages of tumour development*. Math Comput. Modelling., 23(6): 47–87 (1996).

[31] M. Chaplain, L. Graziano, L. Preziosi. *Mathematical modelling of the loss of tissue compression responsiveness and its role in solid tumour development.* Math. Med. Biol., 23: 197–229 (2006).

[32] A. Chauvière, T. Hillen, L. Preziosi. *Modeling the motion of a cell population in the extracellular matrix*. Discr. Cont. Dyn. Sys. (Supplements), Special Issue: 250–259 (2007).

[33] A. Chauvière, T. Hillen, L. Preziosi. *Modeling cell movement in anisotropic and heterogeneous network tissues*. Netw. Heterog. Media, 2(2): 333–357, (2007).

[34] C.S. Chen, J. Tan,J. Tien. *Mechanotransduction at cell-matrix and cell-cell contacts.* Annu. Rev. Biomed. Eng., 6: 275–302 (2004).

[35] S. Chien, S. Usami, R.J. Dellenback, M. I. Gregersen. *Blood viscosity: Influence of erythrocyte deformation.* Science, 157: 827–829 (1967).

[36] S. Chien, S. Usami, R.J. Dellenback, M. I. Gregersen, L. B. Nanninga, M. Mason-Guest. *Blood viscosity: Influence of erythrocyte aggregation.* Science, 157: 829–831 (1967).

[37] S. Chien, K.L.P. Sung, R. Skalak, S. Usami, A.C. Usami. *Theoretical and experimental studies on viscoelastic properties of erythrocyte membrane*. Biophys. J., 24: 463–487 (1978).

[38] B.D. Coleman, W. Noll. *Foundations of linear viscoelasticity.* Rev. Modern. Phys., 33: 329–349 (1961).

[39] M. Dembo, Y.L. Wang. *Stresses at the cell-to-substrate interface during locomotion of fibroblasts.* Biophys. J., 76(4): 2307–2316 (1999).

[40] A. Di Carlo and S. Quiligotti. *Growth and Balance*. Mech. Res. Comm., 29: 449–456 (2002).

[41] R.E. Durand. *Multicellular spheroids as a model for cell kinetic studies.* Cell Tissue Kinet., 23: 141–159 (1990).

[42] W. Ehlers, B. Markert. *A linear viscoelastic biphasic model for soft tissues based on the theory of porous media*. J Biomech Eng., 123: 418–424 (2001).

[43] M. Epstein and G. A. Maugin. *Thermomechanics of volumetric growth in uniform bodies*. Int. J. Plasticity, 16: 951–978 (2000).

[44] A.C. Eringen, *Mechanics of Continua.* Huntington, New York, R.E. Krieger Publ. Co. 2nd edition (1980).

[45] E.A. Evans. *New membrane concept applied to the analysis of fluid shear and micropipette-deformed red blood cells.* Biophys. J., 13: 941–954 (1973).

[46] E.A. Evans, R. Waugh, L. Melnik *Elastic area compressibility modulus of red cell membrane.* Biophys. J., 16: 585–595 (1976).

[47] E.A. Evans, B. Kukan. *Passive material behavior of granulocytes based on large deformations and recovery after deformation tests.* Blood. 64: 1028–1035 (1984).

[48] E.A. Evans, A. Yeung. *Apparent viscosity and cortical tension of blood granulocytes determined by micropipet aspiration.* Biophys. J., 56: 151–160 (1989).

[49] S. Federico, A. Grillo. *Elasticity and permeability of porous fibre-reinforced materials under large deformations*. Mech. Materials, 44: 58–71 (2012).

[50] J. Folkman. *Tumor angiogeneses*. Cancer, 3: 355–388 (1975).

[51] J. Folkman. *The vascularization of tumors*. Sci. Am., 234: 58–73 (1976).

[52] G. Forgacs, R.A. Foty, Y. Shafrir, M.S. Steinberg. *Viscoelastic properties of living embryonic tissues: A quantitative study.* Biophys. J., 74: 2227–2234 (1998).

[53] R.A. Foty, G. Forgacs, C.M. Pfleger, M.S. Steinberg. *Liquid properties of embryonic tissues: Measurement of interfacial tensions.* Phys. Rev. Lett., 72: 2298–2301 (1994).

[54] R.A. Foty, G. Forgacs, C.M. Pfleger, M.S. Steinberg. *Surface tensions of embryonic tissues predict their mutual envelopment behavior.* Development, 122: 1611–1620 (1996).

[55] S. Franks, H. Byrne, H. Mudhar, J. Underwood, C. Lewis. *Mathematical modelling of comedo ductal carcinoma in situ of the breast.* Math. Med. Biol., 20: 277–308 (2003).

[56] J.P. Freyer, P.L. Schor. *Regrowth of cells from multicell tumour spheroids.* Cell Tissue Kinet., 20(249) (1987).

[57] J.P. Freyer. *Role of necrosis in regulating the growth saturation of multicellular spheroids.* Cancer Res., 48(9): 2432–2439 (1988).

[58] P. Friedl, E.B. Brocker. *The biology of cell locomotion within three-dimensional extracellular matrix*. Cell. Mol. Life Sci., 57(1): 41–64 (2000).

[59] P. Friedl, K. Wolf. *Tumour-cell invasion and migration: diversity and escape mechanisms*. Nat. Rev. Cancer., 3(5): 362–374 (2003).

[60] P. Friedl, B. Weigelin. *Interstitial leukocyte migration and immune function.* Nat Immunol., 9(9): 960–969 (2008).

[61] P. Friedl, K. Wolf. *Proteolytic interstitial cell migration: a five-step process*. Cancer Metastasis Rev., 28(1-2): 129–135 (2009).

[62] P. Friedl, K, Wolf, J. Lammerding. *Nuclear mechanics during cell migration*. Curr. Opin. Cell. Biol., 23(1): 55–64 (2011).

[63] Y.C. Fung. *Microrheology and constitutive equation of soft tissue.* Biorheology, 25: 261–270 (1978).

[64] Y.C. Fung. *Motion, Flow, Stress, and Growth*. Springer-Verlag Inc., New York (1990).

[65] L. Fusi, A. Farina, D. Ambrosi. *Mathematical modelling of solid liquid mixture with mass exchange between constituents*. Math. Mech. Solids, 11(6): 575–595 (2006).

[66] G. Gerlitz, M. Bustin. *The role of chromatin structure in cell migration*. Trends Cell. Biol., 21(1): 6–11 (2011).

[67] F. Graner, J. A. Glazier. *Simulation of biological cell sorting using a two-dimensional extended potts model*. Phys. Rev. Let., 69: 2013–2016 (1992).

[68] L. Graziano, L. Preziosi. *Mechanics in tumor growth*. Modeling of Biological Materials. Series: Modeling and Simulation in Science, Engineering and Technology. F. Mollica, L. Preziosi, K.R. Rajagopal Eds. BirkhÃd'user Basel (2007).

[69] H.P. Greenspan. *On the growth and stability of cell cultures and solid tumours.* J. Theor. Biol., 56: 229–242 (1976).

[70] A. Grillo, G. Zingali, D. Borrello, G. Giaquinta. *Transport phenomena in living systems and continuum physics*. La Rivista del Nuovo Cimento, 11(31): 485–562 (2007).

[71] A. Grillo, S. Federico, G. Wittum, S. Imatani, G. Giaquinta, M.V. Mićunović. *Evolution of a fibre-reinforced growing mixture*. Il Nuovo Cimento, 1(32 C): 97–119 (2009).

[72] A. Grillo, G. Wittum, G. Giaquinta, M.V. and Mićunović. *A multiscale analysis of growth and diffusion dynamics in biological materials*. Int. J. Eng. Sci., 47: 261–283 (2009).

[73] A. Grillo, A., S. Federico, G. Wittum. *Growth, mass transfer, and remodeling in fiber-reinforced, multi-constituent materials*. Int. J. Non-Linear Mech., 47: 388âĂŞ-401 (2012).

[74] A. Grillo, C. Giverso, M. Favino, R. Krause, M. Lampe, G. Wittum. *Mass Transport in Porous Media with Variable Mass*. Numerical Analysis of Heat and Mass Transfer in Porous Media. A. Oechsner, L.F.M. da Silva, H. Altenbach Eds. Springer Verlag Germany (2012).

[75] K. Groeber, W. Mueller-Klieser. *Distributions of oxygen, nutrient and metabolic waste concentrations in multicellular spheroids and their dependence on spheroid parameters.* Eur. Biophys. J., 19: 169–181 (1991).

[76] J. Guck, F. Lautenschläger, S. Paschke, M. Beil. *Critical review: cellular mechanobiology and amoeboid migration*. Integr. Biol., 2: 575–583 (2010).

[77] M.E. Gurtin, E. Fried, L. Anand. *The Mechanics and Thermodynamics of Continua.* Cambridge University Press, Cambridge, New York, Melbourne (2010).

[78] G. Hamilton. *Multicellular spheroids as an in vitro tumour model*, Cancer Lett., 131: 29–34 (1998).

[79] B.A.C. Harley, H. Kim, M.H. Zaman, I.V. Yannas, D.A. Lauffenburger, L.J. Gibson. *Microarchitecture of three-dimensional scaffolds influences cell migration behavior via junction interactions*. Biophys J., 95(8): 4013–4024 (2008).

[80] S.M. Hassanizadeh, W.G. Gray. *Derivation of Conditions Describing Transport Across Zones of Reduced Dynamics Within Multiphase Systems*. Water Resources Res., 25: 529–539 (1989).

[81] R.J. Hawkins, M. Piel, G. Faure-Andre, A.M. Lennon-Dumenil, J.F. Joanny, J. Prost, R.Voituriez. *Pushing off the walls: a mechanism of cell motility in confinement.* Phys. Rev. Lett. 102 (5), 058103 (2009).

[82] W. Helfrick. *Elastic properties of lipid bilayers: theory and possible experiments*. Z. Naturforsch, 28c: 693–703 (1973).

[83] R.M. Hochmuth. *Measuring the mechanical properties of individual human blood cells.* J Biomech Eng., 115(4B): 515–519 (1993)

[84] R.M. Hochmuth. *Micropipette aspiration of living cells.* J. Biomech., 33: 15–22 (2000).

[85] M.H. Holmes, V. C. Mow. *The nonlinear characteristics of soft gels and hydrated connective tissues in ultrafiltration.* J. Biomech., 23(11): 1145–1156 (1990).

[86] J. Humphrey, K. Rajagopal. *A constrained mixture model for growth and remodeling of soft tissues.* Math. Mod. Meth. Appl. Sci., 22: 407–430 (2002).

[87] J. Humphrey, K. Rajagopal. *A constrained mixture model for arterial adaptations to a sustained step change in blood flow.* Biomech. Model. Mechanobiol., 2: 109–126 (2003).

[88] D.E. Ingber. *Cellular tensegrity: defining new rules of biological design that govern the cytoskeleton*. J. Cell Sci., 104: 613–627 (1993).

[89] D.E. Ingber. *Tensegrity I. Cell structure and hierarchical systems biology*. J. Cell Science, 116 (7): 1157–1173 (2003).

[90] A. Iordan, A. Duperray, C. Verdier. *Fractal approach to the rheology of concentrated cell suspensions.* Phys. Rev. E, 7: 011911 (2008).

[91] W.R. Jones, H.P. Ting-Beall, G.M. Lee, S.S. Kelley, R.M. Hochmuth, F. Guilak. *Alterations in the Young's modulus and volumetric properties of chondrocytes isolated from normal and osteoarthritic human cartilage*. J. Biomech., 32(2): 119–127 (1999).

[92] T.P. Kole, Y. Tseng, I. Jiang, J.L. Katz, D. Wirtz. *Intracellular mechanics of migrating fibroblasts*. Mol. Biol. Cell., 16: 328–338 (2005)

[93] S. Kumar, V.M. Weaver. *Mechanics, malignancy, and metastasis: The force journey of a tumor cell*. Cancer Metastasis Rev., 28: 113–127 (2009).

[94] R.M. Kuntz, W.M. Saltzman. *Neutrophil motility in extracellular matrix gels: mesh size*

and adhesion affect speed of migration. Biophys. J., 72(3): 1472–1480 (1997).

[95] L.A. Kunz-Schughart, M. Kreutz, R. Knuechel. *Multicellular spheroids: a three-dimensional in vitro culture system to study tumour biology*. Int. J. Exp. Path., 79: 1–23 (1998)

[96] T. Lämmermann, B.L. Bader, S.J. Monkley, T. Worbs, R. Wedlich-Söldner, K. Hirsch, M. Keller, R. Förster, D.R. Critchley, R. Fässler, M. Sixt. *Rapid leukocyte migration by integrin-independent flowing and squeezing*. Nature 453: 51-55 (2008).

[97] F. Lautenschläger, S. Paschke, S. Schinkinger, A. Bruel, M. Beil, J. Guck. *The regulatory role of cell mechanics for migration of differentiating myeloid cells*. Proc. Nat. Acad. Sci. USA, 106(37): 15696–15701 (2009).

[98] E.H. Lee. *Elastic-plastic deformation at finite strains*. ASME Transaction on J. Appl. Mech., 36: 1-6 (1969).

[99] W.R. Legant, J.S. Miller, B.L. Blakely, D.M. Cohen, G.M. Genin, C.S. Chen. *Measurement of mechanical tractions exerted by cells in three-dimensional matrices.* Nat. Methods, 7(12): 969–971 (2010).

[100] M. Lekka, P. Laidler, D. Gil, J. Lekki, Z. Stachura, A.Z. Hrynkiewicz. *Elasticity of normal and cancerous bladder cells studied by scanning force microscopy.* Eur. Biophys. J., 28: 312–316 (1999).

[101] K. Liu. *Deformation behaviour of soft particles: a review*. J. Phys. D: Appl. Phys., 39: 189–199 (2006).

[102] B. Loret, F.M.F. Simões. *A framework for deformation, generalized diffusion, mass transfer and growth in multi-species multi-phase biological tissues.* Eur. J. Mech. A/Solids, 24: 757–781 (2005).

[103] J.S Lowengrub, H.B Frieboes, F. Jin, Y.L Chuang, X. Li, P. Macklin, S.M. Wise, V. Cristini. *Nonlinear modelling of cancer: bridging the gap between cells and tumours*. Nonlinearity, 23: R1–R91 (2010).

[104] V. A. Lubarda and A. Hoger. *On the Mechanics of Solids with a Growing Mass*. Int. J. Solids and Structures, 39: 4627–4664 (2002).

[105] J.E. Marsden, T.J.R. Hughes. *Mathematical Foundations of Elasticity*. Prentice-Hall, Englewood Cliffs, N.J. (1983).

[106] W. Mueller-Klieser. *Multicellular spheroids: a review on cellular aggregates in cancer research*. J. Cancer Res. Clin. Oncol., 113: 101–122 (1987).

[107] R.W. Ogden. *Non-Linear Elastic Deformations*. Dover Publications, INC. Mineola, New York (1984).

[108] T. Olsson, A. Klarbring. *Residual stresses in soft tissue as a consequence of growth and remodeling: application to an arterial geometry.* Eur. J. Mech. A/Solids, 27: 959–974 (2008).

[109] K.J. Painter. *Modelling cell migration strategies in the extracellular matrix*. J. Math. Biol., 58: 511–543 (2009).

[110] P. Panorchan, M.S. Thompson, K.J. Davis, Y. Tseng, K. Konstantopoulos, D. Wirtz. *Single-molecule analysis of cadherin-mediated cell-cell adhesion.* J. Cell Sci., 119: 66–74 (2006).

[111] M.J. Paszek, N. Zahir, K.R. Johnson, J.N. Lakins, G.I. Rozenberg, A. Gefen, C.A. Reinhart-King, S.S. Margulies, M. Dembo, D. Boettiger, D.A. Hammer, and V. M. Weaver. *Tensional homeostasis and the malignant phenotype.* Cancer Cell, 8: 241-254 (2005).

[112] V. Peschetola, V. Laurent, A. Duperray, R. Michel, D. Ambrosi, L. Preziosi, C. Verdier. *Time-dependent traction force microscopy for cancer cells as a measure of invasiveness*. [submitted]

[113] C.P. Please, G.J. Pettet, D.L.S. McElwain. *A new approach to modelling the formation of necrotic regions in tumours.* Appl. Math. Lett., 11: 89–94 (1998).

[114] C.P. Please, G.J. Pettet, D.L.S. McElwain. *Avascular tumour dynamics and necrosis.* Math. Models Methods Appl. Sci., 9: 569–579 (1999).

[115] L. Preziosi, D. Ambrosi, C. Verdier. *An elasto-visco-plastic model of cell aggregates*. J. Theor. Biol., 262: 35–47 (2010).

[116] L. Preziosi, G. Vitale. *A multiphase model of tumour and tissue growth including cell adhesion and plastic reorganisation.* Math. Mod. Meth. Appl. Sci., 21(9): 1901–1932 (2011).

[117] L. Preziosi, G. Vitale. *Mechanical aspects of tumour growth: Multiphase modelling, adhesion, and evolving natural configurations*, in M. Ben Amar, A. Goriely, M. M. Müller, L. F. Cugliandolo, Eds., New Trends in the Physics and Mechanics of Biological Systems, Lecture Notes of the Les Houches Summer School, 92: 177-228, Oxford University Press (2011).

[118] S. Quiligotti. *On bulk growth mechanics of solid-fluid mixtures: kinematics and invariance requirements*. Theor. and Appl. Mech., 28–29: 277–288 (2002).

[119] K.R. Rajagopal, L. Tao. *Mechanics of Mixtures*. Advances in Mathematics for Applied Sciences. World Scientific, Singapore. Vol. 35 (1995).

[120] K.R. Rajagopal. *Multiple natural configurations in continuum mechanics*. Rep. Inst. Comput. Appl. Mech., 6 (1995).

[121] K.R. Rajagopal, A.R. Srinivasa. *Mechanics of the inelastic behavior of materials - Part I, theoretical underpinning*. Int. J. Plast., 14: 945–967 (1998).

[122] K.R. Rajagopal, A.R. Srinivasa. *Mechanics of the inelastic behavior of materials - Part II: inelastic response*. Int. J. Plast., 14: 969–995 (1998).

[123] K.R. Rajagopal, A.R. Srinivasa. *On thermodynamical restrictions of continua*. Proc. R. Soc. Lond. A., 460: 631–651 (2004).

[124] J. Renkawitz, M. Sixt. *Mechanisms of force generation and force transmission during interstitial leukocyte migration.* EMBO Rep. 11(10): 744-50 (2010).

[125] R.T. Rockafellar. *Convex Analysis*. Princeton University Press, Princeton, NJ. (1970).

[126] E.K. Rodriguez, A. Hoger, A. McCulloch. *Stress-dependent finite growth in soft elastic tissues*. J. Biomech., 27: 455–467 (1994).

[127] C.G. Rolli, T. Seufferlein, R. Kemkemer, J.P. Spatz. *Impact of tumor cell cytoskeleton organization on invasiveness and migration: A microchannel-based approach*. PLos ONE, 5(1): e8726 (2010).

[128] F. Sabeh, R. Shimizu-Hirota, S.J. Weiss. *Protease-dependent versus -independent cancer cell invasion programs: three-dimensional amoeboid movement revisited*. J. Cell. Biol., 185(1): 11–19 (2009).

[129] E. Sahai. *Illuminating the metastatic process*. Nat. Rev. Cancer, 7(10): 737–749 (2007).

[130] P. Saramito. *A new constitutive equation for elastoviscoplastic fluid flows.* J. Non-Newtonian Fluid Mech., 145: 1–14 (2007).

[131] P. Saramito. *A new elastoviscoplastic model based on the Herschel-Bulkley viscoplasticity.* J. Non-Newtonian Fluid Mech., 158: 154–161 (2009).

[132] G.W. Schmid-Schonbein, Y. Y. Shih, S. Chien. *Morphometry of human leukocytes*. Blood, 56: 866–875 (1980).

[133] M. Scianna, L. Preziosi, K. Wolf. *A Cellular Potts Model simulating cell migration on and in matrix environments.* Math. Biosci. Engng. [in press] (2013).

[134] M. Scianna, L. Preziosi. *Modelling the influence of nucleus elasticity on cell invasion in fiber networks and microchannels*. [submitted]

[135] J.A. Sherratt, M.A. Chaplain. *A new mathematical model for avascular tumour growth*. J. Math. Biol., 43: 291–312 (2001)

[136] R. Skalak. *Modelling the mechanical behavior of red blood cells*. Biorheology. 19: 229–238 (1973).

[137] R. Skalak, A. Tozeren, R.P. Zarda, S. Chien. *Strain energy function of red blood cell membrane*. Biophys. J., 13: 245–264 (1973).

[138] A.R. Skovoroda, A.N. Klishko, D.A. Gusakyan, Y.I. Mayevskii, V.D. Yermilova, G.A. Oranskaya, A.P. Sarvazyan. *Quantitative analysis of the mechanical characteristics*

of pathologically changed soft biological tissues. Biophysics, 40: 1359–1995 (1995).

[139] M. Sun, J. Graham, B. Hegedus, F. Marga, Y. Zhang, G. Forgacs, M. Grandbois. *Multiple membrane tethers probed by atomic force microscopy*. Biophys. J., 89: 4320–4329 (2005).

[140] R.M. Sutherland, J.A. McCredie, W.R. Inch. *Growth of multicell spheroids in tissue culture as a model of nodular carcinomas*. J. Natl. Cancer Inst., 46: 113–120 (1971)

[141] R.M. Sutherland. *Cell and environment interactions in tumour microregions: the multicell spheroid model*. Science, 240: 177–184 (1988).

[142] R.M. Sutherland, R.E. Durand. *Growth and cellular chacteristics of multicell spheroids*. Recent Results in Cancer Res., 95: 24–49 (1984).

[143] L.A. Taber. *Biomechanics of growth, remodeling and morphogenesis*. ASME Appl. Mech. Rev., 48: 487–545(1995).

[144] L.A. Taber, J.D. Humphrey. *Stress-modulated growth, residual stress, and vascular heterogeneity*. J. Biomech. Eng., 123: 528–535 (2001).

[145] D.P. Theret, M.L. Levesque, M. Sato, R.M. Nerem, L.T. Wheeler. *The application of a homogeneous half-space model in the analysis of endothelial cell micropipette measurements*. J. Biomech. Eng., 110: 190–199 (1988).

[146] R.H. Thomlinson, L.H. Gray. *Histological structure of some human lung cancers and the possible implications for radiotherapy*. Brit. J. Cancer., 9: 539–549 (1955).

[147] C.A. Truesdell. *Sulle basi della termomeccanica*. Lincei - Rend. Sc. Fis. Mat. Nat., 22: 33–38 (1957).

[148] C. Truesdell, R. Toupin. *The classical field theories.* Handbuch der Physik (ed. S. Flügge), Vol. 3. Springer (1960).

[149] G. A. Truskey, F. Yuan, D.F. Katz. *Transport phenomena in biological systems.* Prentice Hall (2009).

[150] Z.C. Tu, Z.C. Ou-Yang. *Geometric theory on the elasticity of bio-membranes*. J. Phys. A: Math. Gen., 37: 11407–11429 (2004).

[151] Z.C. Tu, Z.C. Ou-Yang. *Elastic theory of low-dimensional continua and its applications in bio- and nano-structures*. J. Comput. Theor. Nanosci., 5: 422–448 (2008).

[152] N.H. Valerius, O. Stendahl, J.H. Hardwig, T.P. Stossel. *Distribution of actin-binding protein and myosin in polymorphonuclear leukocytes during locomotion and phagocytosis.* Cell, 24: 195–202 (1981).

[153] A. Vaziri, A. Gopinath. *Cell and biomolecular mechanics in silico*. Nat. Materials, 7: 15–23 (2008).

[154] C. Verdier. *Review. Rheological properties of living materials: From cells to tissues.* J.

Theor. Medicine, 5: 67–91 (2003).

[155] C. Verdier, J. Etienne, A. Duperray, L. Preziosi. *Review: Rheological properties of biological materials*. C. R. Phys., 10: 790–811 (2009).

[156] M. Versaevel, T. Grevesse, S. Gabriele. *Spatial coordination between cell and nuclear shape within micropatterned endothelial cells*. Nature Comm., 3 (2012).

[157] R. Waugh, E.A. Evans. *Thermoelasticity of red blood cell membrane*. Biophys. J., 26: 115–132 (1979).

[158] E. Wibe, T. Lindmo, O. Kaalhus. *Cell kinetic chacteristics in different parts of multicellular spheroids of human origin.* Cell Tissue Kinet., 14: 639–651 (1981).

[159] B.S. Winters, S.R. Shepard, R.A. Foty. *Biophysical measurement of brain tumor cohesion.* Int. J. Cancer, 114: 371–379 (2005).

[160] K. Wolf, Y.I. Wu, Y. Liu, J. Geiger, E. Tam, C. Overall, M.S. Stack, P. Friedl. *Multistep pericellular proteolysis controls the transition from individual to collective cancer cell invasion*. Nat. Cell. Biol., 9: 893–904 (2007).

[161] K. Wolf, S. Alexander, V. Schacht, L.M Coussens, U.H von Andrian, J. van Rheenen, E. Deryugina, P. Friedl. *Collagen-based cell migration models in vitro and in vivo*. Semin. Cell. Dev. Biol., 20(8): 931–941 (2009).

[162] K. Wolf, P. Friedl. *Extracellular matrix determinants of proteolytic and non-proteolytic cell migration*. Trends. Cell. Biol., 21(12): 736–744 (2011).

[163] I.V. Yannas, E. Lee, D.P. Orgill, E.M. Skrabut, G.F. Murphy. *Synthesis and characterization of a model extracellular matrix that induces partial regeneration of adult mammalian skin*. Proc. Natl. Acad. Sci. USA, 86: 933–937 (1989).

[164] A. Yeung, E. Evans. *Cortical shell-liquid core model for passive flow of liquid-like spherical cells into micropipets*. Biophys. J., 56: 139–149 (1989).